UNIVERSITY OF ADELAIDE LIBRARY
3.2.99

CROSSHOLE RESISTIVITY AND ACOUSTIC VELOCITY IMAGING: 2.5-D HELMHOLTZ EQUATION MODELING AND INVERSION

by

Zhou Bing

B.Sc., M.Sc. (China)

Department of Geology and Geophysics

The University of Adelaide

SA 5005, Australia

Submitted in fulfillment of the requirements for
the degree of Doctor of Philosophy

September 1998

Contents

Abstract

Crosshole resistivity and seismic velocity imaging (diffraction tomography or waveform inversion with the acoustic approximation) are two very useful techniques in geophysical exploration, because they may be employed to map conductivity or velocity inhomogeneities (geological anomalies) between boreholes. Such imaging techniques, when considered in mathematical terms, both reduce to 2.5-D Helmholtz equation modeling and inversion. This thesis presents (1) new finite element solutions for two specified forms of this kind of equation, which define 2.5-D resistivity and 2.5-D acoustic wave problems, as well as an extension to 2.5-D elastic waves solution; (2) iterative algorithms for tackling inversion problems, including Tikhonov regularisation, the smoothest model solution and the subspace solution, in which the generalised algorithms and their inter-relations are formulated, and new approximations for the Fréchet and second derivatives are developed; (3) numerical and physical model experiments for crosshole resistivity imaging with different electrode arrays (or configurations) and synthetic simulations for crosshole acoustic velocity imaging with different full-waveform spectral data (real and imaginary components, amplitude and phase, and the Hartley spectra).

The modeling examples for resistivity and acoustic wavefield show that the presented methods are effective and flexible to compute the 3-D physical response for 2-D arbitrary media. Furthermore, it is shown that the accuracy of the modeling mainly depends upon the wavenumber range and the number of wavenumber samples, both of which can be evaluated in terms of the typical shape of the transformed potential in the resistivity case and the critical values of the wavenumber of the media around the seismic source in the acoustic wave case, respectively. The constant-point approximation based on the explicit expressions for the Fréchet and second derivatives has been shown to be a robust and efficient algorithm for inversion. The numerical and physical imaging experiments show that some specified three- and four-electrode arrays are more suitable for crosshole resistivity imaging than the pole-pole array. For acoustic imaging with spectral data, the real and imaginary components, the Fourier amplitude

and the Hartley spectra are suitable for full-waveform inversion with a known source wavelet, but the phase data do not permit satisfactory object field reconstruction. It is shown in the thesis that the normalised Fourier/Hartley spectral data can be used for imaging when the seismic source wavelet is unknown.

Statement

This work contains no material which has been accepted for the award of any degree or diploma in any university or other tertiary institution and, to the best of my knowledge and belief, contains no material previously published or written by another person, except where due reference has been made in the text.

I give consent to this copy of my thesis, when deposited in the University Library, being available for loan and photocopying.

Zhou Bing

September 30, 1998

Acknowledgments

This thesis would have been impossible without the support and encouragement of my supervisor, Professor Stewart Greenhalgh, who often gave me constructive suggestions and helpful opinions to my project. He also spent much time on correcting the text, the formulations and the results of the thesis so as to reach its present state.

I particularly want to thank Dr. Shunhua Cao for some useful discussion and providing me with the LU program code for when I studied the 2.5-D acoustic wave modeling. Dr. Deepak Raj Pant supplied me with physical modeling (laboratory) data for resistivity imaging tests.

I also greatly appreciate the following people: Mr. Jingping Zhe, Mr. Thomas Gruber and Miss Samantha Bierbaum for their kind help during my PhD study.

This work has been supported by an Australian Overseas Postgraduate Research Scholarships taken up at Flinders University (April,1995-November,1997) and The University of Adelaide (December, 1997-September, 1998).

Finally, I wish to thank my family for their help and moral support.

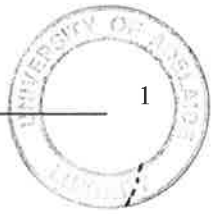

Chapter 1
Introduction

1.1 Crosshole Resistivity Imaging

Direct current (DC) electric surveying (sounding and profiling) along the Earth's surface is a well known geophysical exploration technique. Due to its conceptual simplicity, low equipment cost and ease of use, the method is widely applied to mining exploration, archaeological detection, civil and hydrologic engineering, and environmental investigations. In traditional DC electrical resistivity surveying, various current-potential electrode arrangements, such as pole-pole, pole-bipole, bipole-pole and bipole-bipole (dipole-dipole) arrays, are used, depending on the prospecting goals and the surface situation(e.g. site access). With greater computer power made available in recent years, there has been increasing interest in DC resistivity imaging based on geophysical inversion theory. A number of research articles have appeared on 2-D and 3-D DC resistivity imaging using surface scanning pole-pole and bipole-bipole data (Smith and Vozoff, 1984; Park and Van, 1991; Li and Oldenburg, 1992; Eill and Oldenburg, 1994b; Dabas et al., 1994; Sasaki, 1994; Zhang et al., 1995; Loke and Barker, 1995, 1996). Xu and Noel (1993) discussed some independent measurements of the surface surveys using two-, three- and four-electrode configurations for the 2-D or 3-D resistivity imaging.

Crosshole DC electrical surveying, in which the source electrode (current injection point) and the potential electrode (measuring point) are placed downhole in two horizontally separated boreholes and moved over a range of depths, is able to yield detailed information on the variation of electrical conductivity between the boreholes (Daniels, 1977, 1984; Shima, 1992). Such crosshole measurements permit the detection and delineation of interesting geological conditions between various source and detector locations. They offer potential advantages for greatly improving the effectiveness of a test boring program by locating the targets more accurately. Furthermore, the downhole electric measurements greatly extend the anomaly detection capability beyond the

performance limits of surface electric surveying. Owen (1983) discussed crosshole bipole-bipole electric surveying to search for buried caves and tunnels. Daniels and Dyck (1984) demonstrated a variety of applications of the borehole resistivity measurements to mineral exploration. Unfortunately, they did not intend to image the targets under the ground.

In recent years, there has been great interest in developing crosshole DC electrical surveying so as to image the 2-D and 3-D structure of the earth. Crosshole resistivity imaging or tomography (Daily and Owen, 1991; Shima, 1992) is used to reconstruct the conductivity structure of the earth using crosshole scanning data. In theory, the technique is no more than a geophysical inversion procedure with various array aperture data. With the merits of crosshole measurements, it is possible to image the targets between the boreholes. Most researchers have dealt with crosshole resistivity imaging using pole-pole array data (e.g. Daily and Owen, 1991; Shima, 1992), which is the simplest one of all the electrode arrays. In practical situations, the pole-pole array has two additional remote electrodes that have to be placed a long distance away from the working site (theory assumes the current sink and voltage reference point to be zero at infinity but they never are in practice). Obviously, it is not suitable to conduct such work in populated areas because the data can be easily contaminated by noise from other electric sources (e.g. power lines, leakage currents) along the wires connecting the remote electrodes. According to Van et al.'s (1991) field experiment and Park and Van's result (1991), it is not possible to accurately collect data with a true pole-pole configuration in the field (about 15 percent of their data did not satisfy reciprocity). The finite contribution of two remote electrodes introduces a systematic error in the inversion. Naturally, it prompts us to investigate other electrode arrays for performing crosshole electric surveys.

One way to reduce the influence of remote electrodes may be to decrease the number of remote electrodes or re-deploy them in crosshole data acquisition, e.g. applying the pole-bipole array to measure the potential difference between the two potential electrodes, or the bipole-pole array to measure the potential with two opposite-polarity current points (source and sink), or the bipole-bipole array to measure the potential difference between two electrodes with two opposite-polarity current sources. If these data are available for crosshole resistivity imaging, it not only reduces the effect of remote electrodes, but also

avoids the disturbance of random noise outside the working site and makes it possible for the crosshole resistivity imaging technique to be applied to problems in civil engineering, groundwater studies and environmental investigations within built-up areas. On the other hand, we believe that these electrode arrays, with various crosshole surveying configurations, have different responses and sensitivities to the structure of the ground because of the differences in the distribution of current lines and the observed quantities (potential, potential difference and gradient). Consequently, it is worth exploring the relative merits and effectiveness of crosshole resistivity imaging using such different electrode arrays.

1.2 Crosshole Seismic Imaging

Imaging the velocity structure of the earth with crosshole seismic data, like crosshole resistivity imaging, is a geophysical inversion procedure. In other words, an image of the inter-borehole region may be obtained by acquiring crosshole seismic data and using an inversion algorithm. Theoretically, crosshole seismic kinematic data (travel-times of different events on the seismograms) or dynamic data (waveforms in the time-domain or the frequency-domain) may be used for the imaging procedure. The former constitutes a kind of seismic inversion algorithm commonly termed travel-time tomography or ray-tomography, because it is based on a ray-tracing algorithm to compute the travel-times of the events on the seismograms. The latter includes diffraction tomography and waveform inversion, both of which are normally called wave-equation tomography, because they require the wavefield solution of the acoustic or elastic wave-equation in the time-domain or the frequency-domain. Since the 1980's, many researchers have conducted 2-D numerical and physical experiments to show that wave-equation tomography has much better spatial resolution than travel-time tomography (Devaney, 1984; Wu and Toksöz, 1987; Mora, 1989; Willamson, 1991; Pratt and Goulty, 1991; Woodward, 1992). The spatial resolution may reach one-third of a wavelength, provided the aperture (angular coverage) of the survey is sufficient (Dickens, 1994). This spatial resolution is a difficult challenge for travel-time tomography.

Crosshole diffraction tomography or waveform inversion is most likely implemented in the frequency-domain because of the fact that crosshole measurements are usually designed to provide an optimal environment in which to perform seismic tomography or

imaging with many sources and receivers. Sampling the medium between the boreholes with a large number of sources and receivers creates a formidable computational challenge for forward modeling in the time-domain, but by transforming the data to the frequency-domain, useful images of the intervening medium can be formed from single or multiple frequency components in the data (Wu and Toksöz, 1987; Pratt and Worthington, 1990). The original treatment of diffraction tomography in geophysics was given by both Devaney (1984) and Wu and Toksöz (1987), who applied the Born or Rytov approximation to the 2-D Helmholtz equation so that the linear relation between the acoustic velocity variation field (target) and the scattered wavefield (the relative change of wavefield due to the velocity variation) was obtained. The image of the velocity structure may be extracted in terms of this relationship. Woodward (1992) has theoretically summarized the main features of ray-tomography and diffraction tomography. Kaveh and Soumekh (1981) formulated the algorithms and gave error analyses for both Born and Rytov approximations. From all the reports, it has been realized that conventional diffraction tomography is convenient for the case that satisfies the following assumptions: (1) a line-source and a uniform background (a homogenous reference medium); (2) weak scattering and not very strong velocity variation; (3) the distributions of the sources and geophones along lines in accordance with Shamon's sampling criterion (Nyquist). Obviously, these do not conform with most practical considerations in geophysical exploration. One major cause of the limitations lies in the use of a homogeneous Green's function or a uniform background. In order to make diffraction tomography more practical, Pai (1989, 1990) and Dickens (1994) demonstrated layered earth diffraction tomography in which the expansion of the layered earth Green's functions (an analytic solution for multi-layered media) in vertical or horizontal eigenstates was employed so as to image nearly layered media. For an arbitrary reference medium, Gan et al. (1993, 1994) applied a 2-D finite element method and developed a non-linear diffraction tomography algorithm for an inhomogeneous acoustic background media. Deregowski and Brown (1983), Bleisten et al. (1987) and Gelius (1995a, 1995b, 1995c) used ray theory to compute the 3-D Green's function and suggested an iterative procedure for imaging of the complicated media. They called this generalized diffraction tomography. These techniques require event identification and ray-tracing, as well as a smooth model parameterization.

Reviewing the progress of crosshole seismic wave-equation tomography, most approaches (except those using the ray approximations) are based on the 2-D Helmholtz equation for simplicity, which leads to the solution of forward modeling; this cannot be directly used in the inversion in a practical application because of the difference in dynamic properties between the 2-D and 3-D wavefield. In order to apply these imaging algorithms some correction from the 3-D to the 2-D situations must be required in the data processing (Pratt and Worthington, 1988; Tura et al., 1992; Reiter and Rodi, 1996). Such conversions or corrections from 3-D to 2-D are commonly implemented by some filtering methods, which are based on the asymptotic similarity of the kinematics of the 2-D and 3-D problems. Williamson and Pratt (1995) pointed out that each filter has certain limitations for practical situations.

To better approximate the realistic situation and avoid the conversion of 3-D to 2-D, Liao and McMechan (1996) applied a 3-D finite difference method to visco-acoustic full-waveform inversion and Song and Williamson (1995a,b) developed the solution of a 2.5-D finite difference method for crosshole seismic waveform inversion in the frequency-domain. So, the critical problem to make crosshole wave-equation tomography realistic is to develop a flexible and efficient numerical algorithm to calculate the 3-D wavefield or the Green's function for arbitrary media in the frequency-domain or the time-domain.

1.3 2.5-D Approximation

From a methodology viewpoint, either crosshole resistivity imaging or crosshole seismic wave-equation tomography is based on the solution of one kind of partial differential equation. In the theory of partial differential equations, the governing equations for the 3-D direct current (DC) electric potential and the 3-D acoustic pressure wavefield (in the frequency-domain) both belong to the elliptic equation category, even though they define different physical phenomena. The 2.5-D approximation for 3-D situations considers the source to be a point source and the medium properties to be non-changing in the strike (out-of-plane) or y-direction. It follows that the 3-D potential or acoustic wavefield can be calculated by performing pseudo 2-D computations. Although most practical cases are 3-D, the following reasons prompt one to think about the 2.5-D approximation: (1) many geological structures in a sedimentary area are often essentially 2-D; (2) crosshole

geophysical surveys are normally confined to be mostly within a plane (2-D); (3) an economical approach for the 3-D physical field is required. When conducting geophysical surveys in a sedimentary basin, one expects to encounter geological structures such as faults, pinchouts and folds, or other hydrocarbon traps. In mining environments, the ore bodies are often tabular. These geological targets are extended with only minor variation in the strike direction (i.e. they are 2-D structure), but the geophysical field, such as the DC electric potential field or the seismic wavefield, is actually 3-D due to the usage of a point-source. So, it is natural to treat the modeling or inversion with the 2.5-D approximation in the interpretation of the data. Nowdays, the 2.5-D approximation is widely used in DC resistivity modeling and inversion, but unfortunately, in seismic data analysis, most researchers have presented various methods for 2-D (line-source) modeling without consideration of the more realistic situation. Considerable contributions have been made to understanding elastic wave propagation in complicated media with the 2-D modeling. However, these 2-D modeling techniques are not available for crosshole seismic waveform inversion, because of the pronounced differences between line-source and point-source wavefields. On the other hand, crosshole resistivity and seismic surveying are being applied more and more to various kinds of geophysical exploration in which the data contain important information on the volume of earth between the boreholes, and the acquisition is commonly restricted to line-distributions, which is inadequate for implementing 3-D inversions. To analyze crosshole data, the 2.5-D approximation is a reasonable compromise in terms of the practical situation. Reviewing the many studies on 3-D seismic modeling and inversion, most of the algorithms require a great deal of computational work and huge computer memory. Thus they are hardly employed on a routine basis. In comparison, the 2.5-D approximation is more economical and practical in the interpretation of crosshole geophysical data.

In the last decade, there have been many papers in the geophysical literature dealing with 2.5-D acoustic and elastic modeling. Luco et al. (1990) proposed a boundary integral equation method and calculated the 3-D response of a cylindrical canyon. Randall (1991) presented a 2.5-D velocity-stress finite difference technique to calculate multipole excitation of azimuthally nonsymmetric boreholes and formations. Pedersen et al. (1994, 1996) developed an indirect boundary-element method and studied 3-D

scattering by 2-D topography and 3-D diffraction of long-period surface waves. Okamoto (1994) applied a finite-difference method to calculate the 3-D teleseismic synthetics in 2-D media. Recently, Furumura and Takenaka (1996) presented a pseudospectral method for 2.5-D elastic modeling. Takenaka et al. (1996) developed a 2.5-D discrete wavenumber-boundary integral equation method, and Takenaka and Kennett (1996a, 1996b) derived a 2.5-D time-domain elastodynamic equation for plane-wave incidence in a general anisotopic medium. With respect to 2.5-D acoustic wave modeling, Liner (1991) formulated an approximate 2.5-D wave equation for finite-difference modeling in the time-domain. Song and Williamson (1995a, 1995b) applied the finite-difference method to perform successful 2.5-D acoustic wave modeling and inversion in the frequency-domain. Williamson and Pratt (1995) reviewed some important 2.5-D results and pursued an alternative 2.5-D acoustic wave equation. Cao and Greenhalgh (1997) demonstrated another finite-difference scheme, incorporating a 2.5-D absorbing boundary condition. Among all the mentioned 2.5-D algorithms, only the finite-difference method can be applied to crosshole seismic wave-equation tomography due to the ability to simulate a complex medium. The finite-difference method has a singularity point at the source position in the numerical computation. Considering the merits of the finite-element method (Marfurt, 1984; Hughes, 1987; Serón et al., 1996), especially in computing the Green's functions for arbitrary media (the singularity problem is effectively smoothed out in the finite-element formulation), it is necessary to incorporate the 2.5-D approximation with the finite-element method for the two geophysical imaging techniques.

1.4 Objectives of the Study and Outline of Thesis

In this thesis, it will be shown that with 2.5-D approximation crosshole resistivity imaging and crosshole acoustic velocity imaging (diffraction tomography and full-waveform inversion with the acoustic approximation) reduce to 2.5-D Helmholtz equation modeling and inversion. The basic quantity for the modeling and inversion is the 2.5-D Green's function of the equation, which may be solved by the finite-element method for arbitrary media. From the methodological point of view, the two geophysical imaging techniques have similar schemes in the numerical computations. The objectives of the study are firstly to develop the 2.5-D numerical algorithms to calculate the

Green's function (forward modeling), then, incorporating the 2.5-D solutions with the geophysical inversion algorithms, to develop the imaging procedures for crosshole resistivity and seismic measurements. Furthermore, applying the imaging procedures and conducting numerical or physical experiments, we investigate and examine the effectiveness of the crosshole resistivity imaging with different electrode arrays and the crosshole acoustic velocity imaging with different full-waveform spectral data.

Chapter 2 gives the definitions of the 2.5-D Helmholtz equation and the 2.5-D Green's functions. It will be shown that the 2.5-D Helmholtz equation covers the governing equations for the 2.5-D DC electric potential field and the 2.5-D acoustic wavefield to which the basic principles of the finite-element formulation may be applied. Chapters 3 and 4 treat the so-called forward problem of the 2.5-D Helmholtz equations and develops the finite-element solutions for 2.5-D resistivity modeling and 2.5-D acoustic wave modeling in the frequency-domain. The new algorithms are designed to directly calculate the 2.5-D Green's functions so as to easily form the response of any source (forward modeling) and the other quantities (e.g. the derivatives for inversions). Chapter 5 formulates an extension of the 2.5-D approximation to the 2.5-D elastic wave problem. Chapter 6 deals with the so-called geophysical inversion problem in which the most popular solutions or algorithms in the modern geophysical inversion, such as Tikhonov regularization solution, the smoothest model solution (Occam's inversion) and the subspace solution, are formulated in a general form and the relationships between the solutions based on the different algorithms are presented. To implement any one of these inversion algorithms, Chapter 7 derives the explicit and generalized forms of the Fréchet and second derivatives for different resistivity and seismic surveying configurations. Based on the explicit expressions, a new flexible and efficient numerical scheme to calculate the derivatives is proposed. Chapter 8 and Chapter 9 apply our new solutions of the 2.5-D Helmholtz equation and the new algorithm for computing the derivatives to a synthetic study on crosshole resistivity imaging with different electrode arrays (pole-pole, pole-bipole, bipole-pole and bipole-bipole) and to numerical simulations/inversions for crosshole acoustic velocity imaging with different spectral data (real and imaginary components, amplitude and phase spectra, Hartley spectrum). In the last chapter, we summarise all the results of the numerical forward modeling and imaging experiments, and offer some conclusions and suggestions for future research.

Chapter 2
2.5-D Helmholtz Equation

In this chapter, by applying the 2.5-D approximation to 3-D situations and defining the 2.5-D Helmholtz equation, we will show that both the 3-D DC electric potential and acoustic wavefield can be described by the specified forms of the 2.5-D Helmholtz equation so that they have similar methodologies in numerical modeling. Crosshole resistivity and acoustic velocity imaging both entail computing the numerical solution of the 2.5-D Helmholtz equation. As background to what follows, we first give the definition of the 2.5-D Helmholtz equation. Next we develop the specified forms and basic solutions for the 2.5-D DC electric potential and acoustic pressure wavefield. After that we introduce the 2.5-D Green's function and show the reciprocity principle of the 2.5-D Green's function; the last two sections will briefly review the two basic schemes of the finite element method (FEM): Galerkin's solution and the variational principle, which are used in the later chapters for solving the 2.5-D Helmholtz equations.

2.1 2.5-D Helmholtz Equation

As is well known, the 2-D or 3-D Helmholtz equation is

$$\nabla_{2,3}^2\Phi + k^2(c)\Phi = 0\,, \tag{2.1}$$

which governs the propagation of a 2-D (line-source) or 3-D (point-source) acoustic or electromagnetic wavefield Φ when the wavenumber $k = \omega / c$ is given by a positive constant. The quantity ω is the angular frequency and $c=c(r)$ is the wavespeed of the medium that depends on the spatial coordinates $r=(x,y,z)$ (3-D) or $r=(x,z)$ (2-D). Here ∇_2^2 and ∇_3^2 represent the 2-D and 3-D Laplacian operators. This equation carries the name of the physicist Hermann Ludwig Ferdinand von Helmholtz (1821-1894) for his contribution to mathematical acoustics and electromagnetics.

In geophysical applications, especially for processing or interpreting of crosshole geophysical data, the 2.5-D approximation, as mentioned before, is the natural

treatment. This means the 3-D physical field, e.g. the electric potential $\Phi = U(x,y,z)$ or the frequency-domain acoustic wavefield $\Phi = \overline{P}(\omega, x, y, z)$ is calculated for a 2-D medium whose physical property, such as conductivity $\sigma(x,z)$ or velocity $c(x,z)$, does not change along the y-direction

or strike direction (Fig.2-1). This approximation normally leads to the usage of the Fourier-cosine transform with respect to the y-coordinate so that the 3-D governing equations become of similar form to equation (2.1):

$$\nabla \cdot [a(x,z)\nabla\overline{\Phi}] + k_a^2(a(x,z),b(x,z),k_y)\overline{\Phi} = 0, \tag{2.2}$$

where $\nabla = (\partial_x, \partial_z)$, $\overline{\Phi}$ is the Fourier-cosine transform of Φ and $a(x,z)$ and $b(x,z)$ are two arbitrary model functions that represent the physical properties of the medium defined in the *(x,z)*-plane, e.g. $\sigma(x,z)$ or $c(x,z)$. The quantity k_y is the y-component of the 3-D wavenumber, and k_a may be called the apparent wavenumber in the *(x,z)*-plane. The apparent wavenumber is generally a function of the model parameters $a(x,z)$, $b(x,z)$ and wavenumber k_y. Obviously, equation (2.2) is a general form of the ordinary Helmholtz equation and it arises from the 2.5-D approximation. So, we call it the 2.5-D Helmholtz equation with which the following problem may be defined when including a point-source and a mixed boundary condition:

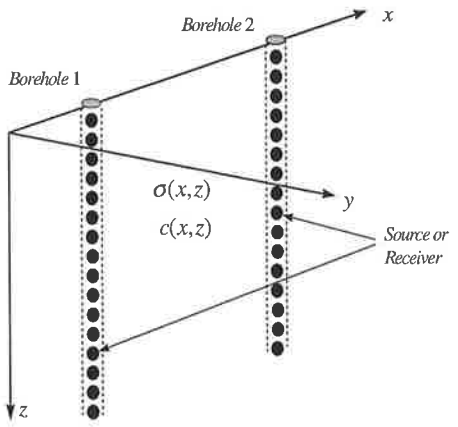

Fig.2-1 Diagram of crosshole geophysical surveying in a 2.5-D earth model. $c(x,z)$ and $\sigma(x,z)$ denote the velocity and conductivity distributions of the medium, respectively.

$$\begin{cases} \nabla \cdot [a(x,z)\nabla\overline{\Phi}] + k_a^2(a(x,z),b(x,z),k_y)\overline{\Phi} = -\dfrac{S}{2}\delta(x-x_s)\delta(z-z_s), & x,z \in \Omega, \\ \dfrac{\partial\overline{\Phi}}{\partial n} + B\overline{\Phi} = 0, & x,z \in \partial\Omega. \end{cases} \tag{2.3}$$

Here S is the magnitude spectrum of the source located at the point $(x_s, 0, z_s)$, the factor 1/2 comes from the Fourier-cosine transform of $\delta(y-0)$, B is a boundary operator and n is the unit normal vector for the boundary $\partial\Omega$ enclosing Ω. It will be seen in the following sections that the above 2.5-D Helmholtz equation (2.3) represents the DC

electric potential field as well as the acoustic wave field. The forward problem of geophysics, or modeling, entails solving equation (2.3) for the physical quantity $\overline{\Phi}$ at some specified spatial positions, e.g. a crosshole survey configuration, with given model parameters $a(x,z)$ and $b(x,z)$; while the inverse problem involves reconstructing the model parameters $a(x,z)$ and $b(x,z)$ by solving equation (2.3) and using a set of the known physical quantities $\{\Phi_i, i = 1,2,...,N_d\}$, such as the data acquired by crosshole resistivity or seismic measurements.

2.2 DC Electric Potential Equation

The principle of DC electric surveying is based on the theory of steady electric current flow in which an essential equation is the continuity law:

$$\oint_S \vec{j} \cdot d\Gamma = \begin{cases} -I, & (inside \quad S) \\ 0, & (outside \quad S). \end{cases} \qquad (2.4)$$

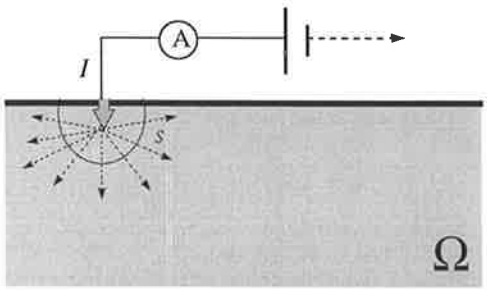

Fig.2-2 Diagram of the continuity law for current injection through an electrode into the ground.

where $\vec{j}$ is current density, S is an arbitrary closed surface in the region Ω, and I is the injected current magnitude through S (see, Fig. 2-2). From equation (2.4) it follows that the rate of decrease of charge within the volume surrounding the surface S is equal to the total current flowing outwards over the bounding surface.

Ohm's law states that

$$\vec{j} = -\sigma \nabla U , \qquad (2.5)$$

where σ is conductivity and which is normally a function of the 3-D coordinates: $\sigma = \sigma(x,y,z)$. U is an electric potential function and ∇ is the 3-D gradient operator. According to Gauss' integral theorem, equation (2.4) is equivalent to

$$\nabla \cdot (\sigma \nabla U) = -I\delta(r - r_c) \qquad r, r_c \in \Omega , \qquad (2.6)$$

where $\vec{r}_c = (x_c, y_c, z_c)$ is the location of the current electrode in Ω. Equation (2.6) is the governing equation for the 3-D DC resistivity measurements. The basic solution of equation (2.6) for a uniform medium (σ=constant) has the simple expression:

$$U(r_c, r) = \frac{I}{4\pi\sigma|r - r_c|}. \tag{2.7}$$

For more complicated media (non-constant conductivity), one has to solve equation (2.6) in conjunction with a boundary condition by some numerical method.

According to the 2.5-D approximation, the current electrode is assumed to be a point-source, and the conductivity σ model is considered to be 2-D, that is, the variation of the conductivity depends upon only the *x*- and *z*-coordinates: $\sigma = \sigma(x,z)$ in equation (2.6). To remove the y-coordinate, we set the source at $(x_c, 0, z_c)$ and take the Fourier-cosine transform with respect to the y-coordinate, which transforms equation (2.6) into:

$$\nabla \cdot (\sigma \nabla \overline{U}) - k_y^2 \sigma \overline{U} = -\frac{I}{2}\delta(x - x_c)\delta(z - z_c), \tag{2.8}$$

where we use $\nabla = (\partial_x, \partial_z)$ for the 2-D gradient in the (*x*,*z*)-plane and

$$\overline{U}(x, z, k_y) = \int_0^\infty U(x, y, z)\cos(k_y y)dy. \tag{2.9}$$

From equation (2.9), the spectrum $\overline{U}(x, z, k_y)$ is the wavenumber-domain form of the 3-D electric potential and is a real valued function. Equation (2.8) becomes the governing equation for the DC electric potential computation with the 2.5-D approximation. Comparing with equation (2.3), it is obviously the specified form of the 2.5-D Helmholtz equation ($a = \sigma(x,z)$, $b =$ constant, $k_a^2 = -k_y^2\sigma(x,z)$ and *S*=*I*). In numerical simulations, only a limited computational range Ω is employed so that some artificial boundary condition must be introduced in the modeling. In general, the boundary condition may be expressed by a mixed-boundary condition that includes Dirichlet and Neumann boundary conditions. So, the defined partial differential equation problem for the DC resistivity measurement becomes

$$\begin{cases} \nabla \cdot (\sigma \nabla \overline{U}) - k_y^2 \sigma \overline{U} = -\dfrac{I}{2}\delta(x - x_s)\delta(z - z_s), & (x,z),(x_s,z_s) \in \Omega; \\ \dfrac{\partial \overline{U}}{\partial n} + B\overline{U} = 0, & (x,z) \in \partial\Omega, \end{cases} \tag{2.10}$$

where the boundary operator *B* will be given in Chapter 3. Our goal is to perform an inversion procedure for crosshole resistivity imaging through solving equation (2.10) for arbitrary media.

2.3 Acoustic Wave Equation

In elastic wave theory, the equation of motion is given by:

$$\rho \partial_{tt} u_j = \partial_i \tau_{ij} + f_j , \tag{2.11}$$

where $\partial_t = \frac{\partial}{\partial t}$, $\partial_j = \frac{\partial}{\partial x_j}$, ρ is density, u_j and f_j (j=1,2,3) are components of the displacement and body force respectively; and τ_{ij} is the stress tensor, which satisfies Hooke's law for a linear elastic material:

$$\tau_{ij} = c_{ijlk} \varepsilon_{lk} . \tag{2.12}$$

and the Einstein summation notation is assumed. Here the strain tensor ε_{lk} is related to the displacement by the expression:

$$\varepsilon_{ij} = \frac{1}{2}(\partial_i u_j + \partial_j u_i) . \tag{2.13}$$

The elastic modulus parameter c_{ijlk} is a fourth-order tensor that describes the physical properties of the medium. For instance, in an isotopic elastic medium, there are only 2 independent elastic constants and the tensor reduces to:

$$c_{ijlk} = \lambda \delta_{ij} \delta_{kl} + \mu(\delta_{ik}\delta_{jl} + \delta_{il}\delta_{jk}) , \tag{2.14}$$

where λ and μ are Lame's constants, and δ_{ij} is the Kronecker delta function ($\delta_{ij} = 1$ if i=j; $\delta_{ij} = 0$, $i \neq j$). Substituting equation (2.14) into equation (2.12), the stress-displacement relationship becomes:

$$\tau_{ij} = \lambda \delta_{ij} \nabla \cdot \vec{u} + \mu(\partial_i u_j + \partial_j u_i) . \tag{2.15}$$

To simplify the elastic equation of motion, the acoustic approximation ($\mu = 0$) is widely used in geophysical exploration. It leads to:

$$\tau_{ij} = -P\delta_{ij} , \tag{2.16}$$

$$-P = \kappa \nabla \cdot \vec{u} , \tag{2.17}$$

which strictly hold only in a gas or liquid medium. Here P and κ are the pressure and bulk modulus (incompressiblity). Comparing equations (2.16) and (2.17) with (2.15), the acoustic approximation actually ignores the effect of the shear stress ($\mu = 0$) in a solid medium, or only involves compressional waves. The '–' sign in equation (2.16) implies a decrease of the compression with the bulk expansion. Applying equations

(2.16) and (2.17) to equation (2.11), and in absence of the body force ($f_j = 0$), the elastic motion equation becomes

$$\partial_{tt} P = \kappa \nabla \cdot (\frac{1}{\rho} \nabla P) . \tag{2.18}$$

In the presence of a point-source $s(t)$ at the position $r_s = (x_s, y_s, z_s)$, and taking the Fourier-transform with respect to time, the acoustic wave equation has the frequency-domain form:

$$\nabla \cdot (\hat{\rho} \nabla \overline{P}) + \omega^2 \hat{\kappa} \overline{P} = -s(\omega) \delta(r - r_s) , \tag{2.19}$$

where $\hat{\rho} = 1/\rho$ and $\hat{\kappa} = 1/\kappa$. This is the general form of the 3-D Helmholtz equation. In a uniform medium ($\hat{\rho}$ and $\hat{\kappa}$ are constant), the causal solutions of equation (2.19) in the 2-D and 3-D cases are given by:

$$\overline{P}^{2D}(\omega, r_s, r) = -\frac{s(\omega)}{4} i H_0^{(2)}(k|r - r_s|) , \tag{2.20}$$

$$\overline{P}^{3D}(\omega, r_s, r) = \frac{s(\omega)}{4\pi |r - r_s|} \exp(-ik|r - r_s|) . \tag{2.21}$$

Here $k = \omega / c$ and $c = \sqrt{\kappa / \rho}$ is the acoustic velocity (wavespeed) of the medium. The quantity $H_0^{(2)}$ is the zero-order Hankel function of the second kind, and i is the imaginary number $\sqrt{-1}$. The solutions (2.20) and (2.21) imply quite different responses

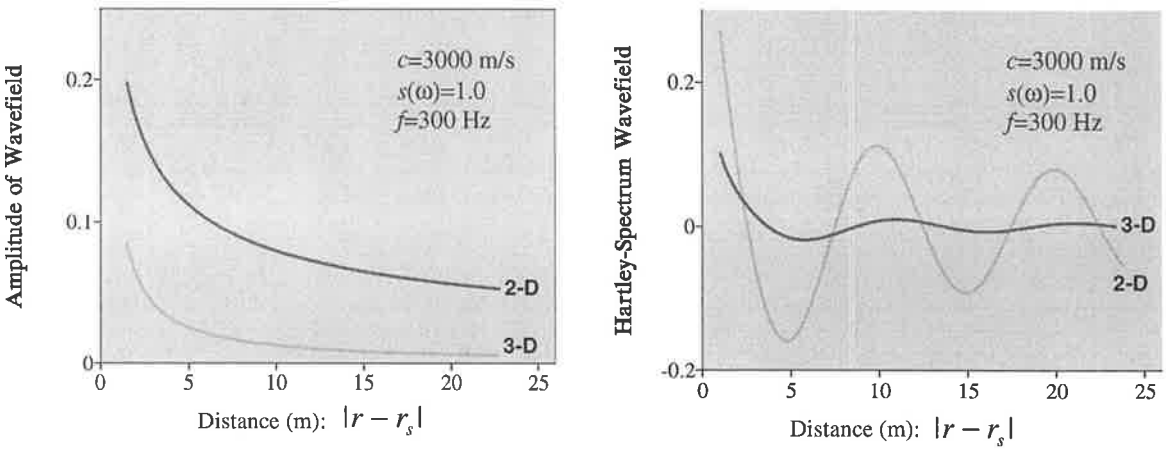

Fig.2-3 The difference between the 2-D and 3-D acoustic wavefields in the frequency-domain. Left: Amplitude of the Fourier spectra of the wavefields; Right: the Hartley spectra of the wavefields.

between the 2-D and 3-D wavefields. Fig.2-3 shows the difference in the frequency-domain. The wavefields are plotted in the amplitude of the Fourier transform and Hartley transform (for illustration and avoidance of complex arithmetic, we prefer representing the wavefield in the Hartley spectrum form, because the Hartley transform uses a real kernel rather than a complex one. Appendix A gives a brief outline of the transform and its properties; more details can be found in Bracewell (1986). The Hartley spectrum may be calculated by the subtraction of the imaginary part from the real part of the Fourier spectrum in terms of the relationship between the two transforms. From Fig.2-3, one can see that there exists quite significant differences in the propagating amplitude and phase delay with distance.

Applying the 2.5-D approximation to equation (2.19) ($\hat{\rho}$ and $\hat{\kappa}$ are just two-coordinate (x,z) functions) and performing the Fourier-cosine transform with respect to the y-coordinate, equation (2.19) becomes

$$\nabla \cdot (\hat{\rho} \nabla \overline{\overline{P}}) + (\omega^2 \hat{\kappa} - \hat{\rho} k_y^2) \overline{\overline{P}} = -\frac{s(\omega)}{2} \delta(x - x_s) \delta(z - z_s) , \tag{2.22}$$

where $\nabla = (\partial_x, \partial_z)$ and

$$\overline{P}(\omega, x, y, z,) = \int_0^\infty \overline{\overline{P}}(\omega, k_y, x, z) \cos(k_y y) dk_y . \tag{2.23}$$

Equation (2.22) is actually the 2.5-D Helmholtz equation (refer to equation (2.3)) with the specified functions: $a(x,z) = \hat{\rho}(x,z)$, $b(x,z) = \hat{\kappa}(x,z)$ and $k_a^2 = \omega^2 \hat{\kappa} - \hat{\rho} k_y^2$, similar to equation (2.8) in the DC resistivity case. Furthermore, equation (2.23), which corresponds to equation (2.9), shows that the frequency-domain solution of the wavefield can be obtained by summation of all the k_y-components $\overline{\overline{P}}(\omega, k_y, x, z)$ of the pressure wavefield.

Sengbush (1983) has reported that density varies much less than velocity in most sedimentary environments. In addition, 2-D synthetic studies have shown that density changes are poorly resolved by crosshole data (Pratt and Worthington, 1990). So, the constant-density assumption is a practical and well-accepted scheme to conduct crosshole diffraction tomography or full-waveform inversion in the frequency-domain. With this assumption, equation (2.22) becomes

$$\nabla \cdot (\nabla \overline{\overline{P}}) + (k^2 - k_y^2)\overline{\overline{P}} = -\frac{s(\omega)}{2}\delta(x - x_s)\delta(z - z_s)\,. \tag{2.24}$$

where the source spectrum $s(\omega)$ represents the normalized spectrum by a constant density. Supplementing this with some artificial boundary condition, the defined partial differential equation problem for the acoustic wavefield can be thus formulated:

$$\begin{cases} \nabla \cdot (\nabla \overline{\overline{P}}) + (k^2 - k_y^2)\overline{\overline{P}} = -\dfrac{s(\omega)}{2}\delta(x - x_s)\delta(z - z_s), & (x,z),(x_s,z_s) \in \Omega; \\ \dfrac{\partial \overline{\overline{P}}}{\partial n} + B\overline{\overline{P}} = 0, & (x,z) \in \partial\Omega, \end{cases} \tag{2.25}$$

where B is a boundary operator (it will be given in Chapter 4). The solution of the defined problem for arbitrary media is the crucial step for seismic waveform inversion in the frequency-domain.

Examining equations (2.10) and (2.25), we see that these two defined problems are very similar to each other in mathematical form except for the physical meaning of the parameters. Both of them entail the solution of the 2.5-D Helmholtz equation subject to the mixed boundary condition. Our goal is to develop a numerical method for the solution so as to perform resistivity inversion and seismic full-waveform inversion in the frequency-domain for crosshole resistivity and acoustic velocity imaging.

2.4 2.5-D Green's Functions

For further discussion of forward modeling and inversion, it will be useful to define the Green's functions of the 2.5-D Helmholtz equations (called the 2.5-D Green's functions), because they allow us to temporarily skip the consideration of the source properties, e.g. current magnitude I or source signal $s(\omega)$. On the other hand, it will be shown in the following chapters that the Green's function is the basic quantity for calculating the synthetic data in modeling, and evaluating the Fréchet and the second derivatives in the inversion.

The 2.5-D Green's functions may be defined by

Direct current: $\overline{G}^{2.5D}(x,k_y,z) = 2\int_0^\infty G^{3D}(x,y,z)\cos(k_y y)dy$; (2.26)

Acoustic wave: $$\overline{\overline{G}}^{2.5D}(\omega,x,k_y,z) = C\int_{-\infty}^{\infty} e^{-i\omega t}dt\int_{0}^{\infty} 2G^{3D}(t,x,y,z)\cos(k_y y)dy\,, \quad (2.27)$$

where $G^{3D}(x,y,z)$ and $G^{3D}(t,x,y,z)$ are the 3-D Green's functions for the DC electric potential field and acoustic wavefield respectively. The factor 2 is to remove the 1/2 factor resulting from the Fourier-cosine transform of $\delta(y-0)$, and C is a normalization constant. Obviously, the Green's functions satisfy the following equations:

$$\begin{cases} \nabla\cdot(\sigma\nabla\overline{G}^{2.5D}) - k_y^2\sigma\overline{G}^{2.5D} = -\delta(x-x_s)\delta(z-z_s)\,, & (x,z),(x_s,z_s)\in\Omega; \\ \dfrac{\partial\overline{G}^{2.5D}}{\partial n} + B\overline{G}^{2.5D} = 0, & (x,z)\in\partial\Omega, \end{cases} \quad (2.28)$$

for DC resistivity measurement and

$$\begin{cases} \nabla\cdot(\nabla\overline{\overline{G}}^{2.5D}) + (k^2-k_y^2)\overline{\overline{G}}^{2.5D} = -\delta(x-x_s)\delta(z-z_s), & (x,z),(x_s,z_s)\in\Omega; \\ \dfrac{\partial\overline{\overline{G}}^{2.5D}}{\partial n} + B\overline{\overline{G}}^{2.5D} = 0, & (x,z)\in\partial\Omega, \end{cases} \quad (2.29)$$

for the acoustic wave problem, respectively. According to the definitions, when $k_y = 0$ the Green's function reduces to the 2-D one (response of a line-source). Comparing equation (2.28) with (2.10) and equation (2.29) with (2.25), the general 3-D response to any source $S=I$ or $S=s(\omega)$ can be obtained by convolution, or frequency domain multiplication, using the relations:

$$U(x,y,z) = \frac{I}{2}\cdot F_c^{-1}\{\overline{G}^{2.5D}(x,k_y,z)\}\,, \quad (2.30)$$

or $$\overline{P}(\omega,x,y,z) = \frac{s(\omega)}{2}\cdot F_c^{-1}\{\overline{\overline{G}}^{2.5D}(\omega,x,k_y,z)\}\,, \quad (2.31)$$

where F_c denotes the Fourier-cosine transform. In a uniform medium (where the conductivity σ and the velocity c are constants), the Green's functions, as the basic solutions of the 2.5-D Helmholtz equations (2.28) and (2.29), may be analytically obtained in terms of the definitions (2.26) and (2.27). Substitution of the 3-D Greens' function for the DC electric potential field (see equation (2.7)) results in the 2.5-D Green's function:

$$\overline{G}^{2.5D}(x,k_y,z) = F_c\left\{\frac{2}{4\pi\sigma\sqrt{x^2+y^2+z^2}}\right\} = \frac{1}{2\pi\sigma}K_0(k_y\sqrt{x^2+z^2})\,, \quad (2.32)$$

where $K_0(x)$ is the modified Bessel function. In the same manner, substituting the time-domain form of the 3-D Green's function given by Aki and Richard (1980, p65)

into equation (2.27), and using the Sommerfeld radiation condition at infinity and tables of the transform (Bateman, 1954) we obtain the 2.5-D Green's function for the acoustic wave case:

$$\overline{\overline{G}}^{2.5D}(\omega,k_y,r)=\begin{cases}-\dfrac{i}{4}H_0^{(2)}(r\sqrt{k^2-k_y^2}), & k_y<k,\\ \dfrac{1}{2\pi}K_0(r\sqrt{k_y^2-k^2}), & k_y>k,\end{cases} \tag{2.33}$$

where $r=\sqrt{x^2+z^2}$. We rewrite the Green's function in the Hartley spectrum form:

$$\overline{\overline{G}}_H^{2.5D}(\omega,k_y,r)=\begin{cases}-\dfrac{1}{4}[Y_0(r\sqrt{k^2-k_y^2})-J_0(r\sqrt{k^2-k_y^2})], & k_y<k,\\ \dfrac{1}{2\pi}K_0(r\sqrt{k_y^2-k^2}), & k_y>k,\end{cases} \tag{2.34}$$

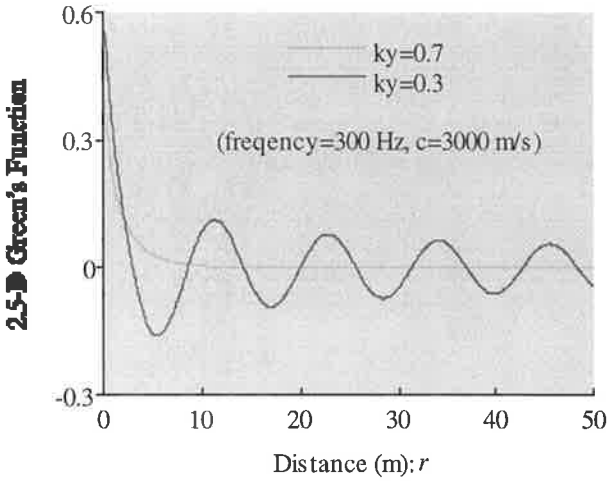

Fig.2-4 The 2.5-D Green's function at k_y=0.3 and k_y=0.7 for a 300 Hz wave in a homogeneous medium (c=3000 m/s).

where $J_0(x)$ and $Y_0(x)$ are Bessel functions of the first and second kind, and the subscript H on the Green's function denotes the Hartley spectrum. Fig.2-4 shows the Green's function (2.34) when taking c=3000 m/s and f=300 Hz ($k\approx 0.628$). It implies that when $k_y=0.3$ ($<k$), the solution describes wave propagation in the medium, but when $k_y=0.7$ ($>k$), the solution becomes a strongly evanescent field (like the potential spectrum, see equation (2.32)) in which the particle vibration in the medium completely disappears. Note that as $k_y\to k$, the Bessel functions $Y_0(x)$ and $K_0(x)$ become infinite, which means that the value $k_y=k$ is a singularity of the functions. *From the physical viewpoint, the point $k_y=k$ can be called the critical value of the medium; it represents transition from propagation to attenuation. So, the 2.5-D Helmholtz equation (2.25) or (2.29) includes two physical phenomena in the frequency-wavenumber domain.*

2.5 Principle of Reciprocity

An important property of the 2.5-D Green's functions is that of reciprocity:

$$G^{2.5D}(k_y, r_s, r_R) = G^{2.5D}(k_y, r_R, r_s), \tag{2.35}$$

where $r = (x, z)$ is restricted to the (x,z)-plane, $G^{2.5D} = \overline{G}^{2.5D}$ or $\overline{\overline{G}}^{2.5D}$, r_s and r_R represent the positions of the source (current or shot) and receiver (potential electrode or geophone). This equation states that the equivalent values of the 2.5-D Green's function can be obtained by exchange of the positions of source and receiver.

In order to prove the identity, we first review the so-called self-adjoint differential operator, which is given by the definition: a differential operator $\boldsymbol{L}$: $N \rightarrow M$ (N and M are two normed spaces) is called a self-adjoint, if for any $u \in N$ and $v \in N$, the symmetric property holds for the integral over the range Ω:

$$\int_{\Omega} vLu d\Omega = \int_{\Omega} uLv d\Omega . \tag{2.36}$$

According to the definition, it is not difficult to make such a deduction: when a differential operator is given in the form

$$Lu = \sum_{i,j=1}^{n} \partial_i \{a_{ij}(x)\partial_j u\} + b(x)u, \tag{2.37}$$

and the boundary condition with an operator B is defined by the following equation

$$\sum_{i,j=1}^{n} a_{ij}(x) n_j \partial_i u + Bu = 0 , \tag{2.38}$$

where $n = (n_1, n_2, \ldots n_n)$ is the outward unit normal vector of the boundary, the operator L is a self-adjoint operator if $a_{ij}(x) = a_{ji}(x)$ and B a symmetric operator with the boundary integral, viz

$$\int_{\partial\Omega} vBu d\Omega = \int_{\partial\Omega} uBv d\Omega . \tag{2.39}$$

In fact, the deduction is a direct result of Green's theorem (Pao, 1992):

$$\int_{\Omega} (uLv - vLu) dr = \int_{\partial\Omega} (u\frac{\partial v}{\partial n} - v\frac{\partial u}{\partial n}) d\Gamma . \tag{2.40}$$

We rewrite the defined partial differential equation problems (2.28) and (2.29) in the operator form:

$$\begin{cases} L(m,k_y)G^{2.5D} = -\delta(r-r_s), & r,r_s \in \Omega; \\ \dfrac{\partial G^{2.5D}}{\partial n} + BG^{2.5D} = 0, & r \in \partial\Omega, \end{cases} \tag{2.41}$$

where $m = \sigma, c$ and

$$L(m,k_y) = \begin{cases} \nabla\cdot(\sigma\nabla) - \sigma k_y^2, & (DC \quad resistivity) \\ \nabla\cdot\nabla + (k^2 - k_y^2). & (Acoustic \quad wave) \end{cases} \tag{2.42}$$

Comparing equations (2.42), (2.41) with (2.37), (2.38) and in terms of the deduction, the operator $L(m,k_y)$ is self-adjoint so long as B is a symmetric boundary operator (this will be shown in Chapter 3 and Chapter 4).

Applying the symmetry of $L(m,k_y)$ (equation (2.36)), we have the following identity for the two Green's functions $G^{2.5D}(k_y,r_s,r)$ and $G^{2.5D}(k_y,r_R,r)$:

$$\begin{aligned} &\int_\Omega [G^{2.5D}(k_y,r_s,r)L(m,k_y)G^{2.5D}(k_y,r_R,r) - G^{2.5D}(k_y,r_R,r)L(m,k_y)G^{2.5D}(k_y,r_s,r)]dr, \\ &= \int_\Omega [G^{2.5D}(k_y,r_s,r)[-\delta(r-r_R)] - G^{2.5D}(k_y,r_R,r)[-\delta(r-r_s)]]dr, \\ &= 0, \end{aligned} \tag{2.43}$$

from which the reciprocity condition (2.35) is obtained. According to the reciprocity of the Green's functions and the relations (2.30) and (2.31), the electric potential U and the frequency-domain acoustic wavefield $\overline{P}$ exhibit the reciprocity property, that is

$$U(r_c,r_p) = U(r_p,r_c), \tag{2.44}$$

$$\text{and} \quad \overline{P}(\omega,r_s,r_g) = \overline{P}(\omega,r_g,r_s) \text{ or } P(t,r_s,r_g) = P(t,r_g,r_s). \tag{2.45}$$

This result indicates that an identical datum in geophysical exploration can be obtained by exchanging the positions of the source and the receiver in an arbitrary medium.

2.6 The Finite Element Method (FEM)

In the previous sections, it was shown that the two geophysical problems (electric and acoustic) may be reduced to boundary-valued problems of the 2.5-D Helmholtz equation (equation (2.10) or (2.25)). To solve the defined partial differential equation problems

for an arbitrary medium, some numerical technique must be employed. The finite element method (FEM) is a mature, powerful numerical technique for solving a differential equation (Mikhlin, 1964; Zienkiewicz, 1971; Huebnent, 1975). The advantage of the FEM as compared with other numerical methods, e.g. the finite-difference method, is that complicated geometry, general boundary conditions and variable or non-linear material properties can be handled relatively easily. Also the FEM has a solid theoretical foundation which gives added reliability. The essence of such a method consists of (1) seeking an approximation whose residual with the true solution vanishes in some average sense (Weighted residual solution or Galerkin's solution) or (2) converting the defined partial differential equation problem into a minimization of a functional (variational principle) so that the solution is finally obtained by solving a system of linear equations. Here, we apply the two schemes and demonstrate the basic formulations of the FEM solutions for the 2.5-D Helmholtz equation. We also show the equivalence of the two schemes.

(1) Galerkin's Solution

In FEM theory, Galerkin's solution is formulated by the so-called weighted residual method, which involves two steps: (1) assuming the general functional behavior of the dependent field variable in some way so as to approximately satisfy the given differential equation and boundary conditions; (2) substituting the approximation into the original differential equation and boundary conditions results in some error called a residual, which is required to vanish with a weighting function over the computational range.

Let there be a defined differential equation problem:

$$\begin{cases} L\Phi = f, & r \in \Omega, \\ \dfrac{\partial \Phi}{\partial n} + B\Phi = 0, & r \in \partial\Omega, \end{cases} \tag{2.46}$$

where f is a known function, Φ is the exact solution. An approximation to Φ may be expressed by

$$\tilde{\Phi}(r) = \sum_i N_i(r)\tilde{\Phi}_i , \tag{2.47}$$

where $\tilde{\Phi}_i$ are the coefficients (unknowns, normally they are the nodal values of $\tilde{\Phi}$ in the FEM mesh) to be determined and $N_i(r)$ are a set of the chosen shape functions that satisfy the boundary condition. Substituting (2.47) into the governing equation in (2.46), we form the residual:

$$R(r) = L\tilde{\Phi} - f \ . \tag{2.48}$$

The weighted residual method seeks the solution $\tilde{\Phi}$ in which the weighted average vanishes over the solution domain, viz

$$\int_{\Omega} W_j(r)R(r)dr = \int_{\Omega} W_j(r)[L\tilde{\Phi} - f]dr = 0, \quad (j = 1,2,3,...m), \tag{2.49}$$

where W_j are chosen as m linearly independent weighting functions. Galerkin' solution just takes the weighting functions to be the same as the shape functions $W_j = N_j(r)$ used to represent $\tilde{\Phi}$, so equation (2.49) becomes

$$\sum_i \int_{\Omega} N_j(r)[LN_i(r)]\tilde{\Phi}_i dr = \int_{\Omega} N_j(r) f dr, \quad (j = 1,2,3,...m). \tag{2.50}$$

Substituting the operator, the source-term and the boundary condition of equation (2.3) into the above equation, then integrating by parts, we obtain

$$\sum_i \{\int_{\Omega} [a\nabla N_i \cdot \nabla N_j - k_a^2(a,b,k_y)N_i N_j]dr + \int_{\partial\Omega} aN_j BN_i d\Gamma\}\tilde{\Phi}_i = \frac{S}{2}N_j\delta_{is} \qquad (j = 1,2,3,...,m), \tag{2.51}$$

where $\delta_{is} = 1$ if $r_i = r_s$ and $\delta_{is} = 0$ if $r_i \neq r_s$. After discretization of the integral range, equation (2.51) reduces to a system of linear equations, which can be solved with a standard algorithm for all the nodal values $\tilde{\Phi}_i$ so that Galerkin's solution of the 2.5-D Helmholtz equation can be obtained.

(2) Variational Principle

The variational principle states that the solution to the partial differential equation in (2.46) is equivalent to the solution that minimizes the following functional subject to the boundary condition:

$$\begin{cases} \delta F(\Phi) = 0, & r \in \Omega, \partial\Omega, \\ \dfrac{\partial\Phi}{\partial n} + B\Phi = 0, & r \in \partial\Omega. \end{cases} \tag{2.52}$$

The functional may be written in the inner product form (Mikhlin, 1964):

$$F(\Phi)=\frac{1}{2}<L\Phi,\Phi>-<\Phi,f>. \tag{2.53}$$

Here the inner product is defined with the integral $<u,v>=\int_{\Omega} uvdr$. The equivalence is easily shown if the operator L has the self-adjoint property. In fact, one can calculate

$$\begin{aligned}\delta F(\Phi)&=\frac{1}{2}\{<L\delta\Phi,\Phi>+<L\Phi,\delta\Phi>\}-<\delta\Phi,f>\\&=\frac{1}{2}\{<L\Phi,\delta\Phi>+<L\Phi,\delta\Phi>\}-<f,\delta\Phi>\\&=<L\Phi-f,\delta\Phi>=0\end{aligned} \tag{2.54}$$

Considering $\delta\Phi\neq 0$ to be any function, equation (2.54) states that $\delta F(\Phi)=0$ if and only if $L\Phi-f=0$. So, the solution to the governing equation in (2.46) is completely equivalent to the solution of the variational equation in (2.52), which is the well-known variational principle. According to the variational principle, the original problem (2.46) reduce to solving the variational equation (2.52).

If we express the functional in the following form:

$$F(\Phi)=\int_{\Omega} f(\Phi,\Phi_x,\Phi_y,\Phi_z)d\Omega-\int_{\partial\Omega} f_0(\Phi)d\Gamma, \tag{2.55}$$

where $(\Phi_x,\Phi_y,\Phi_z)=\nabla\Phi$, f and f_0 are two functions defined on Ω and $\partial\Omega$, another equivalent relationship between minimizing the functional and Euler's equations can be obtained (Zienkiewicz 1971). In fact, calculating the perturbation with the expression, we have

$$\begin{aligned}\delta F(\Phi)&=\int_{\Omega}[\frac{\partial f}{\partial\Phi}\delta\Phi+\frac{\partial f}{\partial\Phi_x}\delta\Phi_x+\frac{\partial f}{\partial\Phi_y}\delta\Phi_y+\frac{\partial f}{\partial\Phi_z}\delta\Phi_z]dr-\int_{\partial\Omega}\frac{\partial f_0}{\partial\Phi}\delta\Phi d\Gamma,\\&=\int_{\Omega}[\frac{\partial f}{\partial\Phi}\delta\Phi+\vec{\xi}\cdot\nabla\delta\Phi]dr-\int_{\partial\Omega}\frac{\partial f_0}{\partial\Phi}\delta\Phi d\Gamma,\\&=\int_{\Omega}(\frac{\partial f}{\partial\Phi}-\nabla\cdot\vec{\xi})\delta\Phi dr+\int_{\partial\Omega}(\vec{\xi}\cdot n-\frac{\partial f_0}{\partial\Phi})\delta\Phi d\Gamma,\\&=0.\end{aligned} \tag{2.56}$$

Here $\vec{\xi}=\{\partial f/\partial\Phi_x,\partial f/\partial\Phi_y,\partial f/\partial\Phi_z\}$. This equation states the necessary and sufficient conditions for $\delta F(\Phi)=0$, that is, $\delta F(\Phi)=0$ if and only if the following differential equations are satisfied:

$$\begin{cases} \nabla \cdot \vec{\xi} - \dfrac{\partial f}{\partial \Phi} = 0, & r \in \Omega \\ \vec{\xi} \cdot n - \dfrac{\partial f_0}{\partial \Phi} = 0, & r \in \partial\Omega \end{cases} \tag{2.57}$$

These are the well-known Euler equations. So, the variational principle gives the following equivalent relation:

$$\delta I(\Phi) = 0 \Leftrightarrow \begin{cases} \nabla \cdot \vec{\xi} - \dfrac{\partial f}{\partial \Phi} = 0, & r \in \Omega, \\ \vec{\xi} \cdot n - \dfrac{\partial f_0}{\partial \Phi} = 0, & r \in \partial\Omega, \end{cases} \tag{2.58}$$

which enables us to convert a differential equation problem described by Euler equations into the minimization of a functional. For example, to solve the boundary-valued problem (2.3) of the 2.5-D Helmholtz equation, the integrand functions in equation (2.55) may be chosen as follows:

$$\begin{aligned} f(\overline{\Phi}, \overline{\Phi}_x, \overline{\Phi}_z) &= \frac{1}{2}[a\nabla\overline{\Phi} \cdot \nabla\overline{\Phi} - k_a^2(a,b,k_y)\overline{\Phi}^2 - S\delta(r - r_s)\overline{\Phi}], \\ f_0(\overline{\Phi}) &= -\frac{a}{2}\overline{\Phi}B\overline{\Phi}. \end{aligned} \tag{2.59}$$

Substituting (2.59) into Euler equations (2.57), the 2.5-D Helmholtz equation and the boundary condition in (2.3) are obtained. This means the solution of (2.3) is equivalent to the solution of (2.52) with the functions (2.59). So, the defined differential equation problem (2.3) becomes

$$\min\{\frac{1}{2}\int_{\Omega}[a\nabla\overline{\Phi} \cdot \nabla\overline{\Phi} - k_a^2(a,b,k_y)\overline{\Phi}^2 - S\delta(r - r_s)\overline{\Phi}]dr + \frac{1}{2}\int_{\partial\Omega} a\overline{\Phi}B\overline{\Phi}d\Gamma\}. \tag{2.60}$$

Actually, the variational equation can be also obtained by using the functional expression (2.53) subject to the boundary condition. This shows the two variational principles to be equivalent.

Substituting the approximation (2.47) for $\overline{\Phi}$, the variational equation (2.60) can be reduced to the same linear equation system as (2.51) where it is based on the Galerkin's solution. So, one can realize the equivalence of the variational principles with Galerkin's solution. These two principles of the FEM may be employed for the 2.5-D Helmholtz equation and they will yield the same results when taking the approximation (2.47). The main advantages of using the Galerkin's solution are that it is a much simpler formulation and is easier to understand in terms of the variational principle.

Chapter 3
2.5-D DC Resistivity Modeling

There are three principal techniques of DC resistivity modeling which have been reported in the literature: integral equation methods, finite-difference methods (FDM) and finite-element methods (FEM). Each technique has its own advantages and is specifically suitable for some model geometries, e.g. the integral equation methods (Dieter et al., 1969; Lee, 1975; Snyder, 1976; Okabe, 1981; Das and Parnasis, 1987; Xu et al., 1988), based on the integral form of the solution of the DC resistivity problem (directly using the Green's function of a uniform medium), are suitable for simple model geometries such as several homogenous sub-regions. The main advantage is the lower cost of computer resources than for other methods in computing the 3-D potential response. However, it is not well suited for modeling of arbitrary media. The FDM (Mufti, 1976; Dey and Morrison, 1979a, 1979b; Mundry, 1984; James, 1985; Lowry et al., 1989; Spitzer, 1995; Zhao and Yedlin, 1996) and the FEM (Coggon, 1971; Fox et al., 1980; Pridmore et al., 1981; Holcombe and Jiracek, 1984; Queralt et al., 1991), although they are computationally demanding, enable us to investigate the complicated potential field of a point-source in arbitrary media. In particular, the FEM has the flexibility to study complicated models, involving the effect of topography. It does not suffer from a singularity problem at the source point in numerical computations (a refinement of the FDM is required for removing the source singularity, Lowry et al., 1989 and Zhao and Yedlin, 1996) in that the source singularity is naturally and effectively smoothed out by finding the weighted residual solution in the integral sense, or minimising an integral-formed functional.

In this chapter, we apply the FEM to 2.5-D DC resistivity modeling, specifically for computing the 2.5-D Green's function of arbitrary media. This is the basic quantity for resistivity modeling and inversion. Actually, the formulation of the FEM was developed by Coggon (1971), who derived an energy functional (variational principle) for 2-D electromagnetic problems, including DC resistivity modeling. Some modifications of the formulation for 3-D situations and for handling topographic variation were made by

Pridmore et al. (1981) and Holcombe and Jiracek (1984). Queral et al. (1991) developed an alternative form of the FEM using Galerkin's solution (weighted residual criterion). These papers all showed that the two principles of the FEM, the variational principle and Garlerkin's solution, may be applied to 2.5-D DC resistivity modeling. They yield the same linear equation system when using the same boundary condition and the same shape function (see Chapter 2). For completeness, we present here in a simple and general way some important aspects of the FEM to calculate the 2.5-D Green's function, such as the mixed-boundary conditions, computation of the inner element and boundary element matrices and recovery of the electrical potential from the transformed potential. We also present some numerical results comparing the FEM solutions with some analytic solutions, and undertake some simulations for the cases of interest in mining exploration and hydrological engineering, to demonstrate the effectiveness of the numerical method.

3.1 Mixed-Boundary Condition

In numerical modeling, a finite region has to be considered for efficiency, so special boundary conditions are used in numerical techniques. The FEM formula (see equation (2.51) or (2.60)) involves the integral over the boundary $\partial\Omega$. This means that the operator B in the mixed-boundary condition in equation (2.10) or (2.28) must be designed for our case. A self-adjoint differential operator B is also desired so as to make the operator $L(k_y,\sigma)$ self-adjoint too, and also to ensure that the resultant element matrix becomes symmetric (see Section 2.5 and equation (2.51) or (2.60)).

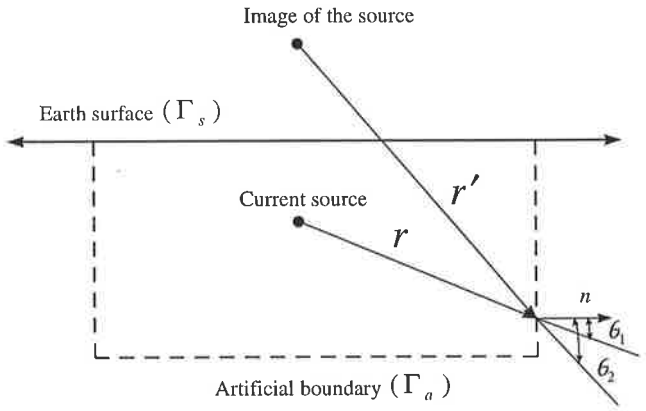

Fig.3-1 Geometry of the boundary condition in 2.5-D DC resistivity modeling.

Normally, the whole boundary consists of two parts: the earth's surface Γ_s and the artificial boundary Γ_a (under the ground–see Fig.3-1). On the earth's surface, because no current crosses it, the Neumann boundary condition should be satisfied, viz.

$$\text{3-D:} \qquad \frac{\partial U}{\partial n} = 0, \quad r \in \Gamma_s, \tag{3.1}$$

where $r = (x, y, z)$ represents the coordinates of the boundary and $n = (n_x, n_y, n_z)$ is the outward unit vector normal to the boundary. In the 2.5-D case, equation (3.1) becomes

$$\text{2.5-D:} \qquad \frac{\partial \overline{U}}{\partial n} = 0, \quad r \in \Gamma_s, \tag{3.2}$$

because n_y=0. For simplicity, we take $n = (n_x, n_z)$ and $r = (x, z)$ in the 2.5-D case. $\overline{U}$ is the Fourier-cosine transform of the 3-D electric potential. On the artificial boundary (the left and right sides and the bottom of the numerical grid), Dey and Morrison (1979a,b) proposed a mixed-boundary conditions in their FDM. Several researchers have shown that the mixed boundary condition produces better numerical solutions than either the classical Dirichlet or Neumann boundary conditions (Zhou and Zhong, 1984). Considering that the current source may be placed underground, e.g. in a borehole, we generalize the mixed-boundary condition as follows:

$$\text{3-D:} \qquad \frac{\partial U}{\partial n} + [\frac{r'^2 \cos\theta_1 + r^2 \cos\theta_2}{rr'\ (r + r')}]U = 0, \qquad r \in \Gamma_a, \tag{3.3}$$

$$\text{2.5-D:} \qquad \frac{\partial \overline{U}}{\partial n} + k_y[\frac{K_1(rk_y)\cos\theta_1 + K_1(r'k_y)\cos\theta_2}{K_0(rk_y) + K_0(r'k_y)}]\overline{U} = 0, \quad r \in \Gamma_a, \tag{3.4}$$

where r, r', θ_1 and θ_2 are shown in Fig.3-1. K_0 and K_1 are the modified Bessel functions of the first kind. Actually, these conditions are approximate boundary conditions obtained using the assumption that the potential U and the transformed potential $\overline{U}$, far from any inhomogeneties, are of the form $U = C(1/r + 1/r')$ (C is a constant) and $\overline{U} = C\,[K_0(rk_y) + K_0(r'k_y)]$ (see equation (2.32)) so that we have the following identities:

$$\frac{\partial}{\partial n}[C(\frac{1}{r} + \frac{1}{r'})] = -C(\frac{\nabla r}{r^2} + \frac{\nabla r'}{r'^2}) \cdot n = -[\frac{r'^2 \cos\theta_1 + r^2 \cos\theta_2}{rr'\ (r + r')}]U, \tag{3.5}$$

$$\begin{aligned} \frac{\partial}{\partial n}\{C \cdot [K_0(rk_y) + K_0(r'k_y)]\} &= -C \cdot k_y[K_1(rk_y)\nabla r \cdot n + K_1(r'k_y)\nabla r' \cdot n], \\ &= -k_y[\frac{K_1(rk_y)\cos\theta_1 + K_1(r'k_y)\cos\theta_2}{K_0(rk_y) + K_0(r'k_y)}]\overline{U}. \end{aligned} \tag{3.6}$$

Clearly, the boundary conditions (3.3) and (3.4) follow directly from equation (3.5) and (3.6), respectively. When the current source is located at the surface Γ_s, the mixed

boundary conditions (3.3) and (3.4) become the original form proposed by Dey and Morrison (1979a,b). So, in our case we take equation (3.4) as the boundary condition on Γ_a, that is, the boundary operator B in equation (2.51) or (2.60) may be presented by the following form in terms of equations (3.2) and (3.4):

$$B=\begin{cases}0, & r\in\Gamma_s\\ k_y[\dfrac{K_1(rk_y)\cos\theta_1+K_1(r'k_y)\cos\theta_2}{K_0(rk_y)+K_0(r'k_y)}], & r\in\Gamma_a\end{cases}. \tag{3.7}$$

It should be noted that the operator B, used in the boundary integral (see equation (2.51) or (2.60)), is dependent on the position of the source when the wavenumber k_y is given. In a practical DC resistivity survey, different source positions (current injection points) are commonly employed to obtain the maximum information about the resistivity variation in the media. If we directly use the boundary operator (3.7), it leads to redundant computations in the boundary integral due to the different source locations for a given wavenumber k_y. An efficient way is to replace the source point in B with the average position of all the current injection points so that the boundary integral is calculated only once for each wavenumber k_y. This saves much computer memory and computer time. Obviously, the replacement is reasonable when the DC resistivity survey is simulated within the relatively small central area of the entire computational range.

3.2 The FEM Formulation

As mentioned in Chapter 2, 2.5-D resistivity modeling may be reduced to solving the integral equation (2.51) or (2.60) via the two principles of the FEM, and computation of the response to any source is completely equivalent to computation of the 2.5-D Green's function for arbitrary media. For simplicity, we prefer the Galerkin's solution as the basic approximation to the variational principle. That is, equation (2.51) reduces to the following for the 2.5-D Green's function in DC resistivity modeling:

$$\sum_i\{\int_\Omega[\sigma\nabla N_i\cdot\nabla N_j+k_y^2\sigma N_iN_j]dr+\int_{\partial\Omega}\sigma N_jBN_id\Gamma\}\overline{G}_i^{2.5D}=N_j\delta_{is},\quad (j=1,2,3,\ldots,N). \tag{3.8}$$

Here N_i ($i=1,2,\ldots,N$) is the i-th shape function in the Galerkin's solution and $\overline{G}_i^{2.5D}$ ($i=1,2,\ldots,N$) is the i-th nodal values of the Green's function. N is the total number of shape

functions. Normally it is equal to the number of the nodes after discretising the range Ω.

To calculate the integrals in equation (3.8), we divide the computational range Ω and the boundary $\partial\Omega$ into a set of subranges (elements) and segments, e.g. $\Omega = \sum_e \Omega_e$ and $\partial\Omega = \sum_e \Gamma_e$, so that the equation reduces to the following linear equation system:

$$M\overline{G}^{2.5D} = b_s, \tag{3.9}$$

where

$$\begin{aligned} M &= \left(M_{ij}\right)_{N\times N}, \quad M_{ij} = \sum_e (A_{ij}^e + B_{ij}^e), \\ \overline{G}^{2.5D} &= \{\overline{G}_i^{2.5D}\}^T, (i = 1,2,\ldots,N), \\ b_s &= \{N_i\delta_{is}\}^T, (i = 1,2,\ldots,N), \end{aligned} \tag{3.10}$$

and

$$A_{ij}^e = \int_{\Omega_e} \sigma(r)[\nabla N_i(r)\cdot\nabla N_j(r) + k_y^2 N_i(r)N_j(r)]dr, \tag{3.11}$$

$$B_{ij}^e = \int_{\Gamma_e} \sigma(r)N_i(r)BN_j(r)d\Gamma. \tag{3.12}$$

These matrices A_{ij}^e and B_{ij}^e may be called the inner element matrix and the boundary element matrix, both of which are symmetric in terms of equations (3.11) and (3.12). From equations (3.10) ~ (3.12), one can see that the coefficient matrix M, assembled with A_{ij}^e and B_{ij}^e, is symmetric too. Once the element matrices are calculated, one can solve the linear equation system (3.9) to obtain the Galerkin's solution for the 2.5-D Green's function. In the following sections we detail the computation of the elemental matrices.

(1) Inner Element Matrix

Reviewing equation (3.11), to calculate the inner matrix A_{ij}^e, one has to chose the geometry of the element Ω_e that comprise the whole range Ω and the shape function $N_i(r)$ corresponding to the specified geometry, In general, an appropriate mesh (dividing the range Ω into a set of elements) and the shape function may be determined in terms of the practical situation and the accuracy requirement in the modeling. Zhou and Zhong (1984) have shown that the different meshes, e.g. asymmetrical and symmetric meshes, may yield different accuracies in the numerical results for DC resistivity modeling. The preferred mesh is the completely symmetric one shown in Fig.3-2. The whole range is divided into two parts: the modeling area (shaded part in Fig.3-2a) and the transition area out to the boundary, both of which consist of the rectangular elements whose size may be

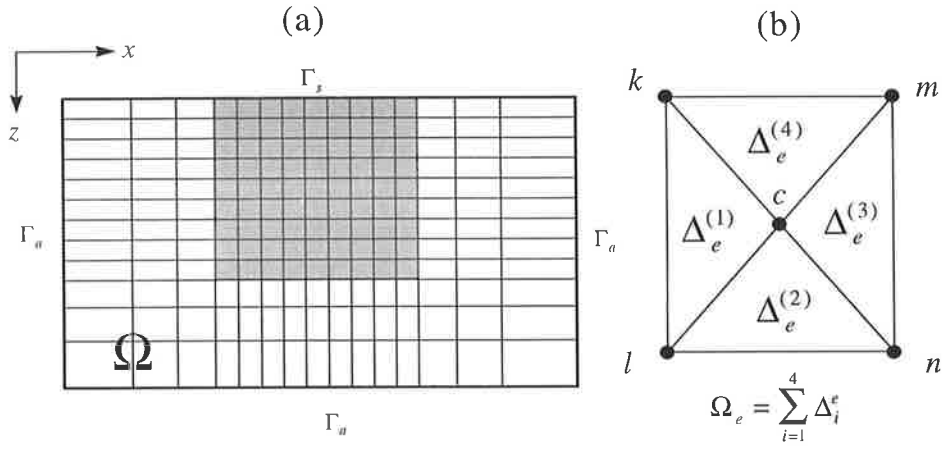

Fig.3-2 Sketch of the whole FEM mesh (a) and a rectangular element with four triangular cells (b) for 2.5-D DC resistivity modeling. The shaded area is the modeling area.

variable and each of the rectangular elements has four triangular cells (labeled with $\{\Delta_e^{(i)}$, $i=1,2,3,4\}$ in Fig.3-2b). Normally, a small size may be chosen for the elements (cells) in the modeling area (shaded area in Fig.3-2a) for satisfactory accuracy and a gradual change in the size (from small to large) in the transition area is used for obtaining the appropriate dimension of the linear equation system. The main advantages of this hybrid mesh are not only the improved accuracy in modeling but also greater flexibility to simulate complicated models. In theory, the artificial boundary Γ_a must be far enough away from the modeling area so that the mixed-boundary condition (3.3) or (3.4) works well. The adjustable size of the rectangular element in the transition area enables us easily to control the dimensions of the mesh. For crosshole resistivity modeling and inversion, we may take the constant size of the rectangular elements in the modeling area (Δx and Δz are not changed for all the elements in the shaded area) and the adjustable size of the rectangular elements in the transition area (linearly changing Δx and Δz with the distance away from the modeling area) so as to have an appropriate dimension of the mesh and to not lose the accuracy and spatial resolution in modeling and inversion.

According to the geometry of the division and the Galerkin' s solution, the inner element matrix becomes the summation of the four triangular integrals (see equation (3.11)):

$$\begin{aligned} A_{ij}^e &= \{\int_{\Delta_e^{(1)}} + \int_{\Delta_e^{(2)}} + \int_{\Delta_e^{(3)}} + \int_{\Delta_e^{(4)}}\}\sigma(r)[\nabla N_i(r)\cdot\nabla N_j(r) + k_y^2 N_i(r)N_j(r)]dr, \\ &= (A_{ij}^e)^{(1)} + (A_{ij}^e)^{(2)} + (A_{ij}^e)^{(3)} + (A_{ij}^e)^{(4)}, \quad (i,j = k,l,m,n,c), \end{aligned} \tag{3.13}$$

where the letters (k,l,m,n,c) stand for the five nodes in the rectangular element (four corners and central point, see Fig.3-2b). $\{(A_{ij}^{e})^{(p)}, p=1,2,3,4\}$ represents the four triangular integrals. This equation reveals an undesirable feature that the mesh or the division of the range Ω has a large number of nodes because of the introduction of the central node in each rectangular element. This implies that to obtain the Green's function one has to solve the large dimensional linear equation system (3.9). For instance, if the mesh has N_x and N_z nodes in the x- and z-directions respectively, the dimension of the linear equation system (3.9) becomes $N=N_x \cdot N_z + (N_x - 1)(N_z - 1)$. Schemes have been suggested by several researchers to reduce the dimension. For example, Zhou and Zhong (1984) demonstrated a method in the variational principle formulation to remove the central node with the four triangular integrals. This scheme deals with a lower dimension of the linear equation system ($N=N_x \cdot N_z$) and does not lose numerical accuracy. The desirable scheme was realized with just one weak assumption: no current injection at the central nodes. Here we adopted the scheme for the Galerkin's solution. For ease of discussion, we arrange the three nodal numbers of the triangular cell in anti-clockwise order, e.g. (k,l,c), (l,n,c), (m,c,n) and (k,c,m) which stand for the nodal number sets of the four triangles: $\Delta_e^{(1)}$, $\Delta_e^{(2)}$, $\Delta_e^{(3)}$ and $\Delta_e^{(4)}$ respectively (see Fig.3-2b). As an example to calculate the triangular integrals, here we will calculate the first one in equation (3.13). The others can be obtained in similar manner.

In the first triangular cell, we have the three linear shape functions defined as follows for the three nodes k, l and c (Zienkiewicz, 1971):

$$
\begin{aligned}
N_k^{(1)}(x,z) &= \frac{1}{2\Delta_e^{(1)}}\begin{vmatrix} 1 & x & z \\ 1 & x_l & z_l \\ 1 & x_c & z_c \end{vmatrix} = \frac{1}{2\Delta_e^{(1)}}[a_k^{(1)} + b_k^{(1)}x + c_k^{(1)}z], \\
N_l^{(1)}(x,z) &= \frac{1}{2\Delta_e^{(1)}}\begin{vmatrix} 1 & x_k & z_k \\ 1 & x & z \\ 1 & x_c & z_c \end{vmatrix} = \frac{1}{2\Delta_e^{(1)}}[a_l^{(1)} + b_l^{(1)}x + c_l^{(1)}z], \\
N_c^{(1)}(x,z) &= \frac{1}{2\Delta_e^{(1)}}\begin{vmatrix} 1 & x_k & z_k \\ 1 & x_l & z_l \\ 1 & x & z \end{vmatrix} = \frac{1}{2\Delta_e^{(1)}}[a_c^{(1)} + b_c^{(1)}x + c_c^{(1)}z],
\end{aligned}
\tag{3.14}
$$

where the superscript (1) and the symbol $\Delta_e^{(1)}$ stand for the first triangle and its

corresponding area. The points (x_k, z_k), (x_l, z_l) and (x_c, z_c) are the coordinates of the three nodes of the triangle. According to the definitions (3.14), the shape functions have the property: $\{N_i^{(1)}(x_j, z_j) = \delta_{ij},\ i,j=k,l,c\}$ and the coefficients in equation (3.14) are calculated by the following expressions:

$$\begin{aligned} a_k^{(1)} &= x_l z_c - z_l x_c, \quad b_k^{(1)} = \Delta z/2, \quad c_k^{(1)} = \Delta x/2; \\ a_l^{(1)} &= x_c z_k - z_c x_k, \quad b_l^{(1)} = \Delta z/2, \quad c_l^{(1)} = -\Delta x/2; \\ a_c^{(1)} &= x_k z_l - z_k x_l, \quad b_c^{(1)} = -\Delta z_l, \quad c_c^{(1)} = 0. \end{aligned} \tag{3.15}$$

Supposing the conductivity $\sigma(x,z)$ within the triangle is assumed to be constant, then by substituting the shape functions (3.14) into the integral (3.13), we obtain:

$$(A_{ij}^e)^{(1)} = \frac{\sigma_e^{(1)}}{4\Delta_e^{(1)}}(b_i^{(1)} b_j^{(1)} + c_i^{(1)} c_j^{(1)}) + \frac{\sigma_e^{(1)}}{12}\Delta_e^{(1)}(1+\delta_{ij})k_y^2, \quad (i,j = k,l,c). \tag{3.16}$$

Here we used the following identity:

$$\int_{\Delta_e^{(1)}} N_i^{(1)}(r) N_j^{(1)}(r) dr = \frac{\Delta_e^{(1)}}{12}(1+\delta_{ij}). \tag{3.17}$$

Reviewing equation (3.16) one can directly write out similar results for the other three integrals:

$$(A_{ij}^e)^{(2)} = \frac{\sigma_e^{(2)}}{4\Delta_e^{(2)}}(b_i^{(2)} b_j^{(2)} + c_i^{(2)} c_j^{(2)}) + \frac{\sigma_e^{(2)}}{12}\Delta_e^{(2)}(1+\delta_{ij})k_y^2, \quad (i,j = l,n,c), \tag{3.18}$$

$$(A_{ij}^e)^{(3)} = \frac{\sigma_e^{(3)}}{4\Delta_e^{(3)}}(b_i^{(3)} b_j^{(3)} + c_i^{(3)} c_j^{(3)}) + \frac{\sigma_e^{(3)}}{12}\Delta_e^{(3)}(1+\delta_{ij})k_y^2, \quad (i,j = m,c,n), \tag{3.19}$$

$$(A_{ij}^e)^{(4)} = \frac{\sigma_e^{(4)}}{4\Delta_e^{(4)}}(b_i^{(4)} b_j^{(4)} + c_i^{(4)} c_j^{(4)}) + \frac{\sigma_e^{(4)}}{12}\Delta_e^{(4)}(1+\delta_{ij})k_y^2, \quad (i,j = k,c,m), \tag{3.20}$$

where

$$\begin{aligned} &b_l^{(2)} = \Delta z/2, \quad b_n^{(2)} = -\Delta z/2, \quad b_c^{(2)} = 0, \\ &c_l^{(2)} = -\Delta x/2, \quad c_n^{(2)} = -\Delta x/2_c, \quad c_c^{(2)} = \Delta x, \\ &b_m^{(3)} = -\Delta z/2, \quad b_c^{(3)} = \Delta z, \quad b_n^{(3)} = -\Delta z/2, \\ &c_m^{(3)} = \Delta x/2, \quad c_c^{(3)} = 0, \quad c_n^{(3)} = -\Delta x/2, \\ &b_k^{(4)} = \Delta z/2, \quad b_c^{(4)} = 0, \quad b_m^{(4)} = -\Delta z/2, \\ &c_k^{(4)} = \Delta x/2, \quad c_c^{(4)} = -\Delta x, \quad c_m^{(4)} = \Delta x/2. \end{aligned} \tag{3.21}$$

Substituting equations (3.16), (3.18), (3.19) and (3.20) into equation (3.13) and using the results of the coefficients (3.15) and (3.21), we have the thirteen independent non-zero components of the rectangular element matrix:

$$
\begin{aligned}
A_{kk}^{e} &= \frac{1}{2}\{(\sigma_e^{(4)}+\sigma_e^{(1)})[\frac{\Delta z}{2\Delta x}+\frac{\Delta x}{2\Delta z}+\frac{k_y^2}{12}\Delta x\Delta z]\},\\
A_{kl}^{e} &= \frac{1}{2}\{\sigma_e^{(1)}[\frac{\Delta z}{2\Delta x}-\frac{\Delta x}{2\Delta z}+\frac{k_y^2}{24}\Delta x\Delta z]\},\\
A_{km}^{e} &= \frac{1}{2}\{\sigma_e^{(4)}[\frac{\Delta x}{2\Delta z}-\frac{\Delta z}{2\Delta x}+\frac{k_y^2}{24}\Delta x\Delta z]\},\\
A_{kc}^{e} &= \frac{1}{2}\{-[\sigma_e^{(1)}\frac{\Delta z}{\Delta x}+\sigma_e^{(4)}\frac{\Delta x}{\Delta z}]+\frac{(\sigma_e^{(1)}+\sigma_e^{(4)})}{24}k_y^2\Delta x\Delta z]\},\\
A_{ll}^{e} &= \frac{1}{2}\{(\sigma_e^{(1)}+\sigma_e^{(2)})[\frac{\Delta z}{2\Delta x}+\frac{\Delta x}{2\Delta z}+\frac{k_y^2}{12}\Delta x\Delta z]\},\\
A_{ln}^{e} &= \frac{1}{2}\{\sigma_e^{(2)}[\frac{\Delta x}{2\Delta z}-\frac{\Delta z}{2\Delta x}+\frac{k_y^2}{24}\Delta x\Delta z]\},\\
A_{lc}^{e} &= \frac{1}{2}\{-[\sigma_e^{(1)}\frac{\Delta z}{\Delta x}+\sigma_e^{(2)}\frac{\Delta x}{\Delta z}]+\frac{(\sigma_e^{(1)}+\sigma_e^{(2)})}{24}k_y^2\Delta x\Delta z]\},\\
A_{mm}^{e} &= \frac{1}{2}\{(\sigma_e^{(3)}+\sigma_e^{(4)})[\frac{\Delta z}{2\Delta x}+\frac{\Delta x}{2\Delta z}+\frac{k_y^2}{12}\Delta x\Delta z]\},\\
A_{mn}^{e} &= \frac{1}{2}\{\sigma_e^{(3)}[\frac{\Delta z}{2\Delta x}-\frac{\Delta x}{2\Delta z}+\frac{k_y^2}{24}\Delta x\Delta z]\},\\
A_{mc}^{e} &= \frac{1}{2}\{-[\sigma_e^{(3)}\frac{\Delta z}{\Delta x}+\sigma_e^{(4)}\frac{\Delta x}{\Delta z}]+\frac{(\sigma_e^{(3)}+\sigma_e^{(4)})}{24}k_y^2\Delta x\Delta z]\},\\
A_{nn}^{e} &= \frac{1}{2}\{(\sigma_e^{(2)}+\sigma_e^{(3)})[\frac{\Delta z}{2\Delta x}+\frac{\Delta x}{2\Delta z}+\frac{k_y^2}{12}\Delta x\Delta z]\},\\
A_{nc}^{e} &= \frac{1}{2}\{-[\sigma_e^{(2)}\frac{\Delta x}{\Delta z}+\sigma_e^{(3)}\frac{\Delta z}{\Delta x}]+\frac{(\sigma_e^{(2)}+\sigma_e^{(3)})}{24}k_y^2\Delta x\Delta z]\},\\
A_{cc}^{e} &= \frac{1}{2}\{(\sigma_e^{(1)}+\sigma_e^{(3)})\frac{2\Delta z}{\Delta x}+(\sigma_e^{(2)}+\sigma_e^{(4)})\frac{2\Delta x}{\Delta z}+(\sigma_e^{(1)}+\sigma_e^{(3)}+\sigma_e^{(2)}+\sigma_e^{(4)})\frac{k_y^2}{12}\Delta x\Delta z\}.
\end{aligned}
\tag{3.22}
$$

All of the above expressions for the components have an additional 1/2 factor compared with the literature, e.g. Zhou and Zhong (1984) and Queralt et al. (1991). This is because we calculate the 2.5-D Green's function instead of the original potential. From the above formula, each rectangular element makes the following contribution:

$$\begin{pmatrix} A^e_{kk} & A^e_{kl} & A^e_{km} & 0 & A^e_{kc} \\ A^e_{lk} & A^e_{ll} & 0 & A^e_{\ln} & A^e_{lc} \\ A^e_{mk} & 0 & A^e_{mm} & A^e_{mn} & A^e_{mc} \\ 0 & A^e_{nl} & A^e_{nm} & A^e_{nn} & A^e_{nc} \\ A^e_{ck} & A^e_{cl} & A^e_{cm} & A^e_{cn} & A^e_{cc} \end{pmatrix} \begin{pmatrix} \overline{G}^{2.5D}_k \\ \overline{G}^{2.5D}_l \\ \overline{G}^{2.5D}_m \\ \overline{G}^{2.5D}_n \\ \overline{G}^{2.5D}_c \end{pmatrix} = \begin{pmatrix} \delta_{ks} \\ \delta_{ls} \\ \delta_{ms} \\ \delta_{ns} \\ 0 \end{pmatrix}, \tag{3.23}$$

to the whole linear equation system (3.9). In equation (3.23) we have used the assumption that no current source is located at the central point of the rectangular element so that the component of the right-hand vector is zero. From the last row in the above equation we have the expression for the central value:

$$\overline{G}^{2.5D}_c = -\frac{1}{A^e_{cc}}(A^e_{ck}\overline{G}^{2.5D}_k + A^e_{cl}\overline{G}^{2.5D}_l + A^e_{cm}\overline{G}^{2.5D}_m + A^e_{cn}\overline{G}^{2.5D}_n) \tag{3.24}$$

Substituting (3.24) for the other rows in equation (3.23), we obtain:

$$\begin{pmatrix} (A^e_{kk} - \frac{A^e_{kc}A^e_{kc}}{A^e_{cc}}) & (A^e_{kl} - \frac{A^e_{kl}A^e_{lc}}{A^e_{cc}}) & (A^e_{km} - \frac{A^e_{km}A^e_{mc}}{A^e_{cc}}) & (A^e_{kn} - \frac{A^e_{kn}A^e_{nc}}{A^e_{cc}}) \\ (A^e_{kl} - \frac{A^e_{kl}A^e_{lc}}{A^e_{cc}}) & (A^e_{ll} - \frac{A^e_{lc}A^e_{lc}}{A^e_{cc}}) & (A^e_{lm} - \frac{A^e_{lc}A^e_{mc}}{A^e_{cc}}) & (A^e_{\ln} - \frac{A^e_{lc}A^e_{nc}}{A^e_{cc}}) \\ (A^e_{km} - \frac{A^e_{km}A^e_{mc}}{A^e_{cc}}) & (A^e_{lm} - \frac{A^e_{lc}A^e_{mc}}{A^e_{cc}}) & (A^e_{mm} - \frac{A^e_{mc}A^e_{mc}}{A^e_{cc}}) & (A^e_{mn} - \frac{A^e_{mc}A^e_{nc}}{A^e_{cc}}) \\ (A^e_{kn} - \frac{A^e_{kn}A^e_{nc}}{A^e_{cc}}) & (A^e_{\ln} - \frac{A^e_{lc}A^e_{nc}}{A^e_{cc}}) & (A^e_{mn} - \frac{A^e_{mc}A^e_{nc}}{A^e_{cc}}) & (A^e_{nn} - \frac{A^e_{nc}A^e_{nc}}{A^e_{cc}}) \end{pmatrix} \begin{pmatrix} \overline{G}^{2.5D}_k \\ \overline{G}^{2.5D}_l \\ \overline{G}^{2.5D}_m \\ \overline{G}^{2.5D}_n \end{pmatrix} \tag{3.25}$$

$$= (\delta_{ks}, \delta_{ls}, \delta_{ms}, \delta_{ns})^T.$$

Obviously, equations (3.23) and (3..25) are equivalent, but the latter does not contain the value of the Green's function at the central node ($\overline{G}^{2.5D}_c$). This means that using equation (3.25) to assemble the whole matrix $\boldsymbol{M}$ in equation (3.9) has reduced the dimension of the linear equation system from $N = N_x \cdot N_z + (N_x - 1)(N_z - 1)$ to $N = N_x \cdot N_z$ and it retains the same numerical accuracy as the original, because both employ the same triangular shape functions. So, the new rectangular element matrix may be summarized by the following expression and will still be symmetric:

$$(A')^e_{ij} = A^e_{ij} - \frac{A^e_{ic}A^e_{jc}}{A^e_{cc}}, \quad (i, j = k, l, m, n). \tag{3.26}$$

It is applied to the formation of the matrix M in equation (3.9).

(2) Boundary Element Matrix

To calculate the boundary integral (3.12), we consider the boundary operator B (equation (3.7)) to be a constant operator over each segment Γ_e, that is

$$B_e = \begin{cases} 0, & r \in \Gamma_s \\ k_y[\dfrac{K_1(r_e k_y)\cos\theta_1^e + K_1(r_e' k_y)\cos\theta_2^e}{K_0(r_e k_y) + K_0(r_e' k_y)}], & r \in \Gamma_e, \end{cases} \tag{3.27}$$

where r_e and r_e' are the distances from the source and its image to the mid-point of the segment Γ_e. θ_1^e and θ_2^e are the segmental values of θ_1 and θ_2 (see Fig.3-1). So, the boundary integral (3.12) becomes

$$B_{ij}^e = \sigma_e B_e \int_{\Gamma_e} N_i(r) N_j(r) d\Gamma \tag{3.28}$$

Note that the triangular shape functions (3.14) can be rewritten in the following form for the two nodes i and j of the boundary segment Γ_e:

$$N_i(s) = \frac{\Delta_s}{\Delta_e} = \frac{s}{\Gamma_e}$$
$$N_j(s) = \frac{\Delta_e - \Delta_s}{\Delta_e} = 1 - \frac{s}{\Gamma_e} \tag{3.29}$$

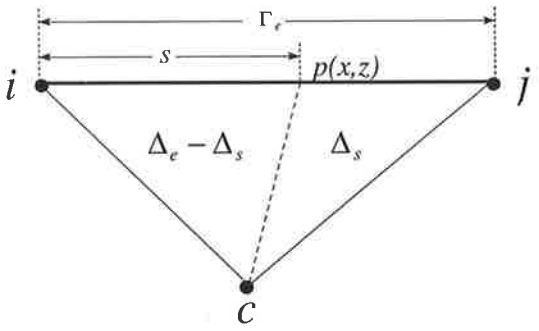

Fig.3-3 A boundary segment of a triangular cell.

where s stands for the length from the node i to the point (x,z) and Δ_s and Δ_e denote the areas of the two triangles (i,c,p) and (i,c,j) (see Fig.3-3). Substituting equation (3.29) for the integral (3.28), the boundary element matrix is obtained as:

$$B_{ij}^e = \begin{cases} \sigma_e B_e \int_0^{\Gamma_e} (\frac{s}{\Gamma_e})(\frac{s}{\Gamma_e}) ds = \frac{1}{3}\sigma_e B_e \Gamma_e, & (i = j), \\ \sigma_e B_e \int_0^{\Gamma_e} (\frac{s}{\Gamma_e})(1 - \frac{s}{\Gamma_e}) ds = \frac{1}{6}\sigma_e B_e \Gamma_e, & (i \neq j). \end{cases} \tag{3.30}$$

or
$$B_{pq}^e = \frac{1}{6}\sigma_e B_e \Gamma_e (1 + \delta_{pq}), \quad (p,q = i,j), \tag{3.31}$$

from which one can find only three contributions: B_{ii}^e, B_{ij}^e and B_{jj}^e to the elemental matrix M_{pq}^e.

3.3 Inverse Fourier Transform

To obtain the spatial potential $U(r_c,r_p)$ or the corresponding Green's function $G^{3D}(r_c,r_p)$, the inverse Fourier transform corresponding to equation (2.30) is required, i.e.

$$U(r_c,r_p) = F_c^{-1}[\overline{U}(k_y,r_c,r_p)] = \frac{2}{\pi}\int_0^{\infty}\overline{U}(k_y,r_c,r_p)\cos(k_y y)dk_y, \tag{3.32}$$

where $\overline{U}(k_y,r_c,r_p) = I\cdot\overline{G}^{2.5D}(k_y,r_c,r_p)/2$. From considerations of computer time the numerical algorithm is normally used to calculate only a few samples of the transformed potential $\{\overline{U}(k_{y_i},r_c,r_p), i=1,2,...,N_y\}$. So, the means to calculate the inverse Fourier transform with the finite samples is important for obtaining a highly accurate spatial potential $U(r_c,r_p)$ or 3-D Green's function $G^{3D}(r_c,r_p)$. Most researchers, when studying analytically transformed potentials for a homogeneous half-space and some simple inhomogeneous models (e.g. stratified model, vertical contact, a horst model), found that they have the same shaped curves in the logarithmic representation (Dey and Morrison, 1979a, 1979b; Zhou and Zhong, 1986; Queralt et al., 1991). For instance, in a homogeneous half-space and a two-layered model, the transformed potentials are given by the following analytic expressions:

Half-space: $$\overline{U}(k_y,r_c,r_p) = \frac{I\rho}{2\pi}F_c\left(\frac{1}{|r_c-r_p|}\right) = \frac{I\rho}{2\pi}K_0(k_y|r_c-r_p|) \tag{3.33}$$

Two-layers: $$\overline{U}(k_y,r_c,r_p) = \frac{I\rho_1}{2\pi}F_c\left[\frac{1}{|r_c-r_p|}+2\sum_{n=1}^{\infty}\frac{R_{12}^n}{\sqrt{|r_c-r_p|^2+(2nh)^2}}\right]$$

$$= \frac{I\rho_1}{2\pi}\left[K_0(k_y|r_c-r_p|)+2\sum_{n=1}^{\infty}R_{12}^n K_0\left(k_y\sqrt{|r_c-r_p|^2+(2nh)^2}\right)\right] \tag{3.34}$$

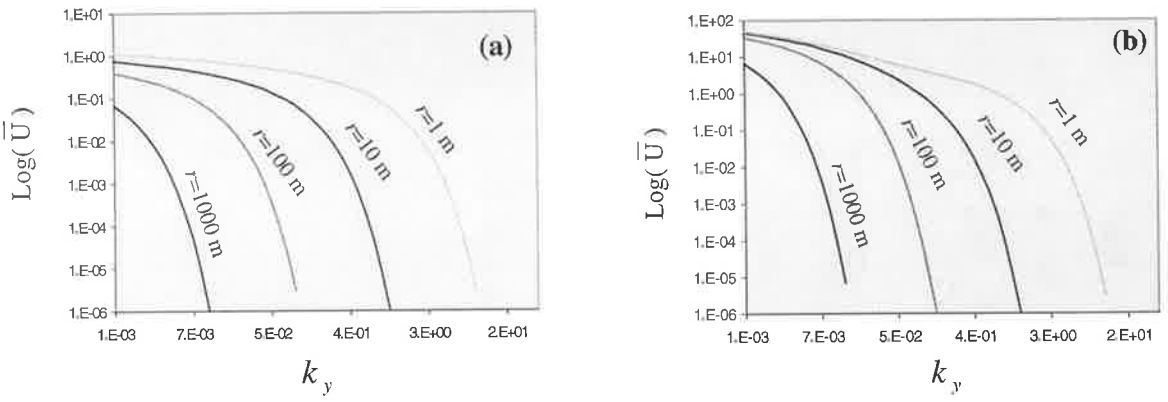

Fig.3-4 Typical shape of the transformed potential for different distances $r = |r_c - r_p|$ in (a) a homogeneous half-space and (b) a two-layered model. The resistivities of the two layers are 10 Ωm and 100 Ωm respectively, and the thickness of the first layer is 10 m.

where h is the thickness of the layer and $R_{12} = (\rho_2 - \rho_1)/(\rho_2 + \rho_1)$ is the reflection coefficient. Fig.3-4 shows the typical shape of the transformed potentials. This logarithmic representation demonstrates the feature that in all of these cases, the behaviour of the transformed potentials is the same: a very slow decrease for small k_y and monotonically decreasing to zero as $k_y \to \infty$. This feature allows one to use the same approach to the transformed potentials for the different distances and arbitrary models. For example, Dey and Morrison (1979a,b) suggested an exponential interpolation for $\overline{U}$ to calculate the inverse Fourier transform (3.32) for an array parallel to the strike direction ($y \neq 0$). Queralt et al. (1991) proposed a combined logarithmic-exponential interpolation for $\overline{U}$. Since the latter approach includes the former one, Queralt et al.'s formula (1991, Appendix B) can be considered as a general form for numerical calculation of the inverse Fourier transform:

$$\begin{aligned} U(r_c, r_p) \approx & \frac{2}{\pi y}[\overline{U}_1 \sin(k_1 y) - si(k_1 y)] \\ & + \sum_n \frac{2}{\pi y} B_n [\ln(\frac{e^{\overline{U}_n / B_n}}{k_n} k_y) \sin(k_y y) - si(k_y y)]_{k_n}^{k_{n+1}} \\ & + \sum_m \frac{2}{\pi(a_m^2 + y^2)} \{\overline{U}(k_y)[y \sin(k_y y) - a_m \cos(k_y y)]\}_{k_m}^{k_{m+1}}, \end{aligned} \tag{3.35}$$

where $B_n = \dfrac{(\overline{U}_n - \overline{U}_{n+1})}{\ln(k_n / k_{n+1})}$, $a_m = \dfrac{\ln(\overline{U}_m / \overline{U}_{m+1})}{k_{m+1} - k_m}$, $si(x) = \displaystyle\int_0^x \frac{\sin(t)}{t} dt$. (3.36)

Here the sequence $\{\overline{U}_1, \overline{U}_2, ..., \overline{U}_N\}$ represents the values of the transformed potential at these samples $\{k_1, k_2, ..., k_N\}$ of k_y. The first and second terms in equation (3.35) are the integral results using the logarithmic interpolation. The last term comes from the exponential interpolation and it should include the integral result over $[k_N, \infty)$ when taking $k_{m+1} = \infty$ and $\overline{U}(\infty) = 0$. There is a critical point that divides the whole range of k_y into two subsets: one for logarithmic interpolation and another for exponential interpolation. Queralt et al. (1991) showed by different numerical tests that the critical point may be determined by the relation $k_y r = 0.5$ and the combined logarithmic-exponential approach is satisfactory. Obviously, if the logarithmic approximation terms in the expression (3.35) are dropped, it becomes the pure exponential approximation (Dey and Morrison, 1979a, 1979b; Zhou and Zhong, 1984).

An alternative case for the inverse Fourier transform is to calculate the potential of an array perpendicular to the strike direction (y=0). This case is the common application of 2.5-D resistivity modeling. In this situation, due to the disappearance of the cosine factor in the integrand of equation (3.32), the numerical calculation becomes simpler. As pointed out by Queralt et al. (1991), no numerical problem arises in this case, an exponential interpolation is sufficient and the improved logarithmic interpolation is not necessary. So, the inverse Fourier transform (3.32) is implemented with the following expression:

$$U(r_c,r_p) \approx \frac{2}{\pi}\overline{U}_1 \cdot k_1 + \frac{2}{\pi}\sum_m^N \frac{(\overline{U}_m - \overline{U}_{m+1})}{\ln(\overline{U}_m / \overline{U}_{m+1})}(k_{m+1} - k_m) + \frac{2\overline{U}_N}{\pi \ln(\overline{U}_{N-1} / \overline{U}_N)}(k_N - k_{N-1}). \tag{3.37}$$

The first term is the rectangular approximation for the integral over the range $(0,k_1]$ considering k_1 to be a very small value, and the last term is the direct result with exponential interpolation for the range $[k_N,\infty)$.

From the above discussion, we see that once the wavenumber samples $\{k_1,k_2,...,k_N\}$ are chosen and the spectral potentials $\{\overline{U}_1,\overline{U}_2,...,\overline{U}_N\}$ are obtained, the potential U can be recovered by equation (3.35) or (3.37) in terms of the electrode array parallel or perpendicular to the strike direction. The typical shape of the transformed potential may help one to determine the distribution of the wavenumber samples, because it shows that each distance $r=|r_c - r_p|$ has a certain range of k_y yielding significant values of the spectral potential (see Fig.3-4). In other words, the maximum k_y for significant values of $\log(\overline{U})$ varies with different distances r. The smaller the distance r, the bigger the maximum k_y. This implies that if resistivity modeling involves the calculation for different distances (this often occurs in practical applications), the right range of k_y is required for all distances. For instance, $\{r_1,r_2,...,r_n\}$ denotes the different distances, having individual ranges of k_y: $\{R(r_1),R(r_2),...,R(r_n)\}$. According to the typical shape of the spectral potential, the right range for sampling k_y in the modeling should be the maximum of them all: $R(r)$= $\max\{R(r_1),R(r_2),...,R(r_n)\}$, so that all the significant values of $\overline{U}$ are included in the calculation. After obtaining the right range, one can distribute the samples $\{k_1,k_2,...,k_N\}$ in $R(r)$ with an equal and unequal logarithmic interval.

It must be mentioned that the calculation for the inverse Fourier transform is only available for the spectral potential of one current source and one potential electrode (pole-pole array), because the shape of the transformed potential involving more electrodes such as pole-bipole, bipole-pole and bipole-bipole may be more complicated than the typical shape. In general, the shape depends on the configuration of the electrodes (sources and receivers) with respect to the model. Queralt et al. (1991, Fig.3) gave an example of the different shape of the transformed potential in a horst model with bipole-pole surveying. *Therefore, to correctly calculate the potential due to several electrodes, each source must be calculated separately and the results (contributions) added algebraically.*

3.4 Implementation of The Method

From the previous formulation, one can see that each rectangular element in the mesh shown in Fig.3-2a makes a contribution to the total matrix M with a 4×4 elemental matrix $(A')^e_{ij}$ given by equation (3.26) and the boundary element matrix B^e_{ij} given by equation (3.31) when involving a segment of the boundary. So, the rectangular element matrix consists of the two matrices in terms of equation (3.10):

$$M^e_{ij} = (A^e_{ij} - \frac{A^e_{ic}A^e_{jc}}{A^e_{cc}}) + \frac{1}{6}\sigma_e B_e \Gamma_e (1+\delta_{ij}), \quad (i,j = k,l,m,n), \tag{3.38}$$

which assembles as $M = \sum_e M^e_{ij}$. This expression shows that the matrix M is a symmetric banded matrix. The maximal width depends upon the number of nodes in the z-direction if ordering is done on the nodes in the z-direction, then in the x-direction. For instance, note that an inner node has four neighbouring rectangular elements (see Fig.3-5), so there are in total 9 non-zero components in the i-th row of M: $\{ M_{i(i-N_z-1)}, \quad M_{i(i-N_z)}, \quad M_{i(i-N_z+1)}, \quad M_{i(i-1)}, \quad M_{ii}, \quad M_{i(i+1)}, \quad$

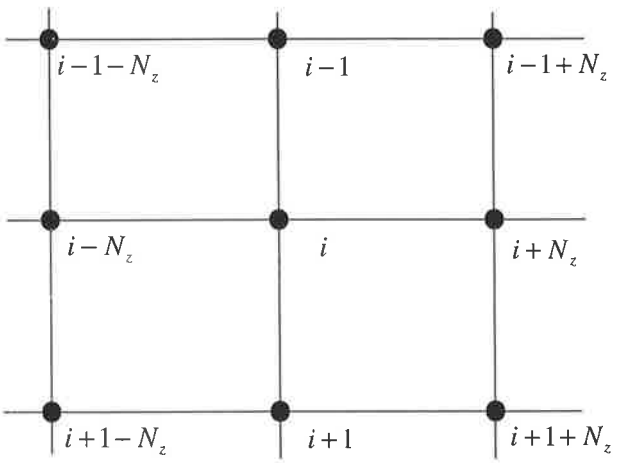

Fig.3-5 The neighbouring nodes of the i-th node in the FEM mesh.

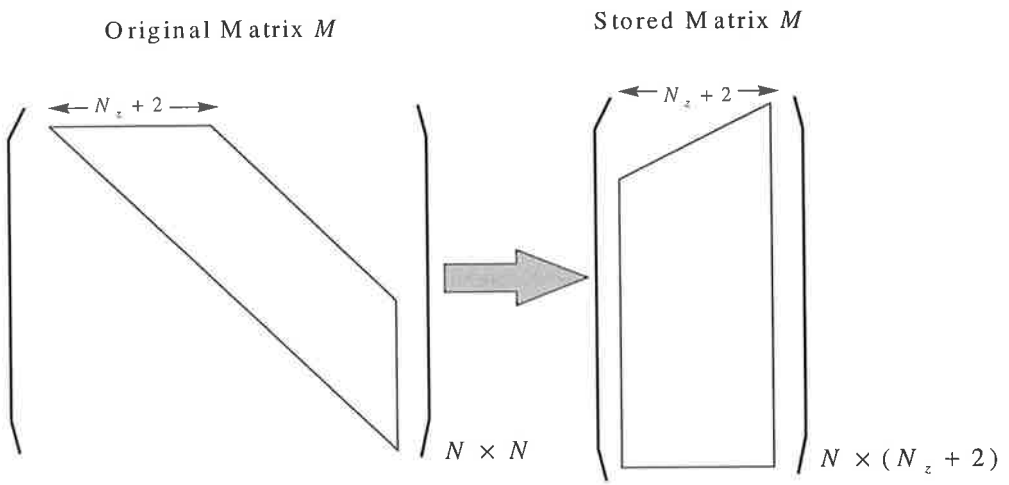

Fig.3-6 Computation and storage scheme for the matrix M.

$M_{i(i+N_z-1)}$, $M_{i(i+N_z)}$, $M_{i(i+N_z+1)}$ }. This implies that the maximal width in the i-th row of M is $(i+1+N_z)$-$(i-1-N_z)=2*(1+N_z)$. Due to the symmetry of the matrix only those components in the upper or lower band need to be calculated and stored in the numerical algorithm. Fig.3-6 shows a scheme for computing and storing M. Obviously, this scheme saves much computer time and memory when dealing with large dimensional modeling. From inspection of Fig.3-6, one can easily obtain the relation of the two matrices:

$$M[i,j]_{N\times N} \Leftrightarrow M[i,N_z+2-(j-i)]_{N\times(N_z+2)}, \quad (j \geq i).$$

Actually, the matrix M is positive-definite, because of the basic requirement for the existence of the solution of the variational principle (equation (2.60)), which is equivalent to the Galerkin's solution when taking the triangular shaped functions (from optimisation theory of quadratic forms, the necessary and sufficient condition for reaching the minima is that the Hessian matrix be positive-definite). This property of M enables us to apply the banded Cholesky decomposition ($M= LL^T$) to solving equation (3.9). It must be mentioned that the matrix M depends upon not only the model parameters σ_e but also upon the wavenumber k_y (see equations (3.22) and (3.38)). It follows that for each wavenumber one has to implement the LL^T decomposition repeatedly to get the k_y-component of the Green's function. For large dimensional modeling, the LL^T decomposition consumes significant computer time, which means that the more sample numbers of the wavenumber k_y that are used, the more computer time is consumed.

After the decomposition, the wavenumber-domain solution $\overline{G}^{2.5D}$ can be obtained by forward-substitution and back-substitution due to the fact that the matrix L is a lower triangular matrix. Substituting the solution for equation (2.30), one can calculate the electrical potential $U(r_c, r_p)$ for arbitrary media.

In resistivity field surveys, the quantity "apparent resistivity" rather than the potential is used to indicate the variation in the electrical properties of subsurface. Apparent resistivity is defined by

$$\rho_a = K\frac{\Delta U}{I}, \tag{3.39}$$

where $\Delta U = U_M - U_N$ is the potential difference between the two potential electrodes, e.g. M and N (one of them may be remote), I is the total current entering the ground and K is a geometric factor, which depends on the electrode array configuration and can be calculated by one of the following expressions in terms of the current (A and B, one of which may be remote) and potential electrode positions:

$$pole-pole: \quad K = 4\pi\left(\frac{r_{AM}\, r_{A'M}}{r_{AM} + r_{A'M}}\right) \tag{3.40}$$

$$pole-bipole: \quad K = 4\pi\left[\frac{r_{AM}\, r_{A'M}\, r_{AN}\, r_{A'N}}{r_{AN}\, r_{A'N}(r_{AM} + r_{A'M}) - r_{AM}\, r_{A'M}(r_{AN} + r_{A'N})}\right] \tag{3.41}$$

$$bipole-pole: \quad K = 4\pi\left[\frac{r_{AM}\, r_{A'M}\, r_{BM}\, r_{B'M}}{r_{BM}\, r_{B'M}(r_{A'M} + r_{AM}) - r_{AM}\, r_{A'M}(r_{B'M} + r_{BM})}\right] \tag{3.42}$$

$$bipole-bipole: \quad K = 4\pi\left[\frac{(r_{AM} + r_{A'M})\, r_{AN}\, r_{A'N} - (r_{AN} + r_{A'N})\, r_{AM}\, r_{A'M}}{r_{AM}\, r_{A'M}\, r_{AN}\, r_{A'N}} - \frac{(r_{BN} + r_{B'N})\, r_{BM}\, r_{B'M} - (r_{BM} + r_{B'M})\, r_{BN}\, r_{B'N}}{r_{BM}\, r_{B'M}\, r_{BN}\, r_{B'N}}\right]^{-1} \tag{3.43}$$

Here $r_{\xi\eta}$ represents the distance from the current electrodes ξ (=A, B or their images A', B') to the potential electrode η (=M or N). Crosshole configurations with these four electrode arrays are discussed in Section 8.1. Substituting equation (2.30) for (3.39), we have

$$pole-pole: \quad \rho_a = K[G^{3D}(r_A, r_M)], \tag{3.44}$$

$$pole-bipole: \quad \rho_a = K[G^{3D}(r_A, r_M) - G^{3D}(r_A, r_N)], \tag{3.45}$$

$$bipole-pole: \quad \rho_a = K[G^{3D}(r_A, r_M) - G^{3D}(r_B, r_M)], \tag{3.46}$$

$$bipole-bipole:\quad \rho_a = K\{[G^{3D}(r_A,r_M)-G^{3D}(r_A,r_N)] - [G^{3D}(r_B,r_M)-G^{3D}(r_B,r_N)]\}, \tag{3.47}$$

where
$$G^{3D}(r_\xi,r_\eta)=\frac{1}{2}F_c^{-1}[\overline{G}^{2.5D}(r_\xi,r_\eta)]. \tag{3.48}$$

In view of the above equations and considering the fact that the Green's function $\overline{G}^{2.5D}(r_\xi,r_\eta)$ vanishes when r_ξ or r_η is infinite (remote electrode), a general form can be obtained for all of these arrays:

$$\rho_a = K[\delta G^{3D}_{MN}(r_A)-\delta G^{3D}_{MN}(r_B)], \tag{3.49}$$

where
$$\delta G^{3D}_{\xi\eta}(r)=\frac{1}{2}F_c^{-1}[\overline{G}^{2.5D}(r_\xi,r)-\overline{G}^{2.5D}(r_\eta,r)]. \tag{3.50}$$

The expression (3.49) is available for any surface or crosshole surveying configuration and demonstrates that the apparent resistivities for different arrays can be directly calculated from the Green's functions in theory. Meanwhile, it shows that the forward modeling for apparent resistivity only involves the computation of the Green's functions for the current electrodes r_A and r_B in an electrode array.

Fig.3-7 gives a flow-chart for 2.5-D resistivity modeling, which consists of two parts. The first part (loop over wavenumber k_{y_i}) is the major part of the algorithm because it calculates the 2.5-D Green's functions: $\overline{G}^{2.5D}(r_{c_j},r)$ ($j=1,2,...,N_c$) for all the current electrodes. The second

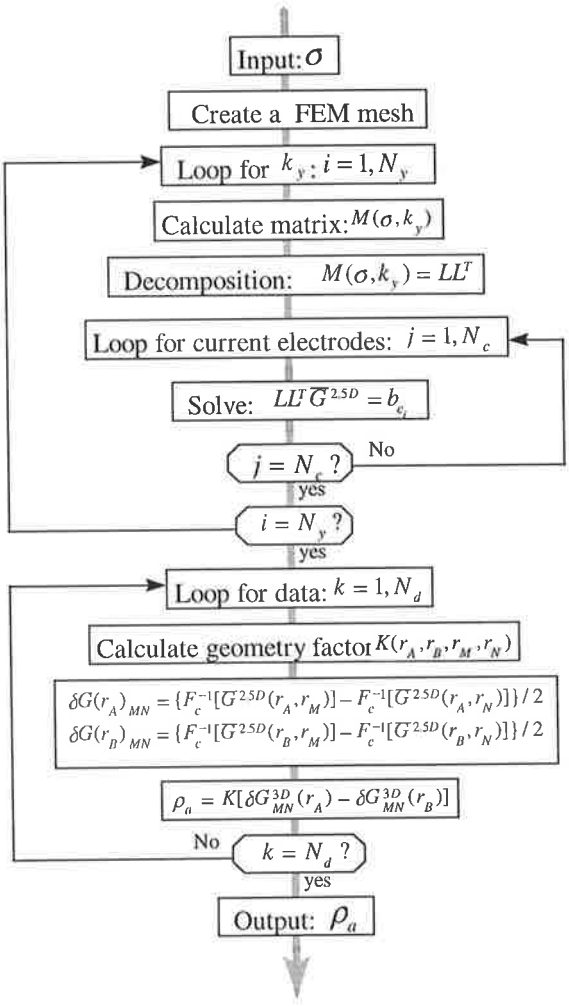

Fig.3-7 Flow-chart for 2.5-D resistivity modeling.

part (loop over all the data) is to calculate the apparent resistivity and it does not cost much computer time after obtaining the Green's functions. So, the amount of computer time consumed really depends on the number of wavenumber samples N_y and the number of current electrodes N_c.

3.5 Examples of Modeling

Numerical modeling allows us to predict or investigate the electric potential response of complicated earth models and is very useful in understanding and interpreting field observations with different array configurations and various practical geological models. In addition, when combined with an inversion algorithm, it can be employed for resistivity imaging with crosshole data or surface profiling data (see Chapter 8).

In this section, some numerical simulations are shown as examples of the application of numerical modeling. First, two analytic solutions (homogeneous half-space and two-layer stratified model) are used to check the program code and to indicate the accuracy of the numerical algorithm. Then, we present modeling examples that simulate some practical situations: resistivity profiling, crosshole potential surveying in mineral exploration, and finally monitoring of underground water injection in hydrological engineering.

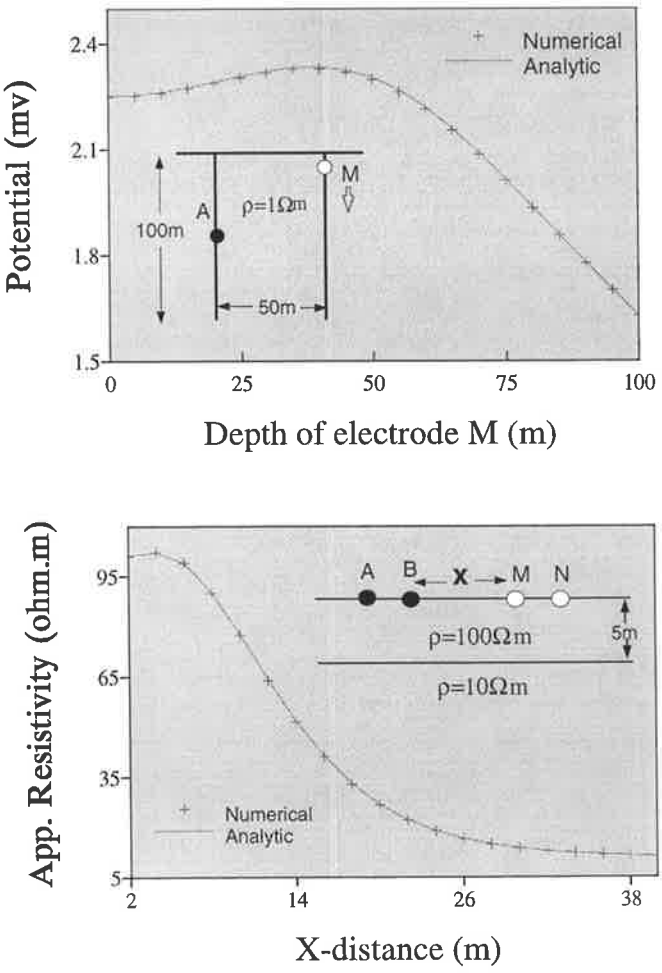

Fig.3-8 Analytic and numerical calculations for crosshole pole-pole surveying in a homogeneous half-space (upper) and bipole-bipole resistivity sounding in a two-layered model (lower). The relative error is less than 1%.

(1) Accuracy of The Method

From many different tests, *we found that with a fixed mesh size, the*

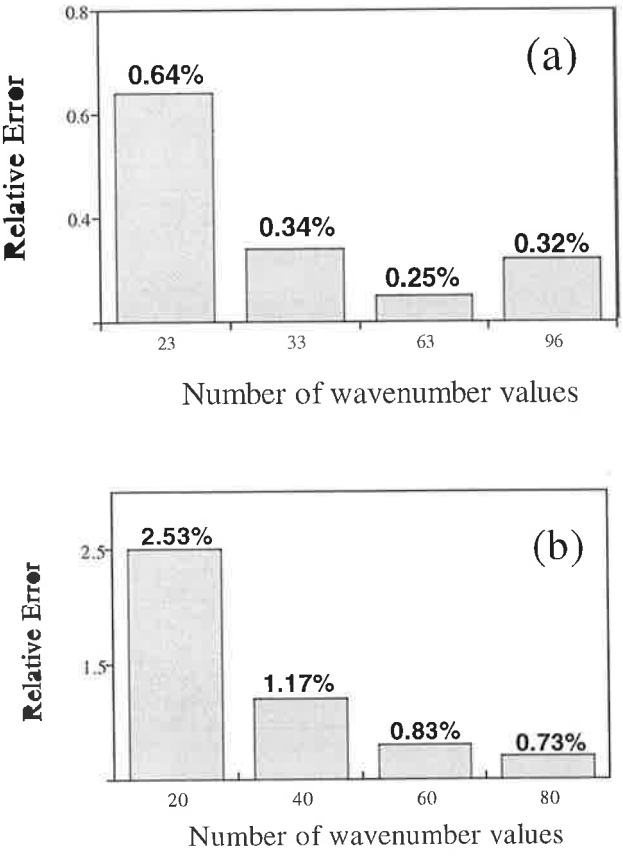

Fig.3-9 Relative errors of the numerical method with different numbers of k_y samples: (a) the half-space model and (b) the two-layered model in Fig.3-8. The k_y samples are distributed in equal logarithmic intervals.

numerical accuracy of the method mainly depends on the choices of the range of wavenumber and the sampling distribution in the range. The important thing to do before modeling is to determine the right sampling range for all the distances involved in the calculation. Unfortunately, except for trial computations or estimates from some approximations, we cannot in advance know the exact range of wavenumber values for a complicated model. Fig.3-4 indicates that an inappropriate k_y range for a small distance r may yield a large error in modeling, because some significant values of the potential may be missed out. But the similar features of the transformed potentials in Fig.3-4 may be applied to estimate the k_y range. For example, to determine the optimum range we may examine the k_y ranges of the analytic solution: $\overline{U} = [K_0(rk_y) + K_0(r'k_y)]/4\pi$ (solution for a homogeneous half-space model) with the practical surveying configuration (a range of distances r), then pick the maximum one. After obtaining the k_y range, we distribute the samples with an equal logarithmic interval in the range.

It is not difficult to obtain the analytic solutions for a homogeneous half-space and a two-layered stratified model (see equations (3.33) and (3.34)). So, one can use these solutions to check the program code and detect the numerical accuracy of the modeling. Fig.3-8 gives the analytic and numerical calculations of crosshole pole-pole measurement and bipole-bipole resistivity sounding for the two models, and shows that the method can

produce satisfactory results. In the first case, the distance range in crosshole surveying is about r=50 m to 70 m, so we deduced the range of the wavenumber to be about $k_y \in [10^{-6}, 0.26]$ for these distances. In a similar way, we have the range $k_y \in [10^{-4}, 9]$ in the second case due to the distances r=2 m to 40 m for resistivity sounding. By repeating the numerical experiments with different numbers of the k_y samples in their k_y ranges, we obtained the relative error variations for the two models (see Fig.3-9). For example, in case 1 the error is 0.34% if 33 wavenumber samples are used. The accuracy of the method is generally improved by increasing the k_y samples, but the improvement is gradual and not necessarily monotonic with an increasing number of k_y samples. This means that even using a large number of k_y samples, the numerical calculation can still have a certain error, which depends on the complexity of the model, the range of k_y and the sample distribution. On the other hand, a large number of k_y samples will consume a great deal of computer resources (see Fig.3-7). So, the number of k_y samples to use depends upon the practical situation and the accuracy requirement of the modeling. In fact, taking an appropriate number (any larger number does not substantially improve the accuracy) of k_y samples in the right range, one can get a satisfactory result which involves a reasonable amount of computer time for complicated modeling.

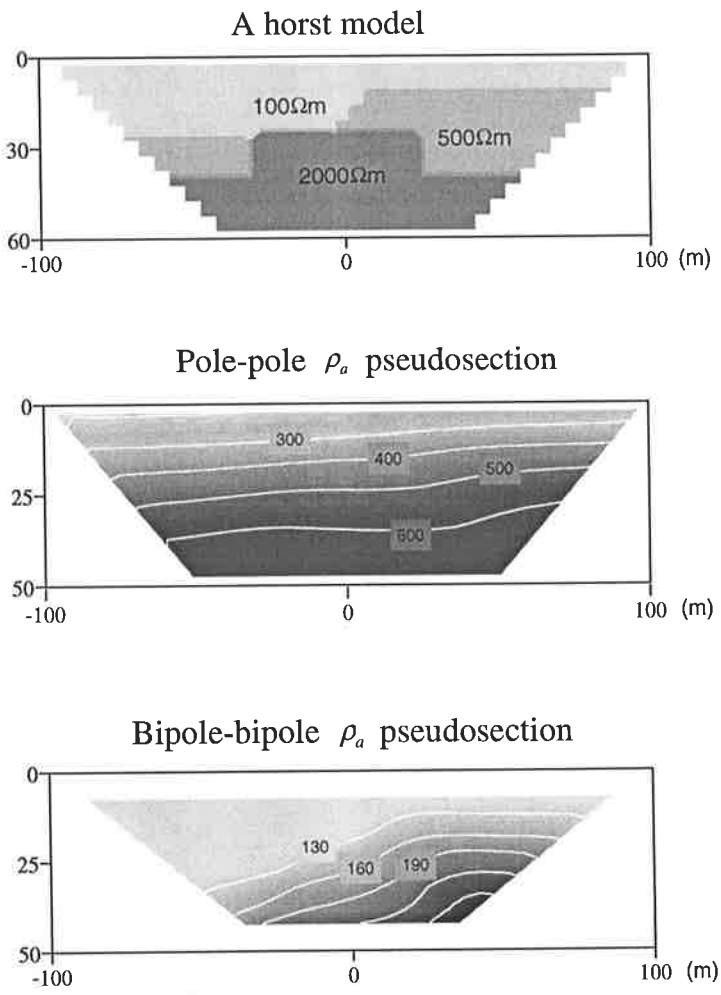

Fig.3-10 Simulation of the apparent resistivity pseudosection for a complicated horst model.

(2) Resistivity Profiling

DC resistivity profiling, which employs various electrode configurations such as pole-pole or dipole-dipole array, and measures the variation in apparent resistivity along the surface, is one of the popular electric exploration techniques because it can directly indicate the vertical and horizontal resistivity variation of the subsurface from the apparent resistivity pseudosection. But, for a complicated earth model it is very difficult to recognise the detail of the model from the pseudosection, because the pseudosection only provides a rough and averaged variation of the actual resistivity. The numerical modeling enables us to simulate any complicated situation in the field measurement and study the features of the pseudosection for a practical model. So, it is helpful to understand and interpret the observed pseudosection. Fig.3-10 gives an example of simulation of the apparent resistivity pseudosection for a complicated horst model with the pole-pole and bipole-bipole arrays. This modeling shows that even with the same model the apparent resistivity pseudosections may be different due to the different electrode arrays and the pseudosections fail to reflect the detail of the deep structure. From this figure, it seems that the bipole-bipole array emphasizes features of the near-surface resistivity variation, while the pole-pole array gives more information on the structure at depth.

(3) Crosshole Applied Potential Surveying

Crosshole applied potential surveying (or mise-á-la-mass surveying) is a technique in mining and mineral exploration which attempts to determine whether conductive units, like mineralisation, encountered in different boreholes are connected. In principle, an electrode is placed in the conductive zone in one borehole, and electric current transmitted into this electrode. A second electrode is placed in another borehole, and voltage measurements taken at various depths. If a higher voltage than others occurs, centred over a conductive zone in the second borehole, then the two zones are assumed to be connected. In practical applications, numerical modeling may be required to supply a more highly constrained geological model for interpreting the field data. Figures 3-11 and 3-12 illustrate this technique in a practical case of a nickel mine in Western Australia. In this example, underground (in-mine) drilling disclosed three ore intersections in one borehole (B, C and D in Fig.3-11) and one intersection in the other (A). In order to investigate the connectivity of the mineralized sections between the boreholes, crosshole applied potential measurements were conducted by placing one of the current electrodes at A in the left

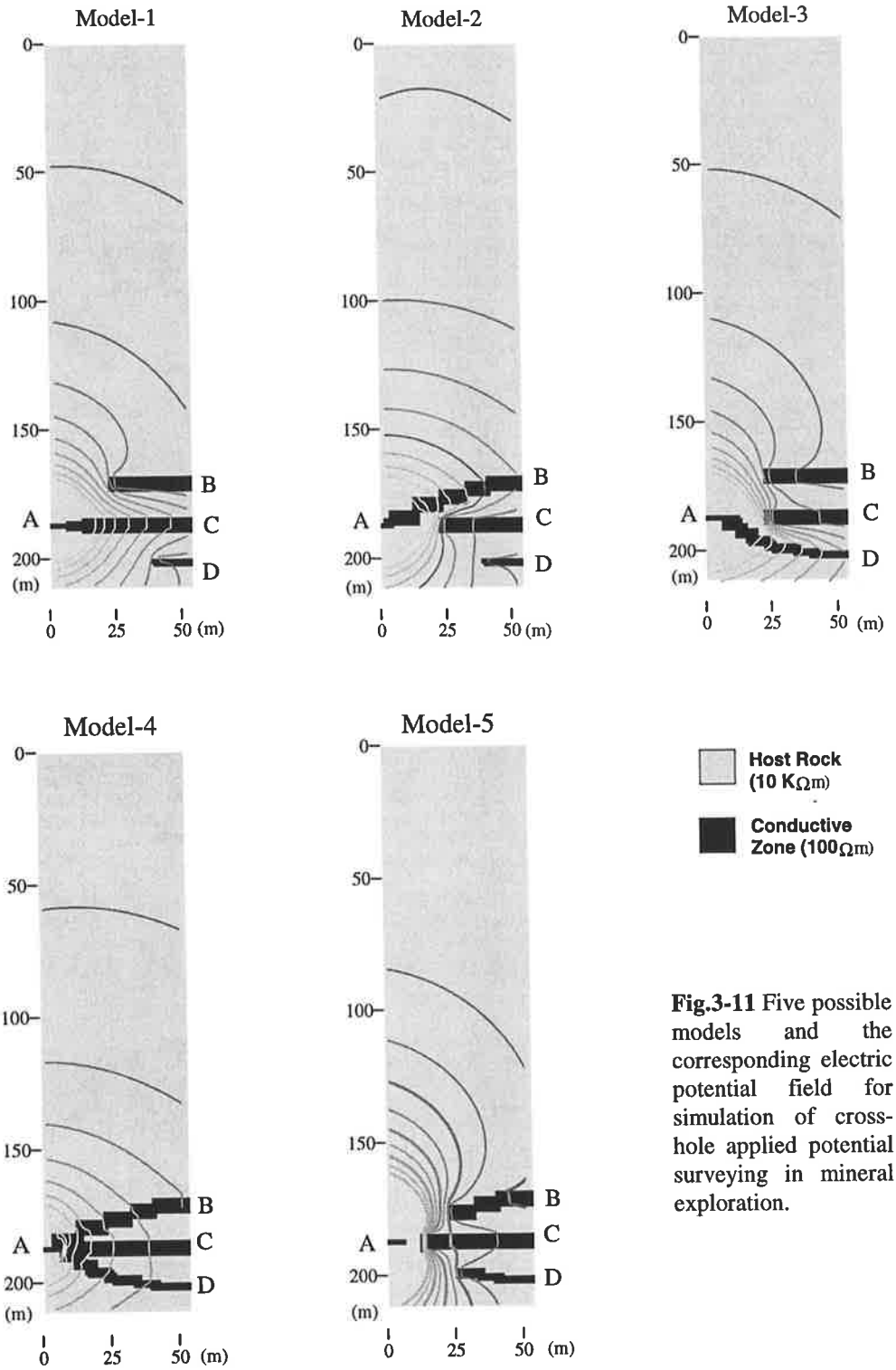

Fig.3-11 Five possible models and the corresponding electric potential field for simulation of cross-hole applied potential surveying in mineral exploration.

borehole and reading the voltage values from the top to bottom in the right borehole. Fig.3-12 gives the observed data (supplied by WMC–the company operating the mine) and the modeling results using five possible models in Fig.3-11. The models indicate various connections (A to C, A to B, A to D, A to all of B, C, D and A does not connect to

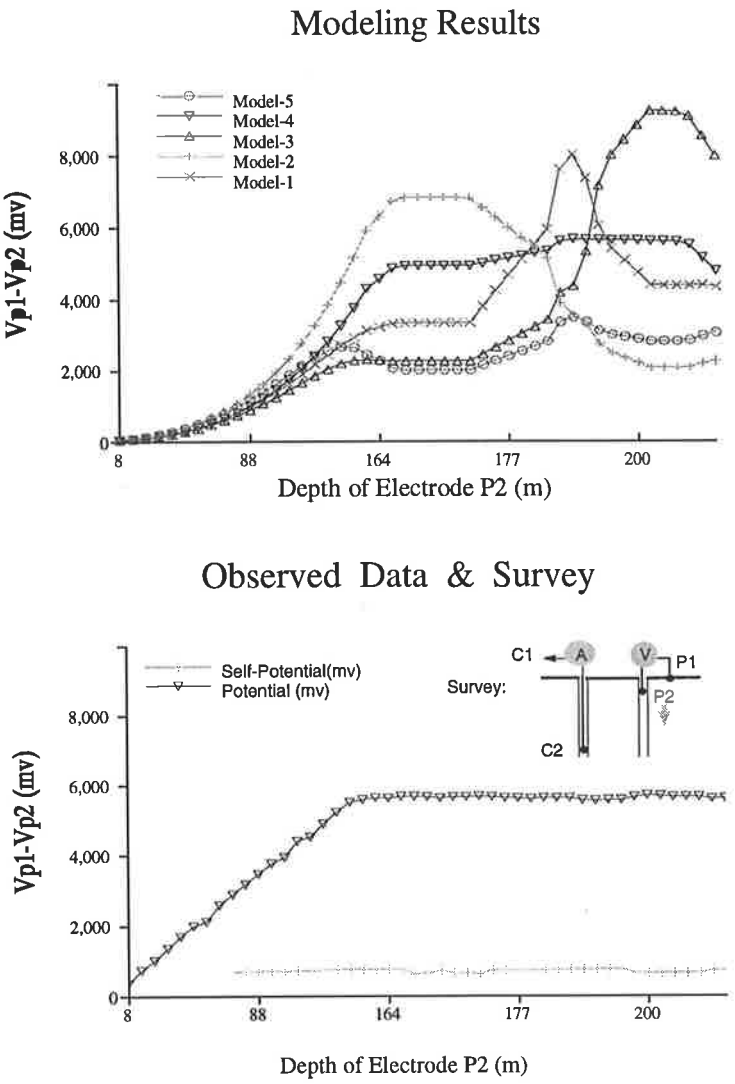

Fig.3-12 Synthetic potential responses (upper diagram) to the five models in Fig.3-11 and observed potential data and surveying configuration (lower diagram).

all of B, C, D). Comparing the field data with the modeling results (Fig.3-12), it is easy to recognize that the synthetic response of Model-4 is very similar to the field data. So, Model-4 is an acceptable model for the field data, which reveals that the three ore intersections B, C and D are connected to intersection A. This example demonstrates that numerical modeling is very helpful to solve a practical mining problem.

(4) Monitoring of Underground Water Injection from Artificial Aquifer Storage

Numerical modeling may be applied to groundwater engineering. For example, to manage natural water resources, aquifer storage and recovery techniques are being attempted in South Australia (Mines and Energy Resource, SA, 1997). This involves the temporary storage of stormwater underground in a suitable aquifer for which the harvesting of surplus water from a variety of sources is injected underground through a borehole. Crosshole resistivity measurements during the fresh water injection into the more saline aquifer may be useful to detect the water dispersion and any preferential flow paths. The numerical modeling may be employed to predict or investigate the responses of the water distribution in the different water injection stages, including before, during and even after (recovery) operations. Fig.3-13 shows a simulation of the situation in which

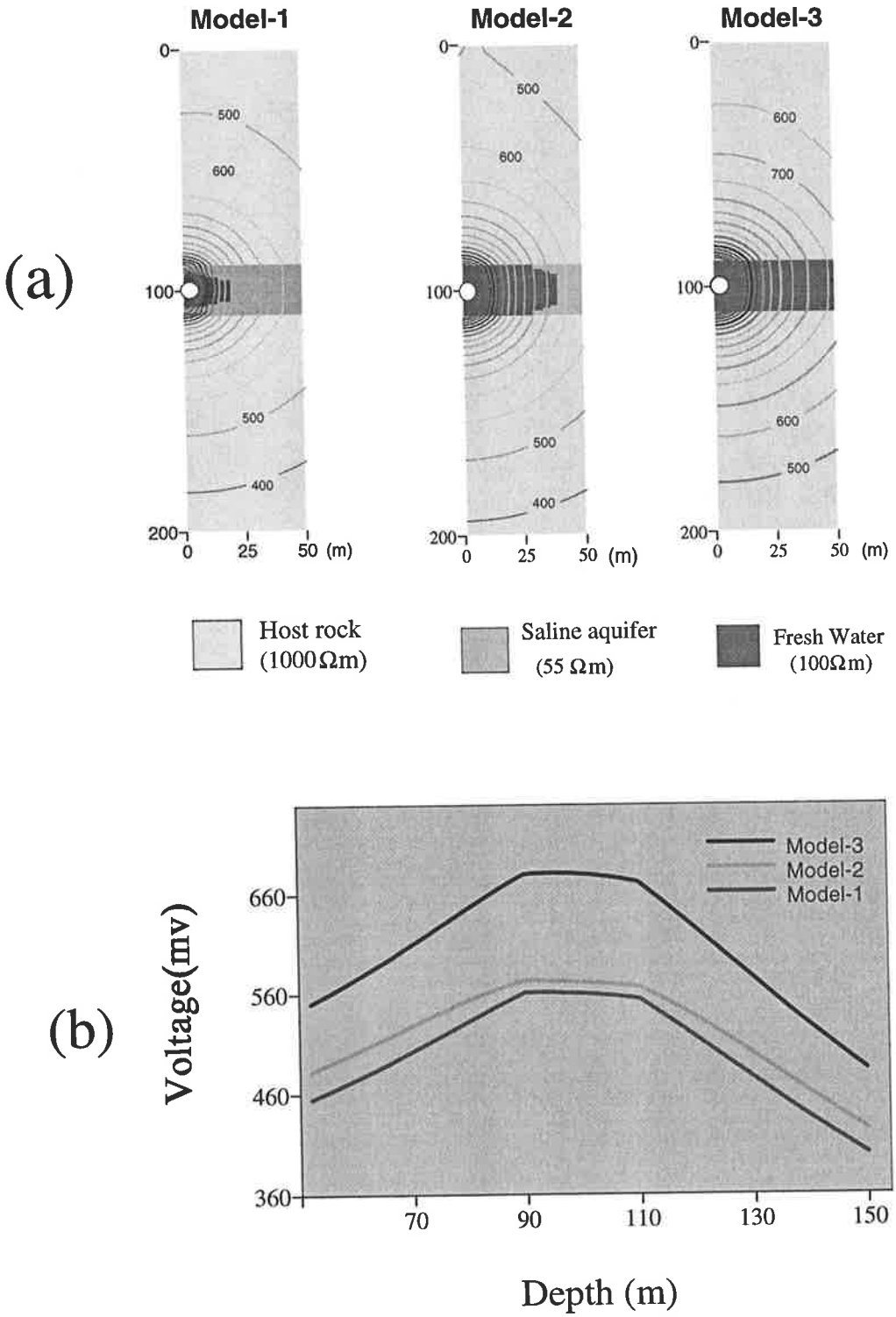

Fig.3-13 A simulation of crosshole electric potential measurements for delineation of the injected water distribution. (a) Model-1, Model-2 and Model-3 represent the three stages of the fresh water injection and (b) the potential responses of the crosshole measurements with a pole-pole array.

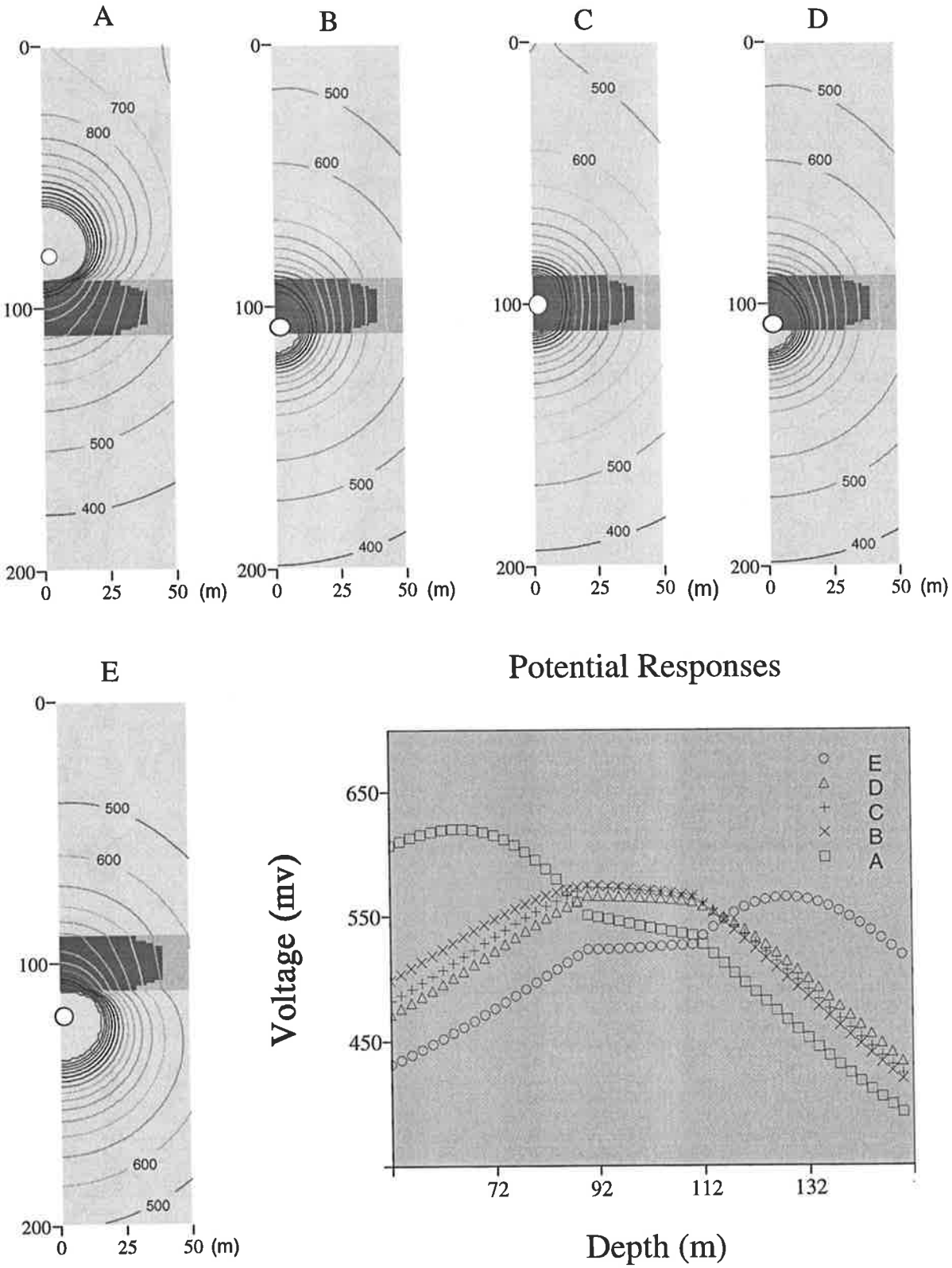

Fig.3-14 Different responses of crosshole pole-pole surveying for five locations of the current electrode for Model-2 in Fig.3-13.

crosshole potential measurements, corresponding to a current electrode at the water injecting depth, are supposed to be carried out at three stages of water injection (see Model-1, Model-2 and Model-3 in Fig.3-13). The more resistive fresh water plume advances between the boreholes. The numerical modeling can illustrate the voltage responses of the crosshole measurements to the water distribution at the different water-injecting stages. From the synthetic results, it is clear that with the movement of the injected water along the porous layer (aquifer), the observed potential curve shifts up but preserves the same shape (see Fig.3-13). This increase of the electric potential with increasing water injection may be used to delineate the water distribution and estimate the water spreading speed in the porous layer. Fig.3-14 gives the different responses of pole-pole surveying to five locations of the current electrode in above model-2. This figure shows that when the current electrode is located above or below the aquifer layer, the resulting potential curves are quite different, but all of the potential responses are very similar in shape (they differ in amplitude) if the current electrode is placed in the aquifer. So, these modeling results are very helpful to interpret such practical monitoring measurements.

Chapter 4
2.5-D Acoustic Wave Modeling in the Frequency-Domain

As shown in Chapter 2, the 2.5-D acoustic wave equation in the wavenumber-frequency domain is a specified form of the 2.5-D Helmholtz equation and is similar to the DC resistivity governing equation. This prompts us to resort to a similar method for 2.5-D acoustic modeling as is used in the DC resistivity problem. But the two forms of the 2.5-D Helmhohz equation define two entirely different physical fields. Therefore, we must be very specific in the numerical implementation. In this chapter, we first develop a general form of the absorbing boundary condition for the 2.5-D acoustic wave modeling. Next, the two numerical algorithms: composite boundary-valued solution and a damping method (Zhou and Greenhalgh, 1998a, 1998b), are presented based on the FEM formulation. Finally, some numerical results of wavefield computations both in the frequency-domain and the time-spatial domain are demonstrated. Comparisons between the numerical solutions and the exact analytic or semi-analytic solutions are also given.

4.1 2.5-D Absorbing Boundary Condition

As is well known, to solve equation (2.25) or (2.29), a kind of absorbing boundary condition (ABC) must be introduced because only a finite-sized model is used in numerical modeling. Otherwise, some reflections from the edges of the artificial grid boundary obscures interesting events on the seismogram (Reynolds, 1978). Several ABCs were suggested for minimization of the edge reflections (Clayton and Engquist, 1977; Bayliss et al., 1982; Higdon, 1991). But all of them are available only for 2-D (line source) problems. Recently, Song and Williamson (1995a,b) applied Clayton and Engquist's 2-D ABC to 2.5-D acoustic wave modeling. Actually, it will be seen that a 2.5-D ABC can be obtained by just following Clayton and Engquist's 2-D method (1977) to handle the 2.5-D problem and it may be generalized by adapting Higdon's formula (1991).

(1) Clayton-Engquist ABC

For simplicity, we take a rectangular boundary (see Fig.4-1). On the boundary $\partial\Omega = \sum_{i=1}^{4} \Gamma_i$, the Fourier transformed form of the 2.5-D acoustic wave equation becomes (see Equation (2.25)):

$$[\nabla^2 + (k^2 - k_y^2)]\overline{\overline{P}} = 0, \tag{4.1}$$

which has the dispersion relation

$$k_z = \pm k_a [1 - (\frac{k_x^2}{k_a^2})]^{1/2}, \tag{4.2}$$

where $k_a = \sqrt{k^2 - k_y^2}$ is assumed to be a positive value ($k_a > 0$), which can be considered as the apparent wavenumber in the (x,z)-plane. Clearly, when $k_x^2 / k_a^2 > 1$, k_z becomes imaginary, which represents an evanescent wave, whereas $|k_x^2 / k_a^2| < 1$ implies a propagating wavefield having the wavenumber k_a. Expanding the square-root of equation (4.2) and neglecting the high order terms (paraxial approximation), the approximation is

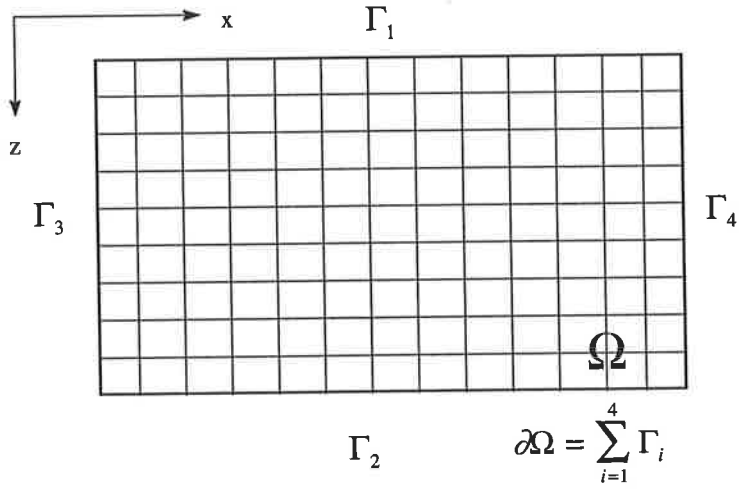

Fig.4-1 Sketch of the rectangular boundary of the FEM mesh.

$$k_z = \pm k_a [1 - \frac{k_x^2}{2k_a^2}]. \tag{4.3}$$

Note that the $\pm$ signs in equation (4.2) or (4.3) stand for waves propagating in the positive and negative directions of the z-coordinate. For the upgoing wave, the positive sign is considered in (4.3) and converting back to the frequency-wavenumber domain via the inverse Fourier transform, it becomes

$$\Gamma_1: \quad \partial_z \overline{\overline{P}} = i(k_a + \frac{1}{2k_a}\partial_{xx})\overline{\overline{P}} . \tag{4.4}$$

For the downgoing wave, it can be written as

$$\Gamma_2: \quad \partial_z \overline{\overline{P}} = -i(k_a + \frac{1}{2k_a}\partial_{xx})\overline{\overline{P}} . \tag{4.5}$$

Equations (4.4) and (4.5) are available for the top and bottom boundaries in the frequency-wavenumber domain. In the same manner, the left and right boundary conditions can be written out in terms of equations (4.4) and (4.5):

$$\Gamma_3: \quad \partial_x \overline{\overline{P}} = i(k_a + \frac{1}{2k_a}\partial_{zz})\overline{\overline{P}} , \tag{4.6}$$

$$\Gamma_4: \quad \partial_x \overline{\overline{P}} = -i(k_a + \frac{1}{2k_a}\partial_{zz})\overline{\overline{P}} . \tag{4.7}$$

Obviously, as $k_y \to 0$, equations (4.4)-(4.7) become Clayton and Engquist's 2-D expressions. So, as long as $k_a > 0$ or $k_y < k$, the boundary conditions (4.4)-(4.7) are the extension of Clayton and Engquist's 2-D ABC to the 2.5-D case.

(2) General Form of The 2.5-D ABC

Higdon (1991) suggested a general form of the absorbing boundary condition for 2-D modeling. For instance, in the positive x-direction, the ABC in the frequency-domain is presented as the product of the various terms:

$$\prod_{i=1}^{m} (ik\cos\alpha_i + \partial_x)\overline{P} = 0 , \tag{4.8}$$

which yields a reflection coefficient for an arbitrary angle of incidence θ (unknown) as:

$$|R| = \prod_{i=1}^{m} \left| \frac{\cos\theta - \cos\alpha_i}{\cos\theta + \cos\alpha_i} \right| . \tag{4.9}$$

Here $k>0$ is the wavenumber and α_i is the predicted angle, which can be chosen to take advantage of á priori information, if available, about directions from which waves are expected to approach the boundary. Equation (4.9) states that if α_i approaches θ, the reflection coefficient goes to zero, which means that the reflection from the artificial boundary will be negligible. The ABC is available for 2-D modeling in the wavenumber-frequency domain, but it can be modified for 2.5-D modeling. In fact, by

defining the apparent wavenumber $k_a = \pm\sqrt{k^2 - k_y^2}$ in the (x,z)-plane it was shown in Chapter 2 that the 2.5-D acoustic wave equation (2.25) has the same appearance as the 2-D Helmholtz equation (2.1). This suggests that we can replace k in equation (4.8) with k_a for the 2.5-D case. For instance, the boundary condition in the positive x-direction should be

$$\prod_{i=1}^{m}(ik_a\cos\alpha_i + \partial_x)\overline{\overline{P}} = 0, \tag{4.10}$$

which still has the reflection coefficient given by equation (4.9) in the (x,z)-plane so long as $k_a > 0$ or $k_y < k$. So equation (4.10) may be a general form of the ABC in the frequency-wavenumber domain for the 2.5-D case. In general, the more factors which are included in the expansion, the better the reduction in the artificial reflections (see equation (4.9)). However, this will involve the computations of the higher derivatives and possible instability. Considering the computational efficiency, we chose the two-factor form of equation (4.10). Taking the first two factors (m=2), an explicit expression of the ABC for the positive x-direction is obtained as:

$$\Gamma_4: \quad \partial_x\overline{\overline{P}} = -\{\nu' - \beta\partial_{xx}\}\overline{\overline{P}}, \tag{4.11}$$

where

$$\nu' = i\frac{k_a\cos\alpha_1\cos\alpha_2}{\cos\alpha_1 + \cos\alpha_2}, \qquad \beta = \frac{i}{k_a(\cos\alpha_1 + \cos\alpha_2)}. \tag{4.12}$$

Replacing the sign '+' in equation (4.10) with '–' results in the ABC in the negative x-direction:

$$\Gamma_3: \quad \partial_x\overline{\overline{P}} = \{\nu' - \beta\partial_{xx}\}\overline{\overline{P}}. \tag{4.13}$$

In the same manner, The ABCs in the positive and negative z-direction can be obtained:

$$\Gamma_2: \quad \partial_z\overline{\overline{P}} = -\{\nu' - \beta\partial_{zz}\}\overline{\overline{P}}, \tag{4.14}$$

$$\Gamma_1: \quad \partial_z\overline{\overline{P}} = \{\nu' - \beta\partial_{zz}\}\overline{\overline{P}}. \tag{4.15}$$

From these results, one can find the difference in the form between the 2.5-D Clayton-Engquist ABCs (equations (4.4)-(4.7)) and the above equations (4.11)-(4.15), which are

valid for wave propagation with an incident angle lying between α_1 and α_2 towards the boundary. The ABCs (4.11)-(4.15) can be rewritten in the general form:

$$\frac{\partial \bar{\bar{P}}}{\partial n} = -B\bar{\bar{P}} = -n \cdot [(\nu' - \beta\frac{\partial^2}{\partial^2 x})\mathbf{e}_x + (\nu' - \beta\frac{\partial^2}{\partial^2 z})\mathbf{e}_z]\bar{\bar{P}}, \quad r \in \partial\Omega. \tag{4.16}$$

Where n is the normal unit vector of the boundary $\partial\Omega$, $\mathbf{e}_x$ and $\mathbf{e}_x$ are the unit vectors indicating the x- and z-axes. Note the fact that wave equation should be satisfied at the boundary, on substituting the source-free 2.5-D wave equation (2.25) for the second derivative into equation (4.16), another form of the ABC is obtained:

$$\frac{\partial \bar{\bar{P}}}{\partial n} = -B\bar{\bar{P}} = -n \cdot [(\nu + \beta\frac{\partial^2}{\partial^2 z})\mathbf{e}_x + (\nu + \beta\frac{\partial^2}{\partial^2 x})\mathbf{e}_z]\bar{\bar{P}}, \quad r \in \partial\Omega, \tag{4.17}$$

where

$$\begin{aligned} \nu &= \nu' + \frac{i}{\cos\alpha_1 + \cos\alpha_2} \\ &= i\frac{k_a(\cos\alpha_1\cos\alpha_2 + 1)}{\cos\alpha_1 + \cos\alpha_2} \end{aligned}. \tag{4.18}$$

Theoretically, Equations (4.16) and (4.17) are two equivalent boundary conditions, both of which may be used for acoustic wavefield numerical modeling in the frequency-wavenumber domain. But it will be shown that the operator B in equation (4.16) is not a self-adjoint operator for the boundary integral but the operator B in equation (4.17) is self-adjoint when incorporated with the FEM. The latter is inherently suitable for the FEM (see 4.3 section). Considering that it is to be used with the FEM, we want a self-adjoint operator B to make the FEM assembled matrix of reasonable dimensional size, and to be symmetric and of appropriate bandwidth properties. Consequently, we prefer using the form (4.17) as the 2.5-D ABC in our case.

According to the general form of the ABC (4.17), the explicit forms for the four sides of the boundary become:

$$\Gamma_1: \quad \partial_z\bar{\bar{P}} = \{\nu + \beta\partial_{xx}\}\bar{\bar{P}}, \tag{4.19}$$

$$\Gamma_2: \quad \partial_z\bar{\bar{P}} = -\{\nu + \beta\partial_{xx}\}\bar{\bar{P}}, \tag{4.20}$$

$$\Gamma_3: \quad \partial_x\bar{\bar{P}} = \{\nu + \beta\partial_{zz}\}\bar{\bar{P}}, \tag{4.21}$$

$$\Gamma_4: \quad \partial_x\bar{\bar{P}} = -\{\nu + \beta\partial_{zz}\}\bar{\bar{P}}. \tag{4.22}$$

By setting $\alpha_1 = \alpha_2 = 0$, equations (4.19)-(4.22) become the 2.5-D Clayton-Engquist ABCs (equations (4.4)-(4.7)). This shows that the 2.5-D Clayton-Engquist ABC is just a special case of equation (4.17).

4.2 Boundary Condition for The Evanescent Field

In the previous sections, we have developed a general form of the 2.5-D ABC, which requires a positive value of the apparent wavenumber: $k_a > 0$ or $k_y < k$. In Chapter 2, it has been pointed out that the 2.5-D acoustic wave equation (equation (2.25)) includes the two physical phenomena: wave propagation ($k_y < k$) and the evanescent field ($k_y > k$). The ABC given by equation (4.16) or (4.17) is available only for the case $k_y < k$. On the other hand, from the definition of the Fourier-cosine transform (equation (2.23)), k_y should lie in the range (0,∞), which means that both physical phenomena will arise in an inhomogeneous medium. So, some complement to the boundary condition has to be made for the case: $k_y > k$. Consider $\overline{\overline{P}}$ to be an evanescent field (non-vibration), which normally has a significant value only in the small area around the source. One can predict that if the boundary is not close to the source, $\overline{\overline{P}}$ should go to zero when $k_y > k$. Actually, whenever $k_y > k$, the wave equation (2.24) at the boundary can be rewritten as

$$(\nabla + k_a')(\nabla - k_a')\overline{\overline{P}} = 0, \tag{4.23}$$

where $k_a' = \sqrt{k_y^2 - k^2}$. For simplicity, taking just the 1-D case to examine the factors of equation (4.23), a general solution is

$$\overline{\overline{P}} = C_1 e^{-k_a' x} + C_2 e^{k_a' x}. \tag{4.24}$$

The two terms describe the evanescent fields in the positive and negative x-directions. By substitution of equation (4.24) for the first factor of equation (4.23), and setting the factor to be zero, we get $C_2 = 0$, which means that only the one-way (positive x-direction) evanescent field exists at this point. This is just the boundary condition we expect at the right-side of the source. In the same way, the second factor of equation (4.23) implies another side boundary condition for the evanescent field. This leads to a

natural complement to the boundary condition for $k_y > k$, which is a mixed-boundary condition:

$$\frac{\partial \overline{\overline{P}}}{\partial n} + k_a' \overline{\overline{P}} = 0, \quad k_a' = \sqrt{k_y^2 - k^2}; \qquad r \in \partial\Omega. \tag{4.25}$$

Obviously, the operator $B=-k_a'$ in equation (4.25) is self-adjoint. *It must be mentioned that the 2.5-D ABC (4.16) or (4.17) has a singularity at $k_a=0$ or $k_y = k$ (critical value). When it occurs, special treatment is required to avoid it.* A simple way is to adjust k_y by a small amount so as to make $k_y < k$ or $k_y > k$, then the boundary conditions (4.17) or (4.25) can be employed for this situation.

4.3 Composite Boundary-Valued Solution

In the frequency-domain, the general response to any source can be obtained by the multiplication of the Green's function with the source spectrum (see equation (2.31). So, computation of the 2.5-D acoustic wavefield in the frequency-domain is completely equivalent to computing the 2.5-D Green's function for an arbitrary medium. Using the result of the previous sections, the boundary-valued problem for the 2.5-D Green's function for acoustic waves is given by:

$$\begin{cases} L\overline{\overline{G}}^{2.5D} = -\delta(r - r_s) & r, r_s \in \Omega, \\ \dfrac{\partial \overline{\overline{G}}^{2.5D}}{\partial n} + B\overline{\overline{G}}^{2.5D} = 0 & r \in \partial\Omega, \end{cases} \tag{4.26}$$

where $L = \nabla^2 + (k^2 - k_y^2)$ and $r=(x,z)$. Also considering a rectangular boundary (see Fig.4-1) and using the general form of the ABC (4.17) and the mixed-boundary condition (4.25), the operator B can be explicitly expressed in the composite form:

$$\frac{\partial \overline{\overline{G}}^{2.5D}}{\partial n} = -B\overline{\overline{G}}^{2.5D} = \begin{cases} \left\{\nu + \beta \dfrac{\partial^2}{\partial^2 x}\right\} \overline{\overline{G}}^{2.5D} & r \in \Gamma_1 \\ -\left\{\nu + \beta \dfrac{\partial^2}{\partial^2 x}\right\} \overline{\overline{G}}^{2.5D} & r \in \Gamma_2 \\ \left\{\nu + \beta \dfrac{\partial^2}{\partial^2 z}\right\} \overline{\overline{G}}^{2.5D} & r \in \Gamma_3 \\ -\left\{\nu + \beta \dfrac{\partial^2}{\partial^2 z}\right\} \overline{\overline{G}}^{2.5D} & r \in \Gamma_4 \end{cases} \quad k_y < k, \\ -k_a' \overline{\overline{G}}^{2.5D}, \qquad r \in \sum_{i=1}^{4} \Gamma_4 \qquad k_y > k, \end{cases} \tag{4.27}$$

So, to compute the Green's function reduces to solving the composite boundary-valued problem.

(1) The FEM Formulation

To solve the composite boundary-valued problem, Galerkin's method may be applied to equation (4.26). According to the residual weighting equation (2.50) and Green's integral theorem, we have the integral equations:

$$\int_{\Omega}[\nabla N_j^e \cdot \nabla \overline{\overline{G}}^{2.5D} + (k_y^2 - k^2) N_j^e \overline{\overline{G}}^{2.5D}]d\Omega + \int_{\partial\Omega} N_j^e B \overline{\overline{G}}^{2.5D} d\Gamma = N_j^e \delta_{is}, \quad (j = 1,2,\ldots,N_r). \tag{4.28}$$

Here N_j^e is a shape function defined in the finite element, N_r is the total number of shape functions. The second term should be a curved path integral along the boundary that involves the boundary condition. Substituting the boundary condition for equation (4.28) and discretising the computation region into finite elements, e.g. $\Omega = \sum_e \Omega_e$, in which the Green's function may be expressed by the combination of the shape functions:

$$\overline{\overline{G}}^{2.5D}(r) = \sum_{i=1}^{N_r} N_i^e(r) \overline{\overline{G}}_i^{2.5D}, \quad r \in \Omega_e, \tag{4.29}$$

the resulting finite element equation becomes a set of linear algebraic equations:

$$(\mathbf{A} + \mathbf{B}) \overline{\overline{G}}^{2.5D} = \overline{b}_s. \tag{4.30}$$

Here $\overline{\overline{G}}^{2.5D}$ is a column vector whose components are nodal values of the Green's function in the finite element mesh, $\overline{b}_s$ is a source vector that has only one non-zero element (=1, see the right-side of equation (4.28)) and whose location coincides with the source. It will be shown that **A** and **B** are sparse, symmetric and banded matrices assembled with all element matrices A^e and B^e, both of which are calculated by the following expressions:

$$a_{ij}^e = \int_{\Omega^e}[\nabla N_i^e \cdot \nabla N_j^e + (k_y^2 - k^2) N_i^e N_j^e]d\Omega, \tag{4.31}$$

$$b_{ij}^e = \begin{cases} \int_{\Gamma_e}[\nu N_i^e N_j^e - \beta(\frac{\partial N_i^e}{\partial x}\frac{\partial N_j^e}{\partial x}, \frac{\partial N_i^e}{\partial z}\frac{\partial N_j^e}{\partial z})] \cdot (dx, dz), & k_y < k, \\ \int_{\Gamma_e} k_a' N_i^e N_j^e (dx, dz), & k_y > k. \end{cases} \tag{4.32}$$

It is obvious that the expression for a_{ij}^e is directly obtained from the first integral on the left-hand side of equation (4.28) after substitution of the approximation (4.29) for $\overline{\overline{G}}^{2.5D}$. The derivation for matrix element b_{ij}^e is given in Appendix B. From the expression for b_{ij}^e that corresponds to the boundary integral of equation (4.28), it follows that the boundary operator B is self-adjoint with the FEM formulation because of the symmetry of the matrix B^e. In addition, if the ABC (4.16) rather than the ABC (4.17) is used as the boundary condition, one has to use some higher order shape functions (twice differentiable) for the second derivative terms in the ABC (4.16) and B^e is no longer symmetric. Obviously, the ABC (4.17) is more suitable than the ABC (4.16) for incorporation into the FEM.

(2) Inner Element Matrix

To compute the matrix A^e, a rectangular element (Fig.4-2) and a bilinear shape function may be chosen (Zienkiewicz, 1971):

$$N_p^e = \frac{1}{4}[1+\xi(x)\xi(x_p)][1+\eta(z)\eta(z_p)]; \quad (p=i,j,m,n) \tag{4.33}$$

where $$\xi(x) = \frac{2}{\Delta x}(x - x_c^e), \eta(z) = \frac{2}{\Delta z}(z - z_c^e).$$

The subscript $p=i, j, m, n$ denotes the nodal numbers of the element in anti-clockwise order. Δx and Δz are the dimensional lengths of the element. The point (x_c^e, z_c^e) is the central coordinate of the element. In view of equations (4.31) and the geometry of the element, a_{ij}^e can be calculated by the following expression:

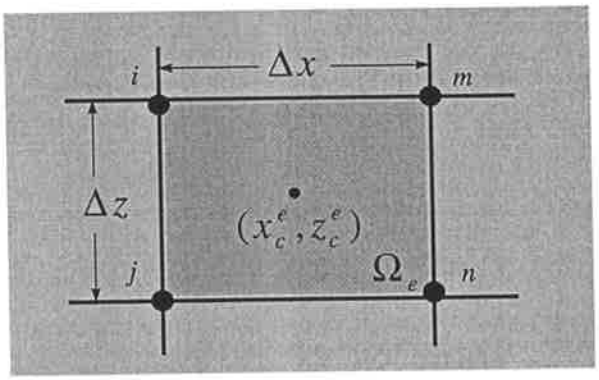

Fig.4-2 Diagram of an inner rectangular element in the FEM mesh shown in Fig. 4-1.

$$a_{pq}^{e}=(\frac{\Delta z}{\Delta x})\int_{-1}^{1}\int_{-1}^{1}\frac{\partial N_p^e}{\partial\xi}\frac{\partial N_q^e}{\partial\xi}d\xi d\eta+(\frac{\Delta x}{\Delta z})\int_{-1}^{1}\int_{-1}^{1}\frac{\partial N_p^e}{\partial\eta}\frac{\partial N_q^e}{\partial\eta}d\xi d\eta$$
$$-\frac{\Delta x\Delta z}{4}\int_{-1}^{1}\int_{-1}^{1}k_a^2N_p^eN_q^ed\xi d\eta,$$
$$(p,\ q=i,\ j,\ m,\ n). \tag{4.34}$$

By substitution of equation (4.33) for the double integrals in equation (4.34), we have the identities:

$$\int_{-1}^{1}\int_{-1}^{1}\frac{\partial N_p}{\partial\xi}\frac{\partial N_q}{\partial\xi}d\xi d\eta=\frac{\xi(x_p)\xi(x_q)}{4}[1+\frac{\eta(z_p)\eta(z_q)}{3}], \tag{4.35}$$

$$\int_{-1}^{1}\int_{-1}^{1}\frac{\partial N_p}{\partial\eta}\frac{\partial N_q}{\partial\eta}d\xi d\eta=\frac{\eta(z_p)\eta(z_q)}{4}[1+\frac{\xi(x_p)\xi(x_q)}{3}], \tag{4.36}$$

$$\int_{-1}^{1}\int_{-1}^{1}N_pN_qd\xi d\eta=\frac{1}{4}[1+\frac{\xi(x_p)\xi(x_q)}{3}][1+\frac{\eta(z_p)\eta(z_q)}{3}]. \tag{4.37}$$

Finally, the ten independent components for A^e are obtained from equations (4.34)-(4.37):

$$a_{ii}^{e}=\frac{1}{3}(\frac{\Delta z}{\Delta x}+\frac{\Delta x}{\Delta z})+\frac{1}{9}(k_y^2-k_e^2)\Delta z\Delta x,$$
$$a_{ij}^{e}=\frac{1}{3}(\frac{\Delta z}{2\Delta x}-\frac{\Delta x}{\Delta z})+\frac{1}{18}(k_y^2-k_e^2)\Delta z\Delta x,$$
$$a_{im}^{e}=\frac{1}{3}(\frac{\Delta x}{2\Delta z}-\frac{\Delta z}{\Delta x})+\frac{1}{18}(k_y^2-k_e^2)\Delta z\Delta x,$$
$$a_{in}^{e}=-\frac{1}{6}(\frac{\Delta z}{\Delta x}+\frac{\Delta x}{\Delta z})+\frac{1}{36}(k_y^2-k_e^2)\Delta z\Delta x,$$
$$a_{jj}^{e}=\frac{1}{3}(\frac{\Delta z}{\Delta x}+\frac{\Delta x}{\Delta z})+\frac{1}{9}(k_y^2-k_e^2)\Delta z\Delta x,$$
$$a_{jm}^{e}=-\frac{1}{6}(\frac{\Delta z}{\Delta x}+\frac{\Delta x}{\Delta z})+\frac{1}{36}(k_y^2-k_e^2)\Delta z\Delta x, \tag{4.38}$$
$$a_{jn}^{e}=\frac{1}{3}(\frac{\Delta x}{2\Delta z}-\frac{\Delta z}{\Delta x})+\frac{1}{18}(k_y^2-k_e^2)\Delta z\Delta x,$$
$$a_{mm}^{e}=\frac{1}{3}(\frac{\Delta z}{\Delta x}+\frac{\Delta x}{\Delta z})+\frac{1}{9}(k_y^2-k_e^2)\Delta z\Delta x,$$
$$a_{mn}^{e}=\frac{1}{3}(\frac{\Delta z}{2\Delta x}-\frac{\Delta x}{\Delta z})+\frac{1}{18}(k_y^2-k_e^2)\Delta z\Delta x,$$
$$a_{nn}^{e}=\frac{1}{3}(\frac{\Delta z}{\Delta x}+\frac{\Delta x}{\Delta z})+\frac{1}{9}(k_y^2-k_e^2)\Delta z\Delta x,$$

where $k_e = \omega / c_e$, and c_e is the element speed value of the medium. Obviously, the matrix depends upon the frequency ω, the wavenumber k_y and the element model parameter c_e. The coefficient matrix **A** in equation (4.30) is assembled with all the element matrices, that is

$$\mathbf{A} = \left(a_{ij}\right)_{N\times N}, \qquad a_{ij} = \sum_{e=1}^{N_e} a_{ij}^e, \tag{4.39}$$

where N and N_e are the total number of the nodes and the number of finite elements (rectangular) in the computational range, respectively.

(3) Boundary Element Matrix

To calculate the boundary element matrix b_{ij}^e given by expression (4.32), the same shape functions as used in the calculation of the inner element matrix a_{ij}^e are applied to the boundary integrals. As an example, we calculate the boundary element matrix on Γ_1. Fig.4-3 gives a boundary rectangular element, one side Γ_e of which coincides with Γ_1 (see Fig.4-1). In terms of equation (4.33), the shape functions on Γ_1 become

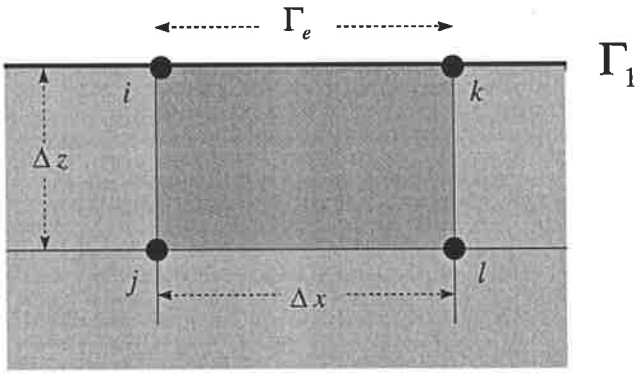

Fig.4-3 Diagram of a boundary rectangular element in the FEM mesh shown in Fig.4-1.

$$\begin{aligned} N_i(x) &= \frac{1}{2}[1-\xi(x)], \qquad N_j(x) = 0; \\ N_k(x) &= \frac{1}{2}[1+\xi(x)], \qquad N_l(x) = 0; \end{aligned} \tag{4.40}$$

where $\xi(x) = \dfrac{2}{\Delta x}[x - (x_k + x_i)/2]$. x_i and x_k are the x-coordinates of the nodes i and k.

Substitution of equation (4.40) for equation (4.32) and using the following identities:

$$\int_{\Gamma_e} N_i N_i dx = \frac{\Delta x}{3}, \qquad \int_{\Gamma_e} N_i N_k dx = \frac{\Delta x}{6},$$

$$\int_{\Gamma_e} N_k N_k dx = \frac{\Delta x}{3}, \qquad \int_{\Gamma_e} \frac{\partial N_i}{\partial x}\frac{\partial N_i}{\partial x} dx = \frac{1}{\Delta x},$$

$$\int_{\Gamma_e} \frac{\partial N_i}{\partial x}\frac{\partial N_k}{\partial x}dx = -\frac{1}{\Delta x}, \qquad \int_{\Gamma_e} \frac{\partial N_k}{\partial x}\frac{\partial N_k}{\partial x}dx = \frac{1}{\Delta x},$$

we have only four non-zero elements as $k_y < k$ and the three are independent due to $b_{ik}^e = b_{ki}^e$, they are

$$\Gamma_1: \begin{cases} b_{ii}^e = (\nu\frac{\Delta x}{3} - \beta\frac{1}{\Delta x}), \\ b_{ik}^e = (\nu\frac{\Delta x}{3} + \beta\frac{1}{\Delta x}), \\ b_{kk}^e = (\nu\frac{\Delta x}{3} - \beta\frac{1}{\Delta x}). \end{cases} \tag{4.41}$$

Equation (4.41) is the final expression for the boundary element integral on Γ_1. These results indicate that only the elements of B^e whose subscript-point locate on the boundary are non-zero (see equation (4.41) and Fig.4-3, the nodal points *i* and *k* locate on Γ_1, so only $b_{ii}^e, b_{ik}^e, b_{ki}^e$ and b_{kk}^e are non-zero). In the same manner, we can obtain similar results for the elements of the boundary element matrix on Γ_2, Γ_3 and Γ_4 respectively:

$$\Gamma_2: \begin{cases} b_{jj}^e = (\nu\frac{\Delta x}{3} - \beta\frac{1}{\Delta x}), \\ b_{jl}^e = (\nu\frac{\Delta x}{3} + \beta\frac{1}{\Delta x}), \\ b_{ll}^e = (\nu\frac{\Delta x}{3} - \beta\frac{1}{\Delta x}); \end{cases} \tag{4.42}$$

$$\Gamma_3: \begin{cases} b_{ii}^e = (\nu\frac{\Delta z}{3} - \beta\frac{1}{\Delta z}), \\ b_{ij}^e = (\nu\frac{\Delta z}{3} + \beta\frac{1}{\Delta z}), \\ b_{jj}^e = (\nu\frac{\Delta z}{3} - \beta\frac{1}{\Delta z}); \end{cases} \tag{4.43}$$

$$\Gamma_4: \begin{cases} b_{kk}^e = (\nu\frac{\Delta z}{3} - \beta\frac{1}{\Delta z}), \\ b_{kl}^e = (\nu\frac{\Delta z}{3} + \beta\frac{1}{\Delta z}), \\ b_{ll}^e = (\nu\frac{\Delta z}{3} - \beta\frac{1}{\Delta z}); \end{cases} \tag{4.44}$$

When $k_y > k$, the boundary element integral is much simpler than when $k_y < k$ (see equation (4.32)). So we can directly write out the following results, referring to the above:

$$\Gamma_1: \quad b_{ii}^e = \frac{\Delta x}{3} k_a', \quad b_{ik}^e = \frac{\Delta x}{6} k_a', \quad b_{kk}^e = \frac{\Delta x}{3} k_a'; \tag{4.45}$$

$$\Gamma_2: \quad b_{jj}^e = \frac{\Delta x}{3} k_a', \quad b_{jl}^e = \frac{\Delta x}{6} k_a', \quad b_{ll}^e = \frac{\Delta x}{3} k_a'; \tag{4.46}$$

$$\Gamma_3: \quad b_{ii}^e = \frac{\Delta z}{3} k_a', \quad b_{ij}^e = \frac{\Delta z}{6} k_a', \quad b_{jj}^e = \frac{\Delta z}{3} k_a'; \tag{4.47}$$

$$\Gamma_4: \quad b_{jj}^e = \frac{\Delta z}{3} k_a', \quad b_{jl}^e = \frac{\Delta z}{6} k_a', \quad b_{ll}^e = \frac{\Delta z}{3} k_a'; \tag{4.48}$$

(4) Numerical Modeling Results

After calculating all the inner and boundary element matrices A^e and B^e, one is ready to assemble the whole matrices **A** and **B**. It is noted that the resultant matrix (**A+B**) is a complex one. To solve the complex linear equation (4.30), the LU decomposition method (Press et al., 1986) can be applied to obtain the solution. It has been shown by Song and Williamson (1995a) that the LU algorithm is efficient for the crosshole configuration. Fig.4-4 gives the flow-chart of the numerical computations for the 2.5-D Green's function. From this chart one can recognize that *the algorithm for 2.5-D acoustic wave modeling is very similar to the first part in Fig.3-7 for 2.5-D DC resistivity modeling except that the linear equation solver here is LU instead of* LL^T, *due to the complex quantities of the wavefield.*

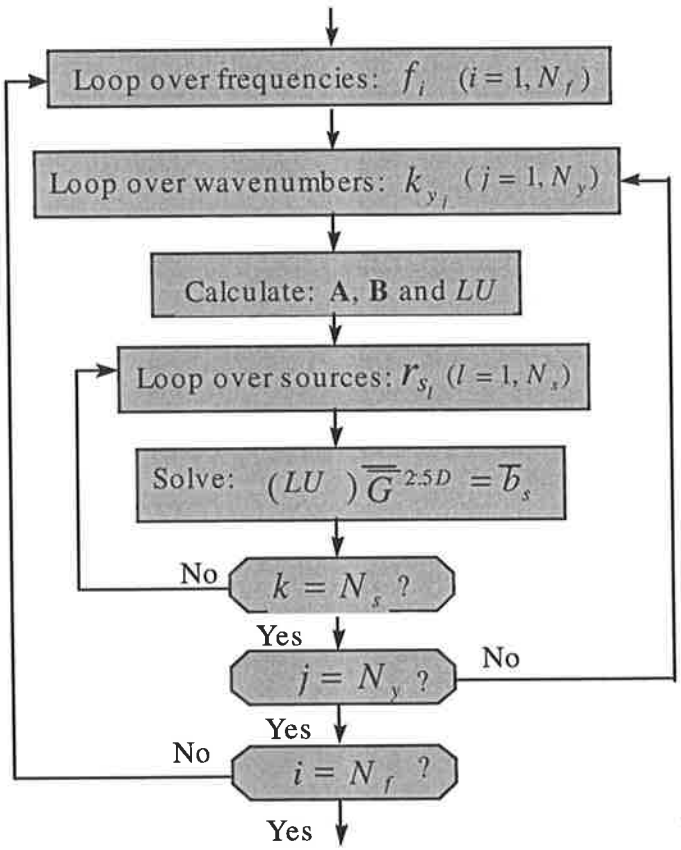

Fig.4-4 Flow-chart of computation for the 2.5-D Green's function in the wavenumber-frequency domain.

The first numerical experiment was to compute the 2.5-D Green's function for a homogeneous medium, because the comparison between the numerical and analytic (equation (2.34)) solutions will demonstrate the accuracy of the method. Fig. 4-5, Fig. 4-6 and Fig. 4-7 show the Hartley-spectral solutions in the k_y-domain for three different frequencies: 100 Hz, 200 Hz and 300 Hz at three wavenumbers. In these plots, the k_y-

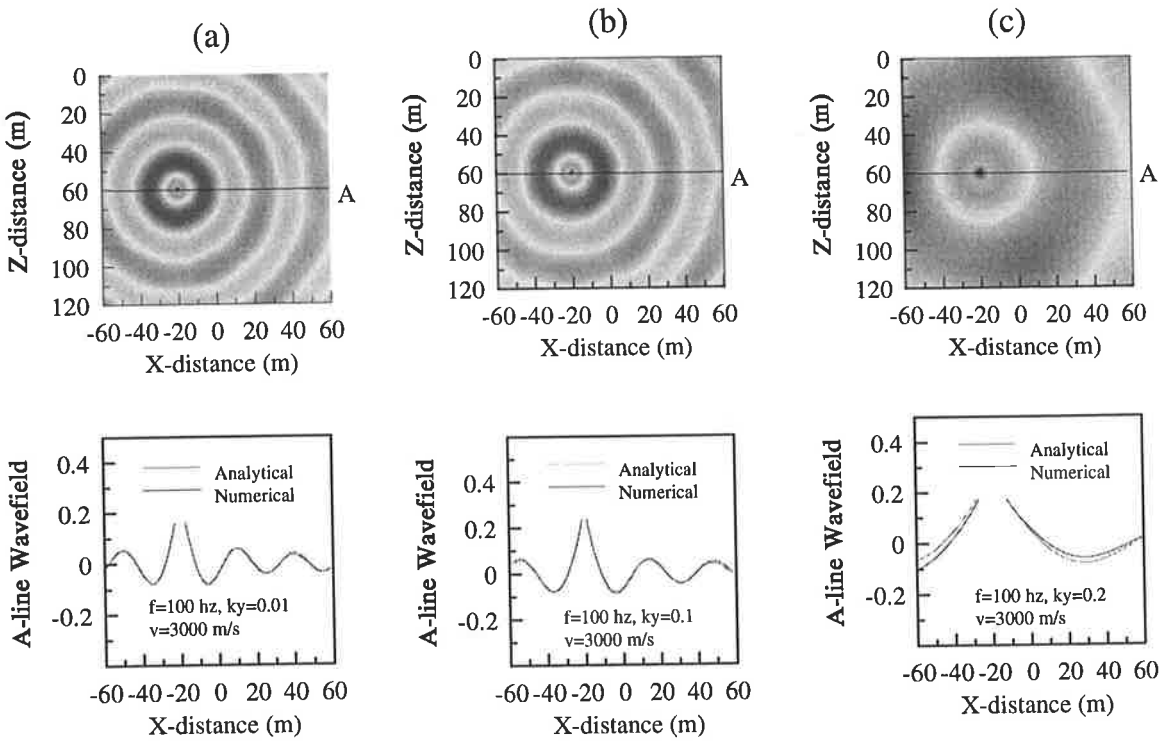

Fig.4-5 The k_y-domain solutions at f=100 Hz for the 2.5-D Green's function in a homogeneous medium (c=3000 m/s) at three wavenumbers: (a) k_y=0.01, (b) k_y=0.1, (c) k_y=0.2. The top three diagrams show the wavefield in plan view. The bottom diagrams are sectional displays along the line marked A, and compare the numerical with the analytical solutions.

components of the three frequencies are checked against the analytic solution along the central line. In these computations, the medium has a constant velocity, c=3000 m/s; the dimension of the finite element mesh is $120\times120\ m^2$; the element size is $1\times1\ m^2$ (which satisfies the one-tenth minimum wavelength criterion) and the predicted angles α_1 and α_2 involved in the ABC were chosen to be 0° and 45° respectively (these were selected after various trials with different pairs of the angles and it was found that the results are not sensitive to the angles). These values seem to

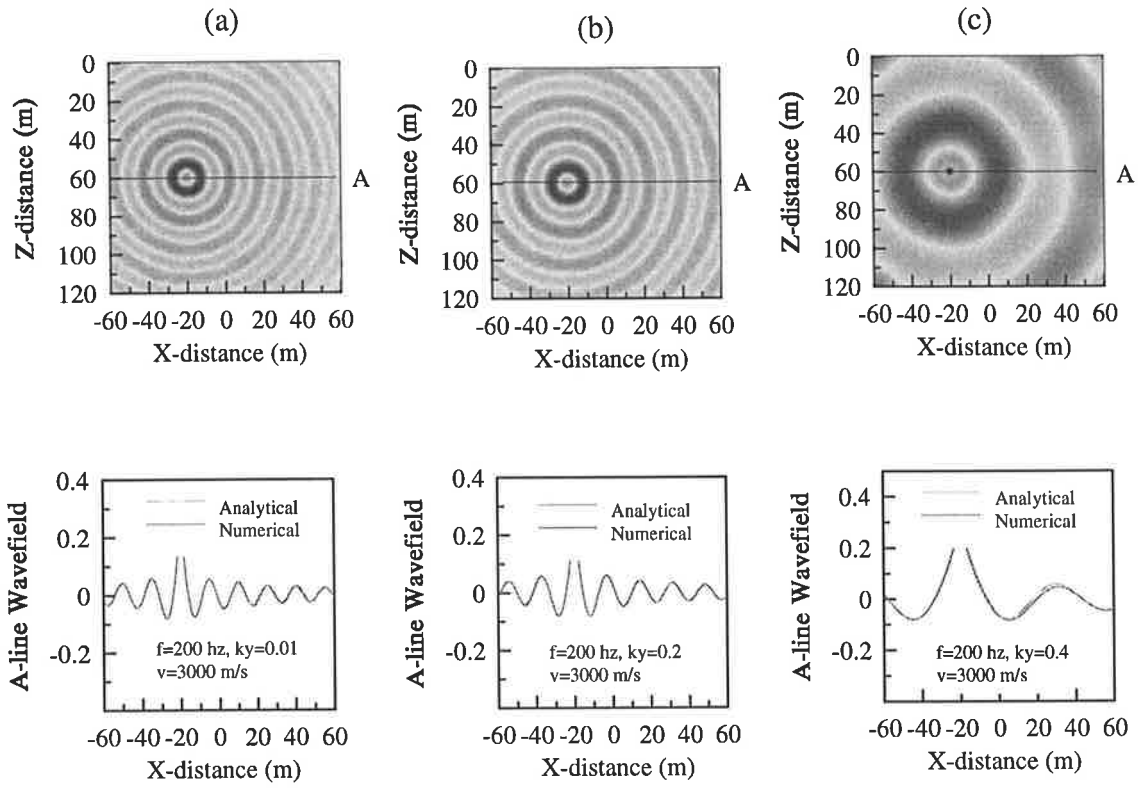

Fig.4-6 The k_y-domain solutions at f=200 Hz for the 2.5-D Green's function in a homogeneous medium (c=3000 m/s) at three wavenumbers: (a) k_y=0.01, (b) k_y=0.2, (c) k_y=0.4.

give the best reduction of the artificial reflections in this case. From these figures one can see that the numerical solutions in the wavenumber-frequency domain, even close to the source, fit the analytical solution very well. A small discrepancy occurs only near the boundary. By successive computations, the boundary condition works satisfactorily over most of the k_y values for the frequency range. A slight artificial boundary effect appears at low frequency (see, Fig. 4-5) or large k_y values (see, Fig. 4-6c and Fig.4-7c), especially close to the critical value (the apparent frequency in the *xz*-plane becomes very low when k_y approaches the critical value). The computations using different predicted angles yielded similar results to Fig.4-5, Fig.4-6 and Fig.4-7. These experiments show that at high frequencies and for most values of k_y, the k_y-domain solution is not very sensitive to the predicted angles. Furthermore, the slight artificial

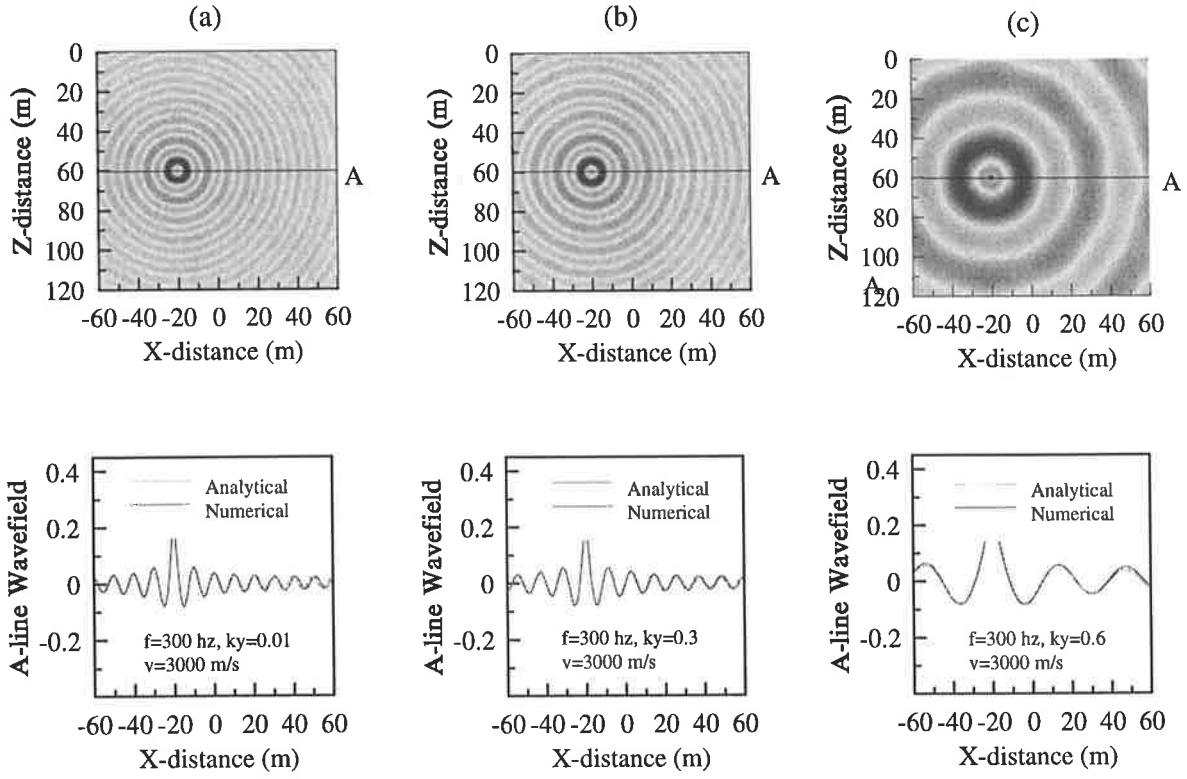

Fig.4-7 The k_y-domain solutions at f=300 Hz for the 2.5-D Green's function in a homogeneous medium (c=3000 m/s) at three wavenumbers: (a) k_y=0.01, (b) k_y=0.3, (c) k_y=0.6.

reflection decreases with the increasing distance between the source and the boundary. Actually, as Higdon (1991) pointed out, an optimal choice of α_j is in general problem-dependent, but the 2-D numerical experiments indicated that the amount of reflection is not overly sensitive to the values of these angles. This is also borne out in our 2.5-D numerical test results. Fig. 4-8 shows the solutions in the frequency-domain for the three above-mentioned frequencies. Comparison between the numerical solutions and the analytic solutions is also made along the central line of the mesh. In these computations, 25 uniform sampled k_y-components (from zero to 0.95 times the critical value of the medium) at each frequency are used to calculate the solutions in terms of equation (2.23). It shows that the numerical solutions provide very good approximations to the analytic solutions in the frequency-domain. There are small

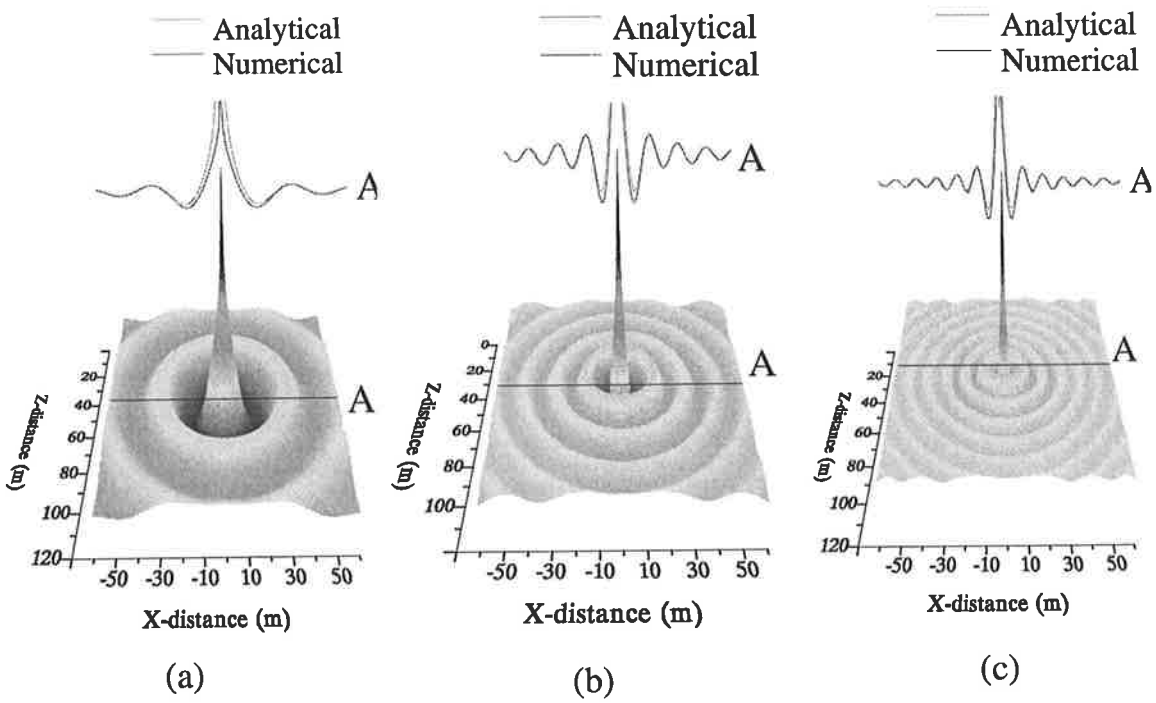

Fig.4-8 The frequency-domain solutions for the 2.5-D Green's function in a homogeneous medium (c=3000 m/s) at (a) f=100 Hz, (b) f=200 Hz, (c) f=300 Hz, obtained by integrating over all wavenumbers k_y. The profiles along the line A, shown at the top of each display, compare numerical with exact analytic results.

deviations near the source. *We found that even if the values adjacent to the source at each k_y-component are very close to the analytic solutions, such as in Fig.4-5, Fig.4-6 and Fig.4-7, the frequency-domain solution (summation of all the k_y-components) has a slight error in the neighborhood of the source. Possible reasons for the error are the finite sampling of k_y and the exclusion of the evanescent field ($k_y > k$).* In order to investigate the sensitivity of the solution to the number of the k_y samples in the fixed k_y range (from zero to the critical value), we repeated the computation with different numbers of k_y-components (from 20 to 60) and calculated the root mean-square error (RMS) with respect to the exact analytic solutions for the three frequencies. Fig.4-9

shows the result. Clearly, *the numerical solutions in the frequency-domain are only mildly sensitive to the number of k_y samples. This implies that the main source of the error in the neighborhood of the source in Fig.4-8 must be the neglect of the contribution of the evanescent field ($k_y > k$).* This can be understood by the fact that the significant values occur only in the small area around the source in the evanescent field.

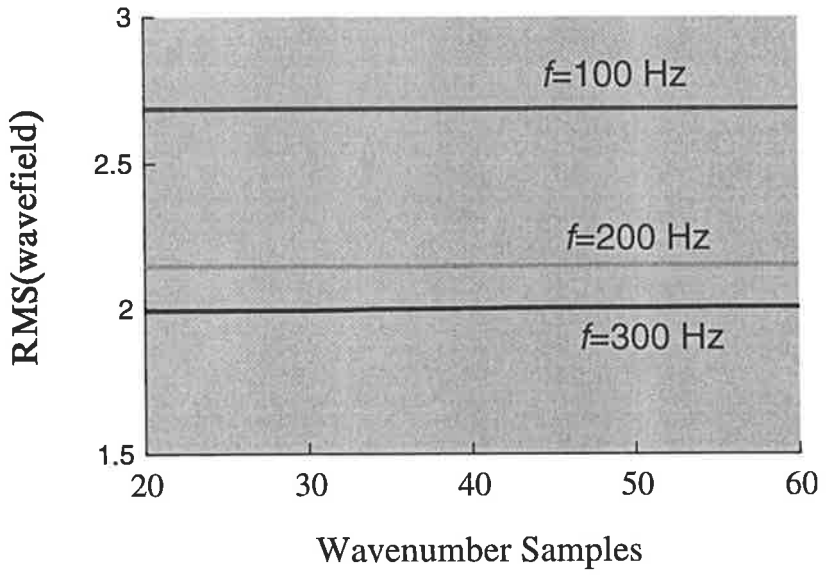

Fig.4-9 The RMS error of the frequency-domain solution versus the k_y samples used for the case of a homogeneous medium (c=3000 m/s). There is minimal change at a given frequency across the wavenumber range displayed, but the error increases with decreasing frequency.

Dropping them leads to the loss of the energy near the source in the frequency-domain, but it has little effect in the rest of area. Fortunately, seismic exploration measurements are not normally conducted near the source, but rather in the far-field. Taking a large range of k_y values increases the computational effort.

Fig.4-10 shows the numerical and analytic solutions in the frequency-domain over the range 100 Hz to 300 Hz (Fig.4-10a,c) and the resulting common-shot gather seismograms (Fig.4-10b,d) for a crosshole geometry. The δ-impulse source is located at position (-20, 60) (see, Fig.4-5) and the 91 receivers are distributed at 1 m vertical spacing over the depth range 15 m to 105 m in a borehole at x=20 m. In this

computation, a 4 Hz sampling interval, 25 k_y-components and the inverse Hartley transform were employed. One can see that the numerical solutions at all the receivers are nearly the same as the analytic solutions in the frequency- and time-domain.

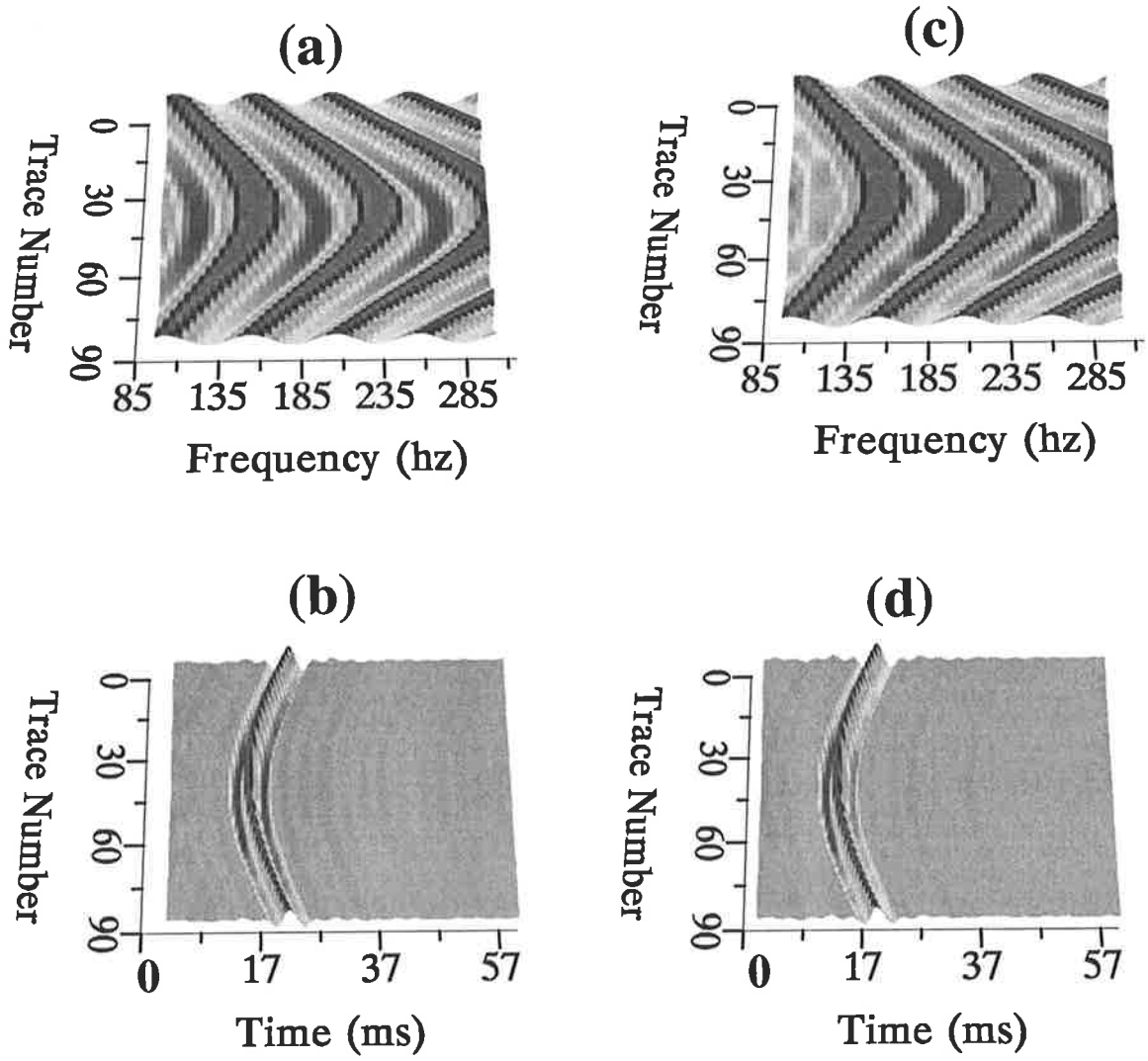

Fig.4-10 The frequency-domain solutions from 100 Hz to 300 Hz and the corresponding time-domain common-shot gather seismograms for a crosshole configuration in a homogeneous medium (c=3000 m/s). Diagrams (a) and (b) are analytic solutions; (c) and (d) are numerical solutions.

Another experiment was performed for an inhomogeneous model involving a low-velocity layer (c=1000 m/s, thickness=20 m) in the background medium whose velocity is c=3000 m/s. Fig. 4-11 and Fig.4-12 are examples of the numerical solutions at 100 Hz

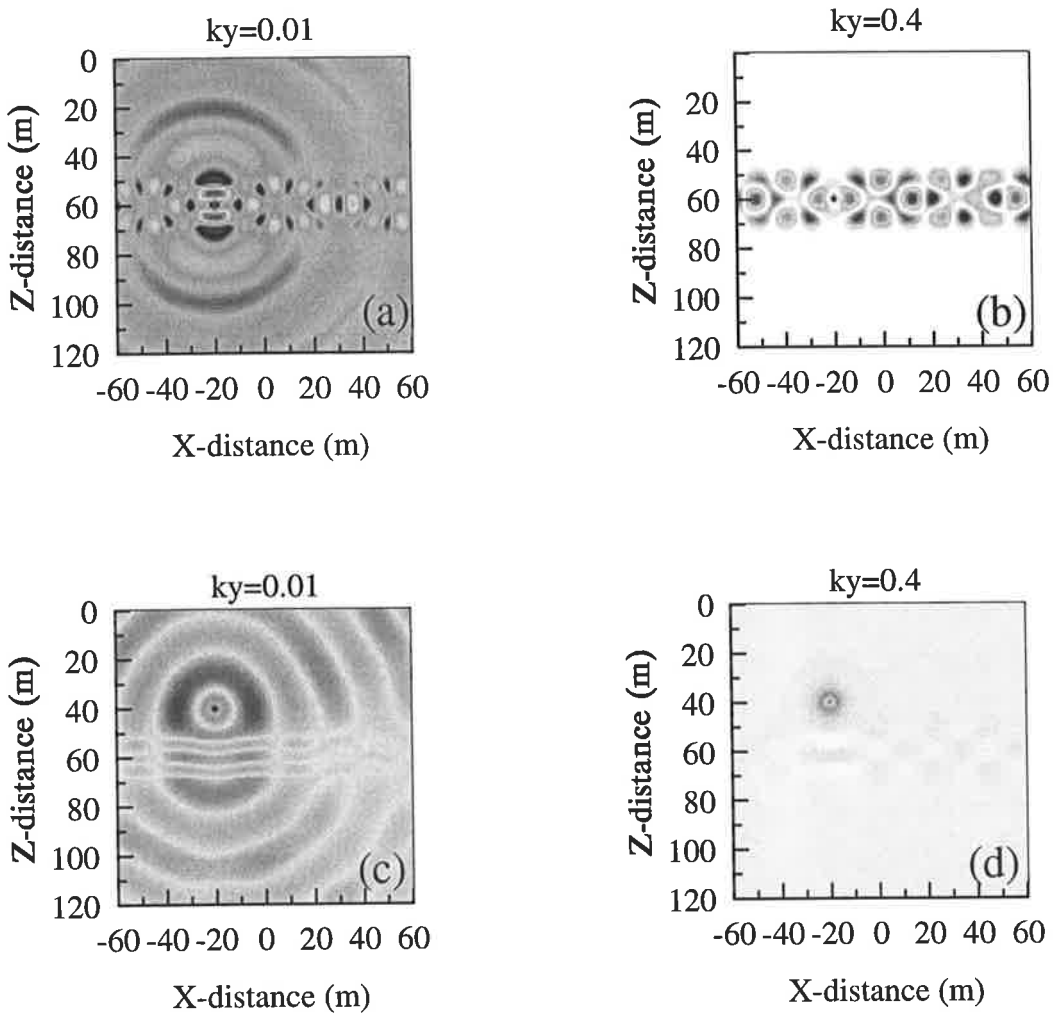

Fig.4-11 The k_y-domain solutions for the 2.5-D Green's function at f=100 Hz in an inhomogeneous medium involving an embedded low-velocity zone (c=1000 m/s) in a constant velocity host rock (c=3000 m/s). Diagrams (a) and (b) are the results for the source in the low-velocity zone; Diagrams (c) and (d) are the results for the source in the host medium. Two values of k_y are displayed (0.01 and 0.4), below and above the critical wavenumbers.

and 300 Hz respectively. For each frequency, the solutions of two k_y-components and two source locations were calculated so as to test the composite boundary condition and investigate the wavefield pattern . This model will have two critical values of k_y for each frequency, e.g. for 100 Hz, the critical values are $k_y \approx 0.209$ in the background medium and $k_y \approx 0.628$ in the low-velocity layer, and for 300 Hz (Fig.4-12), they are $k_y \approx 0.628$ and $k_y \approx 1.885$ in the background medium and low-velocity layer

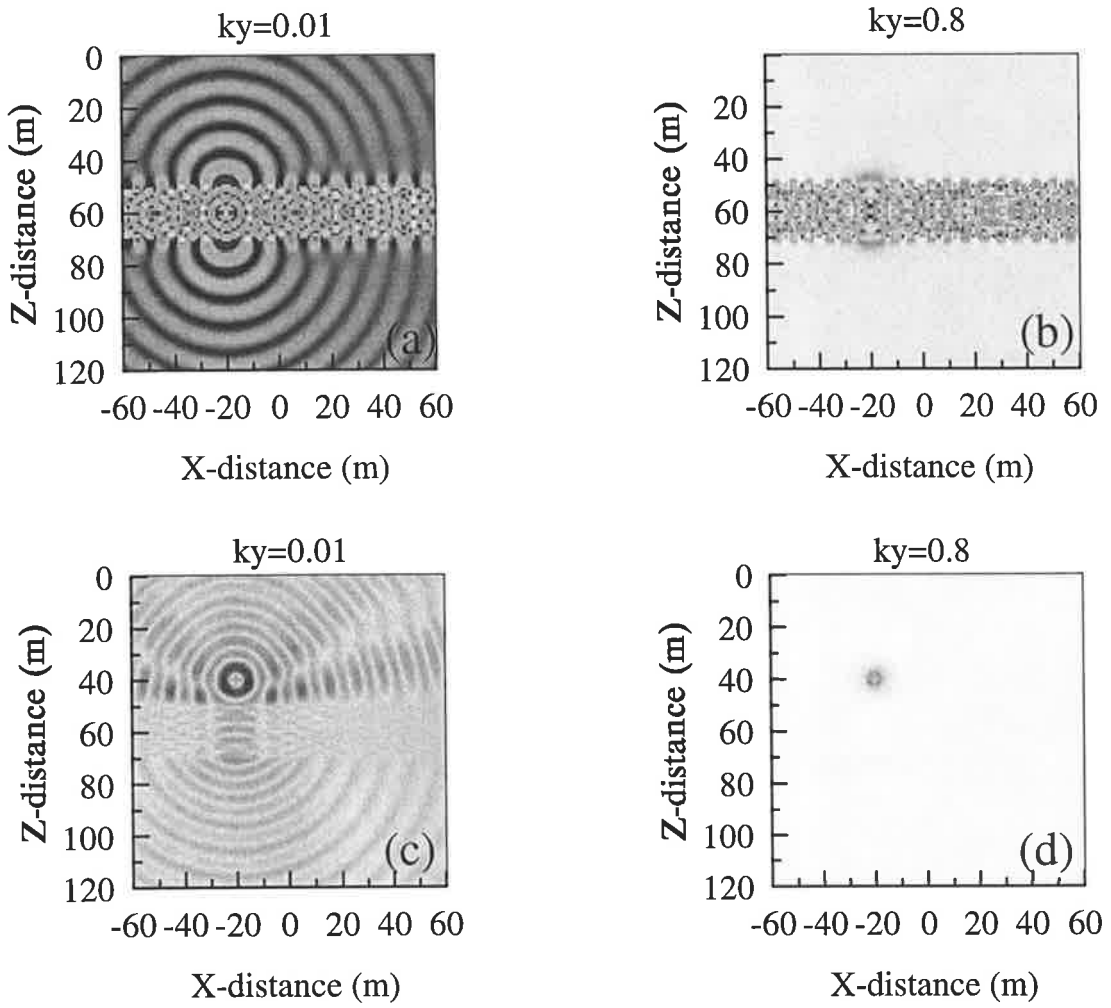

Fig.4-12 The k_y-domain solutions for the 2.5-D Green's function at *f*=300 Hz for the same model as Fig.4-11. Diagrams (a) and (b) are the results for the source in the low-velocity zone; Diagrams (c) and (d) are the results for the source in the host medium. Two values of k_y are displayed (0.01 and 0.8), below and above the critical wavenumbers.

respectively. According to equation (2.23), the sampling k_y must cover the range k_y=0~0.628 for 100 Hz and k_y=0~1.885 for 300 Hz. To demonstrate the wavefield patterns, we put the source first in the low-velocity layer (Fig.4-11a,b and Fig.4-12a,b) and then in the background medium (Fig.4-11c,d and Fig.4-12c,d), and assigned k_y values far removed from the critical values. One can see that at k_y=0.01, the wavefield expands and fills the whole space from the source (Fig.4-11a,c and Fig.4-12a,c), because k_y is under the two critical values of the model. When the source is located

in the low-velocity layer and k_y=0.4 at 100 Hz and k_y=0.8 at 300 Hz, the solution in the background goes to zero quickly but is non-zero in the layer (Fig.4-11b and Fig.4-12b). It seems that the wave energy propagates only in the layer (part of the waveguide) and it can not be supported in the host medium, because k_y is above the critical value of the background and below the critical value of the layer. When the source is located in the background medium and k_y exceeds the critical value of the host material, the wavefield goes to zero quickly too (Fig.4-11d and Fig.4-12d). However, differences can be observed between the high frequency (300 Hz) and low frequency (100 Hz) cases. At 300 Hz, the wavefield is zero except for a small area around the source and no wave energy goes into the layer although k_y is below the critical value of the layer (Fig.4-12d). This means that the evanescent energy from the source is zero when it reaches the layer, so it can not excite the medium particle vibration. At 100 Hz, the evanescent energy is observed not to be zero when it reaches the layer and although very small, it still causes some wave energy to propagate in the layer (Fig.4-11d). It seems that the higher the frequency, the more rapidly the evanescent field decreases. These results imply that *for each frequency the maximum k_y should be just beyond the critical value of the medium around the source so that no wave energy is left out in the computations, meanwhile saving much computer time by avoiding unnecessary calculations for larger k_y due to the strong evanescent field.*

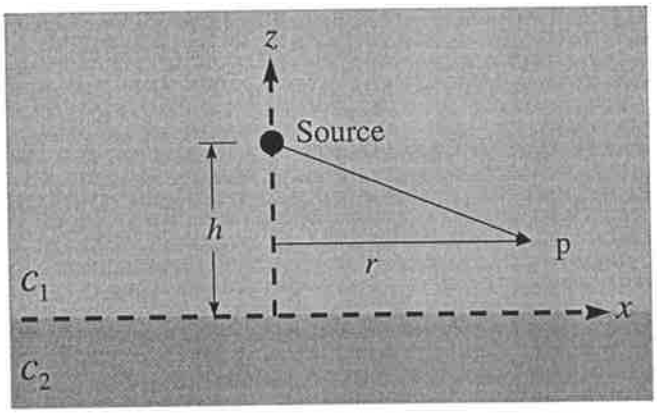

Fig.4-13 Model of two semi-infinite media in contact– c_1 and c_2 are the wavespeeds of the two media.

In order to show the accuracy of the numerical computation in inhomogeneous modeling, a simple model involving two semi-infinite media in contact (see, Fig.4-13), was used to compare the numerical and semi-analytical solutions. The response of the model

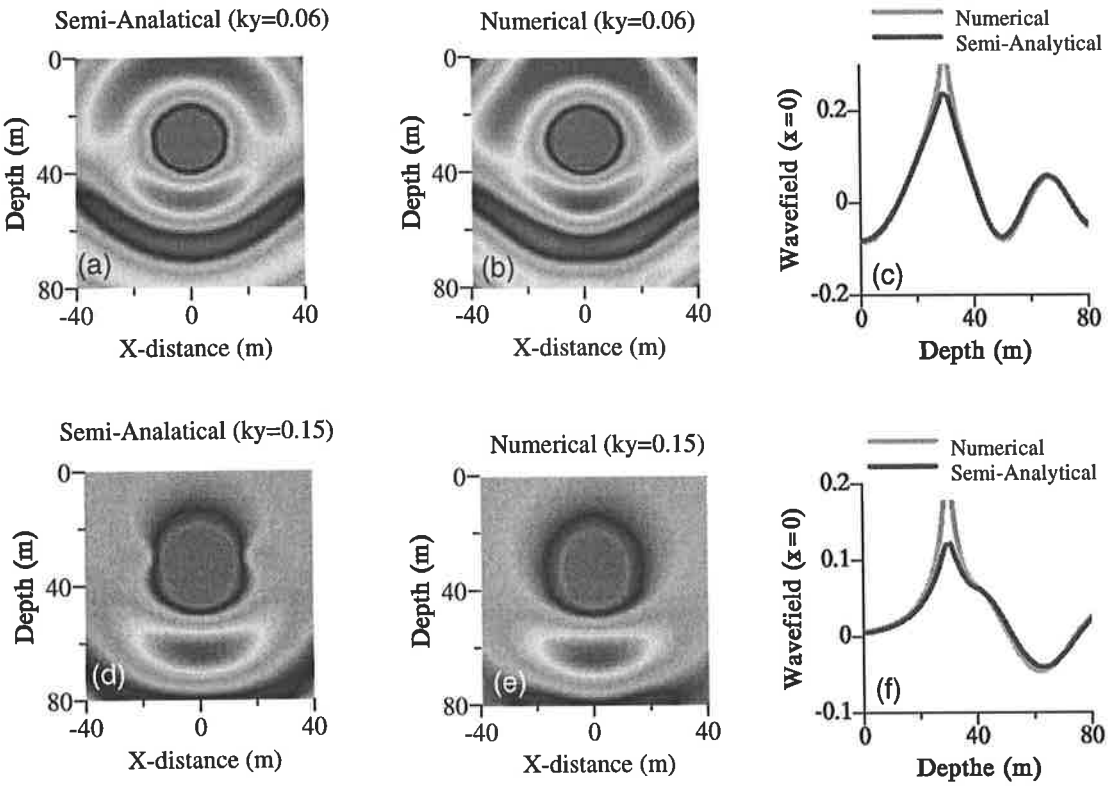

Fig.4-14 The numerical and semi-analytical solutions for a model of two semi-infinite media in contact at 100 Hz in the wavenumber-frequency domain. (a) and (d) are semi-analytical solutions at two wavenumbers: k_y=0.06 and k_y=0.15; (b) and (e) are numerical solutions at the same wavenumbers; (c) and (f) are wavefield values along the central line (x=0) of the two solutions.

can easily obtained by a semi-analytical method (Appendix C). Fig.4-14 and Fig.4-15 give the results for 100 Hz and 300 Hz. The velocities of the two semi-infinite media are c_1=5000 m/s (upper medium) and c_2 =3000 m/s (lower medium) respectively. The model implies that there are two critical values of k_y for each frequency, e.g. for 300 Hz, the critical values are $k_y \approx 0.377$ in the upper medium and $k_y \approx 0.628$ in the lower half-space. From these examples, one can see that the numerical solutions approach very closely to the semi-analytic solutions and they have the same characteristics shown in Fig.4-11 and Fig.4-12: (1) when k_y=0.06, the wavefield propagates in the whole space

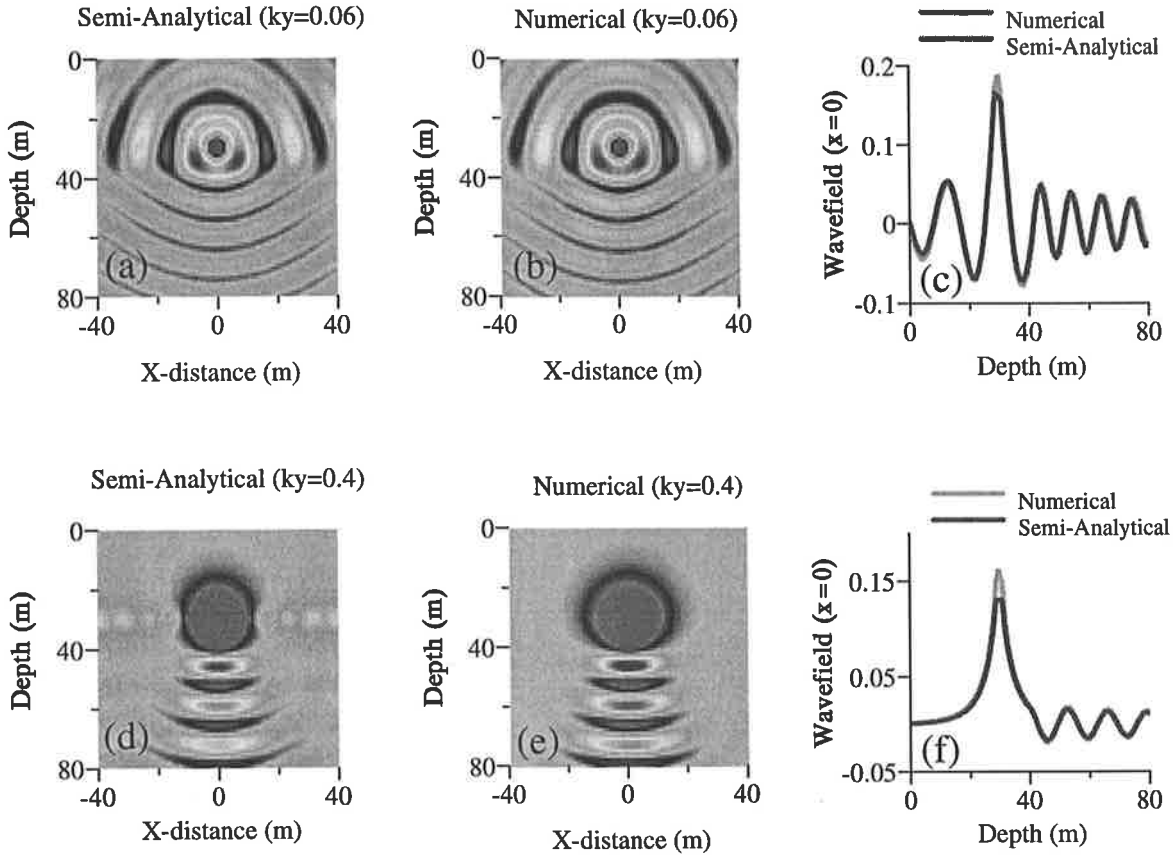

Fig.4-15 The numerical and semi-analytical solutions for a model of two semi-infinite media in contact at 300 Hz in the wavenumber-frequency domain. (a) and (d) are semi-analytical solutions at two wavenumbers: k_y=0.06 and k_y=0.4; (b) and (e) are numerical solutions at same wavenumbers; (c) and (f) are wavefield values at the central line (x=0) of the two solutions.

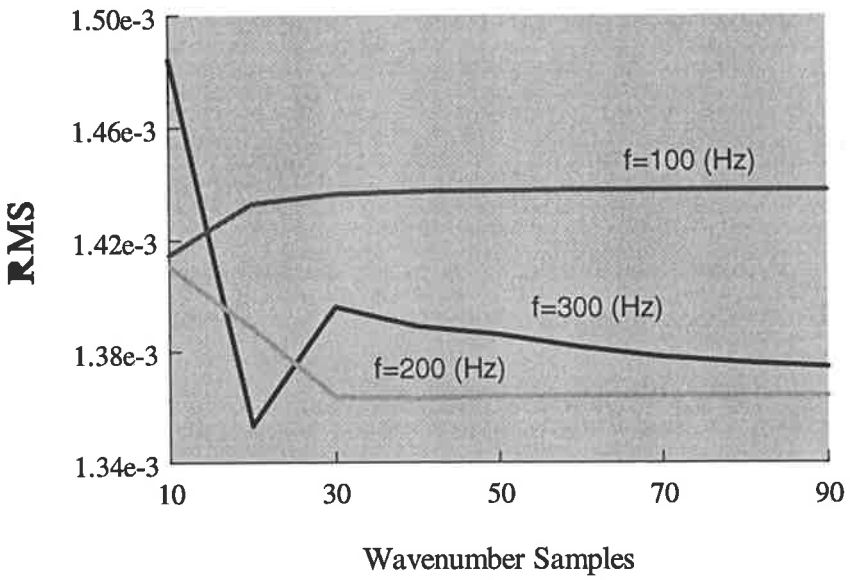

Fig.4-16 The root mean square error (RMS) of the numerical solutions (referred to the semi-analytical solutions) versus the number of wave-number samples for a model of two semi-infinite media in contact.

(see Fig.4-14a, b and Fig.4-15a, b), because the k_y is below the two critical values of the model; (2) when k_y=0.4 at 300 Hz and k_y=0.15 at 100 Hz, the wavefields become evanescent fields in the upper medium but propagate in the lower half-space (see Fig.4-14d, e and Fig.4-15d, e). Here the k_y value is above the critical value of the upper medium but below the critical value of the lower half-space. The sensitivity of the frequency-domain solution to the number of k_y samples was also investigated for inhomogeneous modeling. Fig.4-16 shows the RMS error of the numerical solutions with the semi-analytical solution at each frequency via different numbers of k_y samples. One can see that the RMS error of the three frequencies has a different response to the k_y samples and is quite different from the homogenous case (Fig.4-9). It follows that *the accuracy of the solution for the inhomogeneous medium is not*

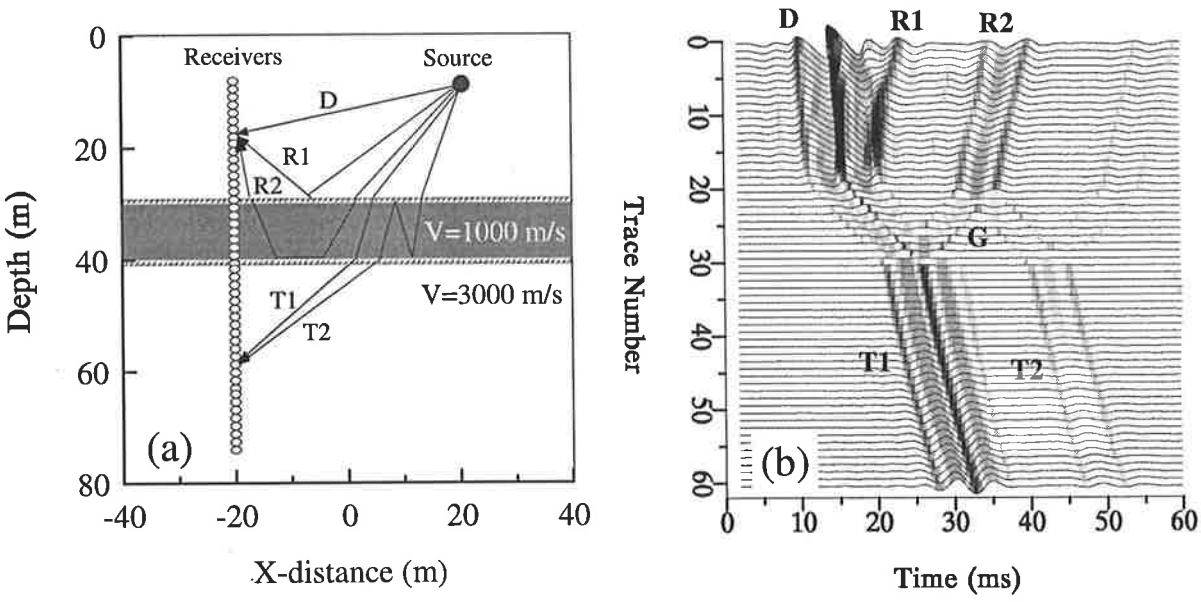

Fig.4-17 Crosshole surveying geometry (a) and the corresponding synthetic seismograms (b) obtained with the new method for an inhomogeneous model involving a low velocity waveguide (e.g. coal seam). The source is outside the waveguide. The various reflected and transmitted arrivals identified in the seismograms can be associated with the wave paths shown in diagram (a).

monotonically improved by increasing the number of k_y samples, due to the complicated wavefield. An appropriate number of k_y samples, e.g. N_y=30 in Fig.4-16, enables us to obtain an accurate numerical solution with reasonable computer cost. Finally, synthetic seismograms for the low-velocity layer model (same as in Fig.4-11 and Fig.4-12) with a crosshole surveying geometry were calculated (Fig.4-17). In this computation, a δ-impulse source, 61 receivers, 30 k_y-components and a 4 Hz sampling interval were employed to calculate the frequency-domain solutions from 100 Hz to 300 Hz. The solutions were then filtered by a Hanning window with the central frequency at 200 Hz. Finally, by performing the inverse Hartley transform, the seismograms were obtained. From the traces, one can easily identify several interesting events due to the low-velocity zone, such as reflected waves (R1 and R2), transmitted waves (T1 and T2) and waveguide arrivals (G), which have different ray-paths (see, Fig.4-17a).

4.4 A Damping Method

In the previous section, we have described the numerical approach to the 2.5-D acoustic wavefield through solving a composite boundary-valued problem. One can find that when the 2.5-D absorbing boundary condition (e.g. equation (4.17)) is employed in conjunction with the FEM, there is a singularity problem when the apparent wavenumber goes to zero ($k_a = 0$ or $k_y = k$) in heterogeneous modeling. Special treatment for this situation must be incorporated in the computations. The damping method, a kind of wave modeling scheme suggested by Sochacki et al. (1987) and successfully applied to 2-D acoustic and elastic wave modeling, is very effective in reducing artificial reflections from the edges of the finite computational mesh. By the simple introduction of a time-damping term in the wave equation and incorporation of an attenuating boundary zone around the discretisation mesh, the wavefield goes to zero with time when passing through the zone. The main advantage of the method is that it is not necessary to use any absorbing boundary condition and it is very easy to build the time-damper into the numerical method. Recently, Serón et al. (1996) applied the method with the FEM and showed satisfactory solutions for 2-D elastic wave modeling in the time-domain. It has been proved that a simple linear time-damper can be chosen and the method is very effective for both acoustic and elastic wave modeling. Considering the merits of the damping method and the finite element method (Marfurt,

1984; Hughes, 1987; Serón et al., 1996), we apply them here to the computation of the 2.5-D Greens' function in the frequency-domain for arbitrary acoustic media.

(1) The FEM Formulation

To solve the 2.5-D acoustic wave equation, we have introduced an absorbing boundary condition to minimize the artificial reflections from the edges of the finite-size mesh. An alternative reduction of the artificial reflections is to introduce a time-damper to the wave equation, so that one solves a damped wave equation rather than the original (undamped, perfectly elastic) wave equation (Sochacki et al. 1987; Serón et al. 1996). Applying the damping method to the 2.5-D problem, the Green's function can be presented as the following homogeneous boundary-valued problem:

$$\begin{cases} \nabla^2 \overline{\overline{G}}^{2.5D} + [(k^2 - k_y^2) + iA(\omega, k_y, r)]\overline{\overline{G}}^{2.5D} = -\delta(r - r_s) & r \in \Omega, \\ \overline{\overline{G}}^{2.5D} \approx 0 & r \in \partial\Omega, \end{cases} \tag{4.49}$$

Note that the Green's function, and its normal derivative, are taken to be essentially zero along the boundary, which is a great distance away. To shorten the equation's notation we use $r = (x, z)$ to stand for the (x,z)-plane coordinates. There is a slight difference from Sochacki et al. (1987) and Serón et al. (1996)'s notation in the damping term. The time-damper $A(\omega, k_y, r)$ represents a general form that may be a function of the frequency, wavenumber and coordinates, considering the fact that the solution will be searched in the wavenumber-frequency domain. When k_y=0, it reverts to the 2-D problem. $A(\omega, k_y, r)$ was termed a time damper because this term relates to the first derivative of the wavefield with respect to time in the time domain; this describes wave propagation in which amplitude decays with travel time. Sochacki et al. (1987) pointed out that in the time domain the time-damper must be positive if the amplitudes of the outgoing waves are to be reduced, and if $A = \partial_x A = \partial_z A = \partial_z A = \partial_{xx} A = \partial_{zz} A = \partial_{xz} A = 0$ on the boundary and $\max\{|\partial_x A|, |\partial_z A|, |\partial_{xx} A|, |\partial_{zz} A|\} \ll 1$, the reflected waves from the edges of the computational range are decayed sufficiently to zero. So, to approach the original solution, a common strategy is to assign the damper as follows: let $A(\omega, k_y, r)$ be zero inside the area of interest and non-zero in the margin area of the whole region so that the wavefield is decayed to zero in this area, and it is expected to satisfy the boundary condition in equation (4.49) and no artificial reflections return to the central region.

Reviewing the FEM theory, the solution of equation (4.49) may be formulated as a variational problem subject to the stationary condition (see equation (2.52)):

$$\delta F(\overline{\overline{G}}^{2.5D}) = 0, \tag{4.50}$$

where $F(\overline{\overline{G}}^{2.5D})$ is some functional. It can be shown that if the differential operator L is a linear self-adjoint operator, the functional can be written in the form (see equation (2.53)):

$$F(\overline{\overline{G}}^{2.5D}) = \frac{1}{2} < L\overline{\overline{G}}^{2.5D}, \overline{\overline{G}}^{2.5D} > - < \overline{\overline{G}}^{2.5D}, f >, \tag{4.51}$$

for a differential equation $L\overline{\overline{G}}^{2.5D} = f$. In view of equation (4.49), we have

$$\begin{aligned} L &= -\nabla^2 + [k_y^2 - k^2 - iA(\omega, k_y, r)], \\ f &= \delta(r - r_s). \end{aligned} \tag{4.52}$$

Substituting equation (4.52) for equation (4.51), then for equation (4.50) and by applying Green's integral theorem, the variational problem is rewritten as

$$\delta\{\frac{1}{2}\int_{\Omega}[\nabla\overline{\overline{G}}^{2.5D} \cdot \nabla\overline{\overline{G}}^{2.5D} + (k_y^2 - k^2 - iA(\omega, k_y, r))(\overline{\overline{G}}^{2.5D})^2 - 2\overline{\overline{G}}^{2.5D}\delta(r - r_s)]d\Omega\}. \tag{4.53}$$

Here we have used the zero-boundary condition due to the introduction of the damping factor. After discretisation of the integral region with rectangular elements, the variational problem is reduced to solving the following linear system:

$$M\overline{\overline{G}}^{2.5D} = \bar{b}_s, \tag{4.54}$$

where $\overline{\overline{G}}^{2.5D}$ is a column vector whose components are nodal values of the Green's function in the finite element mesh, $\bar{b}_s$ is a source vector that has only one non-zero element (=1.0) and whose location coincides with the source. M is a sparse, symmetric and banded matrix assembled with all element matrices M^e, which uses shape functions N_i^e (i=*1,2,3,4*) in a finite element so that they are 4×4 symmetric matrices calculated using the expressions:

$$\begin{aligned} M_{ij}^e &= \int_{\Omega^e}\{\nabla N_i^e \cdot \nabla N_j^e + [k_y^2 - k^2 - iA(\omega, k_y, r)]N_i^e N_j^e\}d\Omega. \\ & (i, j = 1,2,3,4). \end{aligned} \tag{4.55}$$

They can be analytically calculated by substituting the rectangular linear shape function (equation (4.33)). Using equations (4.34)-(4.37), we have ten independent elements of the matrix M^e:

$$
\begin{aligned}
M_{ii}^{e} &= \frac{1}{3}\left(\frac{\Delta z}{\Delta x}+\frac{\Delta x}{\Delta z}\right)+\frac{1}{9}(k_y^2-k^2-iA_e)\Delta z\Delta x,\\
M_{ij}^{e} &= \frac{1}{3}\left(\frac{\Delta z}{2\Delta x}-\frac{\Delta x}{\Delta z}\right)+\frac{1}{18}(k_y^2-k^2-iA_e)\Delta z\Delta x,\\
M_{im}^{e} &= \frac{1}{3}\left(\frac{\Delta x}{2\Delta z}-\frac{\Delta z}{\Delta x}\right)+\frac{1}{18}(k_y^2-k^2-iA_e)\Delta z\Delta x,\\
M_{in} &= -\frac{1}{6}\left(\frac{\Delta z}{\Delta x}+\frac{\Delta x}{\Delta z}\right)+\frac{1}{36}(k_y^2-k^2-iA_e)\Delta z\Delta x,\\
M_{jj}^{e} &= \frac{1}{3}\left(\frac{\Delta z}{\Delta x}+\frac{\Delta x}{\Delta z}\right)+\frac{1}{9}(k_y^2-k^2-iA_e)\Delta z\Delta x,\\
M_{jm}^{e} &= -\frac{1}{6}\left(\frac{\Delta z}{\Delta x}+\frac{\Delta x}{\Delta z}\right)+\frac{1}{36}(k_y^2-k^2-iA_e)\Delta z\Delta x,\\
M_{jn}^{e} &= \frac{1}{3}\left(\frac{\Delta x}{2\Delta z}-\frac{\Delta z}{\Delta x}\right)+\frac{1}{18}(k_y^2-k^2-iA_e)\Delta z\Delta x,\\
M_{mm}^{e} &= \frac{1}{3}\left(\frac{\Delta z}{\Delta x}+\frac{\Delta x}{\Delta z}\right)+\frac{1}{9}(k_y^2-k^2-iA_e)\Delta z\Delta x,\\
M_{mn}^{e} &= \frac{1}{3}\left(\frac{\Delta z}{2\Delta x}-\frac{\Delta x}{\Delta z}\right)+\frac{1}{18}(k_y^2-k^2-iA_e)\Delta z\Delta x,\\
M_{nn}^{e} &= \frac{1}{3}\left(\frac{\Delta z}{\Delta x}+\frac{\Delta x}{\Delta z}\right)+\frac{1}{9}(k_y^2-k^2-iA_e)\Delta z\Delta x,
\end{aligned}
\tag{4.56}
$$

where A_e is the element value of the damping factor and the subscripts (i,j,m,n) denote the four nodes of a rectangular element (see Fig.4-2). The coefficient matrix M in equation (4.54) is assembled with all the element matrices M^e $(e = 1,2,.....N_e)$, that is

$$
M = \left(M_{ij}\right)_{N\times N}; \qquad M_{ij} = \sum_{e=1}^{N_e} M_{ij}^{e}. \tag{4.57}
$$

where N_e and N are the total number of the elements and the number of nodes in the computational mesh, respectively. Finally, we also apply the LU decomposition method to solve the linear equation (4.54).

(2) Choice of The Damping Term

To calculate the matrix given by equation (4.56), the damper $A(\omega,k_y,r)$ must be properly chosen. Sochacki et al. (1987) studied five kinds of damper (linear, power, cubic, Gaussian and exponential) for 2-D acoustic and elastic modeling in the time-domain and concluded that the linear damper best reduced the artificial reflections. Serón et al. (1996) also took the linear damper in 2-D elastic wave modeling and

obtained very satisfactory results. So, the same form as given by Serón et al. (1996) was taken here, but we have modified the coefficient of the linear damper to be a function of frequency and wavenumber rather than just being a constant. This was to take account of the fact that the reflection coefficient of the damping method varies with the frequency and width of the absorbing zone (Cao and Greenhalgh, 1998). This implies that there are different damping effects on various wavelengths of the propagating disturbance with a limited width of the absorbing zone. For a given frequency ω and different wavenumbers $k_y (< k_c)$ the wavefield has various apparent wavelengths ($\lambda_a = \frac{2\pi}{\sqrt{k^2 - k_y^2}}$) in the xz-plane. So, to make compensation for the variation, the expressions for the linear damper $A(\omega, k_y, r)$ must be adjusted as follows:

$$\begin{aligned}
&\text{In region (1):} \quad A(\omega,k_y,r)_1 = C(\omega,k_y)[N_x - (I+1/2)]\Delta x, \\
&\text{In region (2):} \quad A(\omega,k_y,r)_2 = C(\omega,k_y)[N_z - (J+1/2)]\Delta z, \\
&\text{In region (3):} \quad A(\omega,k_y,r)_3 = \max[A(\omega,k_y,r)_1, A(\omega,k_y,r)_2], \\
&\qquad (I=1,2,\ldots,\ N_x\text{-}1;\ J=1,2,\ldots,\ N_z\text{-}1),
\end{aligned} \tag{4.58}$$

where N_x and N_z are the total number of nodes in the absorbing zone in the x- and z-directions, respectively. Δx and Δz are the grid spacings. Region (1), region (2) and region (3) are shown in Fig.4-18. In equation (4.58), we preserve the linear property with the coordinates given by I and J and use $C(\omega, k_y)$ to control the damping effect on different wavelength waves having varying ω and k_y. Once the ranges of frequency ω and wavenumber k_y are given, the coefficient $C(\omega, k_y)$ can be determined by numerical experiments with a fixed mesh size (see next section).

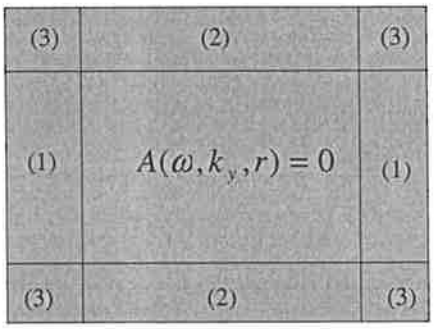

Fig.4-18 Sketch of the definition area of the linear damper. Region (1), (2) and (3) are the non-zero areas of the damper.

(3) Numerical Modeling Results

To check the precision of the numerical method, the first experiment was performed for a homogenous medium to facilitate ease of comparison of the numerical solution with the analytical solution. The Hartley spectra of the wavefield were calculated from the

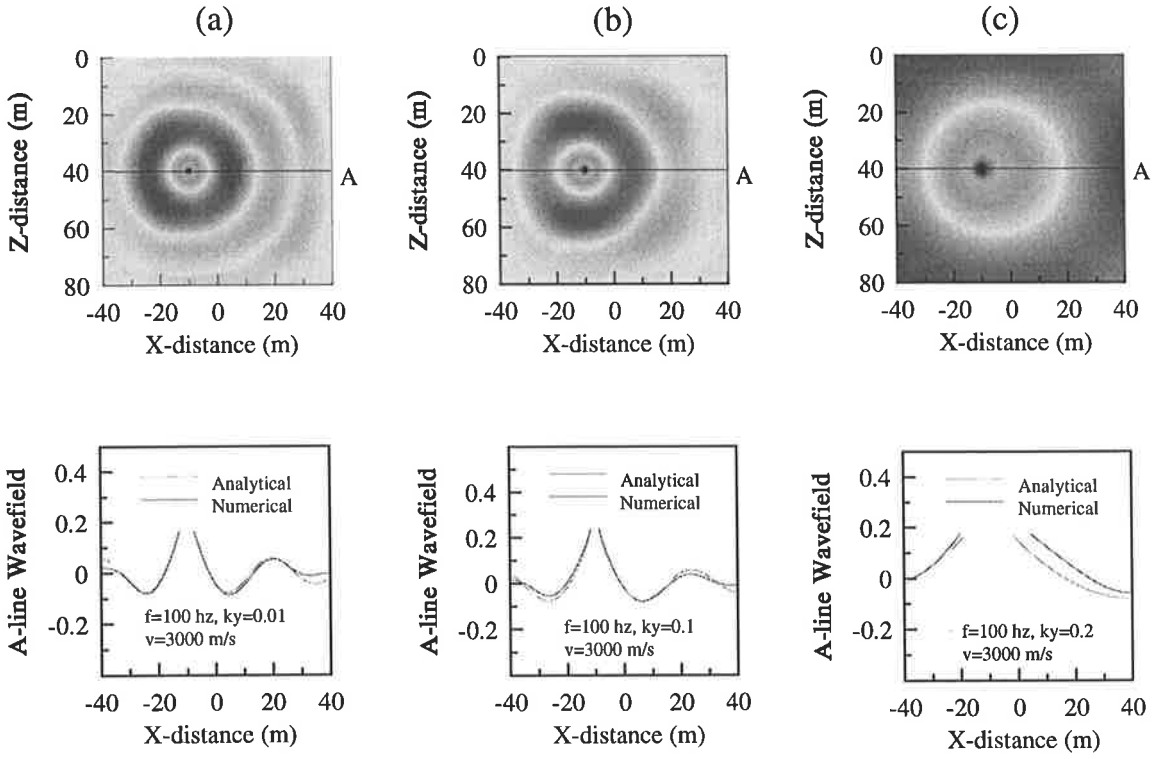

Fig.4-19 The k_y-domain solutions: (a) k_y=0.01, (b) k_y=0.1, (c) k_y=0.2 obtained with the damping method for a homogeneous model (c=3000 m/s) at f=100 Hz.

Fourier spectra with the solution of equation (4.54). Figures 4-19, 4-20 and 4-21 show the results for three k_y-components at three frequencies: 100 Hz, 200 Hz and 300 Hz respectively. Meanwhile, the three k_y-domain solutions are checked against the analytic solutions along the central line. In these computations, the uniform medium has a constant velocity c=3000 m/s; the mesh size is $80\times80\ m^2$; the element size is $1\times1\ m^2$ which satisfies the one-tenth minimum wavelength criterion. The width of the absorbing zone is 20 m ($N_x = N_z = 20$). By means of numerical experiments, we found that $C(\omega,k_y)$ linearly increases with frequency $f = \omega/2\pi$ and decreases with k_y. An acceptable form for the coefficient $C(\omega,k_y)$ in equation (4.58) may be:

$$C(f,k_y)=\begin{cases} C_0\{\dfrac{a_1+(a_2-a_1)(\dfrac{f-f_1}{f_2-f_1})}{1+[b_1+(b_2-b_1)(\dfrac{f-f_1}{f_2-f_1})]\sqrt{k_y}}\} & k_y\in(0,k_c], \\ C_0 & k_y>k_c, \end{cases} \tag{4.59}$$

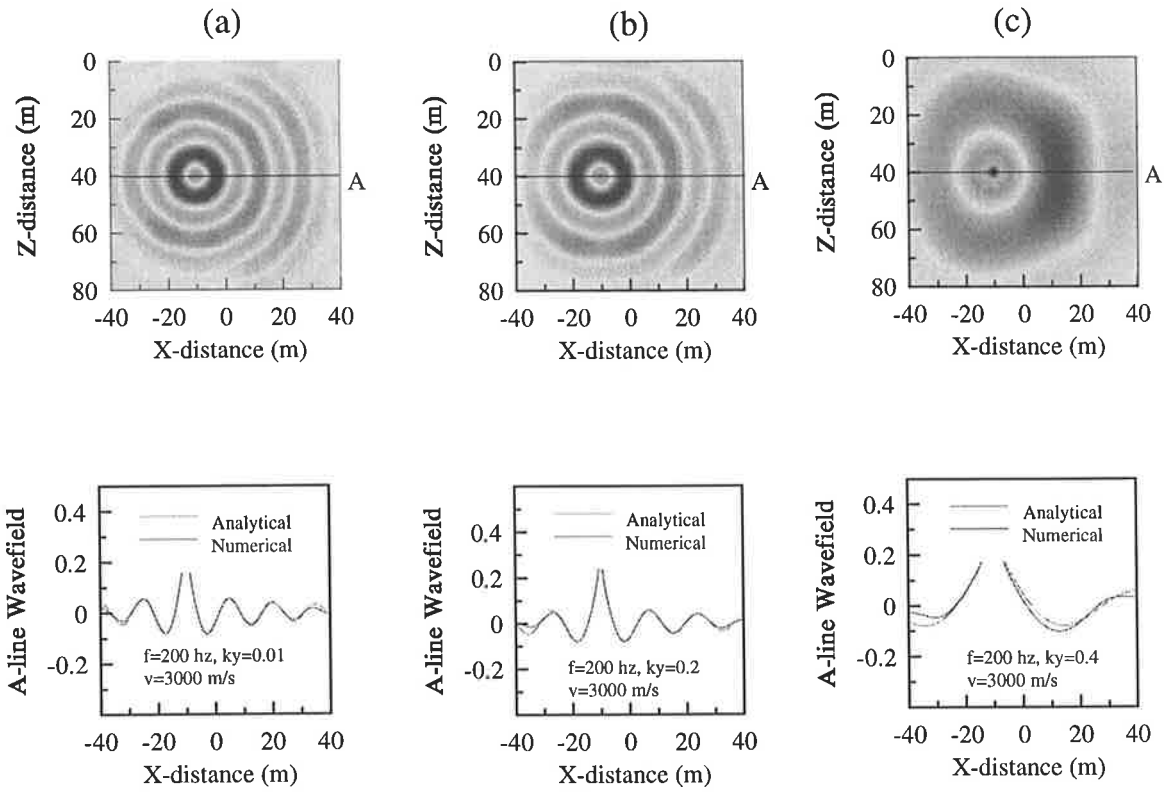

Fig.4-20 The k_y-domain solutions: (a) k_y=0.01, (b) k_y=0.2, (c) k_y=0.4 obtained with the damping method for a homogeneous model (c=3000 m/s) at f=200 Hz.

where C_0 (=0.0001–0.0015) is a positive constant. The quantity k_c is the maximum of the critical wavenumber values for the medium over the frequency range $f_1 \le f \le f_2$. Here a_1, a_2 and b_1, b_2 are four constants at the two extreme frequencies f_1 and f_2. The values a_1 and a_2 can be first determined at k_y=0 by conducting several numerical experiments, then b_1 and b_2 can be detected in successive experiments. In our case (f_1=100 Hz, f_2=300 Hz), C_0=0.0015, k_c=0.628 and the four constants are a_1=2.5, a_2=3.5, b_1=3.0 and b_2=1.0, respectively. It must be mentioned that *the form of equation (4.59) is not unique, because it may be a complicated function of frequency, wavenumber, width of the absorbing zone and the mesh size. But it should have common features in its variation with frequency f and wavenumber* k_y. Equation (4.59) indicates that for any frequency and a fixed width of absorbing zone, the coefficient decreases with an increase in k_y. This implies that the action of the damper is weakened in the

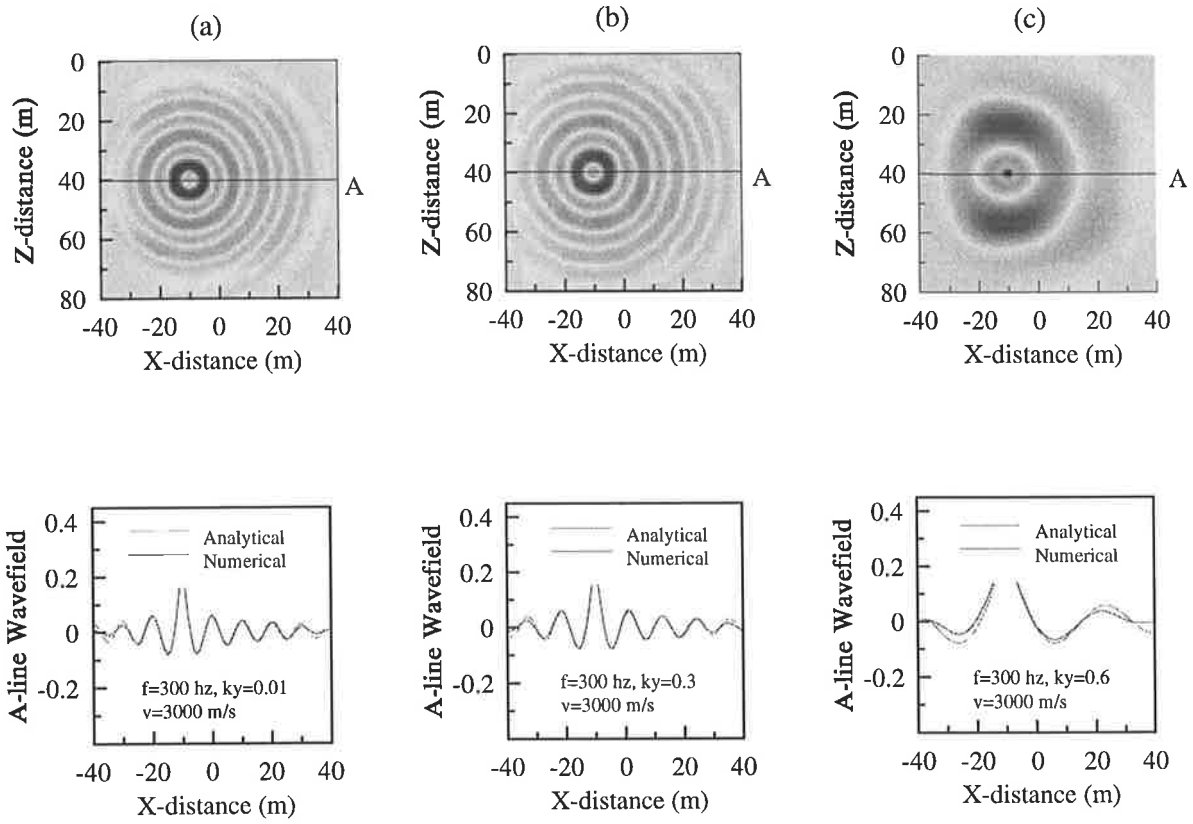

Fig.4-21 The k_y-domain solutions: (a) k_y=0.01, (b) k_y=0.3, (c) k_y=0.6 obtained with the damping method for a homogeneous model (c=3000 m/s) at f=300 Hz.

computation as k_y increases. This can be understood by the fact that with an increase in k_y up to k_c, the wavefield will be changed into an evanescent field (no vibration) for which a smaller damper (C_0 in equation (4.59)) is enough to absorb the energy. In our experience, the coefficient is important to the solution when $k_y < k_c$. If the coefficient is over- or under-estimated, the solution in the area of interest would be disturbed by a poor damper value. In general, the smaller the range of the frequency and the wavenumber and the bigger the mesh size, the easier it is to determine the four constants (a_1, a_2, b_1, b_2). The wider the absorbing zone, the smaller C_0. From these results, one can see that except for slight deviations within the absorbing zone, the numerical solutions in the k_y-domain fit well with the analytical solution, even close to the source location; the high frequency results in the absorbing zone seem better than the low frequency (see Fig.4-19 and Fig.4-21), and the small k_y-value (far away form critical

value) solutions are much better than the large k_y-value solutions (see Fig.4-19a,c; Fig.4-20a,c and Fig.4-21a,c). The differences may relate to the variation in the apparent wavelength in the (x,z)-plane, because the wavefield of a low frequency or larger k_y has a larger wavelength than that of a high frequency or a small k_y. So the cause may be that the fixed width of the absorbing zone is not large enough to attenuate the longer wavelength waves. Cao and Greenhalgh (1998) have shown for a 1-D model that the reflection coefficient of the absorbing zone decreases with an increase in the width of the absorbing zone, but it decreases much less rapidly in the long wavelength range than in the short wavelength range. So, it can be predicted that by taking a bigger mesh and a wider absorbing zone, the result will be improved, but it will increase the computation time.

Fig.4-22 gives the frequency-domain solutions for the homogeneous medium at three frequencies: 100 Hz, 200 Hz and 300 Hz, respectively. Comparison with the analytic solution is also made along the central line of the mesh. In these computations, 25 uniformly sampled k_y-components (from zero to 0.95 times the critical value) at each frequency are used to calculate the solutions. This figure shows that the numerical

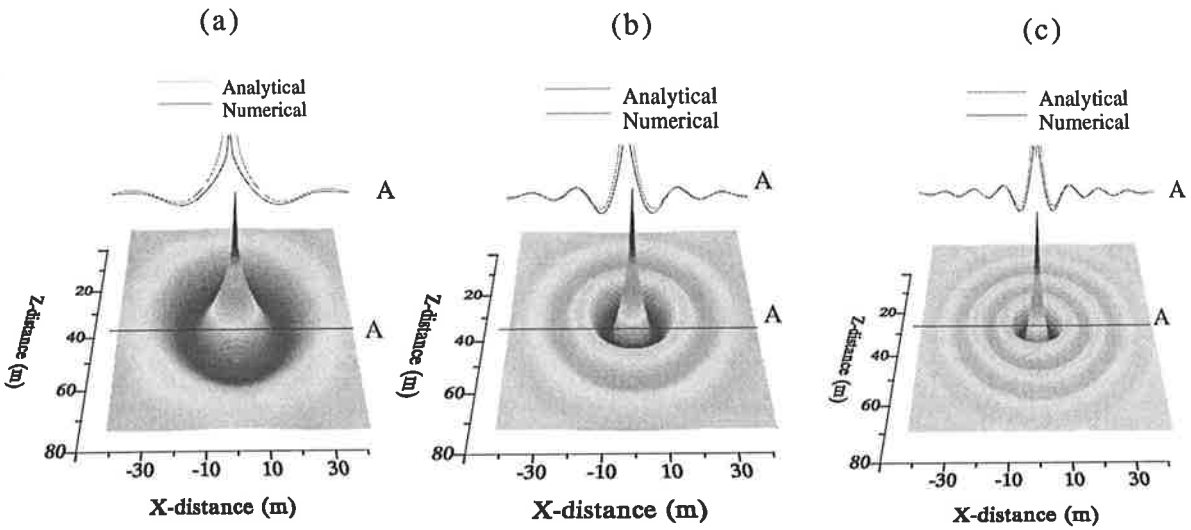

Fig.4-22 The frequency-domain solutions obtained with the damping method for the homogeneous medium (c=3000 m/s) model at three frequencies: (a) f=100 Hz, (b) f=200 Hz, (c) f=300 Hz.

solutions at 200 Hz and 300 Hz are very good approximations to the analytic solutions (Fig.4-22b,c) except there is a slight error in the area adjacent to the source. Although the error for 100 Hz, accumulated from the deviation in the wavenumber-domain, is somewhat larger than that for the higher frequencies (Fig.4-19c), it is still acceptable because it can be seen that the error has little effect on the time-domain solution for a crosshole surveying configuration (Fig.4-23).

Fig.4-23 shows the numerical and analytic solutions in the frequency range from 100 Hz to 300 Hz with 4 Hz sampling interval (Fig.4-23a,c) for a common-shot gather (Fig.4-23 b,d) for the cross-hole geometry: the δ-impulse source is located at (-10, 40) (Fig.4-19) and the receivers are distributed at 1 m spacing along the borehole over the depth range 20 m to 60 m (order No. runs from 0 to 41) at x=10 m. In this computation, 25 k_y-

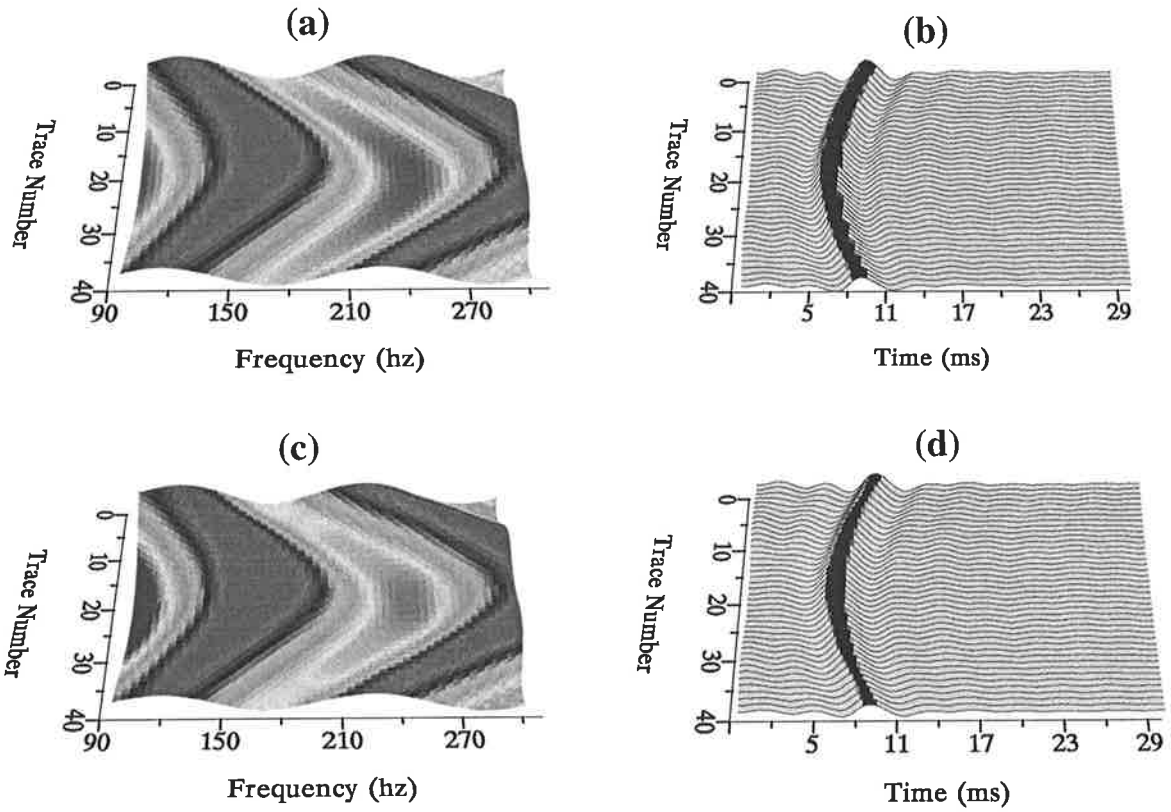

Fig.4-23 The frequency-domain solutions from 100 Hz to 300 Hz and the common-shot gather obtained with the damping method for a crosshole configuration in a homogeneous medium (c=3000 m/s): (a) and (b) are analytical solutions, (c) and (d) are numerical solutions.

components with uniform sampling and the discrete Hartley transform were employed. One can see that the numerical solutions and the seismograms are nearly the same as the analytic solutions in both the frequency- and time-domain.

To test the linear damper for inhomogeneous media modeling, the same embedded low velocity layer model used for testing the composite boundary-valued solution (Section 4.3) was also used here. Figures 4-24 and 4-25 show two k_y-domain solutions with two source locations at 100 Hz and 300 Hz respectively. Comparing these results with

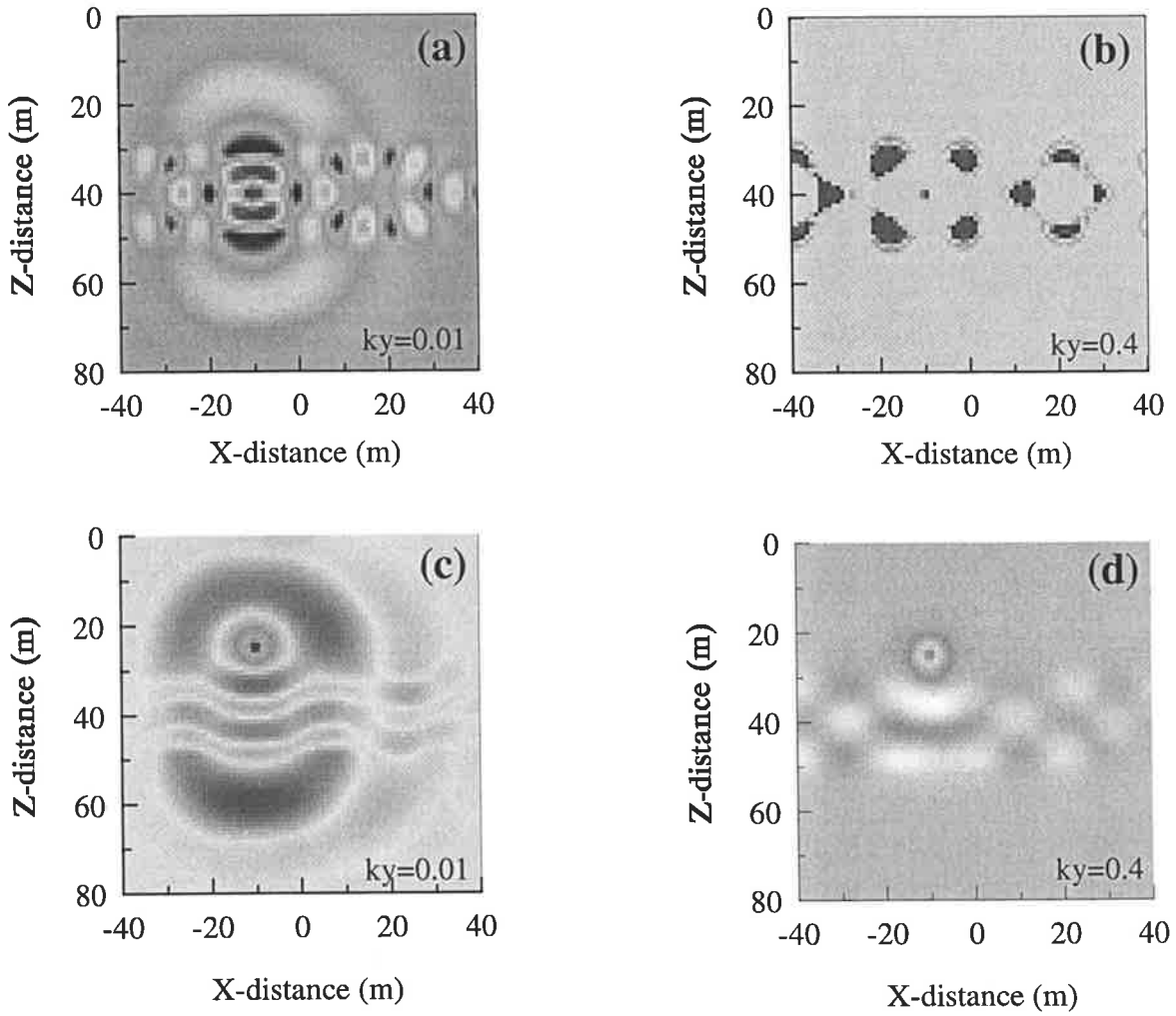

Fig.4-24 The k_y-domain solutions obtained with the damping method for the 2.5-D Green's function at f=100 Hz in the same model as in Fig.4-11. Diagrams (a) and (b) are the results for the source in the low-velocity zone; Diagrams (c) and (d) are the results for the source in the host medium. Two values of k_y are displayed (0.01 and 0.4), below and above the critical wavenumbers.

Fig.4-11 and Fig.4-12, one can find that the wavefield characteristics are very similar to the ones produced with the composite boundary-valued solution (see Fig.4-11 and Fig.4-12). The slight difference is due to the introduction of the absorbing zone where the wavefield is absorbed by the damper in Fig.4-24 and Fig.4-25.

Fig.4-26 gives the common-shot seismograms with the damping method for the cross-hole geometry shown in Fig.4-17a. In this computation, an expanded mesh (120×120 m^2) was used for minimizing the effect of the damper on the seismograms. One can see that the time-domain result is nearly same as one produced by the composite boundary-valued solution (Fig.4-17b).

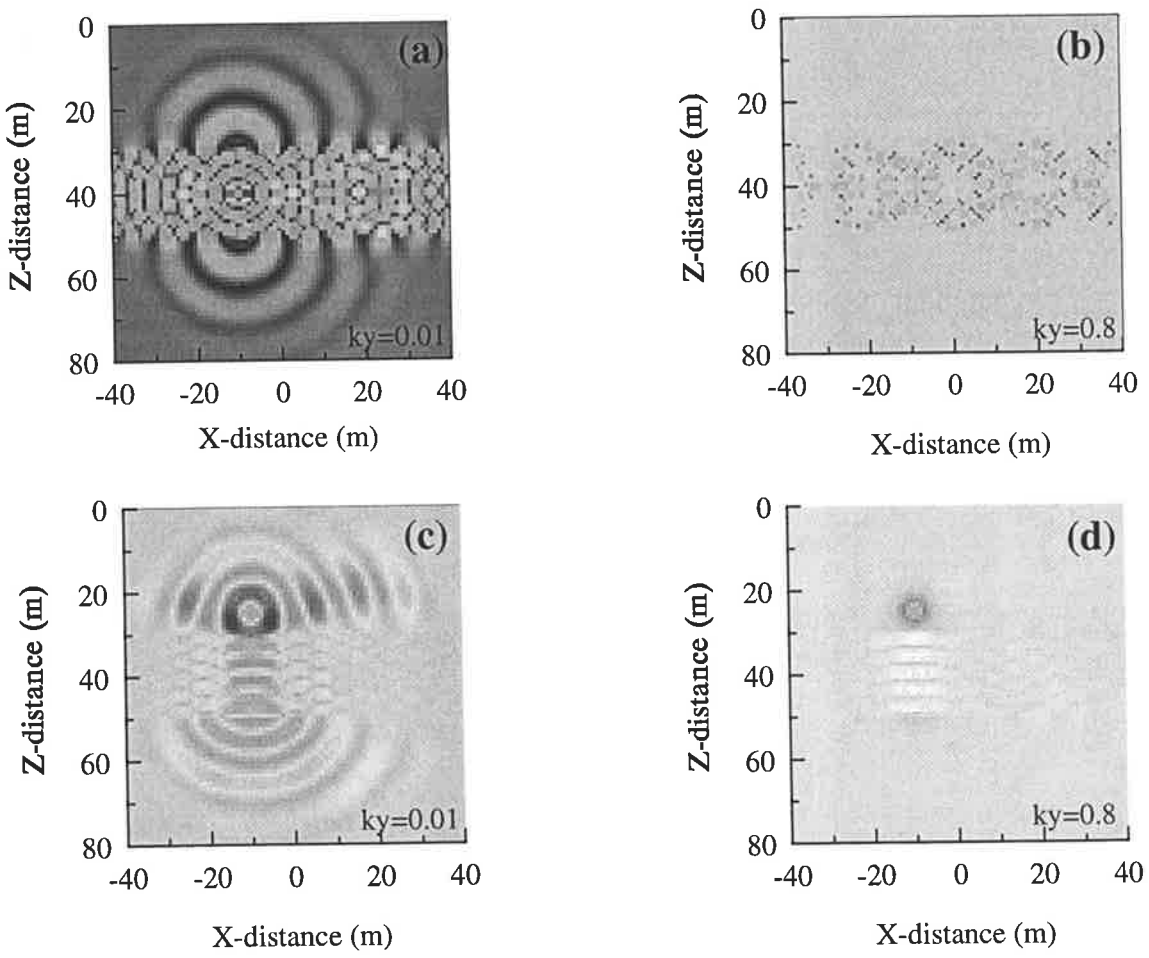

Fig.4-25 The k_y-domain solutions obtained with the damping method for the 2.5-D Green's function at a higher frequency of f=300 Hz for the same model as Fig. 4-24. Diagrams (a) and (b) are the results for the source in the low-velocity zone; Diagrams (c) and (d) are the results for the source in the host medium. Two values of k_y are displayed (0.01 and 0.8), below and above the critical wavenumbers.

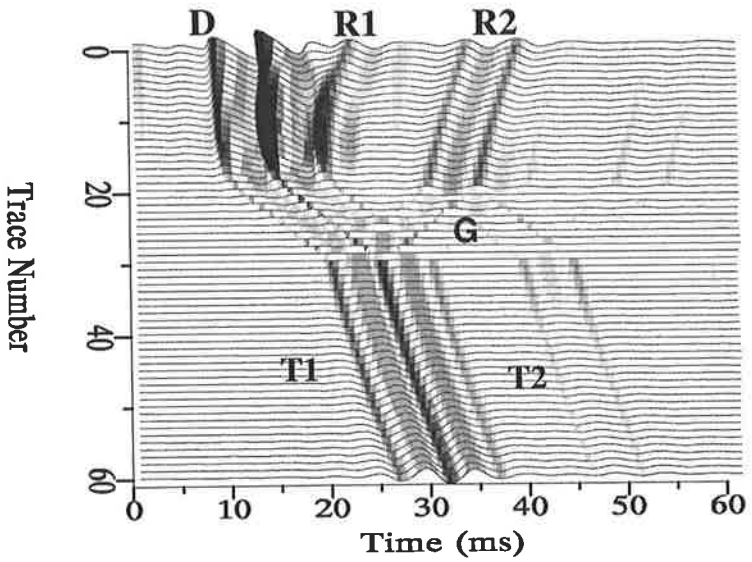

Fig.4-26 The crosshole common-shot synthetic seismograms obtained with the damping method. The model and surveying geometry are the same as shown in Fig.4-17a. The seismograms are nearly the same as the ones produced by the composite boundary-valued solution (Fig.4-17b). The following events can be seen: D is the direct wave, R1 and R2 are reflected waves, T1 and T2 are transmitted waves, and G is the waveguide arrival.

So far, we have described two new numerical algorithms of the FEM for 2.5-D acoustic wave modeling. Meanwhile, by comparison of the numerical results with analytic and semi-analytic solutions it has been shown that both of them can be applied to calculate the wave response (time-domain and frequency-domain) of a point-source in 2-D arbitrary media. *The composite boundary-valued solution requires much less computer memory and is a faster algorithm than the damping algorithm, because the introduction of the effective 2.5-D composite boundary condition enables us to employ a smaller element-mesh in the modeling. But one has to pay attention to the singularity point* ($k_y = k$) *of the boundary condition. The damping method is a simple and easy-to-build method, but the time-damper is important to the solution. A linear damper, as in 2-D time-domain modeling, can be chosen, but it depends on the frequency, the wavenumber and the width of the absorbing zone in the wavenumber-frequency domain modeling. An appropriate time-damper and a reasonable number of* k_y *samples can be determined in terms of the range of frequency and the critical values of the wavenumber of the media. These two methods can reach a satisfactory accuracy for computing the 2.5-D Green's function or wave response for arbitrary acoustic media in the frequency-domain and the time-domain.*

Chapter 5
Extension to 2.5-D Elastic Wave Modeling in the Frequency-Domain

In the previous chapter, we have presented two new FEM algorithms for 2.5-D acoustic wave modeling. This is the simplest case of elastic wave problems for which the shear modulus vanishes ($\mu = 0$, see Section 2.3). Obviously, such acoustic modeling methods are not able to deal with practical situations involving elastic media. With the developments in computer and electronic technology, digital 3-component (vector) seismograms are becoming more and more utilised in seismological research and seismic exploration. This requires the consideration of elastic (P and S) wave modeling and the need to develop some robust and economical numerical algorithms to compute the theoretical multicomponent seismic response so that we can analyse and understand the vector wavefield (triaxial sensor) observations and source dynamics, and implement some imaging techniques with real 3-D data. Unfortunately, full 3-D elastic wave modeling is at present still computationally very intensive due to the requirements of huge computer resources. As mentioned before, the 2.5-D approximation may allow us to calculate the 3-D response at 2-D computational costs. In recent times, many researchers have made considerable efforts to apply this approximation and develop some numerical techniques, such as the indirect boundary element method (IBEM, Pedersen et al., 1994, 1996), the boundary integral equation method (BIEM, Takenaka et al., 1996) and the velocity-stress finite difference method (FDM, Randall, 1991; Okamoto, 1994; Takenaka and Kennett, 1996a,b) for 2.5-D elastic wave modeling. Since they directly employ the analytic Green's function, the IBEM and BIEM are very efficient algorithms for models that consist of several homogeneous bodies, but they lose the ability to deal with more complicated elastic media. The FDM can handle an arbitrary elastic model, but so far most reports have been for modeling with the 2-D velocity-stress version of the FDM in the time-domain in which the FDM calculates all the time sequence of the wavefield parameters: velocities $\dot{\vec{u}}$ and stress τ_{ij} ($i,j=1,2,3$) and

finally obtains the 3-component seismograms. However, in reviewing the merits of modeling in the frequency-domain and the FEM, and for implementing the dynamic analysis of the 3-component spectral data, a flexible and efficient numerical algorithm for 2.5-D elastic wave modeling in the frequency-domain is still required. Unfortunately, there is little published on 2.5-D elastic wave modeling in the frequency-domain with the FEM. In this chapter, by applying the 2.5-D approximation and incorporating the FEM, we derive a numerical algorithm for 2.5-D elastic wave modeling in the frequency-domain. Our aim is to directly calculate the 3-components of the displacement vector (3-D wavefield) for 2-D arbitrary elastic media. Actually, the derivation may be considered a natural extension of our 2.5-D acoustic formulation to the 2.5-D elastic problem. It is structured into three subsections. Firstly, the displacement form of the 2.5-D elastic wave equation in the frequency-wavenumber domain is derived using the double Fourier transform. Secondly, the FEM formulation for obtaining the displacement vector of the elastic wavefield is performed and shows what kind of non-reflecting boundary condition is required. Finally, the boundary condition for 2.5-D elastic wave modeling is presented with the different approximations.

5.1 2.5-D Elastic Wave Equation

The equation of motion (2.11) includes the following three equations of the displacement vector $\vec{u}=(u,v,w)$:

$$\begin{cases} \rho\dfrac{\partial^2 u}{\partial^2 t}=\dfrac{\partial \tau_{11}}{\partial x}+\dfrac{\partial \tau_{21}}{\partial y}+\dfrac{\partial \tau_{31}}{\partial z}+f_1, \\ \rho\dfrac{\partial^2 v}{\partial^2 t}=\dfrac{\partial \tau_{12}}{\partial x}+\dfrac{\partial \tau_{22}}{\partial y}+\dfrac{\partial \tau_{32}}{\partial z}+f_2, \\ \rho\dfrac{\partial^2 w}{\partial^2 t}=\dfrac{\partial \tau_{13}}{\partial x}+\dfrac{\partial \tau_{23}}{\partial y}+\dfrac{\partial \tau_{33}}{\partial z}+f_3, \end{cases} \tag{5.1}$$

where ρ is density and f_i are body forces. The constitutive laws (2.15) gives six independent expressions for the stress tensor components:

$$\tau_{11}=(\lambda+2\mu)\frac{\partial u}{\partial x}+\lambda\left(\frac{\partial v}{\partial y}+\frac{\partial w}{\partial z}\right),$$

$$\tau_{12}=\mu\left(\frac{\partial u}{\partial y}+\frac{\partial v}{\partial x}\right),$$

$$\begin{aligned}
\tau_{13} &= \mu(\frac{\partial u}{\partial z}+\frac{\partial w}{\partial x}),\\
\tau_{22} &= (\lambda+2\mu)\frac{\partial v}{\partial y}+\lambda(\frac{\partial u}{\partial x}+\frac{\partial w}{\partial z}),\\
\tau_{23} &= \mu(\frac{\partial v}{\partial z}+\frac{\partial w}{\partial y}),\\
\tau_{33} &= (\lambda+2\mu)\frac{\partial w}{\partial z}+\lambda(\frac{\partial u}{\partial x}+\frac{\partial v}{\partial y}).
\end{aligned} \tag{5.2}$$

Making the 2.5-D approximation, which means all the elastic parameters (ρ,λ,μ) are the functions of only two coordinates (x,z), and taking the double Fourier transformation defined by the pair of formulas (forward and inverse transform):

$$\tilde{\bar{u}}(\omega,x,k_y,z)=\int_{-\infty}^{\infty}\int_{-\infty}^{\infty}\vec{u}(t,x,y,z)e^{-i(\omega t+k_y y)}dtdy, \tag{5.3}$$

$$\vec{u}(t,x,y,z)=\frac{1}{(2\pi)^2}\int_{-\infty}^{\infty}\int_{-\infty}^{\infty}\tilde{\bar{u}}(\omega,x,k_y,z)e^{i(\omega t+k_y y)}d\omega dk_y, \tag{5.4}$$

to equations (5.1) and (5.2) in the absence of the body force f_i, we have

$$\begin{cases}
\dfrac{\partial\bar{\bar{\tau}}_{11}}{\partial x}+\dfrac{\partial\bar{\bar{\tau}}_{13}}{\partial z}+ik_y\bar{\bar{\tau}}_{12}+\rho\omega^2\bar{\bar{u}}=0,\\
\dfrac{\partial\bar{\bar{\tau}}_{12}}{\partial x}+\dfrac{\partial\bar{\bar{\tau}}_{32}}{\partial z}+ik_y\bar{\bar{\tau}}_{22}+\rho\omega^2\bar{\bar{v}}=0,\\
\dfrac{\partial\bar{\bar{\tau}}_{13}}{\partial x}+\dfrac{\partial\bar{\bar{\tau}}_{33}}{\partial z}+ik_y\bar{\bar{\tau}}_{23}+\rho\omega^2\bar{\bar{w}}=0,
\end{cases} \tag{5.5}$$

and

$$\begin{aligned}
\bar{\bar{\tau}}_{11} &= (\lambda+2\mu)\frac{\partial\bar{\bar{u}}}{\partial x}+\lambda\frac{\partial\bar{\bar{w}}}{\partial z}+i\lambda k_y\bar{\bar{v}},\\
\bar{\bar{\tau}}_{12} &= i\mu k_y\bar{\bar{u}}+\mu\frac{\partial\bar{\bar{v}}}{\partial x},\\
\bar{\bar{\tau}}_{13} &= \mu(\frac{\partial\bar{\bar{u}}}{\partial z}+\frac{\partial\bar{\bar{w}}}{\partial x}),\\
\bar{\bar{\tau}}_{22} &= i(\lambda+2\mu)k_y\bar{\bar{v}}+\lambda(\frac{\partial\bar{\bar{u}}}{\partial x}+\frac{\partial\bar{\bar{w}}}{\partial z}),\\
\bar{\bar{\tau}}_{23} &= \mu\frac{\partial\bar{\bar{v}}}{\partial z}+i\mu k_y\bar{\bar{w}},\\
\bar{\bar{\tau}}_{33} &= (\lambda+2\mu)\frac{\partial\bar{\bar{w}}}{\partial z}+\lambda\frac{\partial\bar{\bar{u}}}{\partial x}+i\lambda k_y\bar{\bar{v}},
\end{aligned} \tag{5.6}$$

According to the definitions (5.3) and (5.4), the double Fourier transform can be accomplished by successive single Fourier transforms, i.e. equation (5.4) is equivalent to the following

$$\vec{\bar{u}}(\omega,x,y,z)=\frac{1}{2\pi}\int_{-\infty}^{\infty}\vec{\bar{\bar{u}}}(\omega,x,k_y,z)e^{ik_y y}dk_y\,, \tag{5.7}$$

$$\vec{u}(t,x,y,z)=\frac{1}{2\pi}\int_{-\infty}^{\infty}\vec{\bar{u}}(\omega,x,y,z)e^{i\omega t}d\omega. \tag{5.8}$$

The first equation shows that the frequency-domain solution $\vec{\bar{u}}(\omega,x,y,z)$ can be obtained by summation of the all k_y-components $\vec{\bar{\bar{u}}}(\omega,x,k_y,z)$ in the frequency-wavenumber domain and the second equation shows that the seismograms (time-domain solution) can be calculated from all of the frequency-domain solutions. So, the basic effort for the 2.5-D problem is to find the solution $\vec{\bar{\bar{u}}}(\omega,x,k_y,z)$ in the frequency-wavenumber domain.

Substituting equations (5.6) into equation (5.5), we obtain the governing equations of the displacement in the frequency-wavenumber domain:

$$\begin{cases}
\dfrac{\partial}{\partial x}[(\lambda+2\mu)\dfrac{\partial\bar{\bar{u}}}{\partial x}]+\dfrac{\partial}{\partial z}(\mu\dfrac{\partial\bar{\bar{u}}}{\partial z})+\dfrac{\partial}{\partial x}(\lambda\dfrac{\partial\bar{\bar{w}}}{\partial z})+\dfrac{\partial}{\partial z}(\mu\dfrac{\partial\bar{\bar{w}}}{\partial x})+ \\
\qquad +ik_y[\dfrac{\partial}{\partial x}(\lambda\bar{\bar{v}})+\mu\dfrac{\partial\bar{\bar{v}}}{\partial x}]+(\rho\omega^2-\mu k_y^2)\bar{\bar{u}}=0, \\
\dfrac{\partial}{\partial x}(\mu\dfrac{\partial\bar{\bar{v}}}{\partial x})+\dfrac{\partial}{\partial z}(\mu\dfrac{\partial\bar{\bar{v}}}{\partial z})+ik_y[\lambda\dfrac{\partial\bar{\bar{u}}}{\partial x}+\dfrac{\partial}{\partial x}(\mu\bar{\bar{u}})+\dfrac{\partial}{\partial z}(\mu\bar{\bar{w}})+ \\
\qquad +\lambda\dfrac{\partial\bar{\bar{w}}}{\partial z}]+[\rho\omega^2-(\lambda+2\mu)k_y^2]\bar{\bar{v}}=0, \\
\dfrac{\partial}{\partial x}(\mu\dfrac{\partial\bar{\bar{w}}}{\partial x})+\dfrac{\partial}{\partial z}[(\lambda+2\mu)\dfrac{\partial\bar{\bar{w}}}{\partial z}]+\dfrac{\partial}{\partial x}(\mu\dfrac{\partial\bar{\bar{u}}}{\partial z})+\dfrac{\partial}{\partial z}(\lambda\dfrac{\partial\bar{\bar{u}}}{\partial x})+ \\
\qquad +ik_y[\dfrac{\partial}{\partial z}(\lambda\bar{\bar{v}})+\mu\dfrac{\partial\bar{\bar{v}}}{\partial z}]+(\rho\omega^2-\mu k_y^2)\bar{\bar{w}}=0.
\end{cases} \tag{5.9}$$

Equation (5.9) is valid for arbitrary linear and isotopic elastic media (satisfying the constitutive laws (2.15)) and can be rewritten in matrix form as:

$$D_1\frac{\partial^2\vec{\bar{\bar{u}}}}{\partial^2 x}+D_2\frac{\partial^2\vec{\bar{\bar{u}}}}{\partial^2 z}+D_3\frac{\partial^2\vec{\bar{\bar{u}}}}{\partial x\partial z}+D_4\frac{\partial\vec{\bar{\bar{u}}}}{\partial x}+D_5\frac{\partial\vec{\bar{\bar{u}}}}{\partial z}+D_6\vec{\bar{\bar{u}}}=0\,, \tag{5.10}$$

where $D_1=diag(\gamma^2,\ \gamma^{-2},\ 1)$, $D_2=diag(1,\ \gamma^{-2},\ \gamma^2)$,

$$D_3 = \begin{pmatrix} 0 & 0 & \gamma^2-1 \\ 0 & 0 & 0 \\ \gamma^2-1 & 0 & 0 \end{pmatrix}, \quad D_4 = \begin{pmatrix} \dfrac{\partial(\lambda+2\mu)}{\mu\partial x} & ik_y(\gamma^2-1) & \dfrac{\partial\mu}{\mu\partial z} \\ ik_y(1-\gamma^{-2}) & \dfrac{\partial\mu}{(\lambda+2\mu)\partial x} & 0 \\ \dfrac{\partial\lambda}{\mu\partial z} & 0 & \dfrac{\partial\mu}{\mu\partial x} \end{pmatrix}, \tag{5.11}$$

$$D_5 = \begin{pmatrix} \dfrac{\partial\mu}{\mu\partial z} & 0 & \dfrac{\partial\lambda}{\mu\partial x} \\ 0 & \dfrac{\partial\mu}{(\lambda+2\mu)\partial z} & ik_y(1-\gamma^{-2}) \\ \dfrac{\partial\mu}{\mu\partial x} & ik_y(\gamma^2-1) & \dfrac{\partial(\lambda+2\mu)}{\mu\partial z} \end{pmatrix}, \quad D_6 = \begin{pmatrix} \beta & ik_y\dfrac{\partial\lambda}{\mu\partial x} & 0 \\ \dfrac{ik_y\partial\mu}{(\lambda+2\mu)\partial x} & \alpha & \dfrac{ik_y\partial\mu}{(\lambda+2\mu)\partial z} \\ 0 & ik_y\dfrac{\partial\lambda}{\mu\partial z} & \beta \end{pmatrix}.$$

where γ is Poisson's ratio, k_p and k_s are the wavenumbers for P- and S-wave propagation. They have the following forms:

$$\begin{aligned} &\gamma = v_p/v_s, \quad k_p = \omega/v_p, \quad k_s = \omega/v_s; \\ &\alpha = k_p^2 - k_y^2, \qquad \beta = k_s^2 - k_y^2, \end{aligned} \tag{5.12}$$

Here v_p and v_s are the compressional and shear wavespeeds respectively. Examining equation (5.11), all the matrix operators D_i (i=1,2,3,4,5,6) depend on the model parameters (ρ, v_p, v_s) and the wavenumber k_y when the frequency ω is given. From equations (5.9) or (5.10), one can see that *each equation contains all the terms of the three components:* $\overline{\overline{u}}$, $\overline{\overline{v}}$ *and* $\overline{\overline{w}}$. *This means that there exists coupling relationships among the three components of the displacement vector* $\overline{\overline{\overline{u}}}$. Setting the wavenumber to zero ($k_y = 0$) in equations (5.9) or (5.10), we obtain the well-known form of 2-D propagation in which there is no coupling between the components ($\overline{\overline{u}}$, $\overline{\overline{w}}$) and $\overline{\overline{v}}$, and the displacement vector $\overline{\overline{\overline{u}}}$ may be obtained by independently solving P-SV ($\overline{\overline{u}}$, $\overline{\overline{w}}$) and SH ($\overline{\overline{v}}$) mode wave equations. This difference between the 3-D and 2-D elastic wavefield should be taken into account in the interpretation of wavefield dynamics for practical seismic data.

5.2 The FEM Formulation

For 2.5-D elastic wave modeling in the frequency-wavenumber domain, like other numerical modeling, a limited computational range Ω and some boundary condition $B(\vec{\vec{u}}) = 0$ for the artificial boundary $\partial\Omega$ must be employed. So, the defined problem reduces to solving the boundary-valued problem:

$$\begin{cases} L(\omega,k_y,m)\vec{\vec{u}} = -\vec{\vec{f}}(\omega)\delta(r-r_s), & r,r_s \in \Omega, \\ B(\vec{\vec{u}}) = 0, & r \in \partial\Omega, \end{cases} \tag{5.13}$$

where $L(\omega,k_y,m) = D_1\dfrac{\partial^2}{\partial^2 x} + D_2\dfrac{\partial^2}{\partial^2 z} + D_3\dfrac{\partial^2}{\partial x\partial z} + D_4\dfrac{\partial}{\partial x} + D_5\dfrac{\partial}{\partial z} + D_6$ and $\vec{\vec{f}}(\omega)$ stands for a point source located at $r_s = (x_s,0,z_s)$. Here m=(ρ,λ,μ) represents the model parameters, all of which are functions of the x- and z-coordinate. According to equation (5.13), the Green's function tensor may be defined by setting the point-source $\vec{f}_i(\omega) = \sum_{k=1}^{3}\delta_{ij}\mathbf{e}_j$ (i=1,2,3), i.e.

$$\begin{cases} L(\omega,k_y,m)\vec{\vec{G}}_i = -\mathbf{e}_i\delta(r-r_s), & r,r_s \in \Omega, \\ B(\vec{\vec{G}}_i) = 0, & r \in \partial\Omega, \end{cases} \quad (i = 1,2,3) \tag{5.14}$$

where $\vec{\vec{G}}_i = (\vec{\vec{G}}_{i1},\vec{\vec{G}}_{i2},\vec{\vec{G}}_{i3})$ and $\mathbf{e}_i$ (i=1,2,3) are the unit vectors of the coordinate system. This equation states that the Green's function tensor is just the response of the wavefield to the three unit point sources at r_s. So, the displacement vector of any point-source is easily calculated by the Green's function tensor:

$$\vec{\vec{u}} = \vec{\vec{f}}(\omega)\cdot\vec{\vec{G}}\,. \tag{5.15}$$

To solve the defined differential problem, the FEM may be applied. For simplicity in the formulation, the Galerkin criterion (weighted residual solution) is used here, which means we seek the solution of the following integral equation (see Chapter 2):

$$\int_{\Omega} N_p(r)[L(\omega,k_y,m)\vec{\vec{u}} + \vec{\vec{f}}(\omega)\delta(r-r_s)]d\Omega = 0\,, \tag{5.16}$$

for any one of the shape functions: $\{N_p(r), p = 1,2,...,N_m\}$ and subject to the boundary condition in equation (5.13). Here r=(x,z) represents the coordinates in the (x,z)-plane and the displacement vector may be approached by the combinations of these shape functions, viz.

$$\vec{\vec{u}} = \begin{pmatrix} \bar{\bar{u}} \\ \bar{\bar{v}} \\ \bar{\bar{w}} \end{pmatrix} = \begin{pmatrix} \sum_{p}^{N_m} N_p(r)\bar{\bar{u}}_p \\ \sum_{p}^{N_m} N_p(r)\bar{\bar{v}}_p \\ \sum_{p}^{N_m} N_p(r)\bar{\bar{w}}_p \end{pmatrix}. \tag{5.17}$$

When the shape function has the property: $N_p(r_q) = \delta_{pq}$, $\vec{\vec{u}}_p = (\bar{\bar{u}}_p, \bar{\bar{v}}_p, \bar{\bar{w}}_p)$ is the discrete value of the displacement vector at the spatial point p.

According to equation (5.5), the condition given by equation (5.16) implies that the following three integral equations must be satisfied:

$$\begin{aligned}
&\int_{\Omega} N_p[\frac{\partial \bar{\bar{\tau}}_{11}}{\partial x} + \frac{\partial \bar{\bar{\tau}}_{13}}{\partial z} + ik_y \bar{\bar{\tau}}_{12} + \rho\omega^2 \bar{\bar{u}} + \bar{f}_1(\omega)\delta(r - r_s)]d\Omega = 0, \\
&\int_{\Omega} N_p[\frac{\partial \bar{\bar{\tau}}_{12}}{\partial x} + \frac{\partial \bar{\bar{\tau}}_{32}}{\partial z} + ik_y \bar{\bar{\tau}}_{22} + \rho\omega^2 \bar{\bar{v}} + \bar{f}_2(\omega)\delta(r - r_s)]d\Omega = 0, \\
&\int_{\Omega} N_p[\frac{\partial \bar{\bar{\tau}}_{13}}{\partial x} + \frac{\partial \bar{\bar{\tau}}_{33}}{\partial z} + ik_y \bar{\bar{\tau}}_{23} + \rho\omega^2 \bar{\bar{w}} + \bar{f}_3(\omega)\delta(r - r_s)]d\Omega = 0.
\end{aligned} \tag{5.18}$$

Integrating by parts, the above equations become:

$$\begin{aligned}
&\int_{\Omega}[(\lambda + 2\mu)\frac{\partial N_p}{\partial x}\frac{\partial \bar{\bar{u}}}{\partial x} + \mu\frac{\partial N_p}{\partial z}\frac{\partial \bar{\bar{u}}}{\partial z} + (\mu k_y^2 - \rho\omega^2)N_p\bar{\bar{u}}]d\Omega \\
&+ ik_y\int_{\Omega}[\lambda\bar{\bar{v}}\frac{\partial N_p}{\partial x} - \mu N_p\frac{\partial \bar{\bar{v}}}{\partial x}]d\Omega + \int_{\Omega}(\lambda\frac{\partial N_p}{\partial x}\frac{\partial \bar{\bar{w}}}{\partial z} + \mu\frac{\partial N_p}{\partial z}\frac{\partial \bar{\bar{w}}}{\partial x}) \\
&- \int_{\partial\Omega} N_p \cdot (\bar{\bar{\tau}}_{11}, \bar{\bar{\tau}}_{13}) \cdot \vec{n}d\Gamma = N_p(r_s)\bar{f}_1(\omega),
\end{aligned} \tag{5.19}$$

$$\begin{aligned}
&ik_y\int_{\Omega}(\mu\bar{\bar{u}}\frac{\partial N_p}{\partial x} - \lambda N_p\frac{\partial \bar{\bar{u}}}{\partial x})d\Omega \\
&+ \int_{\Omega}\{\mu(\frac{\partial N_p}{\partial x}\frac{\partial \bar{\bar{v}}}{\partial x} + \frac{\partial N_p}{\partial z}\frac{\partial \bar{\bar{v}}}{\partial z}) + [(\lambda + 2\mu)k_y^2 - \rho\omega^2]N_p\bar{\bar{v}}d\Omega \\
&+ ik_y\int_{\Omega}(\mu\bar{\bar{w}}\frac{\partial N_p}{\partial z} - \lambda N_p\frac{\partial \bar{\bar{w}}}{\partial z})d\Omega - \int_{\partial\Omega} N_p \cdot (\bar{\bar{\tau}}_{12}, \bar{\bar{\tau}}_{23}) \cdot nd\Gamma = N_p(r_s)\bar{f}_2(\omega),
\end{aligned} \tag{5.20}$$

$$\int_\Omega (\mu\frac{\partial\bar{\bar{u}}}{\partial z}\frac{\partial N_p}{\partial x}+\lambda\frac{\partial N_p}{\partial z}\frac{\partial\bar{\bar{u}}}{\partial x})d\Omega+ik_y\int_\Omega(\lambda\bar{\bar{v}}\frac{\partial N_p}{\partial z}-\mu N_p\frac{\partial\bar{\bar{v}}}{\partial z})d\Omega$$
$$+\int_\Omega[\mu\frac{\partial\bar{\bar{w}}}{\partial x}\frac{\partial N_p}{\partial x}+(\lambda+2\mu)\frac{\partial\bar{\bar{w}}}{\partial z}\frac{\partial\bar{\bar{w}}}{\partial z}+(\mu k_y^2-\rho\omega^2)N_p\bar{\bar{w}}]d\Omega \qquad (5.21)$$
$$-\int_{\partial\Omega}N_p\cdot(\bar{\bar{\tau}}_{13},\bar{\bar{\tau}}_{33})\cdot nd\Gamma=N_p(r_s)\bar{f}_3(\omega),$$

where n is the unit normal vector of the boundary $\partial\Omega$. Alternatively, substituting equation (5.9) for (5.16), we have another set of three integral equations:

$$\int_\Omega[(\lambda+2\mu)\frac{\partial N_p}{\partial x}\frac{\partial\bar{\bar{u}}}{\partial x}+\mu\frac{\partial N_p}{\partial z}\frac{\partial\bar{\bar{u}}}{\partial z}+(\mu k_y^2-\rho\omega^2)\bar{\bar{u}}]d\Omega$$
$$+\int_\Omega(\lambda\frac{\partial N_p}{\partial x}\frac{\partial\bar{\bar{w}}}{\partial z}+\mu\frac{\partial N_p}{\partial z}\frac{\partial\bar{\bar{w}}}{\partial x})d\Omega-ik_y\int_\Omega N_p[\mu\frac{\partial\bar{\bar{v}}}{\partial x}+\frac{\partial}{\partial x}(\lambda\bar{\bar{v}})]d\Omega \qquad (5.22)$$
$$-\int_{\partial\Omega}N_p(\nabla\bar{\bar{u}})^TB_1(\lambda+2\mu,\mu)\cdot\bar{n}d\Gamma-\int_{\partial\Omega}N_p(\nabla\bar{\bar{w}})^TB_2(\mu,\lambda)\cdot nd\Gamma=N_p(r_s)\bar{f}_1(\omega),$$

$$\int_\Omega\{\mu(\frac{\partial N_p}{\partial x}\frac{\partial\bar{\bar{v}}}{\partial x}+\frac{\partial N_p}{\partial z}\frac{\partial\bar{\bar{v}}}{\partial z})+[(\lambda+2\mu)k_y^2-\rho\omega^2]\bar{\bar{v}}\}d\Omega$$
$$-ik_y\int_\Omega N_p[\lambda\frac{\partial\bar{\bar{u}}}{\partial x}+\frac{\partial}{\partial x}(\mu\bar{\bar{u}})]d\Omega-ik_y\int_\Omega N_p[\lambda\frac{\partial\bar{\bar{w}}}{\partial z}+\frac{\partial}{\partial z}(\mu\bar{\bar{w}})]d\Omega \qquad (5.23)$$
$$-\int_{\partial\Omega}\mu N_p(\nabla\bar{\bar{v}})\cdot nd\Gamma=N_p(r_s)\bar{f}_2(\omega),$$

$$\int_\Omega[\mu\frac{\partial N_p}{\partial x}\frac{\partial\bar{\bar{w}}}{\partial x}+(\lambda+2\mu)\frac{\partial N_p}{\partial z}\frac{\partial\bar{\bar{w}}}{\partial z}+(\mu k_y^2-\rho\omega^2)\bar{\bar{w}}]d\Omega$$
$$+\int_\Omega(\mu\frac{\partial N_p}{\partial x}\frac{\partial\bar{\bar{u}}}{\partial z}+\lambda\frac{\partial N_p}{\partial z}\frac{\partial\bar{\bar{u}}}{\partial x})d\Omega-ik_y\int_\Omega N_p[\frac{\partial}{\partial z}(\lambda\bar{\bar{v}})+\mu\frac{\partial\bar{\bar{v}}}{\partial z}]d\Omega \qquad (5.24)$$
$$-\int_{\partial\Omega}N_p(\nabla\bar{\bar{w}})^TB_1(\mu,\lambda+2\mu)\cdot nd\Gamma-\int_{\partial\Omega}N_p(\nabla\bar{\bar{u}})^TB_2(\lambda,\mu)\cdot nd\Gamma=N_p(r_s)\bar{f}_3(\omega),$$

where
$$B_1(p,q)=\begin{pmatrix}p&0\\0&q\end{pmatrix},\quad B_2(p,q)=\begin{pmatrix}0&p\\q&0\end{pmatrix}. \qquad (5.25)$$

Actually, *the two sets of the integral equations (5.19)-(5.21) and (5.22)-(5.24) are completely equivalent and the differences are the expressions of the integrands of the boundary integrals. Reviewing the FEM theory, Galerkin' s solution can be obtained by solving the first set provided that the boundary stresses* ($\bar{\bar{\tau}}_{11}$, $\bar{\bar{\tau}}_{12}$, $\bar{\bar{\tau}}_{13}$, $\bar{\bar{\tau}}_{33}$, $\bar{\bar{\tau}}_{32}$) *effectively suppress the reflections from the boundary, or by solving the second set provided that some elastic wave absorbing boundary condition (ABC) is employed for the gradients* ($\nabla\bar{\bar{u}},\nabla\bar{\bar{v}},\nabla\bar{\bar{w}}$) *on the boundary.* So, the remaining problem of the

modeling is to look for some suitable boundary condition for the requirement of the boundary integrals.

5.3 Boundary Conditions

As a result of the above formulation, to simultaneously solve the integral equations (5.19)-(5.21) or (5.22)-(5.24), either the stress boundary condition: ($\bar{\bar{\tau}}_{11}$, $\bar{\bar{\tau}}_{12}$, $\bar{\bar{\tau}}_{13}$, $\bar{\bar{\tau}}_{33}$, $\bar{\bar{\tau}}_{32}$) or the gradient boundary condition $\nabla\bar{\bar{u}}=(\nabla\bar{\bar{u}},\nabla\bar{\bar{v}},\nabla\bar{\bar{w}})$ must be required for significantly attenuating the reflections from the artificial boundary. This is the key point for 2.5-D elastic wave modeling with the FEM. Unfortunately, all kinds of 2-D elastic wave ABC (Clayton and Engquist, 1977; Reynolds, 1978; Higdon, 1991) are not directly applicable to the 2.5-D problem, because they do not consider the coupling relation between the displacement component v and the others (u, w). Here, we are going to discuss the boundary condition for the 2.5-D elastic wave modeling in the frequency-wavenumber domain. We expect to develop a 2.5-D elastic wave absorbing boundary condition specially suitable for the FEM.

In general, due to the complexity of elastic wavefield, it is very difficult to derive an exact expression of the elastic wave ABC. A common way is to apply some approximation, e.g. using some viscous boundary condition (Lysmer and Roger, 1970), paraxial approximation of the wavenumber (Clayton and Engquist, 1977) or making an extension from acoustic wave analysis (Reynolds, 1978; Higdon, 1991). We still follow these approximations, but apply them to the 2.5-D elastic wave problem.

First of all, a simple 2.5-D viscous boundary condition is presented for the stress boundary condition according to the standard viscous boundary condition (Lysmer and Roger, 1970). Then, a formulation for the gradient boundary condition is performed by applying Clayton and Engquist's paraxial approximation with which one can see the difficulty in obtaining the 2.5-D elastic wave ABC. Finally, a form of the gradient boundary condition is derived by adapting Higdon (1991)'s formula to the 2.5-D elastic case and some results of our 2.5-D acoustic wave modeling. The viscous boundary condition, or adapted Higton's boundary condition, may be applied to the 2.5-D elastic wave modeling with the FEM.

(1) A Viscous Boundary Condition

Lysmer and Roger (1970) studied finite elastodynamic models for infinite media and suggested a standard viscous boundary condition for normal stress σ and tangential stress τ:

$$\begin{cases} \sigma = a\rho v_p \dot{u}_n, \\ \tau = b\rho v_s \dot{u}_t, \end{cases} \tag{5.26}$$

where a and b are constants. v_p and v_s are velocities of the P-wave and S-wave, $\dot{u}_n$ and $\dot{u}_t$ are normal and tangential particle velocities. Their numerical experiments showed that nearly perfect absorption was obtained in the range $\theta > 30^0$ for a=b=1. For P-wave incidence, the viscous boundary condition defined by a=b=1 is 98.5% effective in absorbing P-waves. The results for an incident S-wave are somewhat similar (about 95% effective in absorbing S-waves). This simple viscous boundary condition may be directly applied to our case.

Reviewing the boundary integrals in equations (5.19)-(5.21), the stress boundary condition ($\bar{\bar{\tau}}_{11}$, $\bar{\bar{\tau}}_{12}$, $\bar{\bar{\tau}}_{13}$, $\bar{\bar{\tau}}_{33}$, $\bar{\bar{\tau}}_{32}$) may be approximated by the viscous boundary condition. According to the standard viscous boundary condition (5.26), we may express the spectral forms for the stresses in the frequency-wavenumber domain:

$$\begin{aligned} \bar{\bar{\tau}}_{11} &= a\rho v_p i\omega \bar{\bar{u}}, \\ \bar{\bar{\tau}}_{12} &= b\rho v_s i\omega (\bar{\bar{v}} + \bar{\bar{u}})/2, \\ \bar{\bar{\tau}}_{13} &= b\rho v_s i\omega (\bar{\bar{w}} + \bar{\bar{u}})/2, \\ \bar{\bar{\tau}}_{32} &= b\rho v_s i\omega (\bar{\bar{v}} + \bar{\bar{w}})/2, \\ \bar{\bar{\tau}}_{33} &= a\rho v_p i\omega \bar{\bar{w}}. \end{aligned} \tag{5.27}$$

Here we set the tangential particle velocity to be the average value of the two tangential velocities on the boundary so that they satisfy the identity: $\tau_{ij} = \tau_{ji}$. Obviously, the viscous boundary conditions have simple forms and are easily incorporated with the FEM. Substituting the viscous boundary condition (5.27) for equations (5.19)-(5.21) and discretising the integral range, the 2.5-D elastic wave modeling becomes solvable with the FEM.

(2) Paraxial Approximation

Clayton and Enqguist (1977) first used the paraxial approximation to obtain the absorbing boundary condition for both 2-D acoustic and elastic wave modeling. Here we apply the approximation to the 2.5-D elastic wave case. To simplify the problem, we take the assumption that the elastic parameters (ρ,λ,μ) are constant on the local boundary. Equation (5.10) then becomes:

$$D_1'\frac{\partial^2\tilde{\tilde{u}}}{\partial^2 x}+D_2'\frac{\partial^2\tilde{\tilde{u}}}{\partial^2 z}+D_3'\frac{\partial^2\tilde{\tilde{u}}}{\partial x\partial z}+iD_4'\frac{\partial\tilde{\tilde{u}}}{\partial x}+iD_5'\frac{\partial\tilde{\tilde{u}}}{\partial z}+I\tilde{\tilde{u}}=0, \tag{5.28}$$

where I is the unit matrix and the other terms are given by:

$$D_1'=diag(\gamma^2/\beta,\ \ 1/\alpha\gamma^2,\ \ 1/\beta),\quad D_2'=diag(1/\beta,\ \ 1/\alpha\gamma^2,\ \ \gamma^2/\beta),$$

$$D_3'=\begin{pmatrix}0&0&\frac{\gamma^2-1}{\beta}\\0&0&0\\\frac{\gamma^2-1}{\beta}&0&0\end{pmatrix},\ D_4'=\begin{pmatrix}0&k_y(\frac{\gamma^2-1}{\beta})&0\\\frac{k_y}{\alpha}(1-\gamma^{-2})&0&0\\0&0&0\end{pmatrix},\ D_5'=\begin{pmatrix}0&0&0\\0&0&k_y(\frac{\gamma^2-1}{\alpha\gamma^2})\\0&k_y(\frac{\gamma^2-1}{\beta})&0\end{pmatrix}. \tag{5.29}$$

Clearly, one can see that all the coefficient matrices are real-valued with a given k_y and the governing equation (5.28) is much more complicated than the 2-D elastic case ($k_y=0$). According to equation (5.28) we have the dispersion equation of the elastic wave:

$$I=D_1'k_x^2+D_2'k_z^2+D_3'k_xk_z+D_4'k_x+D_5'k_z. \tag{5.30}$$

We apply the paraxial approximation of the wavenumber k_z:

$$Ik_z\approx\pm(C_1+C_2k_x+C_3k_x^2). \tag{5.31}$$

Here the sign '±' implies the directions of propagation of the elastic waves in the positive or negative z-direction. The matrices C_1, C_2 and C_3 should be real 3×3 matrices and determined by the dispersion equation (5.30). Inserting equation (5.31) into equation (5.30), we have

$$\begin{cases} D_2'C_1^TC_1 + D_5'C_1 = I, \\ D_2'(C_1^TC_2 + C_2^TC_1) + D_3'C_1 + D_4' + D_5'C_2 = 0, \\ D_1' + D_2'(C_1^TC_3 + C_2^TC_2 + C_3^TC_1) + D_3'C_2 + D_5'C_3 = 0, \\ D_2'(C_2^TC_3 + C_3^TC_2) + D_3'C_3 = 0, \\ D_2'C_3^TC_3 = 0, \end{cases} \tag{5.32}$$

which define the matrices C_1, C_2 and C_3. In terms of equation (5.31), the paraxial approximation ABC in the positive and negative z-directions may be obtained in the following form:

$$\frac{\partial \vec{\bar{u}}}{\partial z} = \pm[i(C_1 - C_3\frac{\partial^2}{\partial^2 x}) + C_2\frac{\partial}{\partial x}]\vec{\bar{u}}, \tag{5.33}$$

and the similar form in the positive and negative x-directions:

$$\frac{\partial \vec{\bar{u}}}{\partial x} = \pm[i(C_1 - C_3\frac{\partial^2}{\partial^2 z}) + C_2\frac{\partial}{\partial z}]\vec{\bar{u}}. \tag{5.34}$$

Combining these two expressions (5.33) and (5.34) one can obtain the gradient boundary condition $\nabla\vec{\bar{u}} = (\nabla\bar{\bar{u}}, \nabla\bar{\bar{v}}, \nabla\bar{\bar{w}})$ for solving equations (5.22)-(5.24). Unfortunately, it is very difficult to determine the coefficient matrices C_1, C_2 and C_3 from equation (5.32).

(3) The Modified Higdon Formula

In 2-D elastic wave modeling, Higdon (1991) proposed the following expression of the elastic wave ABC in the (x,z)-plane to suppress the reflections from the artificial boundary: x= positive constant:

$$[\cos(\alpha_p)\frac{\partial}{\partial t} + v_p\frac{\partial}{\partial x}][\cos(\alpha_s)\frac{\partial}{\partial t} + v_s\frac{\partial}{\partial x}]\begin{pmatrix} u_1 \\ u_3 \end{pmatrix} = 0, \tag{5.35}$$

where α_p and α_s are the two propagating angles of the P-wave and the S-wave towards the boundary. He pointed out that the first factor yields perfect absorption for a P-wave travelling at an angle $\pm\alpha_p$, and the second factor yields perfect absorption for an S-wave travelling at an angle $\pm\alpha_s$. A crucial point of the expression is that each factor has a very substantial value in helping absorb the other type of waves. This means that the first factor is oriented toward the P-wave but helps absorb the S-wave; the second factor is oriented toward the S-waves but helps the P-wave attenuation. The frequency-domain form of the ABC can be obtained from equation (5.35):

$$[ik_p\cos(\alpha_p)+\frac{\partial}{\partial x}][ik_s\cos(\alpha_s)+\frac{\partial}{\partial x}]\begin{pmatrix}\bar{u}_1\\ \bar{u}_3\end{pmatrix}=0\,. \tag{5.36}$$

Here $k_p=\omega/v_p$ and $k_s=\omega/v_s$ are the wavenumbers of P-waves and S-waves propagating in the (x,z)-plane. In 2.5-D acoustic wave modeling (see Chapter 4), it was shown that in the frequency-wavenumber domain the wavefield appears in propagation behaviour to have an apparent wavenumber $k_a=\sqrt{k^2-k_y^2}$ when $|k_y|<k$. It becomes an evanescent wavefield in which no vibration occurs when $|k_y|>k$. This fact may be used to make the following assumptions in the 2.5-D elastic case:

(1) in the frequency-wavenumber domain, the P-wave and the S-wave propagate with apparent wavenumbers k_{a1} and k_{a2} defined by:

$$k_{a1}=\begin{cases}\sqrt{k_p^2-k_y^2}, & (|k_y|<k_p),\\ \sqrt{k_s^2-k_y^2}, & (k_p<|k_y|<k_s),\end{cases} \tag{5.37}$$

$$k_{a2}=\sqrt{k_s^2-k_y^2}, \quad (|k_y|<k_s), \tag{5.38}$$

so that equation (5.36) may be adapted as follows:

$$[ik_{a1}\cos(\alpha_p)+\frac{\partial}{\partial x}][ik_{a2}\cos(\alpha_s)+\frac{\partial}{\partial x}]\vec{\bar{u}}=0\,; \tag{5.39}$$

(2) when $|k_y|>k_s>k_p$, the 2.5-D elastic wavefield appears as an evanescent field (no vibration) so that the same boundary condition as in the acoustic case (see equation (4.25)):

$$\frac{\partial\vec{\bar{u}}}{\partial n}+k_a'\vec{\bar{u}}=0, \qquad k_a'=\sqrt{k_y^2-k_s^2} \tag{5.40}$$

can be applied. Obviously, when $k_y=0$ the ABC (5.39) is the 2-D form (5.36). The boundary conditions (5.39) and (5.40) are direct extensions from Higdon's 2-D elastic wave ABC and the results of the 2.5-D acoustic wave modeling. The effectiveness of the boundary condition to absorbing the artificial reflections depends on the deviation between the two assumptions and the true situation (unknown). The boundary condition (5.39) can be rewritten in the general form for whole boundaries (see equation (4.16)):

$$\nabla\vec{\vec{u}} = -\begin{pmatrix} i(\nu_1 - \nu_2 \dfrac{\partial^2}{\partial^2 x}) \\ i(\nu_1 - \nu_2 \dfrac{\partial^2}{\partial^2 z}) \end{pmatrix} \vec{\vec{u}}, \qquad r \in \partial\Omega \tag{5.41}$$

where $$\nu_1 = \frac{k_{a1}k_{a2}\cos\alpha_p \cos\alpha_s}{k_{a1}\cos\alpha_p + k_{a2}\cos\alpha_s}, \quad \nu_2 = \frac{1}{k_{a1}\cos\alpha_p + k_{a2}\cos\alpha_s}. \tag{5.42}$$

Reviewing the usage of the similar form of the ABC (5.41) in 2.5-D acoustic wave modeling (see equation (4.16)), we see that it requires the high-order shape function for computation of the second derivatives in the boundary integrals, and more nodal points in each element. This will give rise to a large dimension in the system of linear equations. To avoid it, an alternative form of the elastic wave ABC is needed.

In fact, the elastic wave equation (5.10) should be satisfied on the boundary. So, according to it the second derivative operator in equation (5.41) can be expressed by

$$\begin{aligned} \frac{\partial^2}{\partial^2 x} &= -[D_1^{-1}D_2 \frac{\partial^2}{\partial^2 z} + D_1^{-1}D_3 \frac{\partial^2}{\partial x \partial z} + D_1^{-1}D_4 \frac{\partial}{\partial x} + D_1^{-1}D_5 \frac{\partial}{\partial z} + D_1^{-1}D_6], \\ \frac{\partial^2}{\partial^2 z} &= -[D_2^{-1}D_1 \frac{\partial^2}{\partial^2 x} + D_2^{-1}D_3 \frac{\partial^2}{\partial x \partial z} + D_2^{-1}D_4 \frac{\partial}{\partial x} + D_2^{-1}D_5 \frac{\partial}{\partial z} + D_2^{-1}D_6]. \end{aligned} \tag{5.43}$$

Substituting (5.43) into equation (5.41), we have the alternative form of the elastic wave ABC:

$$\nabla\vec{\vec{u}} = \begin{pmatrix} [i\nu_1 I + i\nu_2 D_1^{-1}(D_2 \dfrac{\partial^2}{\partial^2 z} + D_3 \dfrac{\partial^2}{\partial x \partial z} + D_4 \dfrac{\partial}{\partial x} + D_5 \dfrac{\partial}{\partial z} + D_6)]\vec{\vec{u}} \\ [i\nu_1 I + i\nu_2 D_2^{-1}(D_1 \dfrac{\partial^2}{\partial^2 z} + D_3 \dfrac{\partial^2}{\partial x \partial z} + D_4 \dfrac{\partial}{\partial x} + D_5 \dfrac{\partial}{\partial z} + D_6)]\vec{\vec{u}} \end{pmatrix}. \tag{5.44}$$

From the above discussion, *the viscous boundary condition (5.27) or the elastic wave ABC (5.44) may be available for solving equations (5.19)-(5.21) or equations (5.22)-(5.24).*

Chapter 6
Inversion Algorithms

The previous chapters have dealt with the so-called forward problem: to numerically calculate the physical response (electric potential or acoustic wavefield) at the observational spatial points in a known medium of specified resistivity or seismic wavespeed. In this chapter, we focus on the inverse problem: to apply inversion algorithms to reconstruct or image the medium structure from the observational data through solving the 2.5-D Helmholtz equations. In the mathematical literature, the inverse problem is formulated as an optimization scheme to find the model (medium structure) that gives the best fit between the synthetic and observed geophysical (and geological) data. There have been several excellent books, such as Menke (1984), Tarantola (1987), Scale and Smith (1994), Parker (1994), and many journal articles, which treat geophysical inversion. Here we present some practical and robust inversion algorithms that may be applied to resistivity and acoustic imaging. They are formulated in a general way for the well-known solutions, such as the Tikhonov regularization solution, the smoothest model solution (Occam's inversion) and the subspace solution. The relationships between the solutions based on the different algorithms are demonstrated. It will be seen that the Tikhonov regularization solution may be approached by three equivalent solutions (general iterative solution, iteratively linearized solution and Levenberg-Marquardt solution) and the conjugate gradient solution; the smoothest model solution is just a subset of the Tikhonov regularization solutions and the subspace solution may be obtained from the Tikhonov or the smoothest model solution by the model parameter transform. Generalized iterative algorithms based on the relations and the quadratic approximation are obtained for all the solutions.

6.1 Objective Functions

In a practical sense, geophysical data are incomplete due to the limited number of sampling points in both space and time. Furthermore, the observations are contaminated

by various forms of noise, so that the geophysical inverse problem is ill-posed (Kirsch, 1996). In other words, geophysical inversion has multiple solutions—in mathematics, there exist many models that produce a satisfactory fit with the observed data, which we must take into account. In order to find a physical model, which at least incorporates some plausible geological or physical features, rather than a pure mathematical solution, or to reduce the multiple solutions, criteria that describe what kind of model to seek and utilize á priori information on the model, must be first set up. Then a linear or non-linear optimization algorithm is employed to find the model subject to these criteria. Normally, the criteria are covered by an objective function or misfit function that gives a quantitative measure of the fit between the calculated and observed geophysical data and the roughness of the model variation. In general, the l_p (e.g. $p=1,2,\infty$)-norm may be used for the definition of the objective function. It has been realized that the usage of the l_1-norm has the merit of fitting most of the data and ignoring some the outliers of the data, but it leads to non-linear normal equations even if applied to a simple linear problem and is not uniquely solvable because of the loss of strict convexity of the norm (Scale and Smith, 1994). Among all the norms, the least squares (l_2) norm is the one that allows the easiest computations, so it is popularly applied to geophysical inversion.

There are two l_2-normed misfit functions for evaluating the goodness of fit in the data-space and the model-space, respectively:

$$\Phi_d(m) = \left\| W_d[d_o - d(m)] \right\|^2 = \frac{1}{2}\sum_{i,j}^{N_d}[d_{oi} - d_i(m)]W_{ij}^d[d_{oj} - d_j(m)], \tag{6.1}$$

$$\Phi_m(m) = \left\| W_m(m - m_0) \right\|^2 = \frac{1}{2}\sum_{i,j}^{N_m}(m_i - m_{0i})W_{ij}^m(m_j - m_{0j}). \tag{6.2}$$

where d_o and $d(m)$ are vectors of the observed and computed data. Here $d(m)$ may be calculated with the FEM method discussed in Chapters 3 and 4 when the model $m=\{m_1, m_2, \ldots, m_{N_m}\}$ is given. The quantities m and m_0 are the unknown (to be determined) and initial primary estimated model-parameter vectors, respectively. W_d and W_m are two symmetric matrices which are called weighting matrices of the data set and the model parameters respectively. They can contain á priori information that is very useful in reducing the multiple solutions.

In practice, there are several choices for W_d and W_m. For instance, W_d may take the form of a unit matrix $W_d = I$ (least squares) or an inverse covariance matrix of the data: $W_d = C_d^{-1}$ (generalized least squares, Tarantola and Valette, 1982). If each of the data points is independent of each other, C_d^{-1} has the simple form: C_d^{-1}=diag$\{ \sigma_{d_1}^{-2}, \sigma_{d_2}^{-2}, ..., \sigma_{d_N}^{-2} \}$ whose component σ_{d_i} is the standard deviation of the observed datum. The subscript N is the number of data. Also, in the generalized least squares formulation, W_m is an inverse covariance matrix of the model parameters, e.g. $W_m = C_m^{-1}$=diag $\{ \sigma_{m_1}^{-2}, \sigma_{m_2}^{-2}, ..., \sigma_{m_M}^{-2} \}$(Tarantola and Valette, 1982), where σ_{m_i} is the covariance of the model parameter. The subscript M is the number of model parameters. In order to get the smoothest model solution (the roughness of the model parameter variation is expected to be as small as possible), the first or second difference operator may be chosen for W_m, that is $W_m = \partial^T \partial$ or $W_m = (\partial\partial)^T (\partial\partial)$ (Menke, 1984; Constable et al., 1987), where ∂ is a difference operator of the first derivative. A general form for the 2-D smoothest model solution was suggested by Ellis and Oldenburg (1994a), who gave a combination of the difference operators: $W_m = \alpha_0 I + \alpha_x \partial_x^T \partial_x + \alpha_z \partial_z^T \partial_z$, where α_0, α_x and α_x are three constants, and ∂_x and ∂_z are the difference operators in the two spatial (x and z) directions. They have shown that the expression for W_m is very flexible and effective to produce a stable and smoothed solution by properly assigning these constants and the operators. Sasaki (1994) proposed a flatness filter operator for W_m, viz $W_m = C^T C$, where $C = \{C_1, C_2, ..., C_M\}^T$ is assembled in terms of a shifting four- or six-point flatness filter, e.g. $\Phi_{m_i} = C_i \delta\hat{m} = \alpha_i [\, \delta m_i^E + \delta m_i^W + \delta m_i^S + \delta m_i^N - 4\, \delta m_i \,]$. The superscripts E, W, S and N denote the four immediate neighbors of the ith model parameter and α_i is called the gradient amplifying factor.

The Tikhonov function defined in the general form (Tikhonov and Arsenin, 1977):

$$\Phi(m) = \Phi_d(m) + \lambda \Phi_m(m) \tag{6.3}$$

is often used in geophysical inversion as a popular objective function for an ill-posed problem. Here λ is termed a regularization parameter that depends on the error in d_o and is normally chosen before one starts to compute the regularization solution of equation (6.3). With the linearized approximation, it can be shown that the optimal

regularization parameter λ depends on the bounds of the exact solution, that are not known in advance (Kirsch, 1996). The parameter is also called the trade-off parameter or damping parameter, because it balances or "trades off" the two undesirable properties of the model: when λ is very large, $\Phi(m)$ effectively measures the model norm $\Phi_m(m)$; when λ is very small, $\Phi(m)$ is proportional to the data misfit $\Phi_d(m)$. The aim of the inversion is to find the model through solving the optimization problem with a given λ:

$$\min\{\Phi(m)\} = \min\{\Phi_d(m) + \lambda\Phi_m(m)\}. \tag{6.4}$$

For the specification $W_d = C_m^{-1}$, $W_d = C_m^{-1}$ and $\lambda = 1$, the solution of equation (4.4) is called the generalized least squares solution (Tarantola and Valette, 1982). Taking different weighting operators with $\lambda = 1$ yields the weighted least squares solution (Menke, 1984). In general, the solution of equation (6.4) may be called the Tikhonov regularization solution.

Alternatively, seeking the solution of the minimum model norm $\Phi_m(m)$, or the so-called smoothest model (Occam's inversion), has been shown to give a kind of stable, effective and flexible practical scheme in geophysical inversion (Constable et al, 1987; Ellis and Oldenburg, 1994a; Oldenburg and Li, 1994; LaBrecque et al., 1996). It involves solving

$$\begin{cases} \min\{\Phi_m(m)\}, \\ \Phi_d(m) = \chi_d, \end{cases} \tag{6.5}$$

instead of equation (6.4). Here χ_d is the desired tolerance of $\Phi_d(m)$. The basic motivation for seeking the smoothest model is that one does not wish to be misled by features that appear in the model but are not essential in matching the noise-contaminated observations. In other words, of all the possible solutions, we seek the simplest (smoothest) one in the sense that it requires the least spurious features not required by the data. This is the principle of parsimony (Occam's Razor). The advantage of inverting for a maximally smooth model is to obtain a specified model whose features we have chosen by taking the different weighting matrix W_m in the model norm $\Phi_m(m)$. This constrained optimization problem can be rewritten as an unconstrained optimization problem using a Lagrange multiplier λ^{-1}:

$$\min\{\Phi_m(m) + \lambda^{-1}[\Phi_d(m) - \chi_d]\}. \tag{6.6}$$

It should be noted that λ^{-1} is an unknown parameter and must be determined in solving equation (6.6), unlike the trade-off parameter λ, to be chosen in advance of attempting a solution of equation (6.4). So, the two optimization problems (6.4) and (6.6) theoretically give two kinds of model solutions and they are two popular objective functions in geophysical inversion. Although the objective functions define the different solutions, the relationships and the similarities between these practical algorithms will be examined in the following sections.

6.2 Tikhonov Regularization Solutions

To solve the optimization problem given by equation (6.4), two kinds of mathematical solvers may be chosen: (1) those based on global minimization search, such as the genetic algorithm (Stoffa and Sen, 1991) and the simulated annealing method (Dittmer and Szymansk, 1995), and (2) those based on the local minimization search, such as linearized iteration, steepest descent, conjugate gradient and quasi-Newton methods (Luenberger, 1984; Minoux, 1986). Although the global minimisation methods are independent of the initial model, they usually consume a large amount of computer time to find the final model in the random model space. They are at present applied only to some simple models (Chunduru et al., 1995, 1996) due to being very expensive for large scale model-parameter inversion like in crosshole resistivity and acoustic velocity imaging. So, they are not be pursued in this thesis. The second kind of inversion algorithms have been shown to offer the advantages in terms of the effectiveness and the computational efficiency to reconstruct the image of the model with a good initial guess (which can be drawn from the integration of basic geological and geophysical observations), and ease of incorporating the á prior information for reduction of the multiple solutions.

From the definitions of the data and model misfit functions (6.1) and (6.2), the objective function (6.3) is differentiable. The solution must be a stationary point:

$$\frac{\partial \Phi}{\partial m} = \frac{\partial \Phi_d}{\partial m} + \lambda \frac{\partial \Phi_m}{\partial m} = 0. \tag{6.7}$$

The derivatives can be obtained using the definitions (6.1) and (6.2):

$$\frac{\partial \Phi_d}{\partial m} = -(\frac{\partial d}{\partial m})^T W_d[d_o - d(m)], \tag{6.8}$$

$$\frac{\partial \Phi_m}{\partial m} = W_m(m - m_0), \tag{6.9}$$

where $\frac{\partial d}{\partial m}$ is the so-called sensitivity (Jacobian) matrix formed by the Fréchet derivative of the synthetic data $d(m)$ with respect to the model parameters. Substitution of equations (6.8) and (6.9) into equation (6.7), results in a nonlinear equation:

$$\lambda W_m(m - m_0) = (\frac{\partial d}{\partial m})^T W_d[d_0 - d(m)], \tag{6.10}$$

whose solution is difficult to directly find because of the non-linear nature of the function $d(m)$. So, an iterative scheme will be used to compute the solution.

(1) General Iterative Solution

A general iterative approach to the solution of equation (6.10) can be constructed in the following way. Firstly, by simultaneously adding the term $(\frac{\partial d}{\partial m})^T W_d(\frac{\partial d}{\partial m})(m - m_0)$ to both sides of equation (6.10) and assuming the operator W_m is invertible (this can be satisfied for most of the choices of W_m), it follows that

$$\begin{aligned}[W_m^{-1}(\frac{\partial d}{\partial m})^T W_d(\frac{\partial d}{\partial m}) + \lambda I](m - m_0) = \\ W_m^{-1}(\frac{\partial d}{\partial m})^T W_d\{[d_0 - d(m)] + (\frac{\partial d}{\partial m})(m - m_0)\},\end{aligned} \tag{6.11}$$

This is equivalent to equation (6.10), Next, considering the matrix $[W_m^{-1}(\frac{\partial d}{\partial m})^T W_d(\frac{\partial d}{\partial m}) + \lambda I]$ to be generally invertible (so long as an appropriate positive value is chosen for the parameter λ), equation (6.11) can be rewritten as follows:

$$\begin{aligned}m = m_0 + [W_m^{-1}(\frac{\partial d}{\partial m})^T W_d(\frac{\partial d}{\partial m}) + \lambda I]^{-g} \\ \cdot W_m^{-1}(\frac{\partial d}{\partial m})^T W_d\{[d_0 - d(m)] + (\frac{\partial d}{\partial m})(m - m_0)\};\end{aligned} \tag{6.12}$$

Finally, an iterative approach to solving equation (6.12) is suggested:

$$m_{k+1} = m_0 + [W_m^{-1}(\frac{\partial d}{\partial m})_k{}^T W_d (\frac{\partial d}{\partial m})_k + \lambda I]^{-g}$$
$$\cdot W_m^{-1}(\frac{\partial d}{\partial m})_k{}^T W_d \{[d_0 - d(m_k)] + (\frac{\partial d}{\partial m})_k (m_k - m_0)\}, \quad (6.13)$$
$$(k = 0,1,2,3,....).$$

where the superscript $-g$ denotes the general inverse matrix. By subtracting m_k from both sides of the above equation then combining the terms of $(m_k - m_0)$, an alternative form for the solution is obtained:

$$m_{k+1} = m_k + [W_m^{-1}(\frac{\partial d}{\partial m})_k{}^T W_d (\frac{\partial d}{\partial m})_k + \lambda I]^{-g}$$
$$\cdot W_m^{-1}(\frac{\partial d}{\partial m})_k{}^T W_d \{[d_0 - d(m_k)] - \lambda(m_k - m_0)\}, \quad (6.14)$$
$$(k = 0,1,2,3,.....).$$

The iterative formulae (6.13) and (6.14) are similar to the total inversion formula given by Tarantola and Valette (1982, where $W_d = C_d^{-1}$, $W_m = C_m^{-1}$ and $\lambda = 0$) and Tarantola (1984, eq. 17, where $W_d = C_d^{-1}$, $W_m = C_m^{-1}$ and $\lambda = 1$) who used the fixed-point theory for solving the generalized least-squares solution. They are also similar to the general solution developed by Carrion (1989, eq. 41, where $W_d = C_d^{-1}$ and $W_m = C_m^{-1}$) for unconstrained non-linear inversion. It will be shown in the next section that the general iterative procedure of Tarantola and Valatte, and that of Carrion are no more than an iteratively, linearized solution, or a specified steepest descent solution.

(2) Iteratively Linearized Solution

Another simple iterative scheme for the Tikhonov regularization solution is the iteratively linearized inversion. Taking the first order approximation of the synthetic data $d(m) \approx d(m_0) + (\frac{\partial d}{\partial m})_{m_0}(m - m_0)$, the stationary point equation (6.10) becomes

$$[(\frac{\partial d}{\partial m})_{m_0}{}^T W_d (\frac{\partial d}{\partial m})_{m_0} + \lambda W_m](m - m_0) = (\frac{\partial d}{\partial m})_{m_0}{}^T W_d [d_o - d(m_0)]. \quad (6.15)$$

A recurrence procedure is suggested in terms of equation (6.15),

$$[(\frac{\partial d}{\partial m})_k{}^T W_d (\frac{\partial d}{\partial m})_k + \lambda W_m](m_{k+1} - m_k) = (\frac{\partial d}{\partial m})_k^T W_d [d_o - d(m_k)], \quad (6.16)$$
$$(k = 0,1,2,3,.....).$$

In the simple case $W_d = I$ and $W_m = I$, the above equation reduces to the Levenberg-Marquardt's equation, which was widely used for resistivity inversion (Pelton et al, 1978; Tripp et al, 1984; Smith and Vozoff, 1984; Dabas et al, 1994). Another iteratively linearized approach may be chosen in the following way. Setting $m_{k+1} = m_k + \delta m_k$ and $d(m_{k+1}) \approx d(m_k) + (\frac{\partial d}{\partial m})_k^T (m_{k+1} - m_k)$ and replacing m with m_{k+1} in (6.10), we have the following form:

$$[(\frac{\partial d}{\partial m})_k{}^T W_d (\frac{\partial d}{\partial m})_k + \lambda W_m](m_{k+1} - m_k) = (\frac{\partial d}{\partial m})_k^T W_d [d_o - d(m_k)] - \lambda W_m (m_k - m_0), \quad (k = 0,1,2,3,.....). \tag{6.17}$$

There is a little difference between (6.16) and (6.17). The former gives the sequence of the solution whose variation $\|W_m(m_{k+1} - m_k)\|^2$ in each iteration is as small as possible under a given trade-off parameter; the latter yields another sequence of the solution and so on, all of which are not going to be far away form the initial guess m_0, because $\|W_m(m_k - m_0)\|^2$ for any k is kept as small as possible under the current trade-off with the data misfit function.

To solve equations (6.16) or (6.17), some linear-equation solvers, e.g. singular value decomposition (SVD) or the modified Gram-Schmidt method, can be employed. A better algorithm has been suggested for equation (6.16) (Lines and Treitel, 1984; Sasaki, 1994), because the solution of equation (6.16) is equivalent to the least squares solution of the following rectangular system:

$$\begin{bmatrix} \sqrt{W_d}(\frac{\partial d}{\partial m})_k \\ \sqrt{\lambda W_m} \end{bmatrix} (m_{k+1} - m_k) = \begin{bmatrix} \sqrt{W_d}[d_0 - d(m_k)] \\ 0 \end{bmatrix}, \tag{6.18}$$

whose solution is well-known to be more accurate than the solution obtained via equation (6.16). Equation (6.18) may be solved with SVD or conjugate gradient least squares (CGLS) (Scales and Smith, 1994), but it should be noted that to solve equation (6.18) with any matrix method, it is necessary to perform the operations on a large dimensional matrix when involving a large scale geophysical inversion; the size of the matrix in equation (6.18) is much larger than the original in equation (6.17).

If W_m is invertible, the coefficient matrix in equation (6.16) or (6.17) may be invertible too provided the parameter λ is a large enough positive value. So, we prefer to rewrite equations (6.16) and (6.17) in the following forms:

$$[W_m^{-1}(\frac{\partial d}{\partial m})_k{}^T W_d(\frac{\partial d}{\partial m})_k + \lambda I](m_{k+1} - m_k) = W_m^{-1}(\frac{\partial d}{\partial m})_k^T W_d[d_o - d(m_k)], \tag{6.19}$$

$$\begin{aligned}[W_m^{-1}(\frac{\partial d}{\partial m})_k{}^T W_d(\frac{\partial d}{\partial m})_k + \lambda I](m_{k+1} - m_k) = \\ W_m^{-1}(\frac{\partial d}{\partial m})_k^T W_d[d_o - d(m_k)] - \lambda(m_k - m_0),\end{aligned} \tag{6.20}$$

$$(k=1,2,\ldots,).$$

from which the following recurrence expressions are obtained:

$$m_{k+1} = m_k + [W_m^{-1}(\frac{\partial d}{\partial m})_k{}^T W_d(\frac{\partial d}{\partial m})_k + \lambda I]^{-g} W_m^{-1}(\frac{\partial d}{\partial m})_k^T W_d[d_o - d(m_k)], \tag{6.21}$$

$$\begin{aligned}m_{k+1} = m_k + [W_m^{-1}(\frac{\partial d}{\partial m})_k{}^T W_d(\frac{\partial d}{\partial m})_k + \lambda I]^{-g} \\ \cdot\{W_m^{-1}(\frac{\partial d}{\partial m})_k^T W_d[d_o - d(m_k)] + \lambda(m_0 - m_k)\},\end{aligned} \tag{6.22}$$

$$(k=1,2,\ldots,).$$

One can see that equation (6.22) is the same as the general iterative formula (equation (6.14)) for the Tikhonov regularization solution. It follows that the general iterative solution (including Tarantola and Valette's total inversion solution and Carrion's general solution) is just the iteratively linearized solution. Furthermore, Tarantola (1984) pointed out that the total inversion formula is a form of the steepest descent method, so the same conclusion can be recognized as the iteratively linearized inversion or the general iterative solution (6.22). That is, the solution (6.22) is equivalent to the one obtained by the steepest descent method

$$m_{k+1} = m_k - \hat{\alpha}_k \cdot \hat{g}_k, \tag{6.23}$$

whose maximum descent direction is given by the vector (equations (6.7), (6.8) and 6.9))

$$-\hat{g}_k = -W_m^{-1}(\frac{\partial \Phi}{\partial m})_k = W_m^{-1}(\frac{\partial d}{\partial m})_k^T W_d[d_o - d(m_k)] + \lambda(m_0 - m_k), \tag{6.24}$$

and the step lengths for correcting the model parameters are scaled by the operator:

$$\hat{\alpha}_k = [W_m^{-1}(\frac{\partial d}{\partial m})_k^T W_d (\frac{\partial d}{\partial m})_k + \lambda I]^{-g}. \tag{6.25}$$

So, the general form of steepest descent algorithm may be

$$m_{k+1} = m_k + \hat{\alpha}\{W_m^{-1}(\frac{\partial d}{\partial m})_k^T W_d [d_o - d(m_k)] + \lambda(m_0 - m_k)\}, \tag{6.26}$$

where $\hat{\alpha}$ is a step length scaling operator. A simple case is $\hat{\alpha} = \alpha I$, which may be determined by the line search for $\min\{\Phi(m_k - \alpha \hat{g}_k)\}$. In practical applications, the line search for the optimal step length α will consume much computer time in a large scale inversion procedure, because for checking the descent of the objective function with a guess α, it is necessary to implement the numerical calculation of the synthetic data $d(m_k - \alpha \hat{g}_k)$ many times to obtain the optimal step length. However, the step length scaling operator given by equation (6.25) efficiently finds the optimal value of the step length in the steepest descent method. Daily and Owen (1991) used the simple form of the formula ($\lambda = 0$, $W_d = I$ and $W_m = I$) in their experiments for crosshole resistivity tomography.

(3) Conjugate Gradient Solution (CGS)

The conjugate gradient method (CG) is a common optimization method which has better convergence properties than the iteratively linearized or steepest descent method (Luenberger, 1984, Chapter 8). Empirical evidence seems to favor the Polak-Ribiere method over other methods of the general type (Luenberger, 1984). The Polak-Ribiere algorithm is implemented by the following steps:

Step 1. Given m_0 compute $\hat{g}_0 = (\frac{\partial \Phi}{\partial m})_0 = (\frac{\partial d}{\partial m})_0^T W_d [d(m_0) - d_0]$ and set $\hat{d}_0 = -\hat{g}_0$;

Step 2. For *k=0, 1, 2, ...,n-1*:

(a) Set $m_{k+1} = m_k + \alpha_k \hat{d}_k$ where α_k minimizes $\Phi(m_k + \alpha_k \hat{d}_k)$,

(b) Compute $\hat{g}_{k+1} = (\frac{\partial \Phi}{\partial m})_{k+1} = (\frac{\partial d}{\partial m})_{k+1}^T W_d [d(m_{k+1}) - d_o] + \lambda W_m (m_{k+1} - m_0)$,

(c) Stopping test $|\hat{g}_{k+1}| \le \varepsilon$. If satisfied, END, otherwise unless *k=n-1*, set $\hat{d}_{k+1} = -\hat{g}_{k+1} + \beta_k \hat{d}_k$, where $\beta_k = \frac{(\hat{g}_{k+1} - \hat{g}_k)^T \hat{g}_{k+1}}{\hat{g}_k^T \hat{g}_k} = \frac{\hat{g}_{k+1}^T \hat{g}_{k+1}}{\hat{g}_k^T \hat{g}_k}$;

Step 3. Replace m_0 with m_n and go back to step 1.

Here n is the number of model parameters. The main advantages of the algorithm are the requirement of less memory storage for the three vectors $\hat{g}_{k+1}$, $\hat{g}_k$ and $\hat{d}_k$ and a significant reduction in computations since the Hessian matrix (the second derivative) does not need to be found in each iteration. The global convergence feature of the method is assured with a periodic restart after n iterations from the last point obtained. Recently, this algorithm has been applied to resistivity inversion (Ellis and Oldenburg, 1994b) and acoustic waveform tomography (Reiter and Rodi, 1996). The drawback of the algorithm is that it is still computer-time extensive because, like the steepest descent method, the search of the optimal step factor α_k is done in each iteration. But, the CG algorithm can be directly applied to solving a linear equation system like equations (6.14) and (6.16) (Luenberger, 1984). So, the search of the optimal α_k is not required for those solutions.

(4) Local-Search Quadratic Approximation CGS

If the objective function $\Phi(m)$ is twice differentiable and the second derivative of $\Phi(m)$ can be computed with reasonable computer time, the line search in the gradient method or the CG can be avoided in the manner of the quadratic approximation, because one can directly calculate the optimal step factor α_k with the second derivatives. Recalling the first derivatives of the misfit functions (6.8) and (6.9), the second derivatives can be obtained as follows:

$$\begin{aligned} \frac{\partial^2 \Phi_m}{\partial^2 m} &= W_m, \\ \frac{\partial^2 \Phi_d}{\partial^2 m} &= [(\frac{\partial d}{\partial m})^T W_d (\frac{\partial d}{\partial m}) + Q], \end{aligned} \tag{6.27}$$

$$\text{where} \quad \begin{cases} Q = (Q_{ij})_{n\times n}, \\ Q_{ij} = \sum_{l,k}^{N_d} [d_l(m) - d_{ol}] W_{lk}^d \dfrac{\partial^2 d_k}{\partial m_i \partial m_j}. \end{cases} \tag{6.28}$$

This forms the Hessian matrix of the objective function:

$$\frac{\partial^2 \Phi}{\partial^2 m} = [(\frac{\partial d}{\partial m})^T W_d (\frac{\partial d}{\partial m}) + Q] + \lambda W_m. \tag{6.29}$$

Using the quadratic approximation

$$\Phi(m) \approx \Phi(m_k) + (\frac{\partial \Phi}{\partial m})_k^T (m - m_k) + \frac{1}{2}(m - m_k)^T (\frac{\partial^2 \Phi}{\partial^2 m})_k (m - m_k), \qquad (6.30)$$

and substituting the recurrence formula $m = m_k + \alpha_k \hat{d}_k$ into the above, then setting the derivative with respect to α_k to zero, we obtain the optimal step factor:

$$\alpha_k = \frac{-(\frac{\partial \Phi}{\partial m})_k^T \hat{d}_k}{\hat{d}_k^T (\frac{\partial^2 \Phi}{\partial^2 m})_k \hat{d}_k} = \frac{\hat{r}_k^T \hat{r}_k}{(\hat{q}_k^T W_d \hat{q}_k + \hat{d}_k^T Q_k \hat{d}_k + \lambda \hat{d}_k^T W_m \hat{d}_k)}, \qquad (6.31)$$

where $\hat{q}_k = (\frac{\partial d}{\partial m})_k \hat{d}_k$, $\hat{r}_k = -(\frac{\partial \Phi}{\partial m})_k$ and we have used the identity $\hat{r}_k^T \hat{d}_k = \hat{r}_k^T (\hat{r}_k + \beta_{k-1} \hat{d}_{k-1}) = \hat{r}_k^T \hat{r}_k$ due to the conjugate property $\hat{r}_k^T \hat{d}_{k-1} = 0$. Using the approximation (6.30) again, we have the expression:

$$(\frac{\partial \Phi}{\partial m})_{k+1} = (\frac{\partial \Phi}{\partial m})_k + \alpha_k (\frac{\partial^2 \Phi}{\partial^2 m})_k \hat{d}_k$$

or $$\hat{r}_{k+1} = \hat{r}_k - \alpha_k [(\frac{\partial d}{\partial m})_k^T W_d \hat{q}_k + (Q_k + \lambda W_m) \hat{d}_k], \qquad (6.32)$$

and the parameter β_k in the Polak-Ribiere algorithm becomes

$$\beta_k = \frac{\hat{r}_{k+1}^T \hat{r}_{k+1}}{\hat{r}_k^T \hat{r}_k}. \qquad (6.33)$$

Replacing the formulas of α_k, $\hat{g}_{k+1}$ and β_k with equations (6.31), (6.32) and (6.33) in the Polak-Ribiere algorithm, the quadratic approximation CG algorithm reduces to the following steps:

Step 1. Given m_0 compute $\hat{r}_0 = -\hat{g}_0 = (\frac{\partial d}{\partial m})_0^T W_d [d_0 - d(m_0)]$ and set $\hat{d}_0 = \hat{r}_0$;

Step 2. For *k=0, 1, 2, ...,n-1*:

(a) Calculate $\hat{q}_k = (\frac{\partial d}{\partial m})_k \hat{d}_k$,

$$\alpha_k = \frac{\hat{r}_k^T \hat{r}_k}{(\hat{q}_k^T W_d \hat{q}_k + \hat{d}_k^T Q_k \hat{d}_k + \lambda \hat{d}_k^T W_m \hat{d}_k)} \text{ and}$$

$m_{k+1} = m_k + \alpha_k \hat{d}_k$;

(b) Compute $\hat{r}_{k+1} = \hat{r}_k - \alpha_k [(\frac{\partial d}{\partial m})_k^T W_d \hat{q}_k + (Q_k + \lambda W_m) \hat{d}_k]$;

(c) Stopping test $|\hat{r}_{k+1}| \le \varepsilon$. If satisfied, END, otherwise unless $k=n-1$, set $\hat{d}_{k+1} = \hat{r}_{k+1} + \beta_k \hat{d}_k$, where

$$\beta_k = \frac{\hat{r}_{k+1}^T \hat{r}_{k+1}}{\hat{r}_k^T \hat{r}_k};$$

Step 3. Replace m_0 with m_n and go back to step 1.

An attractive feature of the algorithm is that no line searching is required at any iterative stage. Also the algorithm converges in a finite number of steps for a quadratic problem (Minoux, 1986). The undesirable feature is that the method requires the evaluation of Q_k, which involves the calculation of the second derivative of the data $\frac{\partial^2 d}{\partial m_i \partial m_j}$ (see equation (6.28)). Therefore, a fast and efficient scheme to approach the second derivative must be employed in the algorithm, otherwise, the algorithm still spend much computer time on such computations. A practical method to compute the second derivative $\frac{\partial^2 d}{\partial m_i \partial m_j}$ for the resistivity case and the 2.5-D acoustic wave problems are discussed in Chapter 7.

Note that in the above procedure the first and second derivatives of the objective function $(\frac{\partial \Phi}{\partial m})_k$ and $(\frac{\partial^2 \Phi}{\partial^2 m})_k$ need to be updated by the computation of $(\frac{\partial d}{\partial m})_k$ and $(\frac{\partial^2 d}{\partial m_i \partial m_j})_k$ during each iteration. This means that the algorithm searches for the minimum of the objective function in the global model-space with the quadratic approximation and the local minimum is directly obtained by the optimal step length α_k in the conjugate direction, viz. $m_{k+1} = m_k + \alpha_k \hat{d}_k$. The Hessian matrix $(\frac{\partial^2 \Phi}{\partial^2 m})_k$ must be positive definite at any kth iteration so as to successively find the local minimum sequence approaching the global minimum. In exact terms, this algorithm may be called the global-search quadratic approximation CG. Strictly speaking, if the objective function deviates from a standard quadratic or if there is violation of the positive definite property, the algorithm is not globally convergent in this form. On the other hand, in practical applications the positive definite property is unknown in advance. Examination of the expression for the Hessian matrix (6.29) shows that appropriate

choices for the regularization parameter λ and the operators W_d and W_m may be helpful to reach the condition. At the very least, this is expected to improve the property of the Hessian matrix so that the algorithm converges to the global minimum. To this end, another iterative scheme with the quadratic approximation is outlined below. That is, to improve the property of the Hessian matrix by proper choice of W_d, W_m and λ so as to successively find the local minimum sequence, we proceed as follows: $\{m_1^*, m_2^*, m_3^* \ldots\}$ satisfying $\Phi(m_1^*) > \Phi(m_2^*) > \Phi(m_3^*) \ldots$ with the quadratic approximation until a desired approach to the global minimum is obtained. We search the local minimum around m_l^* (an instantaneous guess for the model), using the quadratic approximation (6.30) again and set $\frac{\partial \Phi}{\partial m} = 0$. The local minimum becomes the solution of the following equation:

$$\begin{aligned} \{W_m^{-1}[(\frac{\partial d}{\partial m})_{m_l^*}^T W_d (\frac{\partial d}{\partial m})_{m_l^*} + Q_{m_l^*}] + \lambda I\}(m - m_l^*) = \\ W_m^{-1}(\frac{\partial d}{\partial m})_{m_l^*}^T W_d [d_0 - d(m_l^*)] - \lambda(m_l^* - m_0), \end{aligned} \tag{6.34}$$

from which one can see that the coefficient matrix on the RHS can be regularized by an appropriate λ and it is invertible for the solution m_{l+1}^*:

$$\begin{aligned} m_{l+1}^* = m_l^* + \{W_m^{-1}[(\frac{\partial d}{\partial m})_{m_l^*}^T W_d (\frac{\partial d}{\partial m})_{m_l^*} + Q_{m_l^*}] + \lambda I\}^{-g} \cdot \\ \{W_m^{-1}(\frac{\partial d}{\partial m})_{m_l^*}^T W_d [d_o - d(m_l^*)] + \lambda(m_0 - m_l^*)\}, \end{aligned} \quad (l=0,1,2,\ldots). \tag{6.35}$$

This is nothing else but the pure form of iterative Newton's method (Minoux, 1986). Comparing equation (6.35) with the general iterative solution (6.14) or the iteratively linearized solution (6.22), one can conclude that the local-search quadratic approximation solution (6.35) is a natural extension of the iteratively linearized solution or the general iterative solution in which the effect of the Hessian matrices Q associated with the second derivative of the data $\frac{\partial^2 d_l}{\partial m_i \partial m_j}$ is considered. Consequently, the expression (6.35) is the general form of the l_2-norm Tikhonov regularization solution.

Any matrix method to calculate the inverse matrix in equation (6.35), such as SVD or LU decomposition algorithm, may be employed. But the matrix algorithms will consume much computer time and memory when the dimension of the matrix is very large. Actually, the local minimum m_{l+1}^* (solution of equation (6.34)) can be found by applying the quadratic approximation CG and the procedure becomes:

Step 1. Start at m_0^*, for $l=0,1,2,\ldots l_{\max}$ and compute $\hat{r}_0 = -\hat{g}(m_l^*) = W_m^{-1}(\frac{\partial d}{\partial m})_{m_0^*}^T W_d [d_0 - d(m_l^*)] + \lambda(m_0 - m_l^*)$ and set $\hat{d}_0 = \hat{r}_0$;

Step 2. For $k=0, 1, 2, \ldots, k_{\max}$

(a) Calculate $\alpha_k = \dfrac{\hat{r}_k^T \hat{r}_k}{(\hat{q}_k^T W_d \hat{q}_k' + \hat{d}_k^T W_m^{-1} Q_{m_l^*} \hat{d}_k + \lambda \hat{d}_k^T \hat{d}_k)}$ and

$$\hat{m}_{k+1} = \hat{m}_k + \alpha_k \hat{d}_k,\ \hat{q}_k = (\frac{\partial d}{\partial m})_{m_l^*} (W_m^{-1})^T \hat{d}_k,\ \hat{q}_k' = (\frac{\partial d}{\partial m})_{m_l^*} \hat{d}_k;$$

(b) Compute $\hat{r}_{k+1} = \hat{r}_k - \alpha_k [W_m^{-1}(\frac{\partial d}{\partial m})_{m_l^*}^T W_d \hat{q}_k' + W_m^{-1} Q_{m_l^*} + \lambda I)\hat{d}_k]$;

(c) Test $|\hat{r}_{k+1}| \le \varepsilon$. If satisfied, set $m_{l+1}^* = \hat{m}_{k+1}$ and go to *step 3*, otherwise set $\hat{d}_{k+1} = \hat{r}_{k+1} + \beta_k \hat{d}_k$, where $\beta_k = \dfrac{\hat{r}_{k+1}^T \hat{r}_{k+1}}{\hat{r}_k^T \hat{r}_k}$, go to *step 2* for next k;

Step 3. Stopping test $|\Phi(m_{l+1}^*)| < \varepsilon$, if satisfied, stop the procedure, otherwise, go back to *step 1* for next l.

Here $l_{\max}$ and $k_{\max}$ are the maximal iterations for l and k respectively. The main difference between this algorithm and the quadratic approximation CG is that the derivatives $(\frac{\partial d}{\partial m})_{m_l^*}$ and $(\frac{\partial^2 d}{\partial m_i \partial m_j})_{m_l^*}$ are not updated with the iteration k because only the local minimum m_{l+1}^* is searched in the neighborhood of m_l^*. To discriminate this algorithm from the other we call it the *local-search quadratic approximation CGS*. The convergence of the algorithm depends upon whether the local minimum sequence:

$\{m_1^*, m_2^*, m_3^* \ldots\}$ satisfying $\Phi(m_1^*) > \Phi(m_2^*) > \Phi(m_3^*) \ldots > \Phi(m_{l_{\max}}^*)$ is successfully found or not. Fortunately, the regularization parameter λ enables us to control the procedure, because an appropriate positive value of the regularization parameter λ makes the coefficient matrix invertible so that it has only one non-zero solution to be found. The parameter can be determined by the several tests so that the misfit function $\Phi(m_l^*)$ *(l=0,1,2,...)* keeps decreasing as the iterations proceed. If the effect of $Q_{m_l^*}$ is ignored in the algorithm, the solution reverts to the general iterative solution or the iteratively linearized solution, because equation (6.34) becomes equation (6.14) or (6.17). The main advantages of the algorithm are easy control of the convergence by λ and the computational efficiency for obtaining the local minimum sequence. A simple form ($W_m^{-1} = C_m$, $W_d = C_m^{-1}$ and $Q_{m_l^*} \approx 0$) of the algorithm has been applied to non-linear seismic travel-time tomography by Zhou et al. (1992), who demonstrated the effectiveness and the computational efficiency of the algorithm for a large, sparse matrix inverse problem.

The connections or inter-relationships of the above Tikhonov regularization solutions are given in Fig.6-1. The diagram shows that the *three solutions—general iterative, iteratively linearized and Levenberg-Marquardt solutions are equivalent to each other,*

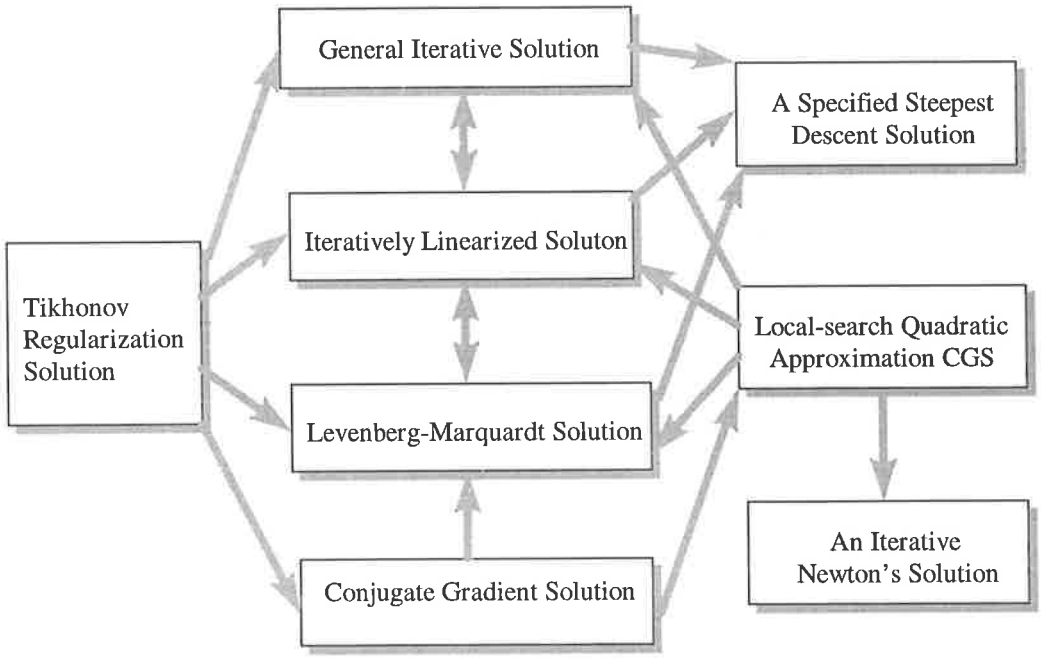

Fig.6-1 Illustration of the inter-relationships of the Tikhonov regularization solutions.

and all of them may be considered as a specified steepest descent solution and solved by the CGS algorithm. Meanwhile, the local-search quadratic approximation CGS is a pure form of iterative Newton's solution and a generalized iterative algorithm for the Tikhonov regularization solutions, because except for the CGS all other solutions can be obtained by just ignoring the term in the second derivative $Q \approx 0$ (see equation (6.27)) in the procedure.

6.3 The Smoothest Model Solution (Occam's Inversion)

As mentioned before, an alternative approach to geophysical inversion is to seek the solution of the smoothest model, that is, to mathematically solve the constrained optimization problem (6.5), which is equivalent to the non-constrained optimization problem (6.6). The solution must satisfy the stationary conditions:

$$\begin{cases} \dfrac{\partial \Phi}{\partial m} = \dfrac{\partial \Phi_m}{\partial m} + \lambda^{-1} \dfrac{\partial \Phi_d}{\partial m} = 0, \\ \dfrac{\partial \Phi}{\partial \lambda} = \Phi_d(m) - \chi_d = 0. \end{cases} \tag{6.36}$$

Substituting equations (6.8) and (6.9) into the above, we obtain:

$$\begin{cases} \lambda W_m (m - m_0) = (\dfrac{\partial d}{\partial m})^T W_d [d_0 - d(m)], \\ [d_0 - d(m)]^T W_d [d_0 - d(m)] = \chi_d. \end{cases} \tag{6.37}$$

By considering the effect of the Lagrange multiplier λ^{-1} as equivalent to the Tikhonov regularization parameter, one can find that the first equation above is the same as equation (6.10) that defines the Tikhonov regularization solution. This reveals that the smoothest model solution is just one subset of the Tikhonov regularization solution, which must satisfy the constrained condition given by the second equation in (6.37). In principle, the Lagrange multiplier λ^{-1} must be first determined from the two equations in (6.37). This differs from the Tikhonov regularization solution where λ must be assigned a value in advance. Due to the non-linear property of $d(m)$ it is very difficult to find the explicit form for λ from (6.37). But, according to the relation to the Tikhonov regularization solution, a practical algorithm to approach the smoothest model solution may be composed of two parts: finding the Tikhonov regularization solutions,

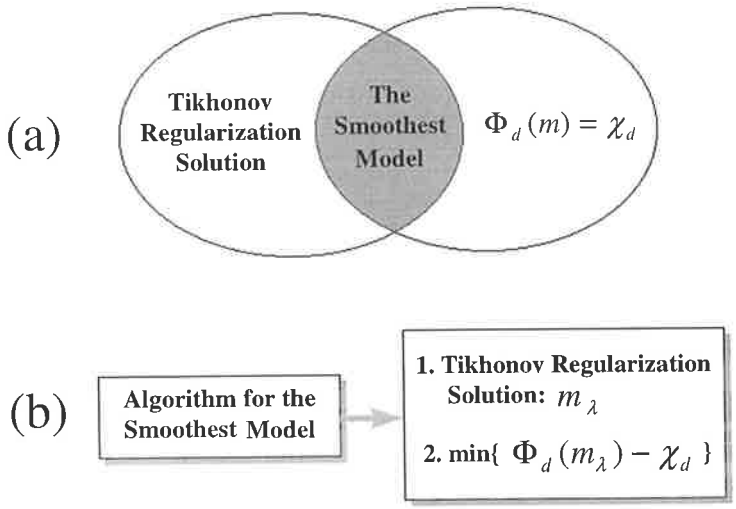

Fig.6-2 Illustration of (a) the relationship between the Tikhonov regularization solution and the smoothest model solution, and (b) a practical algorithm for the smoothest model solution.

then checking criterion of data fit (see Fig.6-2). For example, some schemes were proposed by Constable et al (1987), Ellis and Oldenburg (1994a), Oldenburg and Li (1994) and LaBrecque et al (1996). In fact, a general procedure can be obtained from Fig.6-2, which consists of the following steps:

Step 1. Given $\{ \lambda_i = \lambda_0 + (i-1)\delta\lambda, \quad i = 1,2,\ldots,N_\lambda \}$ and start at $m_l^* = m_0^*$, for $l=0,1,2,\ldots l_{\max}$;

Step 2. For $i=1,2,\ldots, N_\lambda$,

(a) Solve: $\lambda_i W_m (m_{\lambda_i}^{(l)} - m_0) = (\frac{\partial d}{\partial m})^T W_d [d_0 - d(m_{\lambda_i}^{(l)})]$ for $m_{\lambda_i}^{(l)}$;

(b) Calculate $\Phi_d(m_{\lambda_i}^{(l)})$;

Step 3. Obtain the instantaneous solution: $m_l^* = \min_{m_\lambda} \{\Phi_d(m_{\lambda_i}^{(l)})$ $i=1,2,\ldots, N_\lambda\}$;

Step 4. Stopping test $\Phi_d(m_l^*) \le \varepsilon < \chi_d$, if satisfied, stop the procedure, otherwise, go back to *step 1* for next l.

Here ε stands for the stopping criterion. Obviously, the major part of the procedure (*Step 2*) is to solve the same equation as in the Tikhonov regularization problem, so most of the algorithms discussed in the previous sections for the Tikhonov

regularization solution may be directly used for $m_{\lambda_i}^{(l)}$. In other words, this part may be the same as to find the Tikhonov regularization solution with a given λ_i. Actually, *Step 2* is to detect the misfit function of the data with the guess of λ_i. The more the parameter λ_i is used, the more implementations of the algorithm for the Tikhonov regularization solution are required. An efficient scheme is to firstly evaluate the choices of λ with which the computation of *Step 2* consumes the least computer time as possible and the misfit function $\Phi_d(m_\lambda)$ is as small as possible, so that it quickly reaches the desired tolerance χ_d. Due to the non-linear nature of the function $d(m_\lambda)$ there is no analytical method to find the range of λ. As mentioned before, it depends upon the error level of data, the practical choice for the weighting operators W_d and W_m, the model parameterization and the bounds of the true model variation. In a practical application, a trial method or line-search scheme may be used to evaluate the set of λ (or the range) used in *Step 2*. This requires a fast and effective algorithm for the trial computations in *Step 2*. *Step 4* implies the constrained condition in (6.37) and gives the approximation to the smoothest model solution that has the minimal misfit function of the data. The solution procedure seems like an adaptive Tikhonov regularization solution, because in each iteration l an optimal regularization parameter λ or Lagrange multiplier λ^{-1} is determined by the trial computations with the selected set.

From above discussion, it is concluded that *the smoothest model solution is a subset of the Tikhonov regularization solutions, but more reasonable and practicable due to the removal of the undesired solutions:* $\{m_\lambda^* | \Phi_d(m_\lambda^*) > \chi_d\}$ *in the procedure, but it costs much computer time.* From the methodological point of view, the algorithm for the Tikhonov regularization solution is the basis for obtaining the approximation of the smoothest model solution.

6.4 Generalized Subspace Solution

So far, we have discussed the algorithms for two kinds of solutions: Tikhonov regularization and the smoothest model solutions in geophysical inversion. It has been shown that the Tikhonov regularization solution covers the smoothest model solution

and most of the algorithms for the former can be directly applied to the latter. So, the basic algorithms for geophysical inversion may be considered as the Tikhonov regularization solution.

There exists another method, called the subspace method or subspace solution, presented by Skilling and Bryan (1984), who maximized an entropy norm suitable for image reconstruction, and by Kennett and Williamson (1988) and Sambridge et al. (1991) for seismic inversion, and developed by Oldenburg et al. (1993) for large-scale inversion problems. The principal advantages of the method lie in the outstanding computational efficiency and the practical efficacy by judicious choice of the basis vectors spanning the model subspace. Actually, this method is not only valid for the Tikhonov regularization soulution, but also for the smoothest model solution. From the discussion in the previous sections, the algorithm for the Tikhonov regularization solution is easily extended to the smoothest model solution, and the local-search quadratic approximation CGS is a generalized algorithm for the Tikhonov regularization solutions. For simplicity, we firstly present the generalized subspace method in the Tikhonov regularization case, then make the extension.

The primary thrust of the method is to express the model perturbation: $\delta m = m - m_k \in R^{N_m}$ in the form of a q-dimensional subspace $R^q (\subset R^{N_m})$ spanned by the assigned basis vectors $\{\mathbf{b}_i\}$ i=*1,2,...,q,* that is

$$\delta m = \sum_{i=1}^{q} \alpha_i^{(k)} \mathbf{b}_i = \mathbf{B}\hat{\alpha}_k , \tag{6.38}$$

where $\mathbf{B}=(\mathbf{b}_1, \mathbf{b}_2, \ldots, \mathbf{b}_q)$ and $\hat{\alpha}_k = \{\alpha_1^{(k)}, \alpha_2^{(k)}, \ldots, \alpha_q^{(k)}\}$. Substituting the approximation (6.38) for the quadratic approximation form of the objective function (6.30), we have

$$\Phi(\hat{\alpha}_k) \approx \Phi(m_k) + (\frac{\partial \Phi}{\partial m})_k^T \mathbf{B}\hat{\alpha}_k + \frac{1}{2}\hat{\alpha}_k{}^T \mathbf{B}^T (\frac{\partial^2 \Phi}{\partial^2 m})_k \mathbf{B}\hat{\alpha}_k , \tag{6.39}$$

which states that with the subspace approach (6.38) the Tikhonov regularization solution seeks the vector $\hat{\alpha}_k$ by minimizing $\Phi(\hat{\alpha}_k)$. This follows the equation by setting $\frac{\partial \Phi}{\partial \hat{\alpha}_k} = 0$:

$$\mathbf{B}^T (\frac{\partial^2 \Phi}{\partial^2 m})_k \mathbf{B}\hat{\alpha}_k = -\mathbf{B}^T (\frac{\partial \Phi}{\partial m})_k . \tag{6.40}$$

Substitution of the derivatives (6.8), (6.9) and (6.29) into the above equation (6.40) yields:

$$[A_k^T W_d A_k + Q_k' + \lambda W_m'] \hat{\alpha}_k = A_k^T W_d [d_0 - d(m_k)] - \lambda \mathbf{B}^T W_m (m_k - m_0), \tag{6.41}$$

where

$$A_k = (\frac{\partial d}{\partial m})_k \mathbf{B}, \tag{6.42}$$

$$Q_k' = \mathbf{B}^T Q_k \mathbf{B}, \tag{6.43}$$

$$W_m' = \mathbf{B}^T W_m \mathbf{B}. \tag{6.44}$$

From equation (6.41) the Tikhonov regularization solution can be written in the subspace approximation form:

$$\begin{aligned} m_{k+1} = m_k + \mathbf{B}[A_k^T W_d A_k + Q_k' + \lambda W_m']^{-g} \\ \cdot \{A_k^T W_d [d_0 - d(m_k)] + \lambda \mathbf{B}^T W_m (m_0 - m_k)\}. \end{aligned} \tag{6.45}$$

Obviously, when **B=I** (unit matrix, it means the identical transform) the subspace approximation goes back to the whole-space solution (6.35). From equations (6.42)-(6.44), if the basis vectors $\{\mathbf{b}_i\}$ i=*1,2,...,q,* are properly chosen with a small q in a large-scale inversion situation (N_m is very large), the dimensional size ($q \times q$) of the general inverse matrix in equation (6.45) may be much less than that ($N_m \times N_m$) in the original form (6.35) where the solution is solved in the whole model space R^{N_m}. From the result (6.45) the subspace formulation requires us to compute the general inverse of the matrix, but the matrix may be singular if the basis vectors are linearly dependent. So orthonormalizing the vectors is necessary before using them. After choosing the basis vectors the inverse matrix may be much more efficiently obtained by SVD with a given λ than that in the whole-space solution (6.35).

Recalling the general procedure for the smoothest model solution (section 6.3) and using the result (6.45), the subspace approach to the smoothest model solution can be reduced to the following steps:

Step 1. Choose the basis vectors $\mathbf{B}=(\mathbf{b}_1, \mathbf{b}_2, \ldots, \mathbf{b}_q)$ and give

$$\{\lambda_i = \lambda_0 + (i-1)\delta\lambda,, \; i = 1,2,\ldots, N_\lambda\}, \text{ start at } m_l^* = m_0^*,$$

for $l=0,1,2,\ldots l_{\max}$;

Step 2. For $i=1,2,\ldots, N_\lambda$,

(a) Obtain the subspace approximation:

$$m_{\lambda_i}^{(l)} = m_l^* + \mathbf{B}[A_l^T W_d A_l + Q_l' + \lambda_i W_m']^{-g} \cdot \{A_l^T W_d [d_0 - d(m_l^*)] + \lambda_i \mathbf{B}^T W_m (m_0 - m_l^*)\};$$

(b) Calculate $\Phi_d(m_{\lambda_i}^{(l)})$;

Step 3. Obtain the instantaneous solution: $m_l^* = \min_{m_\lambda} \{\Phi_d(m_{\lambda_i}^{(l)})$ $i=1,2,\ldots, N_\lambda\}$;

Step 4. Stopping test $\Phi_d(m_l^*) \le \varepsilon < \chi_d$, if satisfied, stop the procedure, otherwise, go back to *step 1* for next l.

From the above discussion, *the subspace solution is mathematically no more than the introduction of the dimension-decreased transform (6.38) in the formulation for the Tikhonov regularization and smoothest model solutions (see Fig.6-3). The key step is to choose the basis vectors* $\boldsymbol{B}=(\mathbf{b}_1, \mathbf{b}_2, \ldots, \mathbf{b}_q)$. Oldenburg et al. (1993) demonstrated a method to choose the basis vectors, which associates them with the gradients of the data and model misfit functions:

$$\mathbf{b}_k = W_m^{-1} \nabla \Phi_{d_k}(m), \quad (k=1,2,\ldots, q_1) \qquad (6.46)$$

$$\mathbf{b}_k = W_m^{-1} \nabla \Phi_{m_k}(m), \quad (k=1,2,\ldots, q_2), \qquad (6.47)$$

where Φ_{d_k} and Φ_{m_k} are the misfit functions of the data subset $d_k \subset d_0$ and model subset $m_k \subset m$ respectively, and

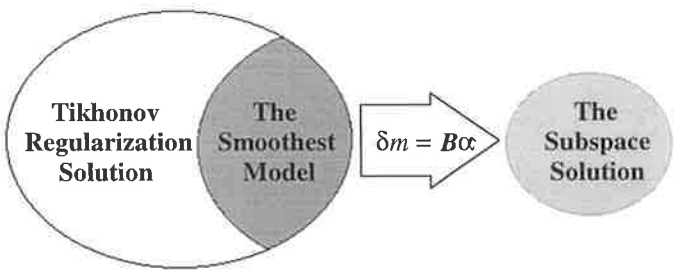

Fig.6-3 Illustration of the relationships for the three solutions: Tikkhonov regularization, the smoothest model and the subspace solutions.

$q_1 + q_2 = q$. The vectors given by (6.46) and (6.47) are actually the steepest ascent directions of the subsets. The segmental misfit functions fabricate the total misfit functions $\Phi_d(m) = \sum_{k=1}^{q_1} \Phi_{d_k}(m)$ and $\Phi_m(m) = \sum_{k=1}^{q_2} \Phi_{m_k}(m)$. Different choices may yield different solutions. So, a judicious choice is the precondition for successful application of the method.

A simple way to choose the basis vectors is to conduct the transform from a fine-grid (for forward modeling) model parameterization to a sparse-grid (for inversion) model parameterization. For instance, the 4-block parameterization may be reduced to the 2-block parameterization (Fig.6-4) if the sparse approximation is reasonable in the inversion. The relation of the two model parameters can be written in the matrix form:

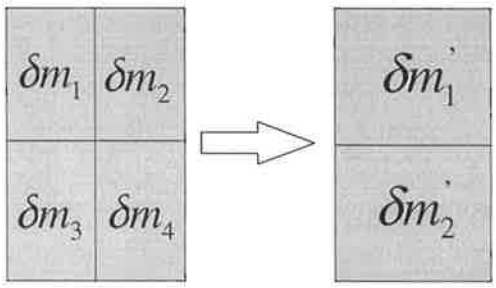

Fig.6-4 Schematics of the reduction from the 4-block parameterization to the 2-block parameterization.

$$\delta m = \begin{pmatrix} \delta m_1 \\ \delta m_2 \\ \delta m_3 \\ \delta m_4 \end{pmatrix} = \begin{bmatrix} 1 & 0 \\ 1 & 0 \\ 0 & 1 \\ 0 & 1 \end{bmatrix} \begin{pmatrix} \delta m_1' \\ \delta m_2' \end{pmatrix} = \mathbf{B}\delta m' . \tag{6.48}$$

From this simple example, a general form of **B** can be obtained:

$$\mathbf{B} = \left[b_{ij} \right]_{N_m \times q}, \; b_{ij} = \frac{\Omega(\delta m_i) \cap \Omega(\delta m_j')}{\sum_{j=1}^{q} \Omega(\delta m_i) \cap \Omega(\delta m_j')} . \tag{6.49}$$

Here $\Omega(\delta m_i)$ stands for the spatial area of the block δm_i. Obviously, the column vectors (the basis vectors) in **B** are independent of each other with this method. This simple subspace method may be useful to reduce the multiple solutions of geophysical inversion problem, because a fine model parameterization is normally employed in the forward modeling for complicated media, but the fine model parameterization is hardly reconstructed completely by the inversion algorithms due to the limited data samples

and error contamination (actually, the data have only limited spatial resolution of the model). So, besides applying the Tikhonov regularization or Occam's criterion, a proper model parametrization, which matches with the data number, may be employed in the inversion procedure of the simple subspace method. The relation (6.48) gives the transform from a fine model parameterization (in forward modeling) to a proper model-parameter set for inversion.

Chapter 7

Computation of the Fréchet and Second Derivatives

From the analysis of the previous chapter, concerning different approaches to geophysical inversion, it was apparent that all inversion algorithms require the computation of the Fréchet derivatives which form the Jacobain matrix of the objective function. In addition, the second derivative is required to assemble the Hessian matrix when taking the quadratic approximation. For a large scale inverse problem, like crosshole resistivity or seismic imaging or wave-equation tomography (involving lots of unknown model parameters and a great number of data), fast computation of the derivatives is very important. A robust and efficient algorithm to compute the derivatives is still required for the inversion. On the other hand, the derivatives may be viewed as sensitivity functions of the data, and used to indicate the sensitivity variation with various surveying configurations, thus aiding survey design and the understanding of resolution.

So far, there have been many papers dealing with the computation of the Fréchet derivative. For example, McGillivray and Oldenburg (1990) made a comparative theoretical study of several methods to compute the Fréchet derivatives in geophysical inversion. In seismic waveform inversion, Tarantola (1984) formulated the Fréchet derivatives with the 2-D acoustic wave-equation. In electromagnetic inversion, Boerner and Holladay (1990) proposed approximate Fréchet derivatives for the 2-D problem. In resistivity inversion, Park and Van (1991) derived an implicit expression for the Fréchet derivative in the 3-D problem. Smith and Vozoff (1984) and Sasaki (1994) calculated the Fréchet derivative by solving the differential equations of the finite difference or finite element linear system. Recently, Loke and Barker (1995,1996) computed the Fréchet derivatives with a homogenous half-space starting model and Broyden's (1965) updating approximation.

In this Chapter, we develop a new method to compute the relevant derivatives for crosshole resistivity imaging and seismic full-waveform inversion in the frequency-

domain (Zhou and Greenhalgh, 1995, 1998d). The computations are based on the numerical solution of the 2.5-D Helmholtz equation and are implemented with nearly the same scheme for both 2.5-D resistivity and acoustic problems. Firstly, by performing some differential calculus and applying the 2.5-D Green's functions, the general expressions for these derivatives are explicitly obtained for any configuration in DC surveying (four kinds of electrode arrays: pole-pole, pole-bipole, bipole-pole and bipole-bipole) and crosshole seismic exploration. Next, two approximations: the constant-point and constant-block model parameterizations are proposed. To approach the derivatives, a two-step procedure is presented: (1) solving the 2.5-D Helmholtz equation with the finite element method (FEM) for all the Green's functions; (2) calculating the derivatives using the Green's functions in terms of the explicit expressions. It will be seen that the new algorithm is a robust and more efficient algorithm than the commonly used ones.

The next section reviews basic definitions of the Fréchet and second derivatives. Thereafter, we recall common algorithms to compute the derivatives. Sections 7.3 and 7.4 give explicit expressions of the derivatives for the 2.5-D DC resistivity and acoustic wave problems. The last section deals with the numerical computation of the derivatives with a two-step scheme, and introduces some numerical examples that show the different patterns of the derivatives.

7.1 Basic Definitions

For completeness, some useful definitions are briefly reviewed here. One can refer to mathematical books, such as Flett (1980) or Griffel (1981), for a more complete treatment.

(1) Bilinear Operator

For any vector spaces N and M, a bilinear operator $f: N \rightarrow M$ is a rule which, given any $h \in N$ and $k \in N$, associates with them an element of M, denoted by $f(h,k)$, such that for any scalars a and b, and any $h, j, k \in N$,

$$\begin{aligned} & f(ah+bj,k) = af(h,k) + bf(j,k), \\ \text{and} \quad & f(h,ak+bj) = af(h,k) + bf(h,j). \end{aligned} \tag{7.1}$$

If $h(x)$ and $k(x)$ are two continuous functions, a simple example would be $f(h,k) = \int_{\Omega}\int_{\Omega} M(x,y)h(x)k(y)dxdy$. For the discrete case: $h = \{h_1, h_2, ..., h_n\}$ and $k = \{k_1, k_2, ..., k_n\}$, the bilinear operator has the quadratic form: $f(h,k) = h^T M k$.

(2) Fréchet and Second Derivatives

An operator $D_1 : N \rightarrow M$ and a bilinear operator $D_2 : N \times N \rightarrow M$ are said to be the Fréchet and second derivatives of $f: N \rightarrow M$ at the point $x \in N$, if

$$f(x+h) = f(x) + D_1(x)h + \frac{1}{2}D_2(x)(h,h) + O(h^3) \quad \text{as } h \rightarrow 0. \tag{7.2}$$

Here f may be the DC electric potential U or the frequency-domain acoustic wavefield $\overline{P}$. Obviously, the definition is a version of Taylor's theorem (series expansion) to second order and implies the way to obtain the two derivatives for a given mapping f with differential calculus. In the mathematical literature, if D_1 and D_2 exist, then f is called Fréchet and twice differentiable. A twice differentiable operator has the common property that is a D_2 symmetric bilinear operator: $D_2(x)(h,k) = D_2(x)(k,h)$ for all h, $k \in N$. This property can be explained by the discrete case: $\partial^2 f / \partial x_i \partial x_j = \partial^2 f / \partial x_j \partial x_i$ in the differential calculation of a multi-variable function. For any continuous function h(x), the operators D_1 and D_2 may be defined by the integrals

$$D_1(x)h = \int_{\Omega} D_1(x,x')h(x')dx' \tag{7.3}$$

and

$$D_2(x,y)(h,h) = \int_{\Omega}\int_{\Omega} D_2(x,y,x',y')h(x')h(y')dx'dy' \tag{7.4}$$

respectively, and for the discrete case, the operators become

$$D_1(x)h = \nabla f^T h \tag{7.5}$$

and

$$D_2(x,y)(h,h) = h^T H h \tag{7.6}$$

in terms of the definition (7.2). Here $\nabla f = \{\partial f / \partial h_i,\ i=1,2,...,N\}$ is the gradient of f to be used to form the *Jacobian* matrix and $H = \{\partial^2 f / \partial h_i \partial h_j,\ i=1,2,...,N\}$ is used to form the *Hessian* matrix. The definition (7.2) implies the way to obtain the Fréchet and second derivatives. The initial step may be to find the operators D_1 and D_2 for a complicated functional $f(x)$, such as the electric potential $U(x,y,z)$ or acoustic pressure wavefield $P(t,x,y,z)$ so that the definition (7.2) is satisfied.

7.2 Common Algorithms

According to the definition of the Fréchet derivative (equation (7.2)), a simple way may be to use the finite difference approximation to the derivative:

$$D_1(m_i) \approx \frac{f(m_i + h) - f(m_i)}{h}, \quad (i = 1,2,\ldots,N_m), \tag{7.7}$$

where h should be a small quantity, m_i is the ith model parameter, e.g. $m_i = \sigma_i$ (conductivity) or $m_i = c_i$ (wavespeed), and N_m is the number of the model parameters. Actually, this is the first order difference formula to approximate the derivative. If N_m is not large, the algorithm is a simple way to obtain the derivative for inversion, but for large N_m, e.g. geophysical tomography or imaging inversion, much computer time is involved in obtaining the whole derivatives, because each value of the derivative will have to be used to twice perform the forward computations. So, it is not an efficient way for crosshole resistivity or acoustic velocity imaging.

Another simple way was recently proposed by Loke and Barker (1995), who based it on Park and Van' s (1991) expression for the 3-D resistivity problem and used a homogeneous half-space as the starting model. They demonstrated an approach to the Fréchet derivative for the 2.5-D resistivity inversion. The change in the potential δU, resulting from a change in the subsurface resistivity $\delta\rho$ is given by (Park and Van, 1991, equation 16):

$$\delta U(r_c, r_p) = \frac{I}{\rho_e^2} \delta\rho \int_V \nabla G^{3D}(r_c, r) \cdot \nabla G^{3D}(r_p, r) dr, \tag{7.8}$$

where it is assumed that the change in the resistivity has a constant value ρ_e in a cubic element V and is zero elsewhere. Here $r_c = (x_c, 0, z_s)$ and $r_p = (x_p, 0, z_p)$ are the positions of the current and potential electrodes. When taking a homogeneous half-space (with current electrode on the surface) as the starting model, the Green's functions can be obtained from equation (2.7):

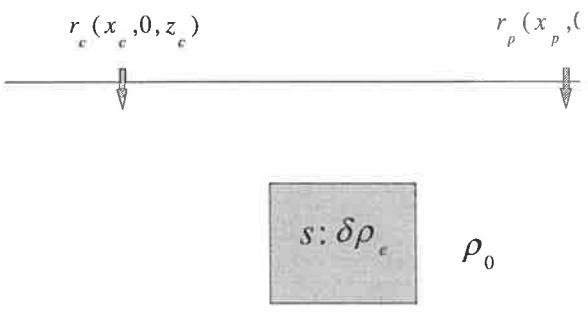

Fig.7-1 Illustration of a rectangular block in a homogeneous half-space model for calculation of

$$G^{3D}(r_c, r) = \frac{\rho_0}{2\pi |r_c - r|}. \tag{7.9}$$

Substituting (7.9) into (7.8) and considering the 2.5-D approximation, the volume integration in equation (7.8) can be calculated by the line integral over the *y*-direction and the surface integral over the rectangular section *s* in the (*x*,*z*)-plane (see Fig.7-1):

$$\frac{\partial U}{\partial \rho_e} = \int_s F_y(x_c, z_c, x_p, z_p, x, z) ds, \tag{7.10}$$

where
$$F_y(x_c, z_c, x_p, z_p, x, z) = \frac{1}{4\pi^2} \int_{-\infty}^{+\infty} \frac{dy}{|r_c - r||r_p - r|}, \tag{7.11}$$

which may be determined analytically (Loke and Barker, 1995, Appendix). After obtaining the function $F_y(x_c, z_c, x_p, z_p, x, z)$, the derivative may be calculated using Gaussian quadrature for the integral over *s* in equation (7.10). Obviously, the numerical integration gives the derivative values for the starting homogeneous earth model. To implement an iterative inversion, they suggested using a quasi-Newton updating formula to obtain subsequent derivatives, e.g. Broyden's formula (1965):

$$\left(\frac{\partial U_i}{\partial \rho_j}\right)^{(k)} = \left(\frac{\partial U_i}{\partial \rho_j}\right)^{(k-1)} + [(U_i^{(k)} - U_i^{(k-1)}) - \frac{1}{\sum_j [\delta\rho_j^{(k-1)}]^2} \sum_j \left(\frac{\partial U_i}{\partial \rho_j}\right)^{(k-1)} \delta\rho_j^{(k-1)}] \delta\rho_j^{(k-1)},$$
$$(k=1,2,\ldots). \tag{7.12}$$

where the superscript *k* denotes the *k*th iteration of the inversion. It is not difficult to apply the method to the 2.5-D acoustic case, but one can find that due to the usage of a homogenous half-space model in the first iteration, this method is *valid only for the case that the practical earth model is not far away from the homogeneous starting model.*

For a general case, a popular algorithm for large N_m is to solve the differential equations of the finite difference or finite element linear system. For example, Smith and Vozoff (1984) and Sasaki (1994) applied this algorithm to 2-D and 3-D resistivity inversion. Due to the similarity between 2.5-D resistivity and acoustic wave modeling, the algorithm is also valid for the acoustic wave case. In Chapters 3 and 4, we showed the FEM linear equation system of the 2.5-D Green's function for the two geophysical problems, e.g. equations (3.9) and (4.30) or (4.54), which may be represented as follows:

$$A(m, k_y) G^{2.5D} = b_s. \tag{7.13}$$

Here $A(m, k_y)$ is the assembled matrix from all of the inner element and boundary element matrices, and it depends upon the model parameters: $m = \{m_1, m_2, \ldots, m_{N_m}\}$ and the

wavenumber k_y. $G^{2.5D} = \overline{G}^{2.5D}$ or $\overline{\overline{G}}^{2.5D}$, a column vector whose components are nodal values of the 2.5-D Green's function. The vector b_s is the source vector whose components are zero except for the one (=1.0) whose position coincides with the source location $r_{c=A,B}$ or r_s. Taking differential calculations with respect to the model parameter m_i on both sides of equation (7.13), we have the differential equation system:

$$A(m,k_y)\frac{\partial G^{2.5D}}{\partial m_i} = -\frac{\partial A(m,k_y)}{\partial m_i} G^{2.5D}. \tag{7.14}$$

Using the relations between the Green's function and the general response of the potential or wavefield to any current injecting or seismic source signal (see equations (2.30) and (2.31)), we can write out the discrete form of the Fréchet drivative:

$$\frac{\partial U}{\partial \sigma_i} = \frac{I}{2}\cdot F_c^{-1}\{\frac{\partial \overline{G}^{2.5D}}{\partial \sigma_i}\}, \qquad \text{(Electric)} \tag{7.15}$$

$$\frac{\partial \overline{P}}{\partial c_i} = \frac{s(\omega)}{2}\cdot F_c^{-1}\{\frac{\partial \overline{\overline{G}}^{2.5D}}{\partial c_i}\}. \qquad \text{(Acoustic)} \tag{7.16}$$

According to these results, the Fréchet drivative can be obtained through solving equation (7.14), then substituting into equation (7.15) or (7.16) for resistivity or acoustic wave problems, respectively. Clearly, the main step of the algorithm is to solve equation (7.14), but one can find that except for the right-hand-side vector the construction of the two systems (7.13) and (7.14) is the same. So, the same solver (LL^T or LU decomposition for resistivity or acoustic wave case) to equation (7.13) may be used again to equation (7.14), but to form the right-hand-side vector requires us to compute the differential matrix $\partial A(m,k_y)/\partial m_i$ in addition to storing all of the Green's functions $G^{2.5D}$ (obtained from the forward modeling). The main advantage of this algorithm is that it is a valid for inversion with any starting earth model, but one has to deal with the large dimensional matrix $\partial A(m,k_y)/\partial m_i$ and repeat solving equation (7.14) for all the model parameters: $\{m_i, i = 1,2,...,N_m\}$.

In the following sections, we are going to present a new algorithm to compute not only the Fréchet derivative but also the second derivative without the calculation of the matrix $\partial A(m,k_y)/\partial m_i$ and solving the differential equation (7.14). *The new algorithm is valid for a large scale inversion with any starting earth model.*

7.3 Explicit Expressions for DC Resistivity

The boundary-valued problem for 2.5-D DC resistivity modeling can be rewritten in the following operator form (see equations (2.10)):

$$\begin{cases} L(\sigma,k_y)\overline{U} = -\dfrac{I}{2}\delta(r-r_c), & r\in\Omega; \\ \dfrac{\partial\overline{U}}{\partial n}+\nu\overline{U}=0, & r\in\partial\Omega; \end{cases} \tag{7.17}$$

where $$L(\sigma,k_y)=\nabla\cdot(\sigma\nabla)-\sigma k_y^2. \tag{7.18}$$

It has been shown in Section 2.5 that the operator $L(\sigma,k_y)$ is self-adjoint. In fact, applying Green's integral theorem, the integral identity can be recognized for any two solutions $\overline{u}$ and $\overline{v}$ of equation (7.17):

$$\int_\Omega \overline{v}L(\sigma,k_y)\overline{u}\,dr = -\int_\Omega \sigma[\nabla\overline{v}\cdot\nabla\overline{u}+k_y^2\overline{v}\overline{u}]dr - \int_{\partial\Omega}\nu\sigma\overline{u}\overline{v}\,ds. \tag{7.19}$$

In addition, in terms of equation (7.18), $L(\sigma,k_y)$ is a linear operator, viz. $L(\sigma_1+\lambda\sigma_2,k_y) = L(\sigma_1,k_y)+\lambda L(\sigma_2,k_y)$ for any constant λ.

In order to derive the expression (7.2) for $\overline{U}$, the perturbation analysis for $\sigma'=\sigma+\delta\sigma$ and $\overline{U}'=\overline{U}+\delta\overline{U}$ is generally conducted with the operator, where $\delta\sigma$ and $\delta\overline{U}$ are small quantities and both $\overline{U}$ and $\overline{U}'$ are solutions of equation (7.17). Using the linear property, one can write out the explicit form of $L(\sigma',k_y)\overline{U}'$, then obtain:

$$L(\sigma,k_y)\delta\overline{U} = -L(\delta\sigma,k_y)(\overline{U}+\delta\overline{U}). \tag{7.20}$$

Defining the conjugate Green's function (current injecting electrode located at r_p):

$$\begin{cases} L(\sigma,k_y)\overline{G}^{2.5D} = -\delta(r-r_p), & r,r_p\in\Omega; \\ \dfrac{\partial\overline{G}^{2.5D}}{\partial n}+\nu\overline{G}^{2.5D}=0, & r\in\partial\Omega; \end{cases} \tag{7.21}$$

where r_p is the coordinate of a potential electrode. Using the self-adjoint property of $L(\sigma,k_y)$, the disturbed potential $\delta\overline{U}$ can be written in the integral form:

$$\begin{aligned} \delta\overline{U}(r_c,r_p) = &\int_\Omega \overline{G}^{2.5D}(r_p,r)L(\delta\sigma)\overline{U}(r_c,r)dr \\ &+\int_\Omega \delta\overline{U}(r_c,r)L(\delta\sigma)\overline{G}^{2.5D}(r_p,r)dr. \end{aligned} \tag{7.22}$$

Here we omit k_y in the variable set to shorten the expression. From this equation, it seems that the first and second terms of the right-hand-side correspond to the perturbing

quantities due to the first-order and higher-order variations in $\delta\sigma$. Assuming $\overline{U}(r_c, r_p)$ is Fréchet differentiable with respect to $\delta\sigma$ and according to the definitions (7.2) and (7.3), there exists an operator D_1 having the expression

$$\begin{aligned}\delta\overline{U}(r_c, r) &= D_1\delta\sigma' + O(\|\delta\sigma'\|^2), \\ &= \int_\Omega \overline{D}_1(r_c, r, r')\delta\sigma' dr' + O(\|\delta\sigma'\|^2).\end{aligned} \tag{7.23}$$

Substituting equation (7.23) for the second integral of equation (7.22) and considering the integral does not change with either the coordinate r or r', we have

$$\begin{aligned}\delta\overline{U}(r_c, r_p) = \int_\Omega \overline{G}^{2.5D}(r_p, r) L(\delta\sigma)\overline{U}(r_c, r)dr + \frac{1}{2}\int_\Omega\int_\Omega [\overline{D}_1(r_c, r, r') \\ \cdot L(\delta\sigma)\overline{G}^{2.5D}(r_p, r)\delta\sigma' + \overline{D}_1(r_c, r', r)L(\delta\sigma') \\ \cdot \overline{G}^{2.5D}(r_p, r')\delta\sigma]dr'dr + O(\|\delta\sigma\|^3).\end{aligned} \tag{7.24}$$

One can find that equation (7.24) is very close to the definition (7.2). Reviewing the integral equation (7.19) and assuming $\delta\sigma|_{\partial\Omega} = 0$ (this assumption is reasonable, because the studied area is normally located in the centre of the computational range Ω), equation (7.24) can be rewritten as follows:

$$\begin{aligned}\delta\overline{U}(r_c, r_p) = -\int_\Omega [\nabla\overline{U}(r_c, r)\cdot\nabla\overline{G}^{2.5D}(r_p, r) + k_y^2\overline{U}(r_c, r)\overline{G}^{2.5D}(r_p, r)]\delta\sigma dr - \\ \frac{1}{2}\int_\Omega\int_\Omega \{\nabla\overline{D}_1(r_c, r, r')\cdot\nabla\overline{G}^{2.5D}(r_p, r) + \nabla'\overline{D}_1(r_c, r', r)\cdot\nabla'\overline{G}^{2.5D}(r_p, r') \\ + k_y^2[\overline{D}_1(r_c, r, r')\overline{G}^{2.5D}(r_p, r) + \overline{D}_1(r_c, r', r)\overline{G}^{2.5D}(r_p, r')]\} \\ \delta\sigma'\delta\sigma\, dr'dr + O(\|\delta\sigma\|^3).\end{aligned} \tag{7.25}$$

Comparing equation (7.25) with the definitions (7.2), (7.3) and (7.4), the Fréchet and second derivative operators in the k_y-domain are directly obtained:

$$\begin{aligned}\overline{D}_1(r_c, r_p)\delta\sigma = -\frac{I}{2}\int_\Omega [\nabla\overline{G}^{2.5D}(r_c, r)\cdot\nabla\overline{G}^{2.5D}(r_p, r) + \\ k_y^2\overline{G}^{2.5D}(r_c, r)\overline{G}^{2.5D}(r_p, r)]\delta\sigma dr,\end{aligned} \tag{7.26}$$

$$\begin{aligned}\frac{1}{2}\overline{D}_2(r_c, r_p)(\delta\sigma, \delta\sigma') = -\frac{1}{2}\int_\Omega\int_\Omega \{\nabla\overline{D}_1(r_c, r, r')\cdot\nabla\overline{G}^{25D}(r_p, r) + \nabla'\overline{D}_1(r_c, r', r)\cdot \\ \nabla'\overline{G}^{2.5D}(r_p, r') + k_y^2[\overline{D}_1(r_c, r, r')\overline{G}^{2.5D}(r_p, r) + \\ \overline{D}_1(r_c, r', r)\overline{G}^{2.5D}(r_p, r')]\}\delta\sigma\delta\sigma' dr dr'.\end{aligned} \tag{7.27}$$

Here we have used the relation $\overline{U} = \frac{I}{2}\overline{G}^{2.5D}$ (equations (2.30)) for equation (7.26) from which the explicit form of $\overline{D}_1(r_c, r, r')$ can be obtained by the definition (7.3). Substituting $\overline{D}_1(r_c, r, r')$ into equation (7.27), one can get the explicit form of $\overline{D}_2(r_c, r_p, r, r')$. The quantities $\overline{D}_1(r_c, r, r')$ and $\overline{D}_2(r_c, r_p, r, r')$ (the kernel functions of the operators) are the k_y-domain forms of the Fréchet and second derivatives for the *constant-point model parameterisation*: $\delta\sigma(r) = \delta\sigma_i\delta(r - r_i)$ (called constant-point approximation). So the following spatial forms are obtained:

$$\frac{\partial U(r_c, r_p)}{\partial \sigma_i} = -\frac{I}{2} F_c^{-1}[\nabla\overline{G}^{2.5D}(r_s, r_i)\cdot\nabla\overline{G}^{2.5D}(r_p, r_i) + k_y^2\overline{G}^{2.5D}(r_s, r_i)\overline{G}^{2.5D}(r_p, r_i)], \tag{7.28}$$

$$\begin{aligned}\frac{\partial^2 U(r_c, r_p)}{\partial\sigma_i\partial\sigma_j} = \frac{I}{4} F_c^{-1}\{&[\nabla\overline{G}^{2.5D}(r_c, r_j)\cdot\nabla\overline{G}^{2.5D}(r_p, r_i) + \nabla\overline{G}^{2.5D}(r_c, r_i)\cdot\nabla\overline{G}^{2.5D}(r_p, r_j)]\\ &\nabla\nabla\overline{G}^{2.5D}(r_i, r_j) + k_y^2[\overline{G}^{2.5D}(r_c, r_j)\nabla\overline{G}^{2.5D}(r_p, r_i) + \overline{G}^{2.5D}(r_c, r_i)\nabla\overline{G}^{2.5D}(r_p, r_j)]\\ &\cdot\nabla\overline{G}^{2.5D}(r_j, r_i) + k_y^2[\overline{G}^{2.5D}(r_p, r_j)\nabla\overline{G}^{2.5D}(r_c, r_i) + \overline{G}^{2.5D}(r_p, r_i)\nabla\overline{G}^{2.5D}(r_c, r_j)]\\ &\cdot\nabla\overline{G}^{2.5D}(r_i, r_j) + k_y^4[\overline{G}^{2.5D}(r_c, r_i)\overline{G}^{2.5D}(r_p, r_j) + \overline{G}^{2.5D}(r_c, r_j)\overline{G}^{2.5D}(r_p, r_i)]\overline{G}^{2.5D}(r_i, r_j)\}.\end{aligned} \tag{7.29}$$

Alternatively, if the range Ω may be divided into many blocks: $\Omega = \sum_e \Omega_e$ and each block has constant conductivity σ_e (*constant-block model parameterization*, called constant-block approximation), the Fréchet and second derivatives become:

$$\frac{\partial U(r_c, r_p)}{\partial \sigma_e} = -\frac{I}{2} F_c^{-1}\{\int_{\Omega_e}[\nabla\overline{G}^{2.5D}(r_c, r)\cdot\nabla\overline{G}^{2.5D}(r_p, r) + k_y^2\overline{G}^{2.5D}(r_c, r)\overline{G}^{2.5D}(r_p, r)]dr\}, \tag{7.30}$$

$$\begin{aligned}\frac{\partial^2 U(r_c, r_p)}{\partial\sigma_e\partial\sigma_{e'}} = \frac{I}{4} F_c^{-1}\{\int_{\Omega_e}\int_{\Omega_{e'}} dr dr'\{&[\nabla'\overline{G}^{2.5D}(r_c, r')\cdot\nabla\overline{G}^{2.5D}(r_p, r) + \nabla\overline{G}^{2.5D}(r_c, r)\cdot\\ &\cdot\nabla'\overline{G}^{2.5D}(r_p, r')]\nabla\nabla'\overline{G}^{2.5D}(r, r') + k_y^2[\overline{G}^{2.5D}(r_c, r')\nabla\overline{G}^{2.5D}(r_p, r) +\\ &\overline{G}^{2.5D}(r_c, r)\nabla'\overline{G}^{2.5D}(r_p, r')]\nabla\overline{G}^{2.5D}(r, r') + k_y^2[\overline{G}^{2.5D}(r_p, r'))]\cdot\\ &\nabla\overline{G}^{2.5D}(r_c, r) + \overline{G}^{2.5D}(r_p, r)\nabla'\overline{G}^{2.5D}(r_c, r'\nabla\overline{G}^{2.5D}(r, r') + k_y^4\\ &[\overline{G}^{2.5D}(r_c, r\overline{G}^{2.5D}(r_p, r') + \overline{G}^{2.5D}(r_c, r')\overline{G}^{2.5D}(r_p, r)]\overline{G}^{2.5D}(r, r')\}\}.\end{aligned} \tag{7.31}$$

Obviously, the second derivative (7.29) or (7.31) is a symmetric bilinear function of $(\delta\sigma_i, \delta\sigma_j)$ or $(\delta\sigma_e, \delta\sigma_{e'})$ and has a much more complicated form than the Fréchet derivative does. Once the geometry of the constant block Ω_e and the interpolating function to approach the Green's functions in the block are chosen, the integrals (7.30) and (7.31) can be calculated with an analytic or numerical method. Appendix D gives an example of the computation with the constant-block approximation.

According to the general form of apparent resistivity (equation (3.49)) for different electrode arrays, the expressions (7.28), (7.29), (7.30) and (7.31) can be generalized to the apparent resistivity for all four kinds of electrode arrays, e.g. with the constant-point approximation, the derivatives become

$$\frac{\partial \rho_a}{\partial \sigma_i} = -\frac{K}{2} F_c^{-1}[\nabla \delta\overline{G}_{AB}(r_i) \cdot \nabla \delta\overline{G}_{MN}(r_i) + k_y^2 \delta\overline{G}_{AB}(r_i)\delta\overline{G}_{MN}(r_i)], \tag{7.32}$$

$$\begin{aligned}\frac{\partial^2 \rho_a}{\partial \sigma_i \partial \sigma_j} = \frac{K}{4} F_c^{-1}\{&[\nabla \delta\overline{G}_{AB}(r_j) \cdot \nabla \delta\overline{G}_{MN}(r_i) + \nabla \delta\overline{G}_{AB}(r_i) \cdot \nabla \delta\overline{G}_{MN}(r_j)] \\ &\cdot \nabla\nabla\overline{G}(r_i, r_j) + k_y^2[\delta\overline{G}_{AB}(r_j)\nabla \delta\overline{G}_{MN}(r_i) + \delta\overline{G}_{AB}(r_i)\nabla \delta\overline{G}_{MN}(r_j)] \\ &\cdot \nabla\overline{G}(r_j, r_i) + k_y^2[\delta\overline{G}_{MN}(r_i)\nabla \delta\overline{G}_{AB}(r_j) + \delta\overline{G}_{MN}(r_j)\nabla \delta\overline{G}_{AB}(r_i)] \\ &\cdot \nabla\overline{G}(r_i, r_j) + k_y^4[\delta\overline{G}_{AB}(r_i)\delta\overline{G}_{MN}(r_j) + \delta\overline{G}_{AB}(r_j)\delta\overline{G}_{MN}(r_i)]\overline{G}(r_i, r_j)\}.\end{aligned} \tag{7.33}$$

Incidentally, one can recognize the similarity between the 3-D and the 2.5-D governing equations. The 3-D formula can be obtained by taking $k_y = 0$, dropping F_c^{-1} and the factor 1/2 and replacing the 2-D gradient operator with a 3-D gradient operator in equations (7.32) and (7.33). So, the derivative expressions for the 3-D case are obtained:

$$\frac{\partial \rho_a}{\partial \sigma_i} = -K[\nabla \delta G_{AB}(r_i) \cdot \nabla \delta G_{MN}(r_i)] \tag{7.34}$$

and

$$\begin{aligned}\frac{\partial^2 \rho_a}{\partial \sigma_i \partial \sigma_j} = \frac{K}{2}\{&[\nabla \delta G_{AB}(r_i) \cdot \nabla\nabla G(r_i, r_j) \cdot \nabla \delta G_{MN}(r_j) \\ &+ \nabla \delta G_{AB}(r_j) \cdot \nabla\nabla G(r_j, r_i)\nabla \delta G_{MN}(r_i)],\end{aligned} \tag{7.35}$$

which is much simpler than that of the 2.5-D case. Equation (7.34) is a general form of Park and Van's result (1991, equation 16) when taking the constant-point approximation. These derivatives can be applied to non-linear resistivity inversion with surface data or crosshole data for any electrode-array surveying configuration.

In summary, all the quantities: ρ_a, $\frac{\partial \rho_a}{\partial \sigma_i}$ and $\frac{\partial^2 \rho_a}{\partial \sigma_i \partial \sigma_j}$ in the 2.5-D DC resistivity problem may be calculated by the Green's functions which are shown in Fig.7-2. This figure illustrates the relation of the quantities to the Green's functions. It is clear that the second derivative needs the maximum number of the Green's functions: $\{\overline{G}(r_i, r_j),\ r_i = 1,2,...\}$ for which one has to take every point r_i in the FEM mesh to be source locations in the computations.

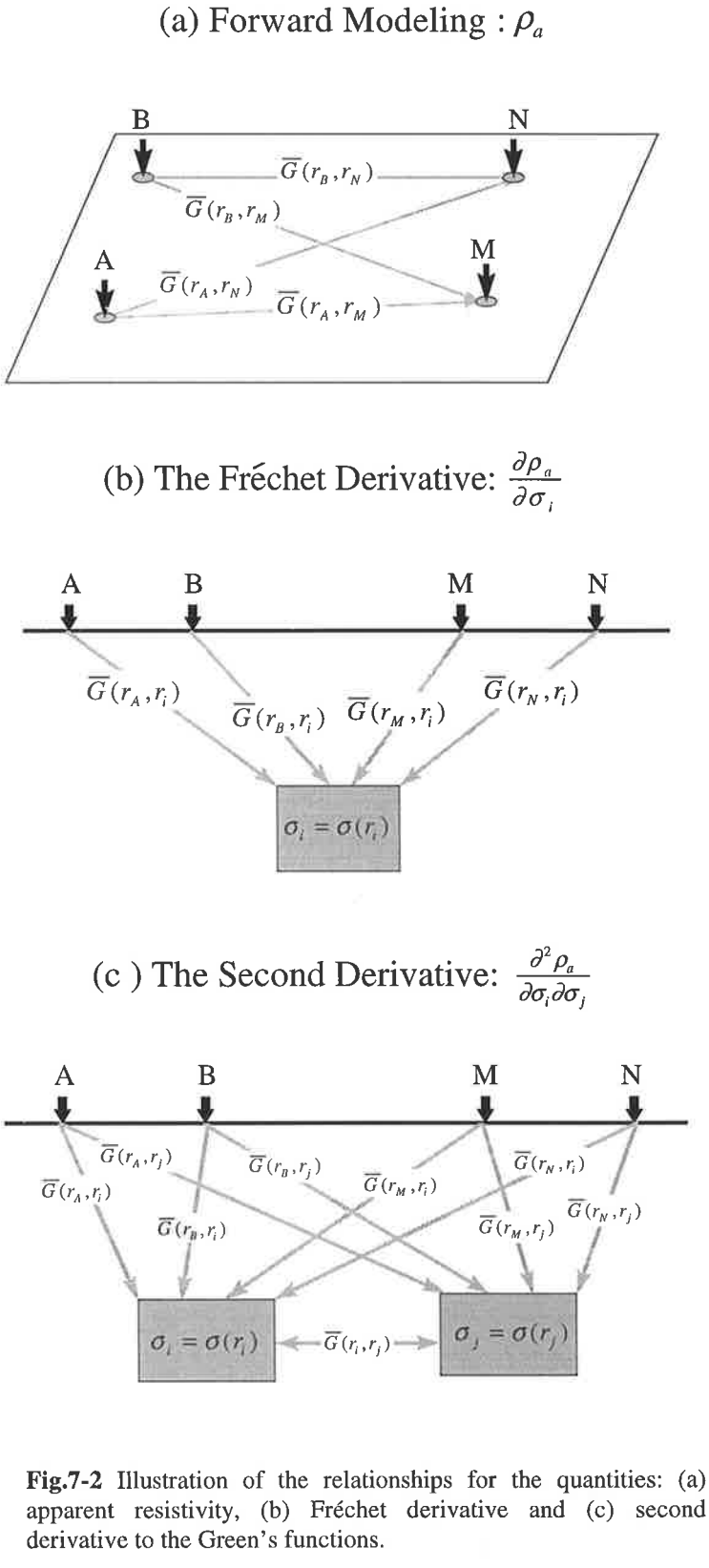

Fig.7-2 Illustration of the relationships for the quantities: (a) apparent resistivity, (b) Fréchet derivative and (c) second derivative to the Green's functions.

7.4 Explicit Expressions for 2.5-D Acoustic Waves

The defined boundary-valued problem for 2.5-D acoustic wave modeling in the frequency-domain can be expressed in operator form (see section 4.2):

$$\begin{cases} L(\hat{\rho},\hat{\kappa},k_y)\overline{\overline{P}} = -\dfrac{s(\omega)}{2}\delta(r-r_s), & r,r_s \in \Omega; \\ \dfrac{\partial \overline{\overline{P}}}{\partial n} + B\overline{\overline{P}} = 0, & r \in \partial\Omega; \end{cases} \tag{7.36}$$

where $$L(\hat{\rho},\hat{\kappa},k_y) = \nabla\cdot(\hat{\rho}\nabla) + (\omega^2\hat{\kappa} - \hat{\rho}k_y^2). \tag{7.37}$$

From results of previous chapters, the operator $L(\hat{\rho},\hat{\kappa},k_y)$ is still self-adjoint due to the symmetric property of B with the boundary integral (see Chapter 4). In fact, we have the integral identity similar to equation (7.19) for the acoustic case:

$$\int_\Omega \overline{\overline{v}} L(\hat{\rho},\hat{\kappa},k_y)\overline{\overline{u}}\, d\Omega = -\int_\Omega [\hat{\rho}\nabla\overline{\overline{v}}\cdot\nabla\overline{\overline{u}} + (\hat{\rho}k_y^2 - \hat{\kappa}\omega^2)\overline{\overline{v}}\,\overline{\overline{u}}]d\Omega - \int_{\partial\Omega}\hat{\rho}\overline{\overline{v}}B\overline{\overline{u}}\, ds. \tag{7.38}$$

Note that the operator $L(\hat{\rho},\hat{\kappa},k_y)$ is not linear with the model parameters: $\hat{\rho}$ and $\hat{\kappa}$ (different from the operator $L(\sigma,k_y)$ in the DC resistivity case) because of

$$L(\hat{\rho}_1 + \lambda\hat{\rho}_2,\hat{\kappa},k_y) = L(\hat{\rho}_1,\hat{\kappa},k_y) + \lambda L(\hat{\rho}_2,\hat{\kappa},k_y) - \lambda\omega^2\hat{\kappa}, \tag{7.39}$$

$$L(\hat{\rho},\hat{\kappa}_1 + \lambda\hat{\kappa}_2,k_y) = L(\hat{\rho},\hat{\kappa}_1,k_y) + \lambda\omega^2\hat{\kappa}_2. \tag{7.40}$$

In a similar way , in order to obtain the Fréchet and second derivatives of the wavefield with respect to $\hat{\rho}$ or $\hat{\kappa}$, we still resort to the perturbation state $\overline{\overline{P}}' = \overline{\overline{P}} + \delta\overline{\overline{P}}$ due to the variations $\hat{\rho}' = \hat{\rho} + \delta\hat{\rho}$ and $\hat{\kappa}' = \hat{\kappa} + \delta\hat{\kappa}$ with small quantities $\delta\overline{\overline{P}}$, $\delta\hat{\rho}$ and $\delta\hat{\kappa}$ (here we still assume $\delta\hat{\rho}$=0 on $\partial\Omega$). Firstly, we consider the wavefield perturbation $\delta\overline{\overline{P}}$ due to the change $\delta\hat{\rho}$. Calculating $L(\hat{\rho}+\delta\hat{\rho},\hat{\kappa},k_y)\overline{\overline{P}}'$ with the operator identity (7.39), we have

$$L(\hat{\rho},\hat{\kappa},k_y)\delta\overline{\overline{P}} = [\omega^2\hat{\kappa} - L(\delta\hat{\rho},\hat{\kappa},k_y)](\overline{\overline{P}} + \delta\overline{\overline{P}}). \tag{7.41}$$

Defining the conjugate Green's function of the acoustic wave:

$$\begin{cases} L(\hat{\rho},\hat{\kappa},k_y)\overline{\overline{G}}^{2.5D} = -\delta(r-r_g), & r,r_g \in \Omega, \\ \dfrac{\partial\overline{\overline{G}}^{2.5D}}{\partial n} + B\overline{\overline{G}}^{2.5D} = 0, & r \in \partial\Omega, \end{cases} \tag{7.42}$$

where $r_g = (x_g, z_g)$ is the position of a geophone in the (x,z)-plane (setting $y_g = 0$), and using the self-adjoint property of $L(\hat{\rho},\hat{\kappa},k_y)$ and the integral identity (7.38), the

implicit form for $\delta\overline{\overline{P}}$ can be obtained for a given frequency ω and wavenumber k_y:

$$\begin{aligned}\delta\overline{\overline{P}}(r_s,r_g) = &\int_\Omega [\nabla\overline{\overline{P}}(r_s,r)\cdot\nabla\overline{\overline{G}}^{2.5D}(r_g,r) + k_y^2\overline{\overline{P}}(r_s,r)\overline{\overline{G}}^{2.5D}(r_g,r)]\delta\hat{\rho}dr + \\ &+\int_\Omega \delta\overline{\overline{P}}(r_s,r)[L(\delta\hat{\rho},\hat{\kappa}) - \omega^2\overline{\kappa}]\overline{\overline{G}}^{2.5D}(r_g,r)dr.\end{aligned} \tag{7.43}$$

Here we also omit k_y in the variable set so as to shorten the expression. Using the Fréchet differentiable property of $\overline{\overline{P}}(r_s,r_g)$, we still have the expression (7.23) for $\delta\overline{\overline{P}}(r_s,r)$ due to $\delta\hat{\rho}$. Substituting the expression into the second integral in equation (7.43) results in:

$$\begin{aligned}\delta\overline{\overline{P}}(r_s,r_g) = &\int_\Omega \overline{\overline{D}}_1(r_s,r_g,r)\delta\hat{\rho}dr - \frac{1}{2}\int_\Omega\int_\Omega \{\nabla\overline{\overline{D}}_1(r_s,r,r')\cdot\nabla\overline{\overline{G}}^{2.5D}(r_g,r) \\ &\nabla'\overline{\overline{D}}_1(r_s,r',r)\cdot\nabla'\overline{\overline{G}}^{2.5D}(r_g,r') + k_y^2[\overline{\overline{D}}_1(r_s,r,r')\overline{\overline{G}}^{2.5D}(r_g,r) \\ &+\overline{\overline{D}}_1(r_s,r',r)\overline{\overline{G}}^{2.5D}(r_g,r')]\}\delta\hat{\rho}\delta\hat{\rho}'dr'dr + O(\|\delta\hat{\rho}\|^3),\end{aligned} \tag{7.44}$$

where $$\overline{\overline{D}}_1(r_s,r_g,r) = -[\nabla\overline{\overline{P}}(r_s,r)\cdot\nabla\overline{\overline{G}}^{2.5D}(r_g,r) + k_y^2\overline{\overline{P}}(r_s,r)\overline{\overline{G}}^{2.5D}(r_g,r)]. \tag{7.45}$$

It can be found that this result is the same as equation (7.25) except for the physical significance of the parameters. So, the Fréchet and second derivatives of the acoustic wavefield with respect to the density ρ have the same expressions as in the DC resistivity case. From equation (7.44) they can be obtained with the constant-point or constant-block approximation, e.g. the Fréchet derivatives with constant-point and constant-block approximations are given by

$$\frac{\partial\overline{\overline{P}}(\omega,r_s,r_g)}{\partial\rho_i} = \frac{s(\omega)}{2\rho_i^2}F_c^{-1}[\nabla\overline{\overline{G}}^{2.5D}(r_s,r_i)\cdot\nabla\overline{\overline{G}}^{2.5D}(r_g,r_i) + k_y^2\overline{\overline{G}}^{2.5D}(r_s,r_i)\overline{\overline{G}}^{2.5D}(r_g,r_i)], \tag{7.46}$$

$$\frac{\partial\overline{\overline{P}}(\omega,r_s,r_g)}{\partial\rho_i} = \frac{s(\omega)}{2\rho_i^2}F_c^{-1}\{\int_{\Omega_e}[\nabla\overline{\overline{G}}^{2.5D}(r_s,r_i)\cdot\nabla\overline{\overline{G}}^{2.5D}(r_g,r_i) + k_y^2\overline{\overline{G}}^{2.5D}(r_s,r_i)\overline{\overline{G}}^{2.5D}(r_g,r_i)]dr\}, \tag{7.47}$$

respectively. Here we have used the identities: $\overline{\overline{P}} = s(\omega)\overline{\overline{G}}^{2.5D}/2$ and $\partial\hat{\rho}/\partial\rho = -1/\rho^2$.

In the same manner, one can use the operator identity (7.40) and the adjoint Green's function (7.41) to obtain the expressions of the derivatives with respect to the bulk modulus $\hat{\kappa} = \hat{\kappa} + \delta\hat{\kappa}$ (density does not change). For practical applications, we prefer using the model parameter c (acoustic wavespeed) to $\hat{\kappa}$. So, in the constant-density case, the operator (7.37) is commonly expressed by (see equation 2.25)

$$L(c,k_y)=\nabla\cdot\nabla+(\omega^2/c^2-k_y^2)\,, \tag{7.48}$$

which is still self-adjoint but non-linear with c. Rewriting the operator as follows for the perturbation state $c'=c+\delta c$:

$$\begin{aligned} L(c',k_y)=L(c+\delta c,k_y)&=\nabla^2+k^2(1+\frac{\delta c}{c})^{-2}-k_y^2,\\ &=\nabla^2+(k^2-k_y^2)-k^2[\frac{2\delta c}{c}-\frac{3\delta c^2}{c^2}+O(\|\delta c\|^3],\\ &=L(c,k_y)-k^2[\frac{2\delta c}{c}-\frac{3\delta c^2}{c^2}+O(\|\delta c\|^3], \end{aligned} \tag{7.49}$$

and multiplying with $(\overline{\overline{P}}+\overline{\overline{\delta P}})$, we have the perturbation equation

$$L(c,k_y)\overline{\overline{\delta P}}=k^2[\frac{2\delta c}{c}-\frac{3\delta c^2}{c^2}+O(\|\delta c\|^3)](\overline{\overline{P}}+\overline{\overline{\delta P}})\,. \tag{7.50}$$

Applying the conjugate Green's function again to equation (7.50), we obtain another implicit integral equation for $\overline{\overline{\delta P}}(r_s,r_g)$ due to δc:

$$\begin{aligned} \overline{\overline{\delta P}}(r_s,r_g)=-\int_\Omega[&\frac{2\omega^2}{c^3}\overline{\overline{P}}(r_s,r)\overline{\overline{G}}^{2.5D}(r_g,r)\delta c+\frac{2\omega^2}{c^3}\overline{\overline{\delta P}}(r_s,r)\\ &\cdot\overline{\overline{G}}^{2.5D}(r_g,r)\delta c-\frac{3\omega^2}{c^3}\overline{\overline{P}}(r_s,r)\overline{\overline{G}}^{2.5D}(r_g,r)\delta c^2]dr+O(\|\delta c\|^3), \end{aligned} \tag{7.51}$$

from which we obtain the explicit equation of $\overline{\overline{\delta P}}(r_s,r_g)$ by substituting the similar expression (7.23) for $\overline{\overline{\delta P}}(r_s,r)$:

$$\begin{aligned} \overline{\overline{\delta P}}(r_s,r_g)=\int_\Omega\overline{\overline{D}}_1(r_s,r_g,r)\delta c\,dr+\frac{1}{2}\int_\Omega\int_\Omega[&-\frac{2\omega^2}{c^3(r)}\overline{\overline{G}}^{2.5D}(r_g,r)\overline{\overline{D}}_1(r_s,r,r')\\ &-\frac{2\omega^2}{c^3(r')}\overline{\overline{G}}^{2.5D}(r_g,r')\overline{\overline{D}}_1(r_s,r',r)+\frac{3\omega^2}{c^4(r)}\overline{\overline{P}}(r_s,r)\cdot\\ &\overline{\overline{G}}^{2.5D}(r_g,r)\delta(r-r')]\delta c\,\delta c'drdr'+O(\|\delta c\|^3), \end{aligned} \tag{7.52}$$

where

$$\overline{\overline{D}}_1(r_s,r_g,r)=-\frac{2\omega^2}{c^3}\overline{\overline{P}}(r_s,r)\overline{\overline{G}}^{2.5D}(r_g,r)\,. \tag{7.53}$$

So, the Fréchet and second derivatives with respect to the wavespeed c can be directly written out in the constant-point approximation form:

$$\frac{\partial\overline{P}(\omega,r_s,r_g)}{\partial c_i}=-\frac{\omega^2}{c_i^3}s(\omega)F_c^{-1}[\overline{\overline{G}}^{2.5D}(r_s,r_i)\overline{\overline{G}}^{2.5D}(r_g,r_i)], \tag{7.54}$$

$$\frac{\partial^2 \overline{P}(\omega, r_s, r_g)}{\partial c_i \delta c_j} = s(\omega)\{\frac{\omega^4}{c_i^3 c_j^3} F_c^{-1}\{[\overline{\overline{G}}^{2.5D}(r_g, r_i)\overline{\overline{G}}^{2.5D}(r_s, r_j) + \overline{\overline{G}}^{2.5D}(r_s, r_i) \cdot \overline{\overline{G}}^{2.5D}(r_g, r_j)]\overline{\overline{G}}^{2.5D}(r_i, r_j) + \frac{3\omega^2}{2c_i^4} F_c^{-1}\{\overline{\overline{G}}^{2.5D}(r_s, r_i)\overline{\overline{G}}^{2.5D}(r_g, r_i)\delta(r_i - r_j)\}\}. \tag{7.55}$$

and in the constant-block approximation form:

$$\frac{\partial \overline{P}(\omega, r_s, r_g)}{\partial c_e} = -\frac{\omega^2}{c_e^3} s(\omega) F_c^{-1}[\int_{\Omega_e} \overline{\overline{G}}^{2.5D}(r_s, r)\overline{\overline{G}}^{2.5D}(r_g, r)dr], \tag{7.56}$$

$$\frac{\partial^2 \overline{P}(\omega, r_s, r_g)}{\partial c_e \delta c_{e'}} = s(\omega) F_c^{-1}\{\frac{\omega^4}{c_e^3 c_{e'}^3} \int_{\Omega_e}\int_{\Omega_{e'}} [\overline{\overline{G}}^{2.5D}(r_g, r)\overline{\overline{G}}^{2.5D}(r_s, r') + \overline{\overline{G}}^{2.5D}(r_s, r) \cdot \overline{\overline{G}}^{2.5D}(r_g, r')]\overline{\overline{G}}^{2.5D}(r, r')drdr' + \frac{3\omega^2}{2c_e^4} \int_{\Omega_e}\int_{\Omega_{e'}} \overline{\overline{G}}^{2.5D}(r_s, r)\overline{\overline{G}}^{2.5D}(r_g, r)\delta(r - r')drdr'\}. \tag{7.57}$$

The Fréchet derivatives (7.46) or (7.47) and (7.54) or (7.56) and the second derivative (7.55) or (7.57) may be applied to non-linear full-waveform inversion with the acoustic spectral data $\overline{P}(\omega, r_s, r_g)$.

Reviewing equation (2.31) and all of the above expressions for the Fréchet and second derivatives, one can find that the quantities: $\overline{P}$, $\partial \overline{P} / \partial c_i$ and $\partial^2 \overline{P} / \partial c_i \partial c_j$ in the 2.5-D acoustic wave problem are also calculated by the Green's functions. The relationships between the Green's functions and the various quantities are shown in Fig.7-3. Note that different numbers of the Green's functions are required in the various computations.

7.5 Numerical Algorithms

From the formulations of the previous two sections, the Fréchet and second derivatives can be explicitly represented by the 2.5-D Green's functions for an arbitrary medium. These expressions imply a two-step procedure to compute the derivatives. Firstly, some numerical method such as the FEM may be applied to calculate the numerical solution of the 2.5-D Green's function (just like the forward modeling), then substituting the solution into the explicit expressions the derivatives can be calculated for arbitrary media. So the Green's functions are the basic quantities for calculating the synthetic data and the derivatives. The first step has actually been solved in Chapter 3 and 4, e.g. the computation of the 2.5-D Green's functions for DC resistivity or acoustic wave problems is reduced to solving the linear equation system (7.13) where $A(m, k_y)$ may be

$A(\sigma,k_y)$ in the DC resistivity case or $A(\omega,c,k_y)$ in the acoustic wave case. $A(\sigma,k_y)$ is a sparse, symmetric and positive definite real matrix so that the LL^T decomposition algorithm was used for solving equation (7.13). $A(\omega,c,k_y)$ is also a sparse and symmetric, but complex matrix, so the LU decomposition algorithm was employed. The Green's function $G^{2.5D}=\overline{G}^{2.5D}$ or $\overline{\overline{G}}^{2.5D}$ is actually obtained by backsubstitution after the decomposition.

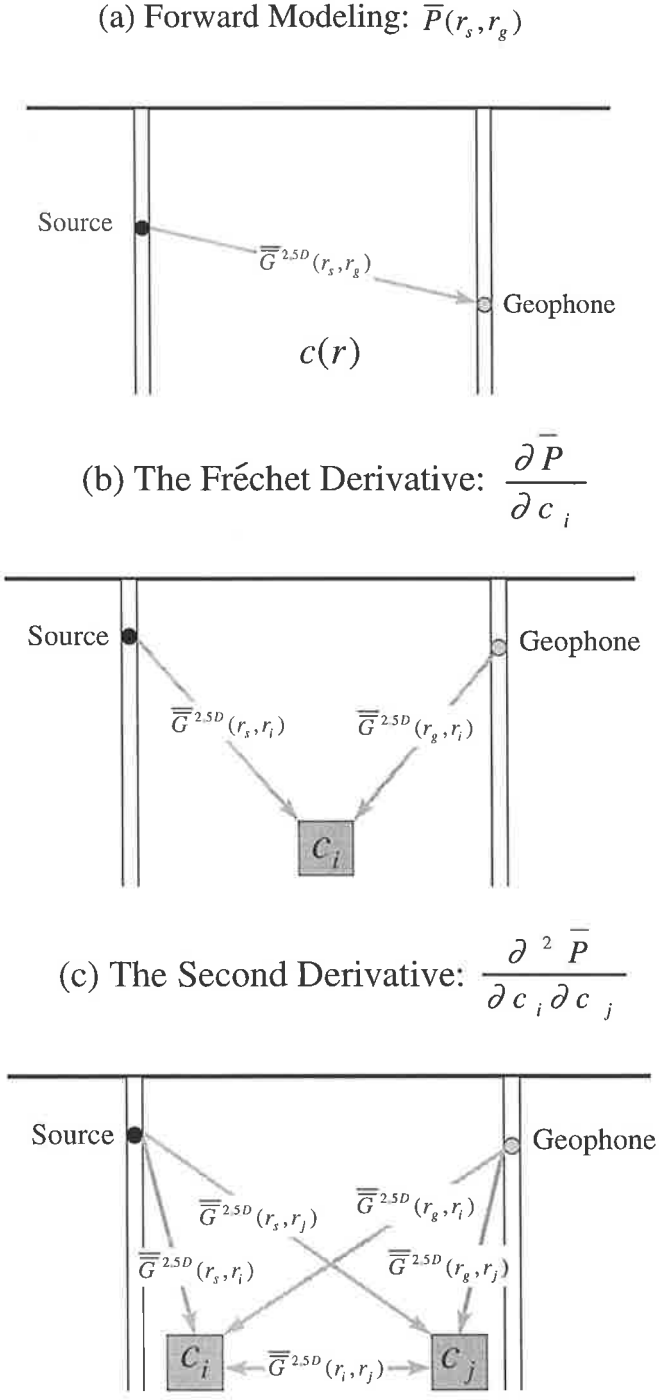

Fig.7-3 Illustration of the relationships of the quantities: (a) pressure wavefield, (b) Fréchet derivative and (c) second derivative to the Green's functions.

For forward modeling, as discussed in Chapter 3 and 4, the synthetic data U_{MN} or $\overline{P}(\omega,r_s,r)$ are calculated by the Greens' functions associated with the source positions, viz. $\delta\overline{G}_{AB}(r)=\overline{G}(r_A,r)-\overline{G}(r_B,r)$ or $\overline{\overline{G}}^{2.5D}(r_s,r)$ (see equations (2.30), (2.31) and Fig.7-2a, Fig.7-3a). This means that if we have N_S source-position points in a field measurement and N_y samples of k_y in the k_y-domain, we need to solve the linear system equations (7.13) $N_y \times N_S$ times to obtain the synthetic data, exactly. There will be N_y runs of the LL^T or LU decomposition for $A(\sigma,k_y)$ or $A(\omega,c,k_y)$ and

$N_y \times N_S$ operations of the backsubstitution algorithm for the Green's functions (see Fig.3-7 and Fig.4-4).

Reviewing the expressions (7.32) in the DC resistivity case or equations (7.46) and (7.54) in the acoustic wave case, the Fréchet derivative include two types of Green's functions: $\delta\overline{G}_{AB}(r)=\overline{G}^{2.5D}(r_A,r)-\overline{G}^{2.5D}(r_B,r)$ and $\delta\overline{G}_{MN}(r)=\overline{G}^{2.5D}(r_M,r)-\overline{G}^{2.5D}(r_N,r)$ or $\overline{\overline{G}}^{2.5D}(r_s,r)$ and $\overline{\overline{G}}^{2.5D}(r_g,r)$ (see Fig.7-2b and Fig.7-3b), which relate to the source-position points: (r_A, r_B or r_s) and receiver-position points: (r_M, r_N or r_g). For clarity, we call the first one the source-position Green's function and the second one the receiver-position Green's function (called adjoint Green's function), respectively. This means that to compute the Fréchet derivative, the computations for all the receiver-position Green's functions $\delta\overline{G}_{MN}(r)$ or $\overline{\overline{G}}^{2.5D}(r_g,r)$ must be done in addition to all the source-position Green's functions (for the synthetic data). This is simply implemented by replacing the source vector $b_{c,s}$ in equation (7.13) with the receiver vector b_R whose components are zero except for the one whose position coincides with the receiver-position point: r_M, r_N or r_g and then solving the equations. In other words, if we have N_R receiver-position points in the field measurement, the additional effort is just N_R times the backsubstitution involved for the forward computations at each k_y when solving equation (7.13). In total, it requires N_y times the LL^T or LU decomposition for $\mathrm{A}(\sigma,k_y)$ or $\mathrm{A}(\omega,c,k_y)$ and $N_y \times (N_S + N_R)$ times the backsubstitution for all the Green's functions.

From the expressions of the second derivatives, e.g. equations (7.33) and (7.55), we see that the Green's function: $\overline{G}^{2.5D}(r,r')$ or $\overline{\overline{G}}^{2.5D}(r,r')$ ($r,r' \in \Omega$, see $\overline{\overline{G}}^{2.5D}(r_i,r_j)$ in Fig.7-2c and Fig.7-3c) is involved besides the two types of the Green's functions mentioned above. In the discrete case, if there are N_X and N_Z nodes in the *x*- and *z*-directions of a rectangular imaging range ($\subset \Omega$), to get $\overline{G}^{2.5D}(r,r')$ or $\overline{\overline{G}}^{2.5D}(r,r')$ is equivalent to obtaining $\overline{G}^{2.5D}(r_i,r_j)$ or $\overline{\overline{G}}^{2.5D}(r_i,r_j)$ for all the nodes ($i,j = 1,2,\ldots,N_Z \times N_X$). This can be done by replacing the source vector $b_{c,s}$ in

equation (7.13) with the vector $\overline{\delta_i} = (0,0,\ldots,\delta_{ij},0,0,\ldots,0)$,$(i = 1,2,\ldots,N_Z \times N_X)$ and then solving the equations. Obviously, $\overline{G}^{2.5D}(r_i,r_j)$ or $\overline{\overline{G}}^{2.5D}(r_i,r_j)$ includes all the source- and receiver-position Green's functions $\overline{G}^{2.5D}(r_{c=A,B},r_j)$ and $\overline{G}^{2.5D}(r_{p=M,N},r_j)$ or $\overline{\overline{G}}^{2.5D}(r_s,r_j)$ and $\overline{\overline{G}}^{2.5D}(r_g,r_j)$, because the source- and receiver-position nodes are included in the total nodes, e.g. $\{ r_{c=A,B}, r_{p=M,N} \}$ or $\{ r_s, r_g \} \in \{r_i, i = 1,2,..N_Z \times N_X \}$ and normally $(N_S + N_R) << (N_Z \times N_X)$. So, the computational work to obtain all the Green's functions is evaluated as N_y times the LL^T or LU decomposition for $\mathrm{A}(\sigma,k_y)$ or $\mathrm{A}(\omega,c,k_y)$ and $N_y \times (N_Z \times N_X)$ times the backsubstitution.

For comparison, the computational effort for the Green's functions are given in Table7-1:

Table 7-1 Computational effort for the Green's functions

Task	LL^T or LU (times)	backsubstitution (times)	Max. array: $G^{2.5D} = \overline{G}^{2.5D}$ or $\overline{\overline{G}}^{2.5D}$
synthetic data	N_y	$N_y \times N_S$	$G^{2.5D}(N_y, N_S, N_Z \times N_X)$
Fréchet derivative	N_y	$N_y \times (N_S + N_R)$	$G^{2.5D}(N_y, N_S + N_R, N_Z \times N_X)$
Second derivative	N_y	$N_y \times (N_Z \times N_X)$	$G^{2.5D}(N_y, N_Z \times N_X, N_Z \times N_X)$

which says that the additional work to obtain the Green's functions for the Fréchet and second derivatives only increases the backsubstitutions of the linear equations (7.13). Fortunately, the backsubstitution does not cost much computer time, but the memory required for the second derivative is much larger than that for others.

After obtaining all the Green's functions (first step), one is ready to calculate the synthetic data, the Fréchet and second derivatives (second step). As mentioned above, the first step is not computer-time intensive and the computer program is nearly the same as normal forward modeling. The second step takes the major computer-time in calculations for the derivatives. In view of the previous formulations, there are two

approximations for the derivatives: constant-point and constant-block model parameterizations. The former is simpler than the latter due to the avoidance of the integral over the constant block, especially for a large-scale inversion (lots of unknown model parameters to be determined), but the latter has the advantage that it enables one to reduce the number of inversion parameters by choosing a few of the blocks σ_e or c_e ($e = 1,2,\ldots,N_e$) in the inversion. Also one can find that the second step involves the computations of the gradients $\nabla\delta\overline{G}_{AB}(r)$ and $\nabla\delta\overline{G}_{MN}(r)$ (see equations (7.32)) or $\nabla\overline{\overline{G}}^{2.5D}(r_s,r)$ and $\nabla\overline{\overline{G}}^{2.5D}(r_g,r)$ (see equation (7.46)) for the Fréchet derivative, and $\nabla\nabla\overline{G}^{2.5D}(r_i,r_j)$ or $\nabla\nabla\overline{\overline{G}}^{2.5D}(r_i,r_j)$ (see equation (7.33)) for the second derivative. To compute the gradients, the following approximation may be applied:

$$(\frac{\partial G}{\partial \xi}) \approx b(\xi) + 2c(\xi)\xi, , \quad (5.53)$$

where $\xi = x,z$ and

$$b(\xi) = \frac{1}{\Delta(\xi)}\begin{vmatrix} 1 & G_{i,j-1} & \xi_{-1}^2 \\ 1 & G_{i,j} & \xi^2 \\ 1 & G_{i,j+1} & \xi_{+1}^2 \end{vmatrix},$$

$$c(\xi) = \frac{1}{\Delta(\xi)}\begin{vmatrix} 1 & \xi_{-1} & G_{i,j-1} \\ 1 & \xi & G_{i,j} \\ 1 & \xi_{+1} & G_{i,j+1} \end{vmatrix},$$

$$\Delta(\xi) = \begin{vmatrix} 1 & \xi_{-1} & \xi_{-1}^2 \\ 1 & \xi & \xi^2 \\ 1 & \xi_{+1} & \xi_{+1}^2 \end{vmatrix}, \quad (7.59)$$

and $G_{i,j}$ is the value of the Green's function at the node (x_i,z_j) $(i = 2,3,\ldots,N_X - 1;$

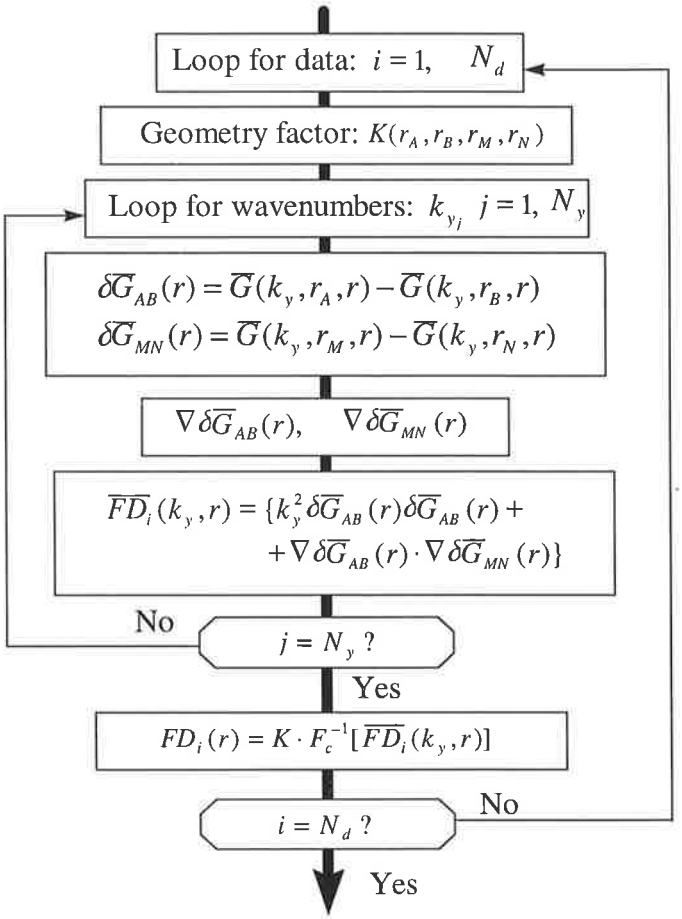

Fig.7-4 Flow-chart for computation of the Fréchet derivative with the constant-point approximation in the DC resistivity case.

$j = 2,3,\ldots,N_z - 1$). It must be mentioned that when considering the constant-density approximation in the acoustic wave case, both the Fréchet and second derivatives do not require the gradient computation and only use the Green's functions (see equation (7.54)-(7.57)). So it is much simpler than that in the variable density case. Fig.7-4 and Fig.7-5 give the flow-charts for computation of the Fréchet derivative in the DC resistivity and acoustic wave cases, both of which are based on the constant-point model parameterization formulas. Due to the similar expressions between $\frac{\partial U}{\partial \sigma}$ and $\frac{\partial \overline{P}}{\partial \rho}$, an algorithm for $\frac{\partial \overline{P}}{\partial \rho}$ can be adopted from Fig.7-4. An example of the constant-block approximation is given in Appendix D where the rectangular geometry of the block is chosen so that the integral over the block is analytically calculated. From

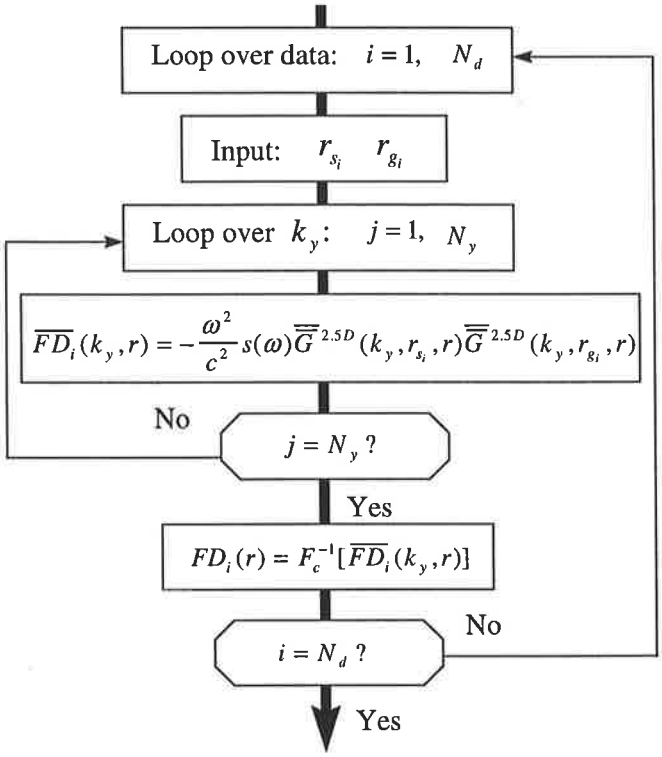

Fig.7-5 Flow-chart for computation of the Fréchet derivative with the constant-point approximation in the 2.5-D acoustic case.

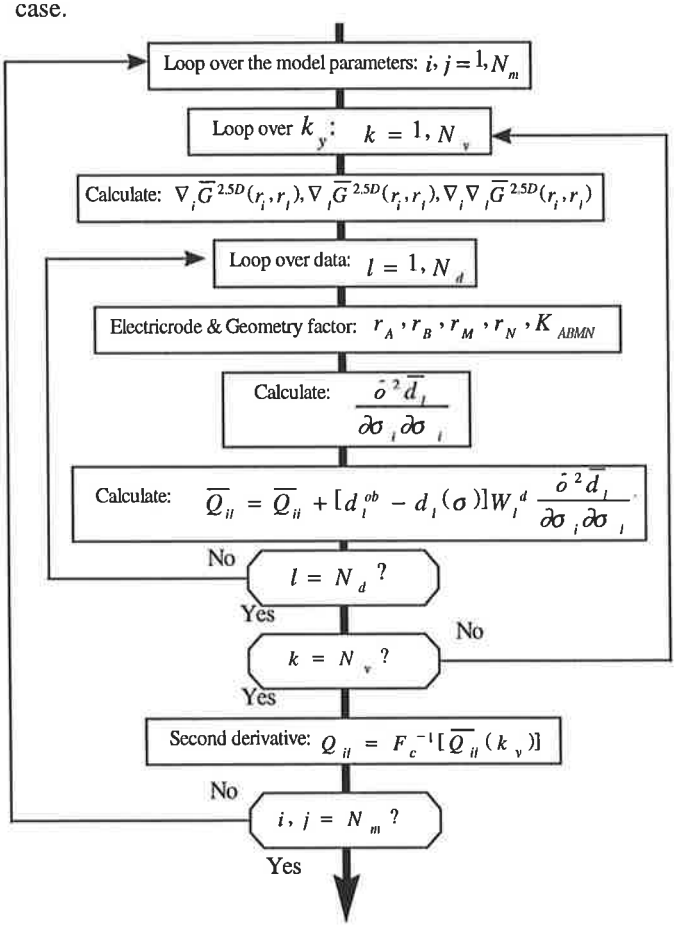

Fig.7-6 Flow-chart for computation of the second derivative with the constant-point approximation in the DC resistivity case.

numerical tests (see next section), the results of the approximation are very similar to those of the constant-point approximation, but the constant-point approximation for computing the Fréchet derivative is a faster scheme to form the Jacobian matrix for a large scale inverse problem (Zhou and Greenhalgh, 1995).

As an example of the computation of the second derivative, Fig.7-6 gives the flow-chart based on equations (7.28) and (7.33) in DC resistivity surveying. For the 2.5-D acoustic case, the computational scheme for the derivative with respect to density is similar to Fig.7-4; for $\partial^2 \overline{P} / \partial c_i \partial c_j$, it is much simpler than this in terms of equation (7.55).

7.6 Synthetic Examples

To investigate the patterns of the Fréchet and the second derivatives, we use the above algorithms to compute them, first in a homogeneous medium and then in some specified inhomogeneous media. They are given for both DC resistivity surface surveying and crosshole seismic surveying configurations. These patterns are helpful to understand the sensitivity of different practical measurement configurations.

(1) Patterns in a Homogeneous Background

Fig.7-7 and Fig.7-8 are the Fréchet derivatives with constant-point and constant-block approximations for pole-pole, pole-bipole, bipole-pole and bipole-bipole measurements

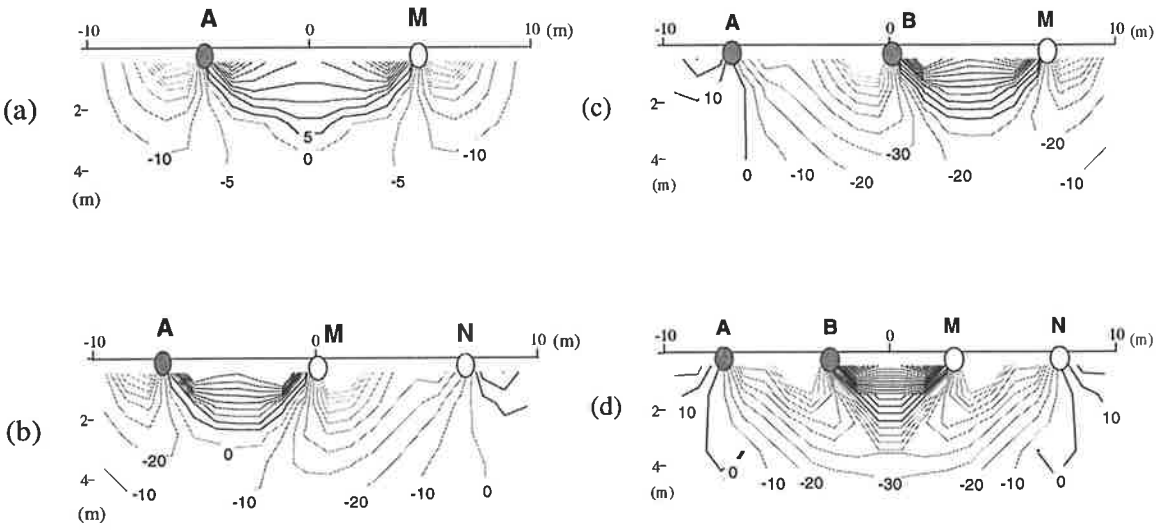

Fig.7-7 The Fréchet derivative ($\partial U/\partial \sigma$) obtained with the constant-point approximation for (a) pole-pole, (b) pole-bipole, (c) bipole-pole and (d) bipole-bipole arrays in a uniform medium (ρ=100 Ωm).

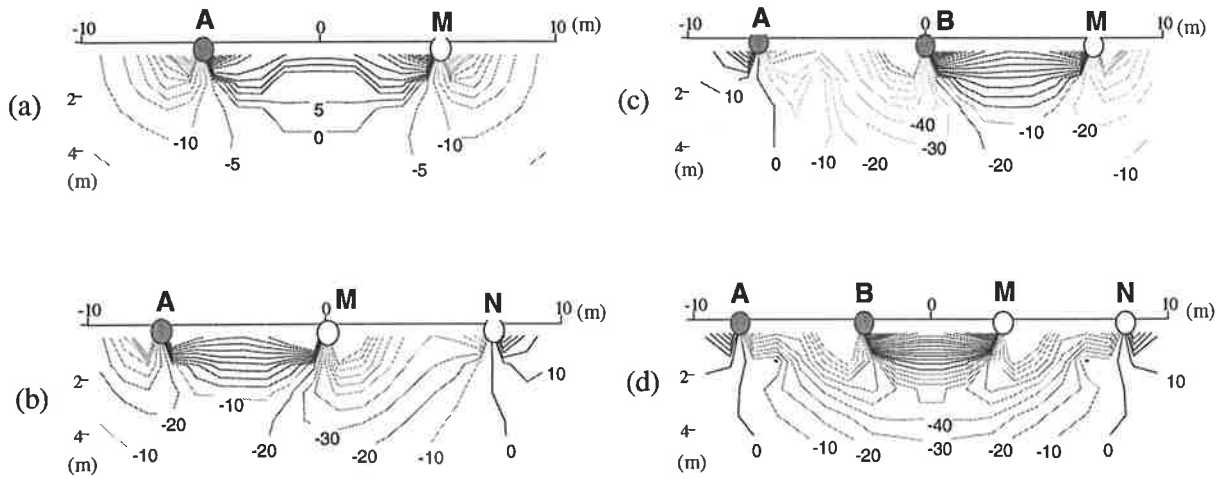

Fig.7-8 The Fréchet derivatives ($\partial U/\partial\sigma$) obtained with the constant-block approximation for (a) pole-pole, (b) pole-bipole, (c) bipole-pole and (d) bipole-bipole arrays in a uniform medium (ρ=100 Ωm).

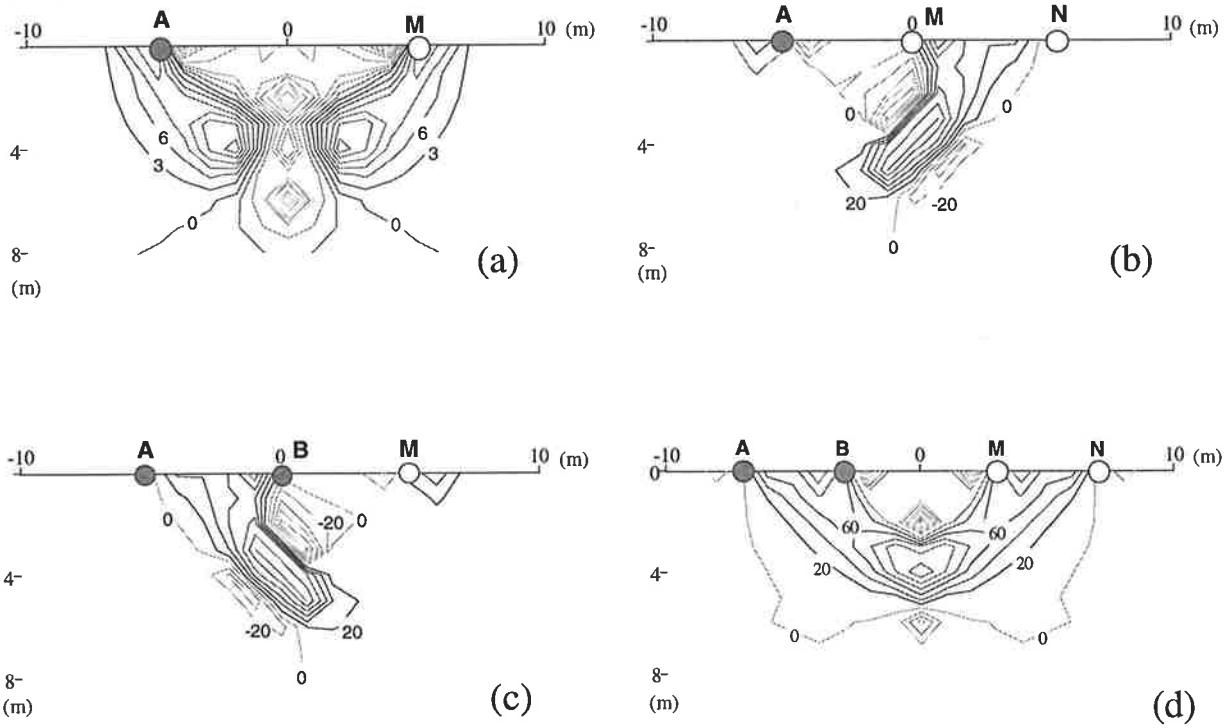

Fig.7-9 The second derivatives obtained with the constant-point approximation for (a) pole-pole, (b) pole-bipole, (c) bipole-pole and (d) bipole-bipole arrays in a uniform medium (100 ohm-m). The point *p* is located at (0,5).

on the surface over a uniform earth. Fig.7-9 shows the patterns of the second derivatives of these arrays. In these computations, a uniform background (100 Ωm) and $1\times1\ m^2$ element-size were used. From these examples, one can see that the two approximations give very similar results, but as mentioned before, the computation with the constant-point approximation is much faster than that with constant-block approximation for a large number of model parameters, because the integral over the constant-block is not required with the constant-point approximation. In Fig.7-9, the point: p= (0, 5) was fixed for computing ($\partial^2\rho_a / \partial\sigma_p\partial\sigma$). These figures show *two features: (1) the different surveying configurations have different patterns of the Fréchet derivatives in which the most of significant values appear around the electrodes (see Fig.7-7 or Fig.7-8); (2) the second derivatives of these four kinds of electrode arrays also have different patterns and they quite differ from the Fréchet derivatives, that is, the significant values of the derivatives no longer appear around the electrode but around the fixed point p= (0, 5)* (see Fig.7-9). As is well known, the derivatives, as sensitivity functions of a certain surveying configuration, represent the data variation corresponding to a small disturbance in the model parameter at each spatial point. The larger values mean greater weights in the inversion. The two features reflect that the two derivatives have different sensitivity properties to the spatial model parameters, that is, the Fréchet derivative is sensitive to the model parameters around the electrodes, but the second derivative is sensitive to the model parameters just around the point in question. It seems that the two derivatives would play different and complementary roles in inversion.

Fig.7-10 and Fig.7-11 are the Fréchet and second derivatives for the 2.5-D acoustic wavefield. In these computations, a uniform background (c=3000 km/s), $\delta(t)$-source, and $1\times1\ m^2$ element-size are used. One finds that the derivatives have quite different features from the DC resistivity case. The significant values of the Fréchet derivative are not only near the source at (-10, 15) and the receiver at (10,15) but also radiate out from the source and converge on the receiver (called frequency-domain ray-path, see Fig.7-10). From Fig.7-11, one can see that the absolute values of the second derivatives are much smaller than the Fréchet derivatives. It seems that the second derivatives have a lesser weighting effect if involved in an inversion than the Fréchet derivative does.

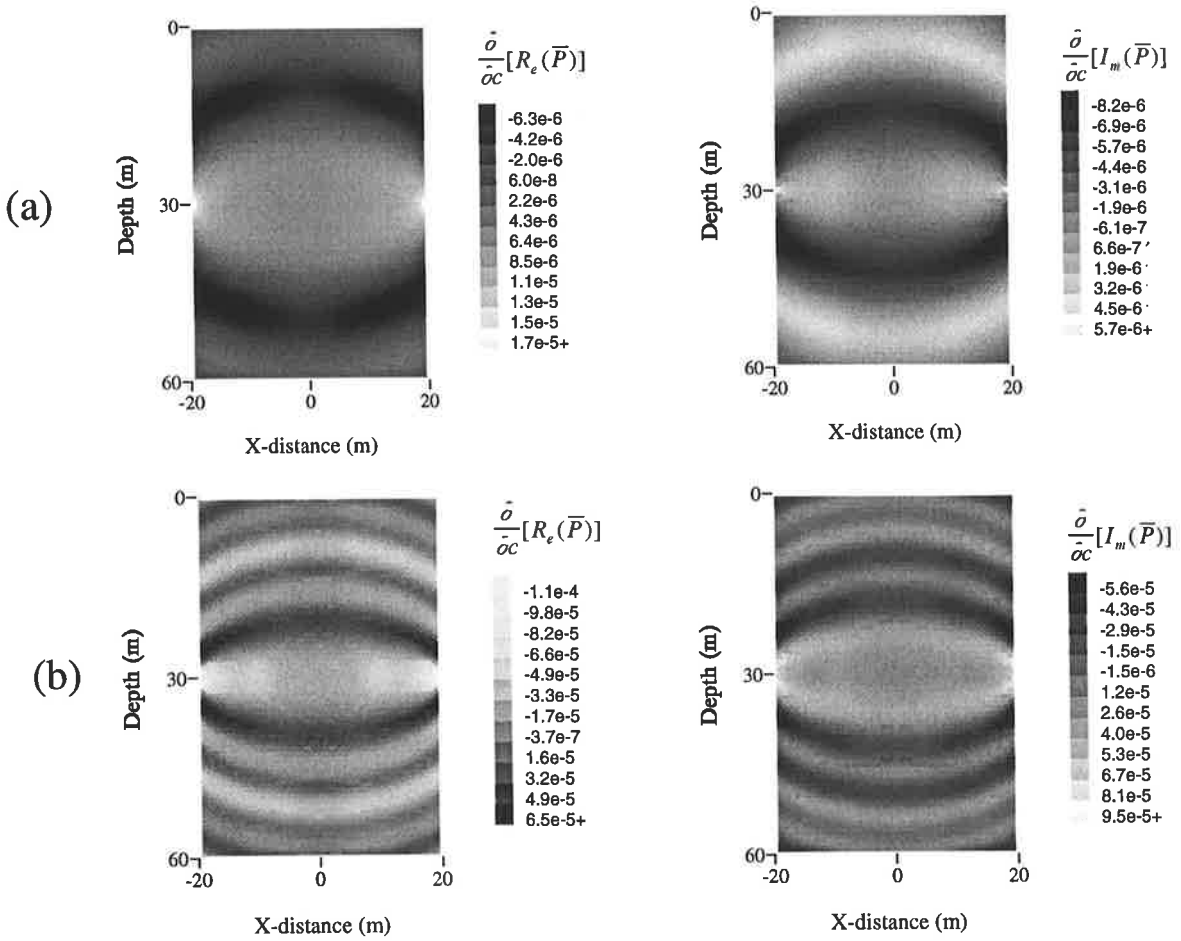

Fig.7-10 The Fréchet derivatives of the 2.5-D acoustic wavefield at (a) f=100 Hz and (b) f=300 Hz in a uniform background (c=3000 m/s). Source and receiver located at (-20,30) and (20,30), respectively.

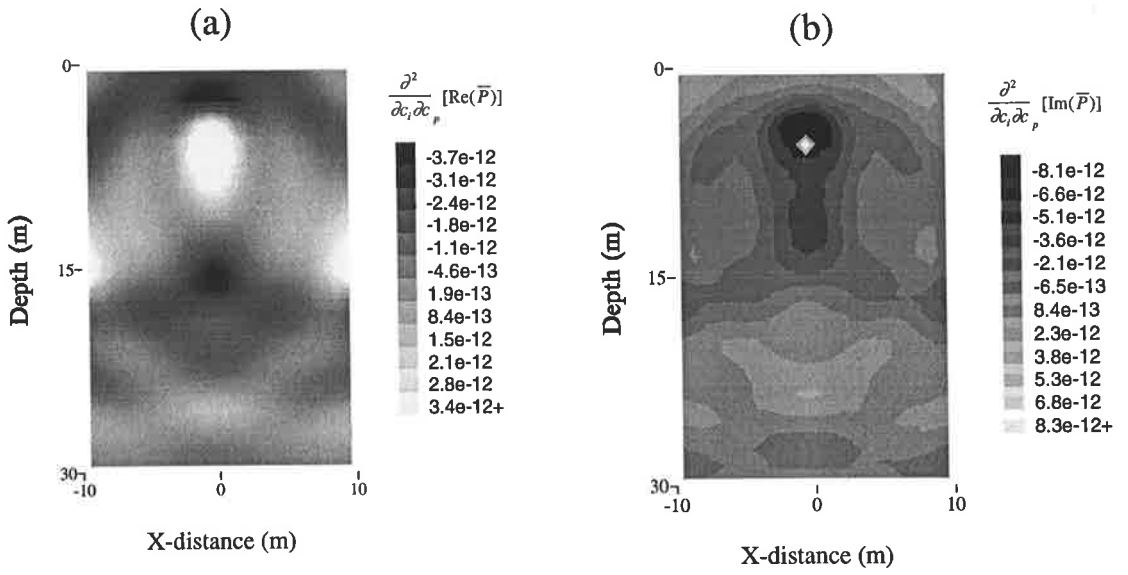

Fig.7-11 The second derivatives of the 2.5-D acoustic wavefield in the frequency-domain (f=300 Hz): (a) real and (b) imaginary components. Source and receiver locate at (-20,30) and (20,30). The point p is located at (0,5).

(2) Patterns for Imhomogeneous Models

In order to show the patterns of the derivatives in an inhomogeneous medium, we calculated the Fréchet derivatives for two-layer models using pole-pole and bipole-bipole arrays. Fig.7-12 gives the results of two separations of the pole-pole array for two-layered models with resistive and conductive basements. This figure shows that the Fréchet derivative or sensitivity values in the resistive basement are very small (see Fig.7-12a, b), but in the conductive basement they have much larger values and with an increase in the separation of the two electrodes the sensitive area becomes larger and larger (see Fig.7-12c,d). This implies that the pole-pole array has a different sensitivity to a conductive basement than to a resistive basement. It seems that the pole-pole array is more sensitive to the conductive basement. Fig.7-13 shows the results of bipole-bipole arrays. From this figure one can find similar features to the pole-pole array shown in Fig.7-12, but in both cases of a resistive basement and conductive basement, the bipole-bipole array has a larger gradient in the first layer than the pole-pole array does. This implies that *the bipole-bipole array is more sensitive to the shallow part of the ground than the pole-pole array.* This is consistent with the feature of the ρ_a-pseudosection in our modeling results for resistivity profiling (see Fig.3-10). Fig.7-14 shows the patterns of the Fréchet derivative of pole-pole and bipole-bipole arrays in another inhomogeneous model, in which a resistive target (1000Ωm) and a conductive target (10Ωm) are embedded in a homogenous background (100Ωm). This figure shows that the significant sensitive values appear around the conductive target, not in the area of the resistive target. It means that *both pole-pole and bipole-bipole arrays are much more sensitive to a conductive target than to a resistive target in surface resistivity surveying.* It will be proved in Chapter 8 that due to these patterns a conductive target can be more clearly imaged by inverse processing than a resistive target in the same DC resistivity profiling.

Fig.7-15 gives the Fréchet derivative patterns at 300 Hz for crosshole acoustic measurements in rectangular-shaped anomaly models. In the computations, we put a low-velocity rectangle (1 km/s, see Fig.7-15a,b) and a high-velocity rectangle (5 km/s, see Fig.7-15c,d) at the center and assign the background velocity of 3 km/s. A source and a receiver are located at (-20,30) and (20,30) respectively. Comparing this figure with Fig.7-10b, it shows the variation of the Fréchet derivative patterns due to the

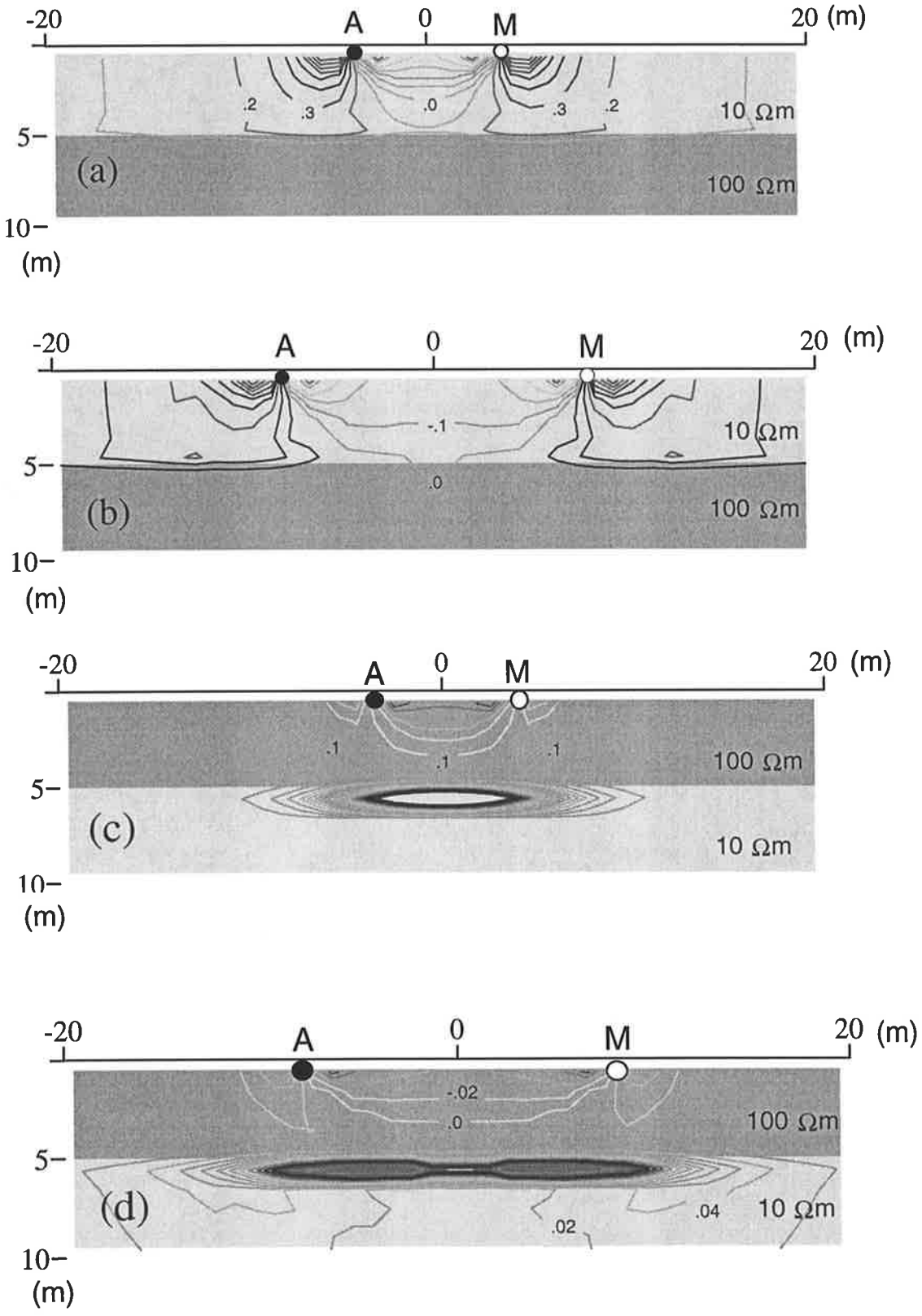

Fig.7-12 The Fréchet derivative patterns of pole-pole surface surveying in two-layered models. (a) and (b) have a resistive basement. (c) and (d) have a conductive basement.

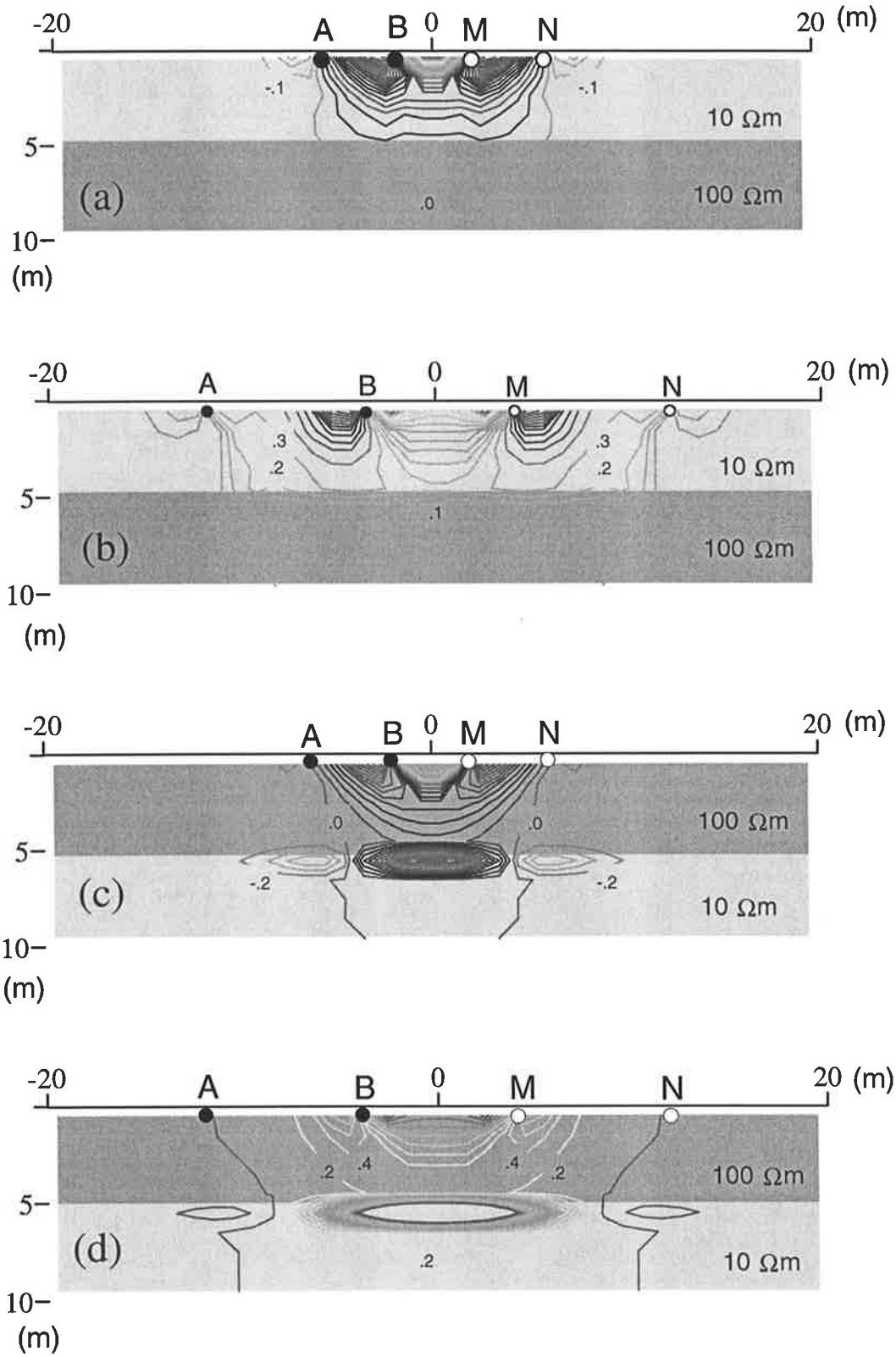

Fig.7-13 The Fréchet derivative patterns of bipole-bipole surface surveying in two-layered models. (a) and (b) have a resistive basement. (c) and (d) have a conductive basement.

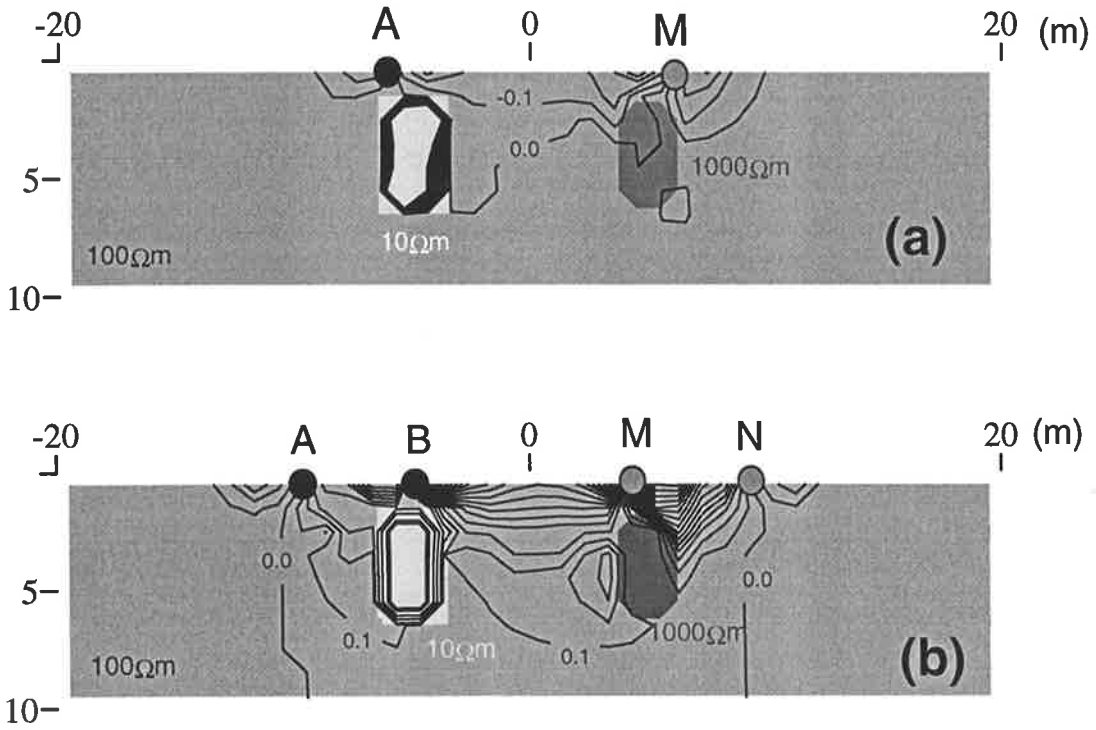

Fig.7-14 The Fréchet derivatives of (a) pole-pole and (b) bipole-bipole arrays in a two-target (double inclusion) model.

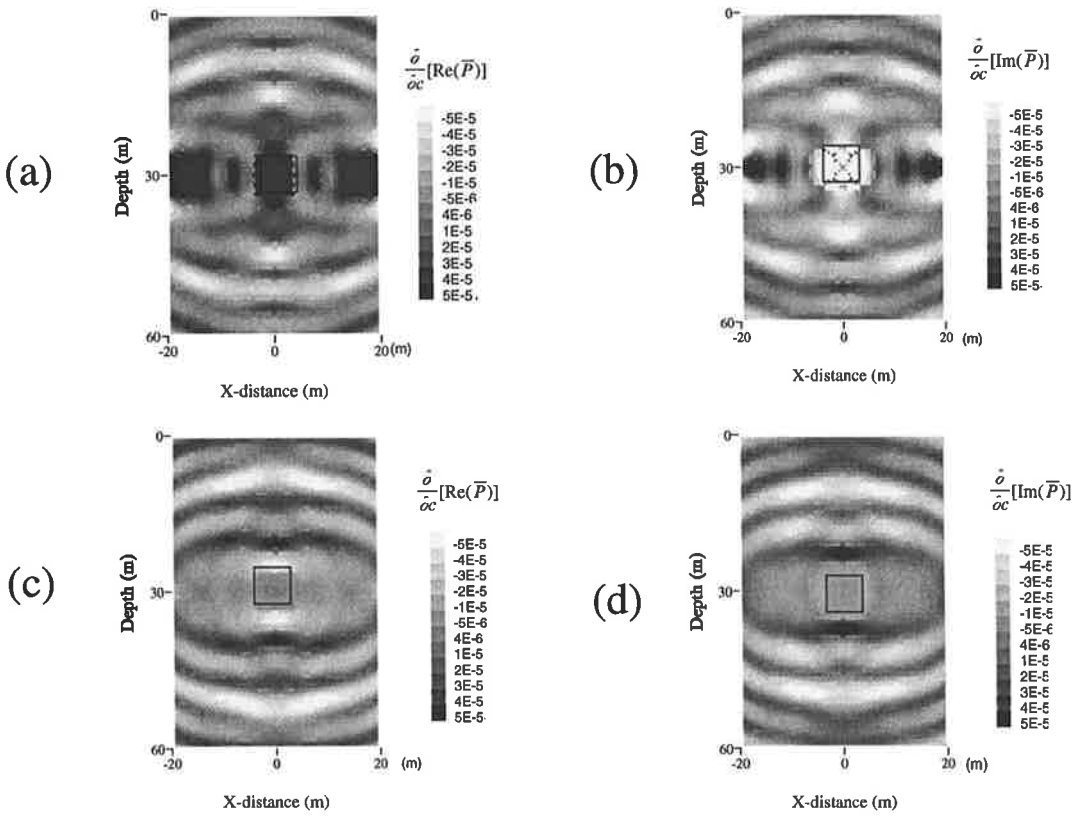

Fig.7-15 The Fréchet derivative patterns of crosshole acoustic measurements involving rectangular target models. (a) and (b) are the real and imaginary spectra in a low velocity rectangle at the center (1 km/s); (c) and (d) are the real and imaginary spectra in a high velocity rectangle at the center (5 km/s). The velocity of the background is 3 km/s.

rectangular target. One cannot see much difference in these patterns between the low-velocity and high-velocity targets.

So far, we have derived the explicit expressions for the Fréchet and the second derivatives for resistivity and 2.5-D acoustic wave problems, and presented a numerical algorithm for approximating them. Theoretically, these approximations may be employed in the inversion algorithms described in Chapter 6. The two-step algorithms, especially to compute the Fréchet derivatives, are obviously robust and more efficient than common algorithms for imaging. But it must be noted that the computation of the second derivative requires much more computer memory and computer time than the computation of the Fréchet derivative. In the following chapters, we will apply the approximations of the Fréchet derivative to crosshole resistivity and acoustic velocity imaging further to prove the effectiveness of the algorithm.

Chapter 8
Synthetic Study on Crosshole Resistivity Imaging

This chapter, which entails numerical and physical experiments, investigates crosshole resistivity imaging effectiveness with different electrode arrays (Zhou and Greenhalgh, 1997). Specifically, we focus on such aspects as: (1) the possible configurations of three- and four-electrode arrays for crosshole resistivity imaging; (2) the sensitivity variation of these measurement configurations; (3) the effectiveness of crosshole resistivity imaging with the different electrode arrays. For simplicity, the effect of the borehole (cylindrical conductivity anomaly) on the observations is ignored in the following analysis.

The structure of the chapter is as follows. In the first two sections, an investigation of possible configurations and sensitivities of crosshole pole-bipole, bipole-pole and bipole-bipole surveying are discussed in theory and by illustrations. The third and fourth sections demonstrate numerical imaging experiments with the different configurations of crosshole resistivity measurement and profiling data. The last section shows some water-tank experiments of crosshole resistivity imaging.

8.1 Crosshole Surveying Configurations

In order to represent the various configurations of crosshole pole-pole, pole-bipole, bipole-pole and bipole-bipole arrays, a symbol convention is first adopted. The italic capital letters A and B stand for positive (source) and negative (sink) current electrodes, M and N denote two potential electrodes in an electrode array. Using the symbol "-" separating the four letters represents a crosshole configuration of a specified electrode array, i.e. A-M gives a configuration of the crosshole pole-pole surveying in which the positive current electrode A is placed in the left borehole and the observational potential electrode M is placed in the right borehole. Missing letters (B and N) imply remote

electrodes (i.e. at infinity). The *A-M* and *M-A* are called a pair of symmetric configurations that are obtained by exchanging the positions of the electrodes in the two boreholes. Obviously, both *A-M* and *M-A* configurations are the pole-pole data and they are equivalent in terms of reciprocity principle (see Chapter 2).

The pole-pole array, having two remote electrodes, is a simple crosshole configuration in DC electric surveying. Theoretically, the two remote electrodes should be placed at an infinite distance away from the working site (boreholes) so that the reference potential of the point-source is assumed to be zero and no disturbance (noise pickup) occurs along the wires connecting the remote electrodes. But in practice, it is hard to achieve this situation due to the spatial limitation and existence of other electric sources as already mentioned. To overcome such disadvantages, alternatives are to use the pole-bipole, bipole-pole or bipole-bipole array in crosshole surveying, because these arrays require only one (pole-bipole and bipole-pole surveys) or no (bipole-bipole survey) remote electrodes. From simple combinatorics, there are $3!\times 2=12$ configurations for crosshole pole-bipole and bipole-pole surveying respectively, and $4!=24$ configurations for crosshole bipole-bipole surveying. According to equations (3.49) and (3.50), and the reciprocity principle: $G(r_A, r_M) = G(r_M, r_A)$, the equivalent configurations (the same data

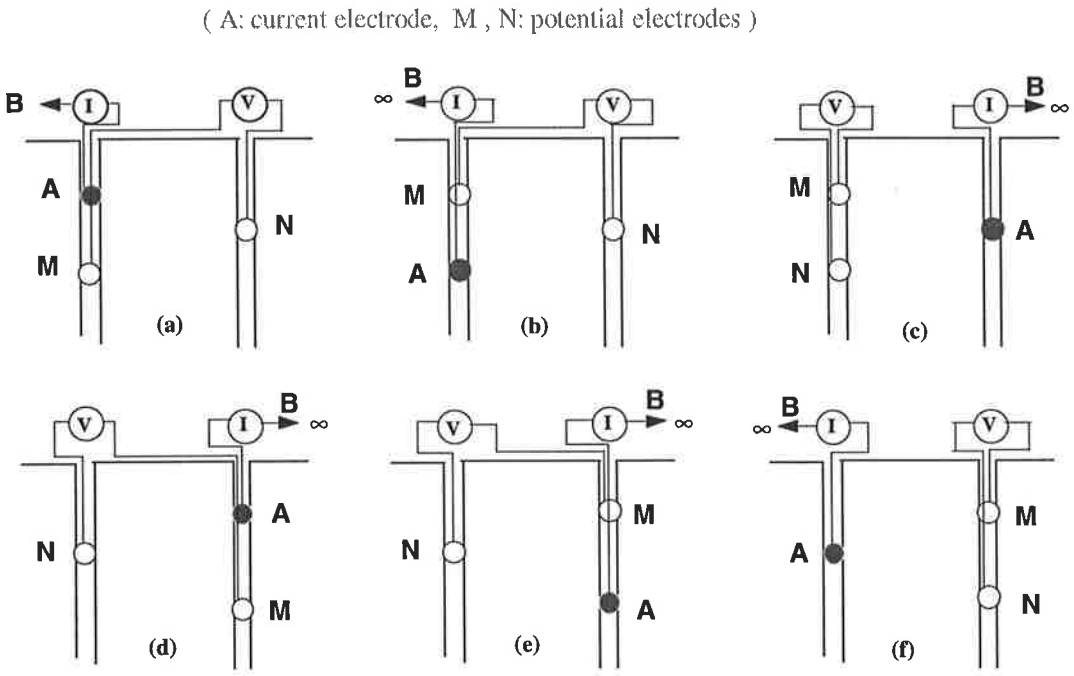

Fig.8-1 Six independent configurations for crosshole pole-bipole surveying: (a) *AM-N*, (b) *MA-N*, (c) *MN-A*, (d) *N-AM*, (e) *N-MA*, (f) *A-MN*

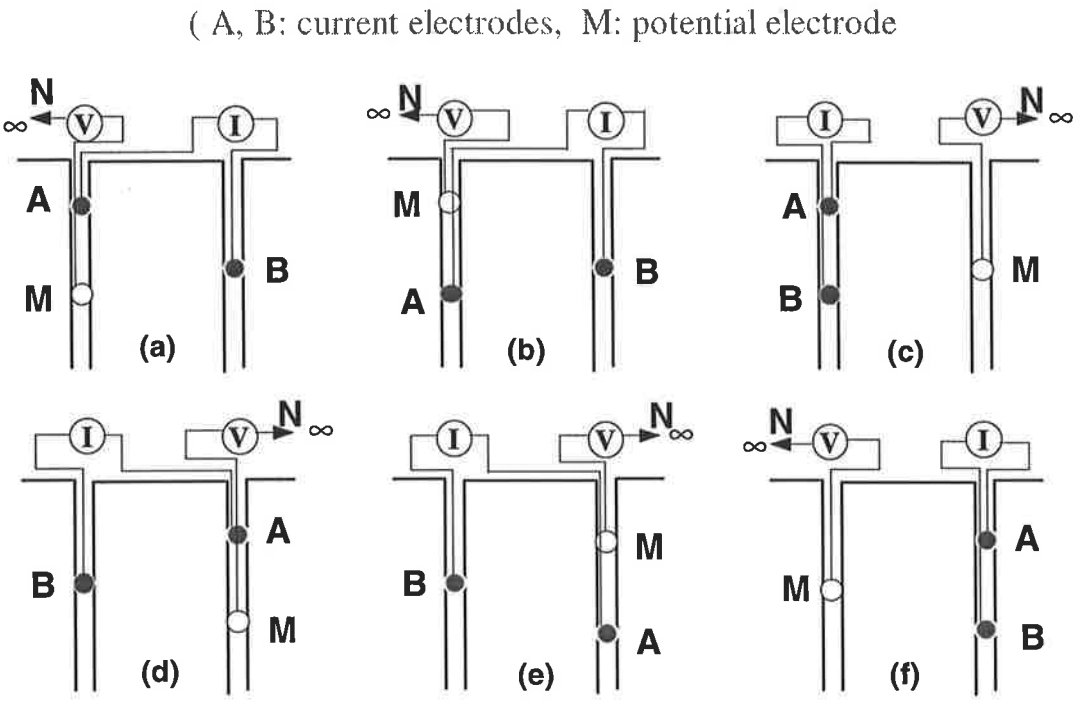

Fig.8-2 Six independent configurations for crosshole bipole-pole measurement: (a) *AM-B;* (b) *MA-B;* (c) *AB-M;* (d) *B-AM;* (e) *B-MA;* (f) *M-AB.*

are obtained with the equivalent surveying configurations) can be found for the crosshole pole-bipole survey, e.g. *AM-N=AN-M*, *MA-N=NA-M*, *MN-A=NM-A*. It follows that there are six independent configurations: *AM-N*, *MA-N*, *MN-A* and their symmetric configurations: *N-AM*, *N-MA* and *A-MN* for the crosshole pole-bipole array (see Fig.8-1). In the same manner, we get six independent configurations for the crosshole bipole-pole array (see Fig.8-2). Meanwhile, the equivalent configurations between the crosshole pole-bipole and bipole-pole surveys are also obtained; they are *AM-N=MA-B*, *MA-N=AM-B* and *MN-A=AB-M*. For the crosshole bipole-bipole surveying, only three configurations: *AM-BN*, *AM-NB* and *AB-MN* are independent (see Fig.8-3).

It must be mentioned that as the current and potential electrodes are located below the surface, the apparent resistivity may have a singularity that is caused by the presence of a zero equipotential surface in the zone of potential measurement (Daniels, 1977). To avoid the singularity, Daniels (1977, 1984) and Militer et al. (1979) chose some specific downhole resistivity techniques, which were applied to detect caves, tunnels and mineral deposits, but not intended to image the targets. For resistivity imaging, the scanning

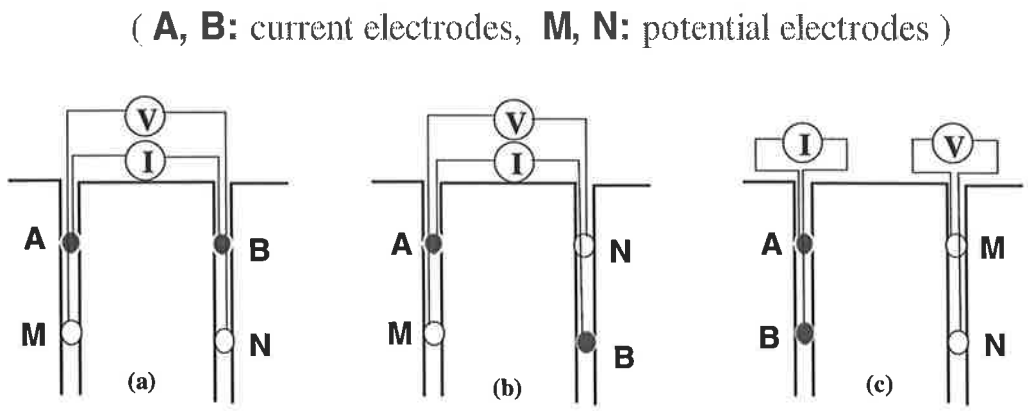

Fig.8-3 Three independent configurations for crosshole bipole-bipole measurement: (a) *AM-BN;* (b) *AM-NB;* (c) *AB-MN.*

observation, e.g. for the configuration *AM-N*, fixing *AM* in the left borehole and moving *N* along the right borehole, then changing *AM* and moving *N* again, is necessarily adopted to get the detail of the variation of the apparent resistivity or the electric potential. It should be known which configuration has no singularity for these independent configurations. Following Daniels' method, the geometry factors given by equations (3.40)-(3.43) are calculated for determining the singularities of all of the independent configurations. In these computations, we normalised the horizontal and vertical distance with the separation of a pair of electrodes in the left borehole, and supposed the same separations of two pairs of electrodes: *AM* (*MA, AB*) and *BN* (*NB, MN*) for the bipole-bipole array. We find that *AM-N*, *MA-N* (equivalent to *MA-B* and *AM-B*), *AM-BN* and *AM-NB*, including their symmetric configurations, have no singularity in the geometry factor; this means that these independent configurations are available for crosshole scanning apparent-resistivity observations. The singularity occurs in those configurations in which two current electrodes or two potential electrodes are located in the same borehole (see Fig.8-4). Due to the singularity distribution, one can not calculate the apparent resistivity using the configurations: *A-MN*, *AB-M* and *AB-MN* in the scanning observation.

In terms of inverse algorithms one may think about directly using the normalised electric potential data U_M / I (pole-pole and bipole-pole arrays) or normalised potential subtraction $\Delta U_{MN} / I$ (pole-bipole and bipole-bipole arrays) rather than the apparent resistivity as the input data for crosshole resistivity imaging so as to avoid the

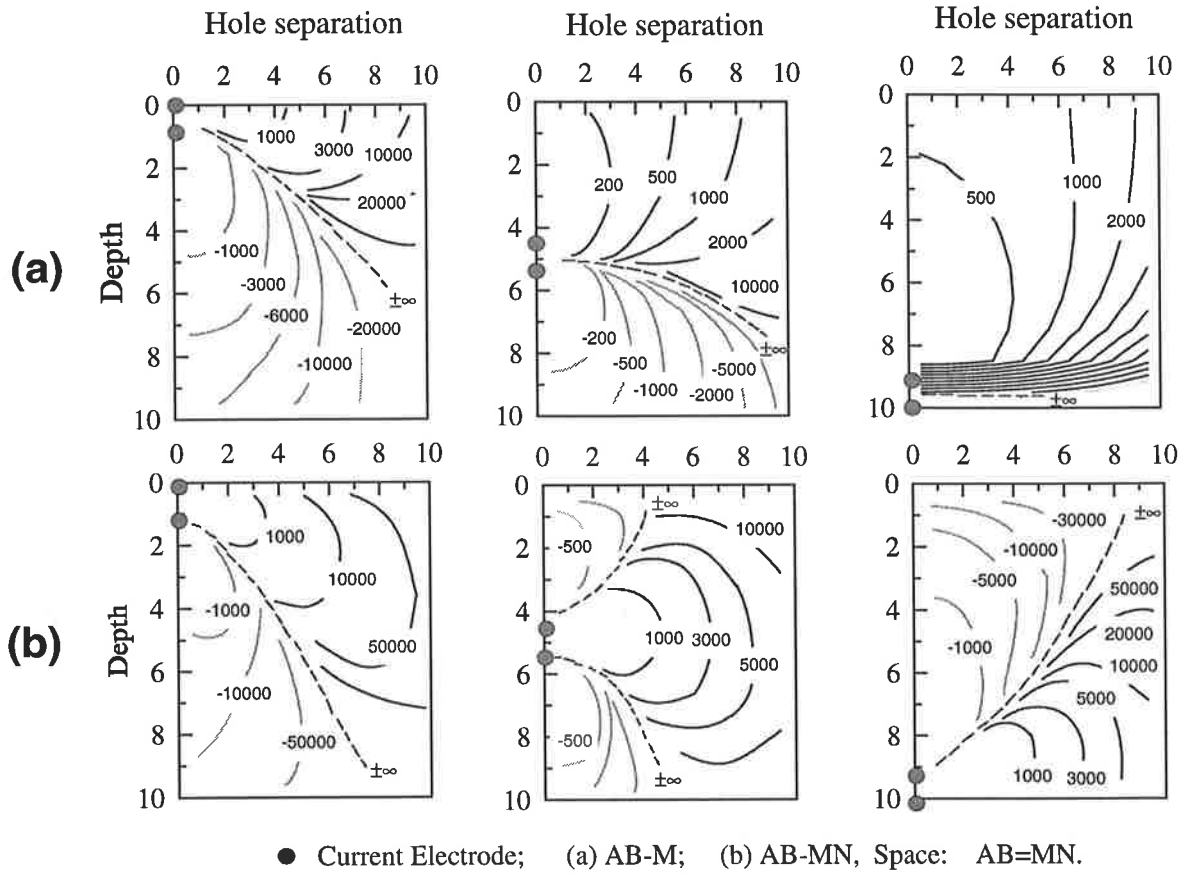

Fig.8-4 Singularity distributions in the geometry factors for crosshole resistivity surveying configurations: (a) bipole-pole *AB-M* (equivalent to *MN-A*), (b) bipole-bipole *AB-MN*.

singularity problem. But, it must be noticed that the presence of the singularity means that zero electric potential occurs and the potential U_M or potential subtraction ΔU_{MN} changes sign from positive (or negative) to negative (or positive) in the resistivity scanning. Obviously, the normalised values of the scanning observations around the singularity must be very small and it may make for low signal-to-noise ratio of the data. This is not good for crosshole resistivity imaging.

Consequently, all of the independent configurations involving the pole-bipole, bipole-pole and bipole-bipole arrays are available for crosshole scanning surveying, and the six configurations: *A-MN, MN-A, AB-M, M-AB, AB-MN,, MN-AB* have the singularity problem with computation of apparent resistivity. The results are summarised in Table 8-1.

Table 8-1 Crosshole surveying configurations for different electrode arrays

Electrode array	Total No.	Independent No.	Independent configurations	ρ_a singularity configurations
pole-pole	2	1	*A-M*	
pole-bipole	12	6	*AM-N, MA-N, MN-A, N-AM, N-MA , A-MN*	*A-MN, MN-A*
bipole-pole	12	6	*AM-B, MA-B, AB-M B-AM, B-MA, AM-AB*	*AB-M, M-AB*
bipole-bipole	24	3	*AM-BN ,AM-NB, AB-MN*	*AB-MN, MN-AB*
Equivalent array	*pole-bipole: AM-N, MA-N and MN-A= bipole-pole: MA-B, AM-B and AB-M*			

It follows that the four electrode arrays have a different number of independent configurations in crosshole measurement, that is, the pole-pole array has only one, but the others have more. This implies that if a certain number of electrodes are located in two boreholes, i.e. total=2n, then the maximum number of independent pole-pole data is $n \times n = n^2$ due to only one independent crosshole surveying configuration, but the other arrays provide more configurations for acquiring the maximum data about the variation in electrical resistivity of the medium. It is also shown that employing the equivalent configurations between the crosshole pole-bipole and bipole-pole arrays (*AM-N=MA-B* and *MA-N=AM-B*)—although the measurements are quite different (the former is to measure the potential difference of a source, the later is to measure the potential of a pair of sources)—inherently equivalent data can be obtained. Due to the singularity problem the configurations *A-MN* (*M-AB*) and *AB-MN* are not suitable for crosshole scanning measurements. It is concluded that besides the crosshole pole-pole configuration *A-M*, six other independent surveying configurations: *AM-N*, *MA-N*, *AM-B*, *MA-B*, *AM-BN* and *AM-NB* (see Table 8-1) are available for crosshole scanning observations, and they may be employed for crosshole resistivity imaging.

8.2 Sensitivity Variation of Crosshole Measurements

It follows from the above that, besides the pole-pole array, the three- and four-electrode arrays may be used with their independent configurations in crosshole scanning mode.

The question of sensitivity of these configurations to the target between two boreholes naturally arises. To reveal the sensitivity variations of these independent crosshole configurations, we carry out comparative analysis by computation of the Fréchet and second derivatives and the anomaly effect (AE, defined by Militer et al., 1979)) of these configurations. As mentioned in Chapter 7, the Fréchet derivative (equation (7.27)), or sensitivity function, and the second derivative (equation (7.28)) represent the data variation corresponding to a small disturbance in the model parameter at each spatial point. Larger values of the derivatives means greater weights in the inversion. In chapter 7 we developed the algorithm to compute the derivatives and it has been shown that the computations for the three- and four-electrode arrays use the same FEM-code and cost nearly the same computer time as for the pole-pole array. Meanwhile, we have shown the sensitivity functions of different surface-surveying configurations. Here, we calculate the sensitivity functions and the second derivatives for these crosshole configurations. Fig.8-5 gives the results of a crosshole pole-pole measurement; Fig.8-6 shows the results for two crosshole pole-bipole configurations: *AM-N* (upper) and *A-MN* (lower); Fig.8-7 shows the results for two crosshole bipole-pole surveys: *AM-B* (upper) and *AB-M* (lower), and Fig.8-8 gives the results for three crosshole bipole-bipole measurement configurations:

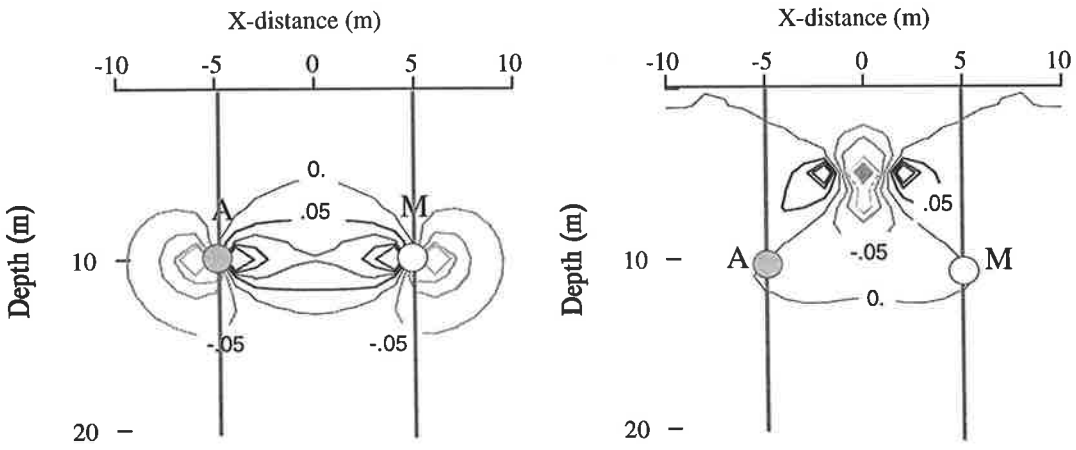

Fig.8-5 Sensitivity functions–the Fréchet (left) and second (right) derivatives of the crosshole pole-pole array. *A* and *M* are current and potential electrodes, respectively. The background resistivity is 100 Ωm and the point *p* is placed at (0,5).

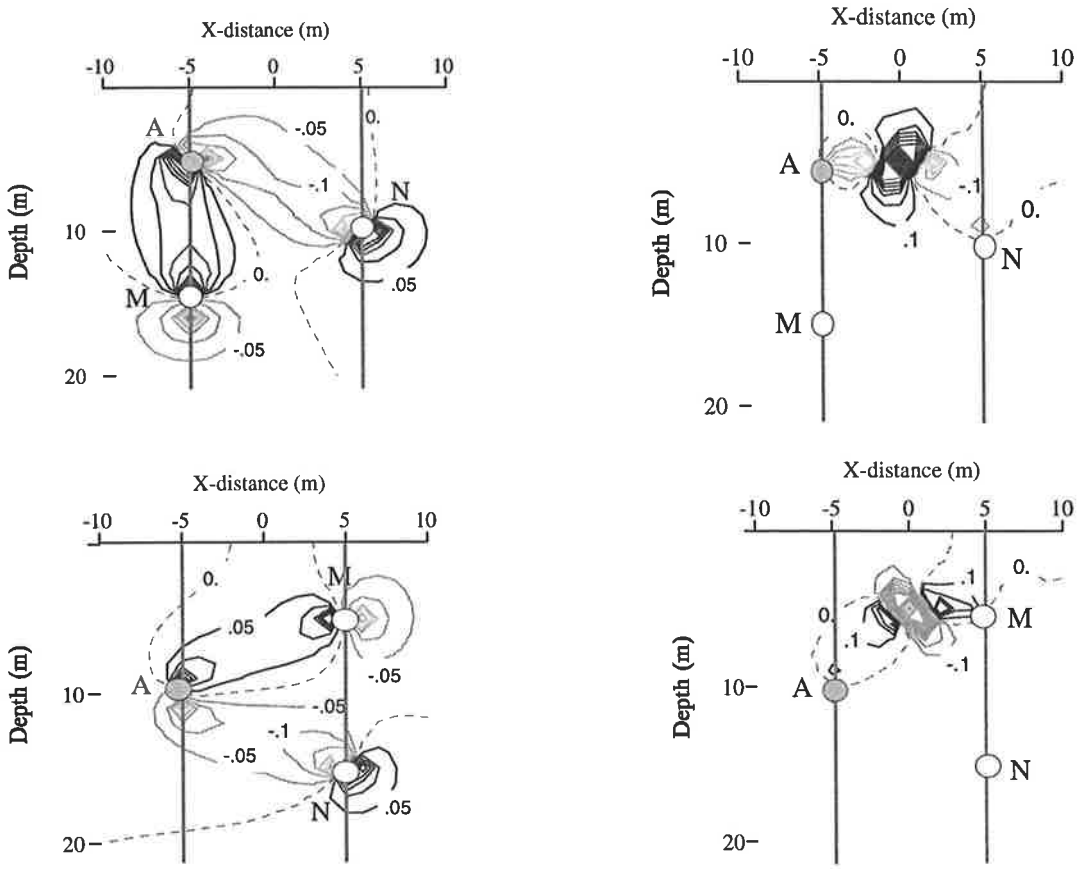

Fig.8-6 Sensitivity functions–the Fréchet (left panel) and second derivatives (right panel) for the crosshole pole-bipole array. *A* is a current electrode. *M* and *N* are potential electrodes. The background resistivity is 100 Ωm and the point *p* is placed at (0,5).

AM-BN (top), *AM-NB* (middle) and *AB-MN* (bottom). From these results, one can obtain results for other configurations with reference to the equivalent or symmetric configurations given in Table 8-1. For comparison, a uniform medium (100 Ωm) and $1\times1\ m^2$ element-size was used in these computations and the point: p= (0,5) is fixed for the second derivative ($\frac{\partial^2 U}{\partial\sigma\partial\sigma_p}$). These figures shows that the sensitivity functions of the different crosshole configurations have different patterns from those in the surface- surveying cases, but most of the significant values still appear around the electrodes (see $\frac{\partial U_M}{\partial\sigma}$ or $\frac{\partial U_{MN}}{\partial\sigma}$ in Fig.8-5~Fig.8-8). The second derivatives of the different crosshole configurations have the common feature similar to the surface-

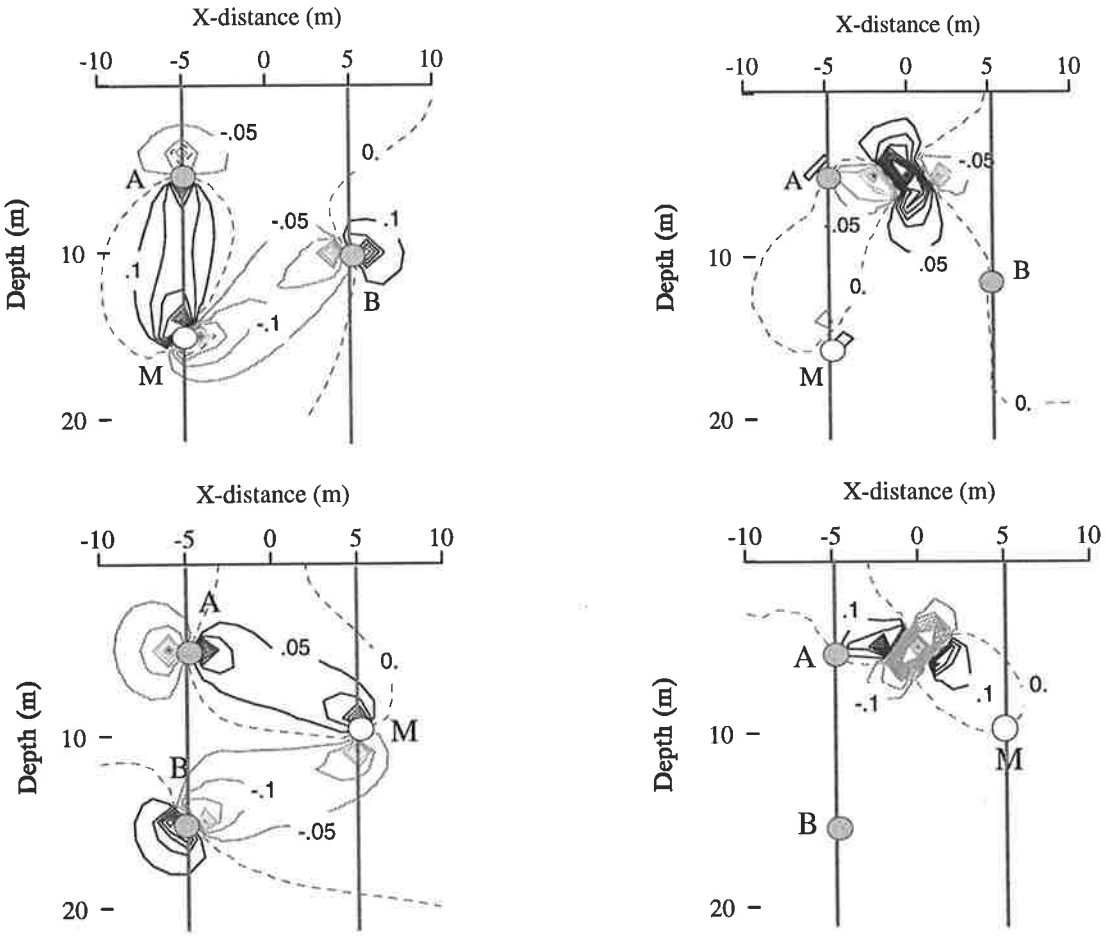

Fig.8-7 Sensitivity functions–the Fréchet (left panel) and second derivatives (right panel) for the crosshole bipole-pole array. *A* and *B* are current electrodes. *M* is a potential electrodes. The background resistivity is 100 Ωm and the point *p* is placed at (0,5).

surveying cases: the significant values of the derivatives appear around the point p=(0,5) under consideration (see $\frac{\partial^2 U_M}{\partial \sigma_p \partial \sigma}$ or $\frac{\partial^2 U_{MN}}{\partial \sigma_p \partial \sigma}$ in Fig.8-6 and Fig.8-5~Fig.8-8).

Obviously, the different sensitivity patterns in these specified configurations arise from the differences in spatial measurement. The crosshole pole-bipole, bipole-pole and bipole-bipole surveys have much more complicated sensitivity patterns than the crosshole pole-pole array and the detection area is enlarged by employing more electrodes in these arrays. Another difference can be found in the sign of the sensitivity values between the boreholes. A positive value implies that the data variation is

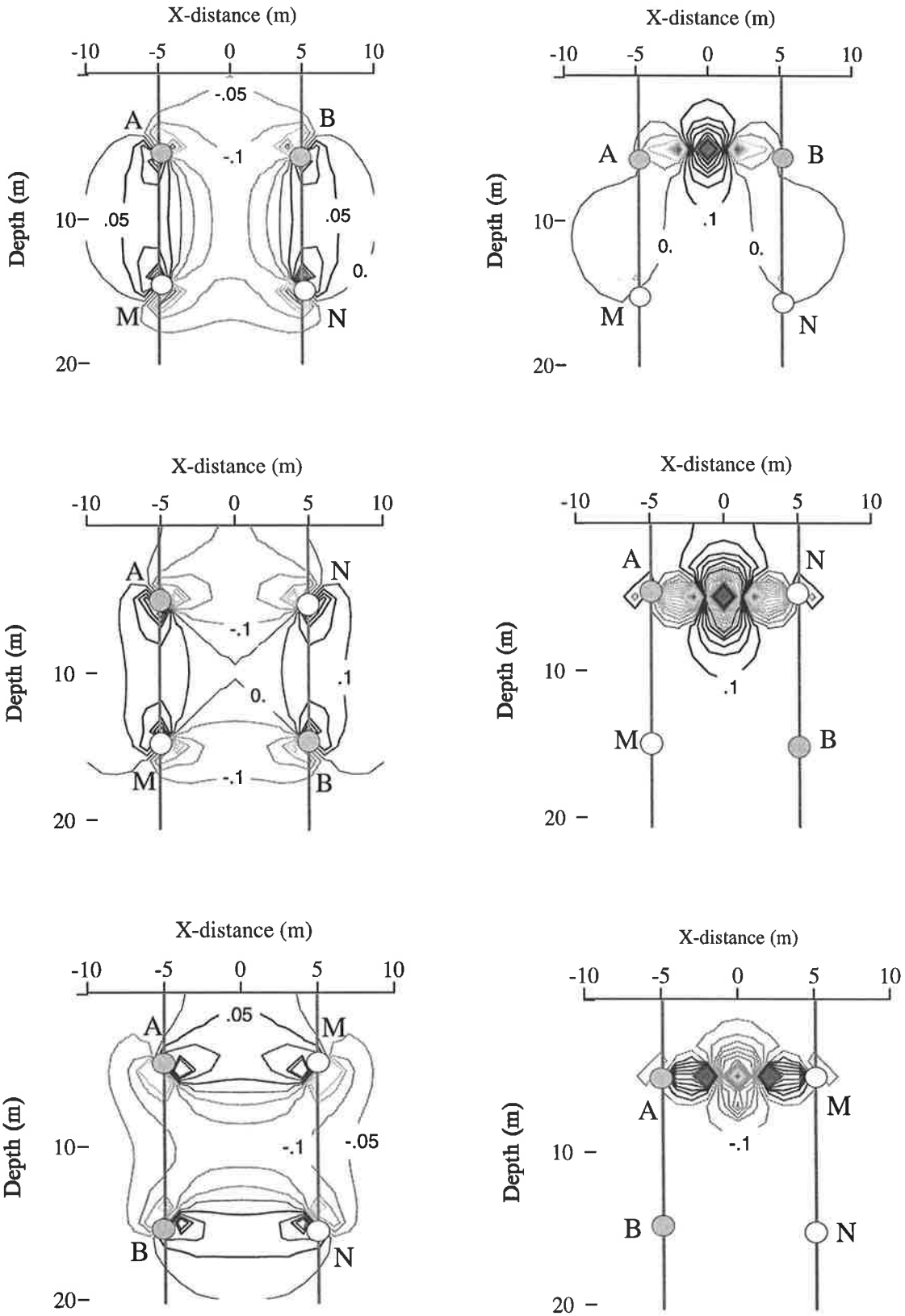

Fig.8-8 Sensitivity functions–the Fréchet (left panel) and second derivatives (right panel) for the crosshole bipole-bipole array. *A* and *B* are current electrodes. *M* and *N* are potential electrodes. The upper, middle and lower diagrams are respectively for the *AM-BN*, *AM-NB* and *AB-MN* configurations. The background resistivity is 100 Ωm and the point *p* is placed at (0,5).

proportional to the model parameter and a negative value represents a reverse change. The pole-pole array always has positive values in the Fréchet derivative between two boreholes, but the pole-bipole, bipole-pole and bipole-bipole arrays have both positive and negative values when the different configurations are adopted. These results imply that the four crosshole electrode arrays have quite different sensitivities in the detection area. In theory, the sensitivity of pole-pole data is unchangeable in crosshole surveys, because the data mostly depend on the distance between the two boreholes, but the crosshole pole-bipole, bipole-pole and bipole-bipole configurations depend not only upon the distance between boreholes but also upon the relative positions of the electrode in the arrays, e.g. by fixing the electrode N in the configuration AM-N , one can obtain different data with different separations of A and M in the crosshole pole-bipole survey. This leads to the possibility of adjusting the sensitivity of the array by choosing suitable separations of the electrodes for acquiring optimal data. To illustrate the sensitivity variation with the separation of electrodes, the sensitivity curves at the centre of the two boreholes ($\left.\frac{\partial U_M}{\partial \rho}\right|_{x=0}$ or $\left.\frac{\partial U_{MN}}{\partial \rho}\right|_{x=0}$) for different separations of the electrodes are plotted for some configurations. Fig.8-9 gives the results for the pole-bipole surveys (*AM-N* and *MA-N*); it is also valid for the bipole-pole surveys (*MA-B* and *AM-B*) in terms of the equivalent relation. Fig.8-10 is for the bipole-bipole surveys (*AM-BN* and *AM-NB*). From the resolution point of view, the desired curve should have a reasonable width and a large peak. From these figures, it is found that with increasing separation of *AM* (*MA*), the central sensitivity values vary from small to large. This means an expanding variation of the sensitive area from the wall of the boreholes to the midway position between the boreholes with the exception of the configuration *MA-N* (*AM-B*). The peak of the curve decreases as the separation exceeds the distance of the boreholes (see Fig.8-9 and Fig.8-10). The width of the curve becomes wider and wider (see Fig.8-10). It seems that for the crosshole pole-bipole and bipole-bipole surveys, the best separation of *AM* for detecting the target in the central area is about half of the distance between the two boreholes. In summary, the sensitivities of these kinds of configurations can be adjusted by choosing a suitable separation of *AM* (*MA*). For resistivity imaging, one can use two or three electrode separations to get information about physical changes in the region between the two boreholes. These kinds of measurement configurations yield

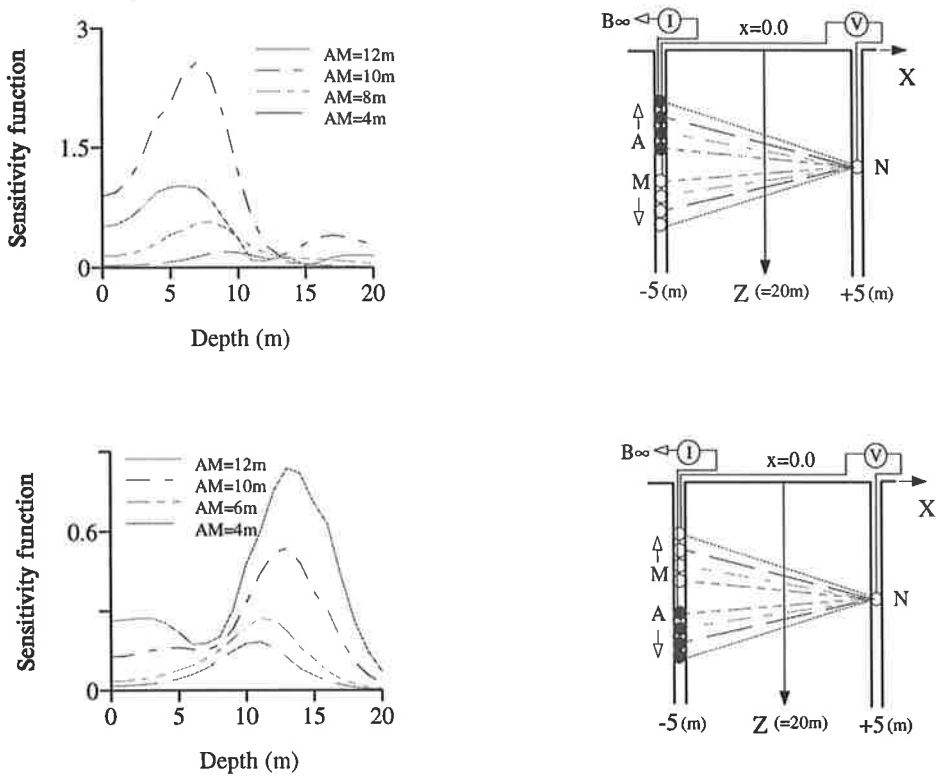

Fig.8-9 Central sensitivity-function curves for crosshole pole-bipole *AM-N* (upper) and *MA-N* (lower) surveys in a homogeneous medium ($\rho = 100$ Ωm).

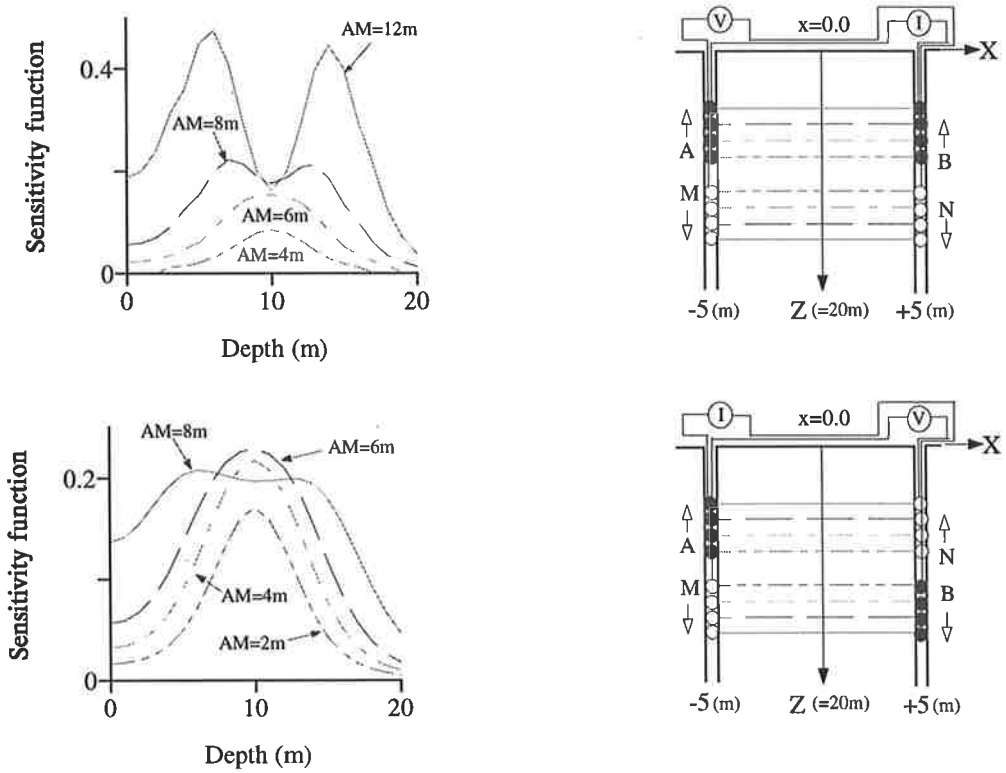

Fig.8-10 Central sensitivity-function curves for crosshole bipole-bipole *AM-BN* (upper) and *AM-NB* (lower) surveys in a homogeneous medium ($\rho = 100$ Ωm).

greater flexibility in crosshole surveying.

For comparative evaluation of target detection, the anomaly effect (AE) developed by Militer et al. (1979) is calculated for these crosshole configurations. AE is represented in terms of the extreme value of normalised apparent resistivity:

$$AE = (\frac{\rho_a}{\rho_0})_{\max} - (\frac{\rho_a}{\rho_0})_{\min} \tag{8.1}$$

where ρ_0 is the resistivity of the host medium. In our computations, a square-shaped target is located at the centre of the two boreholes, both in the x- and z-directions. The resistivity ratio of the target to the background ranges from $10^{-3} \sim 10^{3}$ and the size varies from 1/20~1/5 the separation distance between the two boreholes. The apparent resistivity scans are achieved by fixing the electrode (s) in the left borehole at the target depth and moving the other electrode (s) in the right borehole from top to bottom. Fig.8-

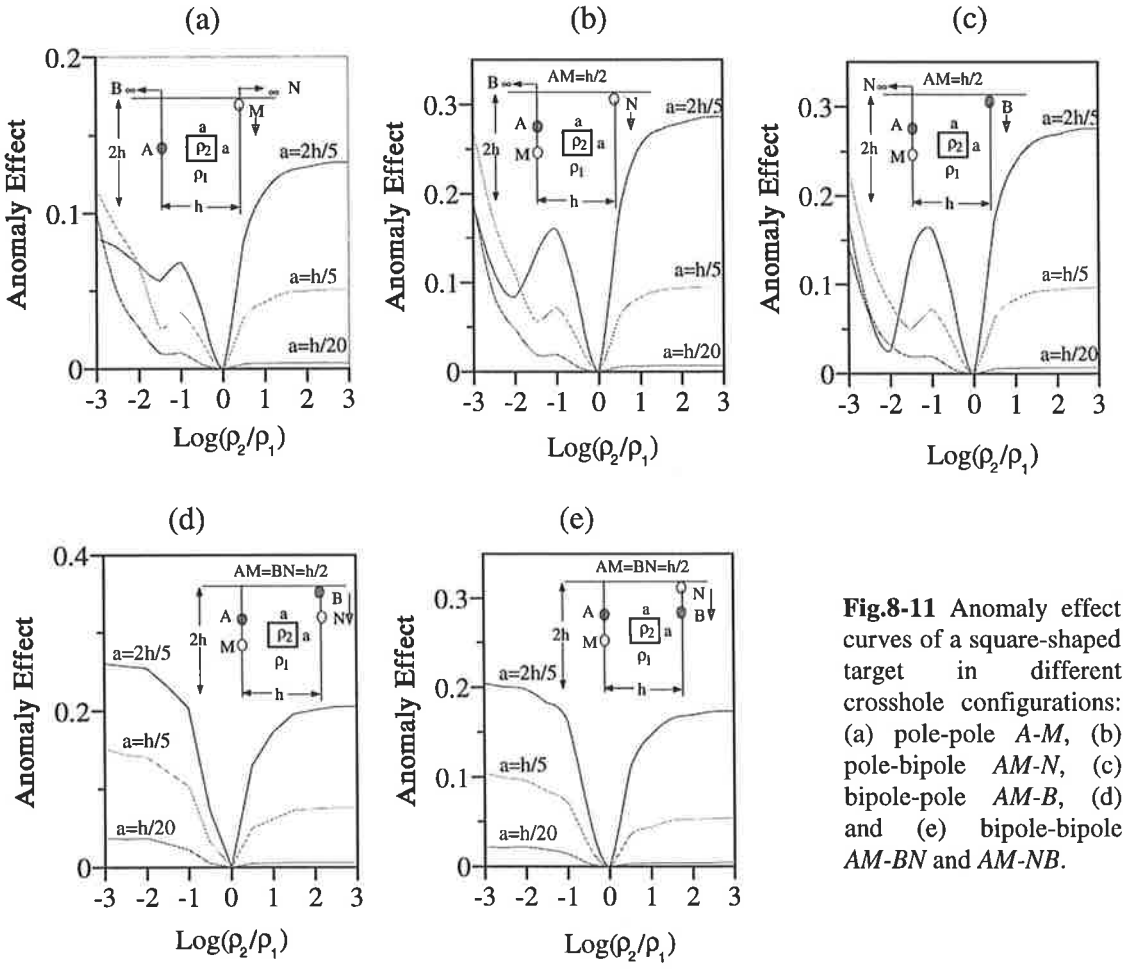

Fig.8-11 Anomaly effect curves of a square-shaped target in different crosshole configurations: (a) pole-pole *A-M*, (b) pole-bipole *AM-N*, (c) bipole-pole *AM-B*, (d) and (e) bipole-bipole *AM-BN* and *AM-NB*.

11 gives the AE curves for different sizes of the target and different resistivity contrasts for five crosshole surveying configurations. It is clear that the configurations: pole-pole, pole-bipole (*AM-N*) and bipole-pole (*AM-B*) show very similar behaviour in AE, but not in amplitude. The AE drop is of the form $\log(\rho_2 / \rho_1) = -1.5$ in that the relative amplitude of the response becomes very small in this case. In general, the higher the contrast and the larger the target, the greater the AE for these surveying configurations. The two configurations of the bipole-bipole array (*AM-BN* and *AM-NB*) have nearly the same trend in the AE. The AE value for the conductive target is larger than that for the resistive target. This means that these configurations are more sensitive to a conductive target than to a resistive target. Also one can find that over most of the range the pole-pole array has the lowest values of AE among the five configurations. This means that the pole-pole data are not the best for detection of the target. On the contrary, the pole-bipole (*AM-N* or *MA-N*), bipole-pole (*AM-B* or *MA-B*) and bipole-bipole (*AM-BN* or *AM-NB*) are better than the pole-pole data in terms of AE in this case.

8.3 Numerical Experiments of Crosshole Imaging

In the previous sections, it was shown that some specific crosshole surveying configurations involving pole-bipole, bipole-pole and bipole-bipole arrays can be adopted for crosshole scanning measurements with better sensitivity and AE than with a pole-pole configuration. To further study the imaging possibilities with these arrays, some synthetic experiments were conducted for the two models named Model-1 and

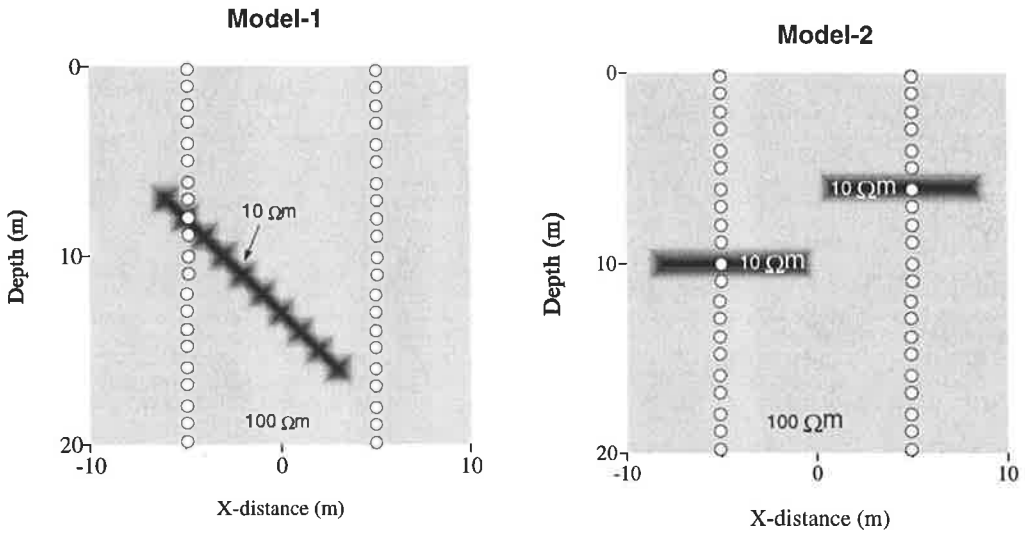

Fig.8-12 Two models for numerical simulation of crosshole resistivity imaging.

Model-2 (see Fig.8-12). The first model comprises a dipping conductive strip ($10\Omega m$) and second model a dislocated fault ($10\Omega m$), both embedded within a uniform background ($100\Omega m$) respectively. Both models are discretised into cells 1×1 m^2 size (total 20×20=400 model parameters) and there are 21 electrodes evenly spaced 10m apart in each of two boreholes. The numerical experiments are individually implemented with the independent crosshole surveying configurations: pole-pole, pole-bipole, bipole-pole and bipole-bipole arrays, each of which is accomplished using noise-free data and noise-contaminated data (a Gaussian random sequence is used to simulate the background noise). For ease of comparison of the imaging effectiveness with the different electrode arrays, the same inversion algorithm (local-search quadratic approximation CGS, Chapter 6), the same starting model (uniform medium of ρ=100 Ωm) and the same constraints on the resistivities at the electrodes are used in all the following experiments. To avoid the singularity problem with apparent resistivity, the potential U_m or the potential difference ΔU_{MN} data are directly used for the inversion.

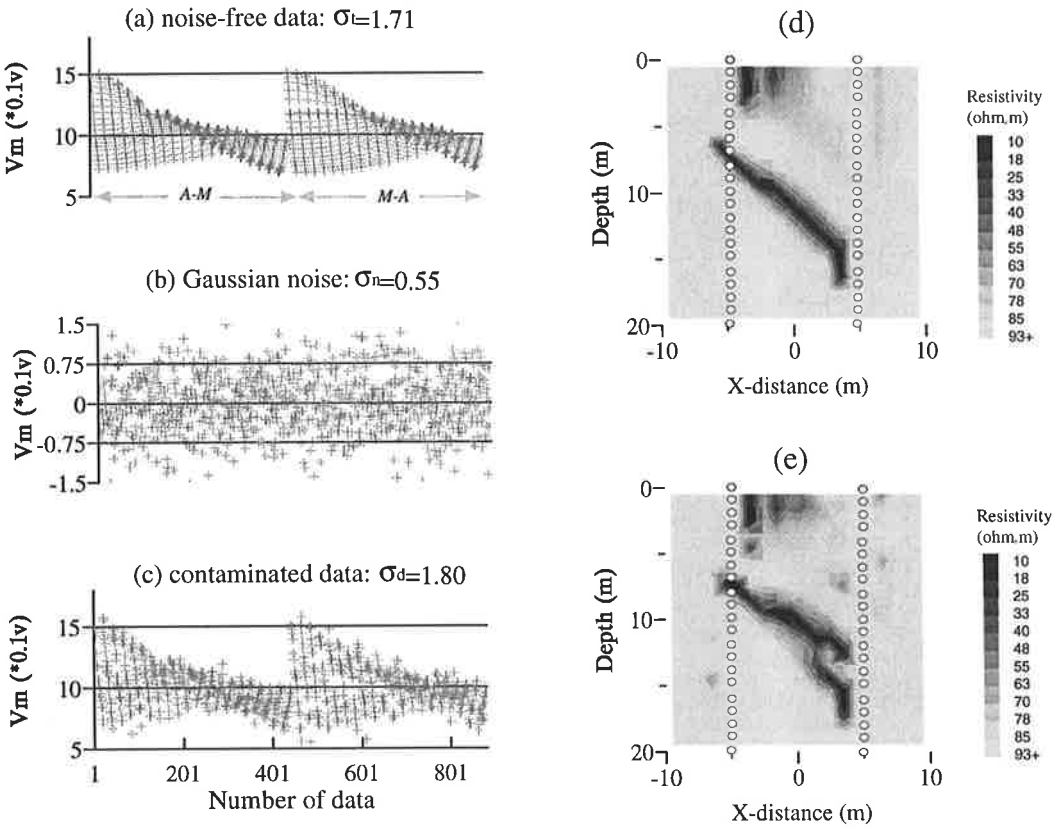

Fig.8-13 Synthetic data and imaging results obtained with crosshole pole-pole *A-M* (*M-A*) configuration for Model-1. (a) noise-free data; (b) Gaussian noise; (c) noise-contaminated data (=(a)+(b)); (d) inversion result with (a); (e) inversion result with (c). The standard covariances ($\sigma_t, \sigma_n, \sigma_d$) of the different data are given.

(1) Pole-Pole Array

The pole-pole data were calculated by taking each of the electrodes (total=42) as a transmitter and all the electrodes in the other borehole as receivers, so we have 2× 21×21=882 pole-pole measurements for inversions. Fig.8-13 and Fig.8-14 give the noise-free data and the Gaussian noise-contaminated data (different noise levels) for the pole-pole array experiments respectively. The diagrams also show the imaging results obtained in each case. These figures shows that the images of the two models produced by the noise-free data are very clear, but when the data are contaminated by Gaussian noise (standard covariance $\delta_n = 0.55$ and $\delta_n = 0.38$ in Model-1 and Model-2 respectively), the dipping conductive strip is distorted in Model-1 (see Fig.8-13d) and the faulted bed targets in Model-2 are not reconstructed completely even though the noise level is lower than that in Model-1. This means that the crosshole pole-pole data

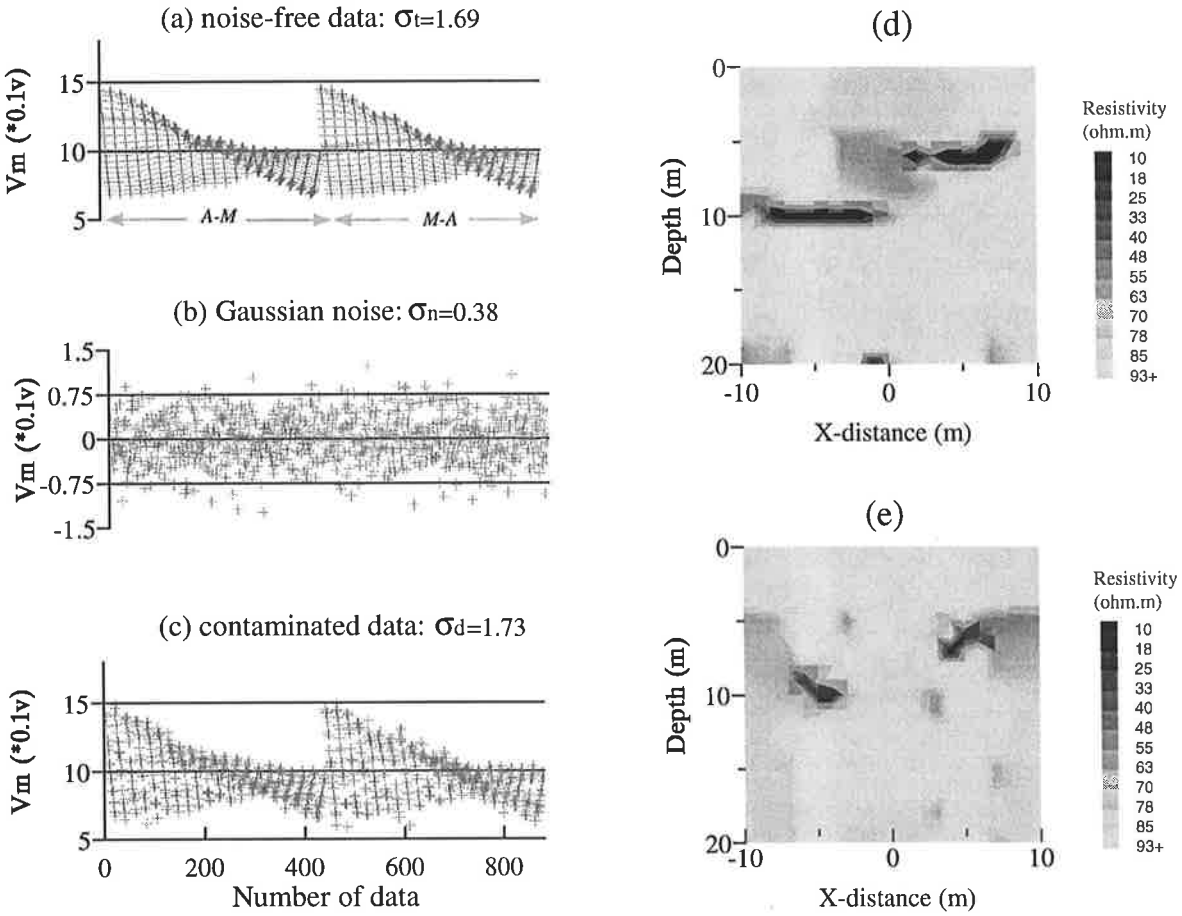

Fig.8-14 Synthetic data and imaging results obtained with crosshole pole-pole *A-M* (*M-A*) configuration for Model-2. (a) noise-free data; (b) Gaussian noise; (c) noise-contaminated data (=(a)+(b)); (d) inversion result with (a); (e) inversion result with (c). The standard covariances ($\sigma_t, \sigma_n, \sigma_d$) of the different data are given.

have different resolution capabilities in the x- and z-directions. It seems that the crosshole pole-pole data exhibits better resolution in the z-direction than in the x-direction. This may be understood from the fact that the potential function is sampled only in the z-direction in a crosshole survey.

(2) Pole-Bipole Array

The pole-bipole crosshole survey has six independent configurations (see Fig.8-1). Actually, the configurations *AM-N* and *MA-N* (see (a) and (b) in Fig.8-1) have not much difference in the data acquisition geometry, only the two configurations *AM-N* and *A-MN* are inherently different and the others are the symmetric configurations of them. We performed numerical imaging experiments for Model-1 & Model-2 with the configurations *AM-N* (including *N-AM*) and *A-MN* (including *MN-A*). Fig.8-15 and Fig.8-16 show the synthetic data and the imaging results obtained for the two models.

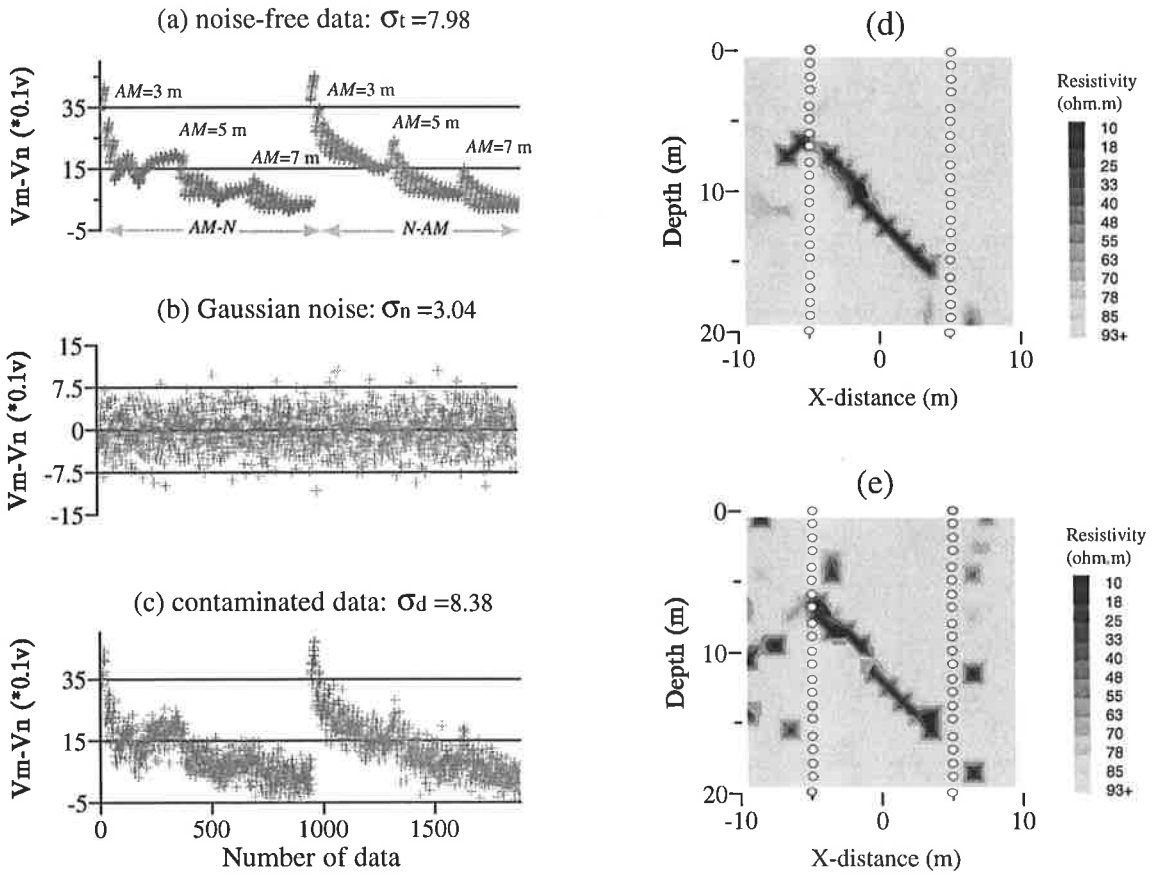

Fig.8-15 Synthetic data and imaging results obtained with crosshole pole-bipole *AM-N* (*N-AM*) configuration for Model-1. (a) noise-free data; (b) Gaussian noise; (c) contaminated data (=(a)+(b)); (d) inversion result with (a); (e) inversion result with (c). The standard covariances ($\sigma_t, \sigma_n, \sigma_d$) of the different data are given.

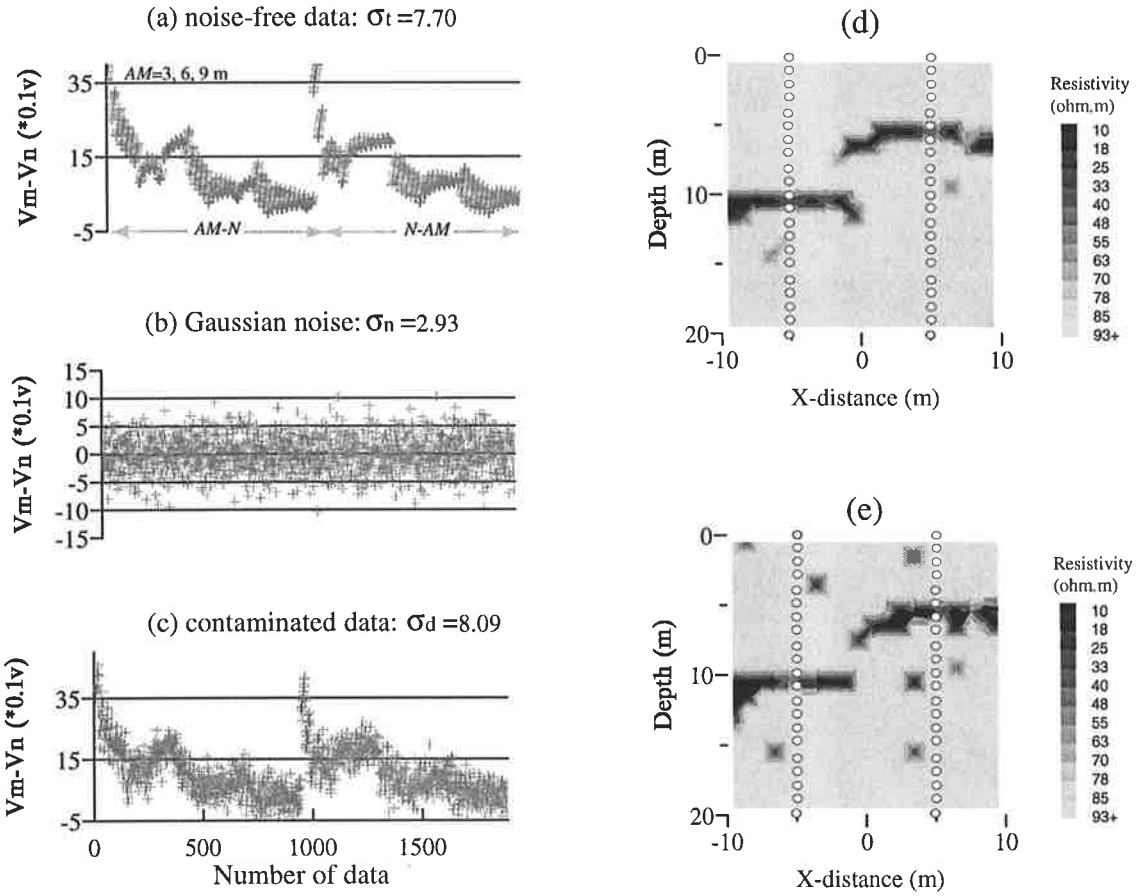

Fig.8-16 Synthetic data and imaging results obtained with crosshole pole-bipole *AM-N* (*N-AM*) configuration for Model-2. (a) noise-free data; (b) Gaussian noise; (c) noise-contaminated data (=(a)+(b)); (d) inversion result with (a); (e) inversion result with (c). The standard covariances ($\sigma_t, \sigma_n, \sigma_d$) of the different data are given.

The pole-bipole *AM-N* and *N-AM* data were computed by choosing three separations of a pair of electrodes *AM* (*AM*=3m, 5m,7m for Model-1 and *AM*=3m, 6m, 9m for Model-2) in one borehole and shifting *N* along the other borehole with the configuration *AM-N*, then repeating the procedure, maintaining a symmetric geometry *N-AM*. So, we have in total 1890 data measurements to use in the imaging. These figures show that the noise-free data yields very clear images of the two targets and the noisy data gives resolvable images, which are much better than that with the crosshole pole-pole configuration (comparing Fig.8-13 and Fig.8-14 with Fig.8-15 and Fig.8-16).

Fig.8-17 and Fig.8-18 show another set of experiments with the crosshole pole-bipole *A-MN* configuration. The synthetic data were calculated with three separations of a pair of electrodes *MN* (=2 m, 4 m, 6 m) for each current electrode *A* (see Fig.8-17a and Fig.8-

18a). The potential subtraction $V_M - V_N$ is directly used as the input data to avoid the singularity problem in the computation. From these figures, one can see that (1) the synthetic data for this configuration involve much smaller voltages than that of the configuration *AM-N* (*N-AM*) and (2) there are more artefacts in the imaging results than for the configuration *AM-N* (*N-AM*), especially for imaging the horizontal fault target in Model-2. Actually, Fig.8-18d shows that the configuration fails at imaging Model-2, even when using the noise-free data. It seems that the configuration is only sensitive to the area around the borehole in the *x*-direction. These results suggest that this configuration is not suitable for crosshole imaging, because the smaller potential subtraction $V_M - V_N$ is easily obscured by background noise. These experiments indicate that the pole-bipole *AM-N* configuration has better imaging effectiveness than the pole-pole *A-M* and pole-bipole *A-MN* configurations.

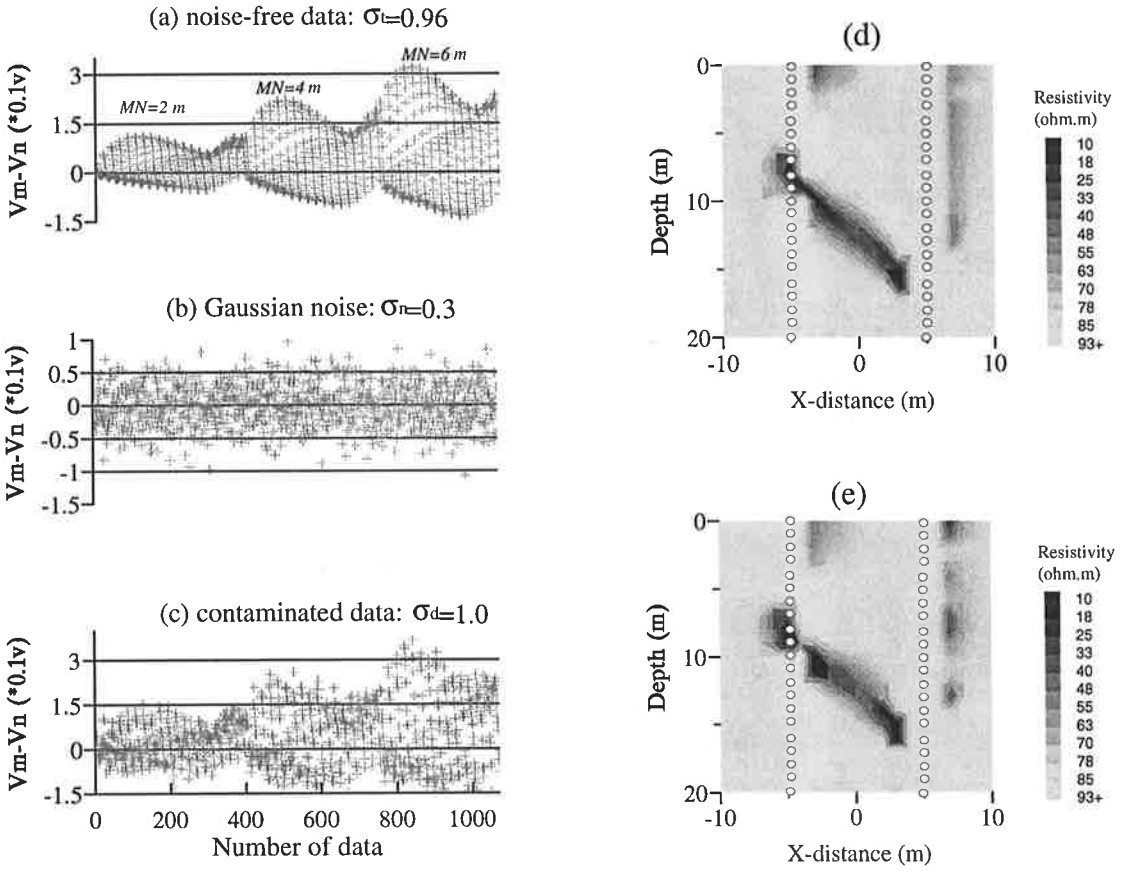

Fig.8-17 Synthetic data and imaging results obtained with crosshole pole-bipole *A-MN* (*MN-A*) configuration for Model-1. (a) noise-free data; (b) Gaussian noise; (c) noise-contaminated data (=(a)+(b)); (d) inversion result with (a); (e) inversion result with (c). The standard covariances ($\sigma_t, \sigma_n, \sigma_d$) of the different data are given.

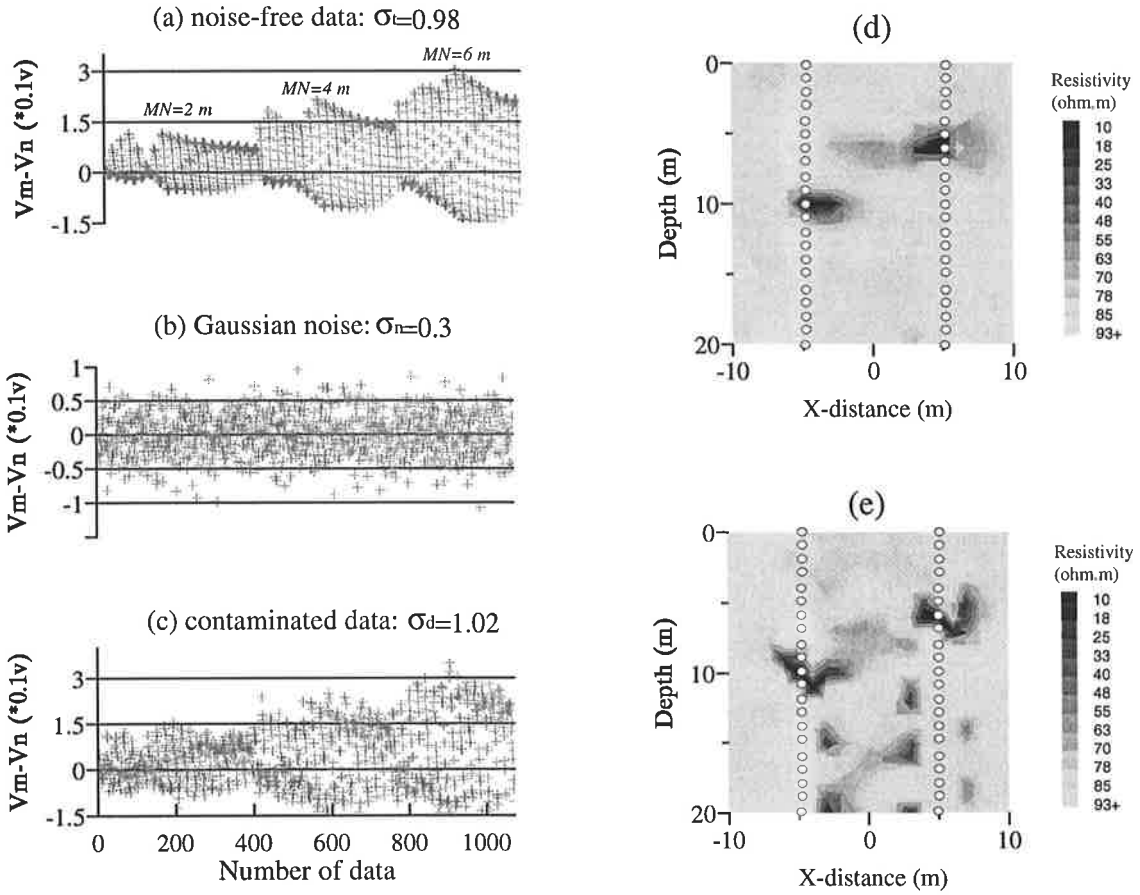

Fig.8-18 Synthetic data and imaging results obtained with crosshole pole-bipole *A-MN* (*MN-A*) configuration for Model-2. (a) noise-free data; (b) Gaussian noise; (c) noise-contaminated data (=(a)+(b)); (d) inversion result with (a); (e) inversion result with (c). The standard covariances ($\sigma_t, \sigma_n, \sigma_d$) of the different data are given.

(3) Bipole-Pole Array

In the six independent configurations of the crosshole bipole-pole surveying (see Fig.8-2), only two: *AM-B* and *AB-M* may be considered as representative of these configurations, because the others are similar to them or just their symmetric configurations. According to the reciprocity principle, the configuration *AB-M* is equivalent to *MN-A*, which has been already tested for imaging the two models (see Fig.8-17 and Fig.8-18). Here, we employ the bipole-pole *AM-B* configuration to conduct the numerical experiments. Fig.8-19 and Fig.8-20 give the synthetic data and the imaging results for the two models. The synthetic data were calculated with three separations of a pair of electrodes *AM* (=4m, 6m, 8m) for each current electrode *B* (see Fig.6-19a and Fig.6-20a). These results show that the bipole-pole *AM-B* configuration

can yield very clear images of the two models even when using the noisy data. Comparing these results with the previous results produced by the pole-pole (Fig.8-13 and Fig.8-14), pole-bipole *AM-N* (Fig.8-15 and Fig.8-16) and *A-MN* configurations (Fig.8-17 and Fig.8-18), we find that this configuration produces less distortion and more complete images of the models than the pole-pole *A-M* and pole-bipole *A-MN* configurations, and similar results to those produced by the pole-bipole *AM-N* configuration.

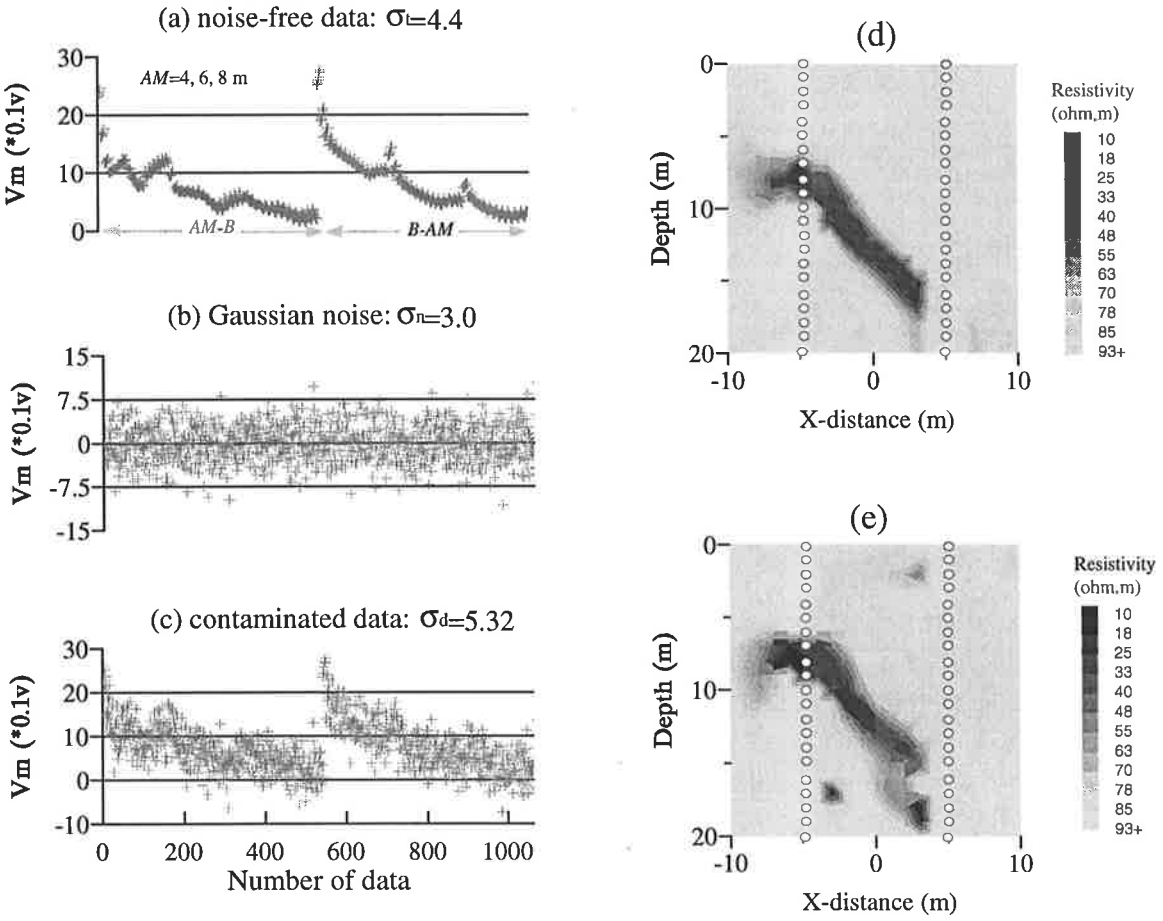

Fig.8-19 Synthetic data and imaging results obtained with crosshole bipole-pole *AM-B* (*B-AM*) configuration for Model-1. (a) noise-free data; (b) Gaussian noise; (c) noise-contaminated data (=(a)+(b)); (d) inversion result with (a); (e) inversion result with (c). The standard covariances ($\sigma_t, \sigma_n, \sigma_d$) of the different data are given.

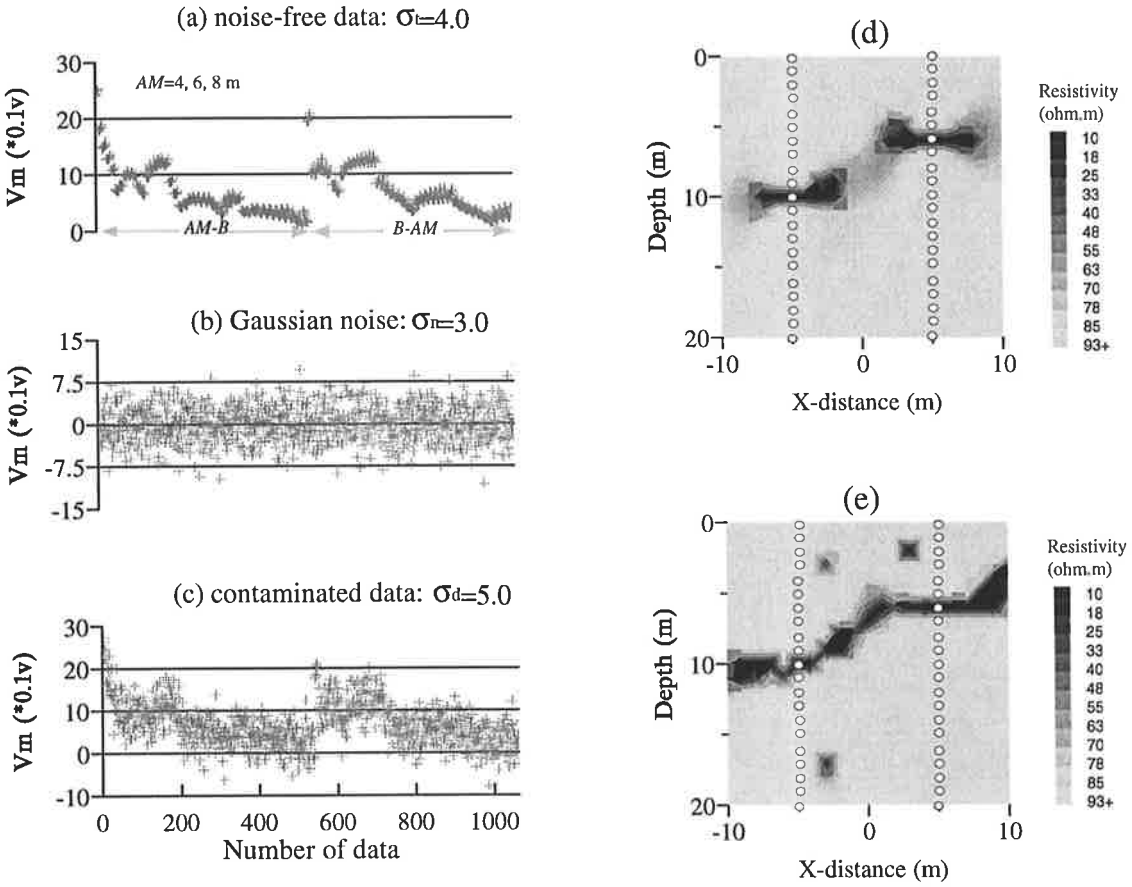

Fig.8-20 Synthetic data and imaging results obtained with crosshole bipole-pole *AM-B* (*B-AM*) configuration for Model-2. (a) noise-free data; (b) Gaussian noise; (c) noise-contaminated data (=(a)+(b)); (d) inversion result with (a); (e) inversion result with (c). The standard covariances ($\sigma_t, \sigma_n, \sigma_d$) of the different data are given.

(4) Bipole-Bipole Array

The bipole-bipole array has only three independent crosshole surveying configurations: *AM-BN*, *AM-NB* and *AB-MN* (see Fig.8-3). Firstly, we test the imaging effectiveness with the *AM-BN* configuration. Fig.8-21 and Fig.8-22 give the synthetic data and the imaging results for the two models. In computing the synthetic data, the separation of a pair of electrodes *BN* is kept the same as *AM* (*AM=BN*) and three separations of the two electrodes *AM* (*AM=BN*=3m, 5m, 7m) are employed (see Fig.8-21a and Fig.8-22a). These results show that the *AM-BN* configuration produces satisfactory images of the two models, even when inverting with the noise-contaminated data. Comparing the

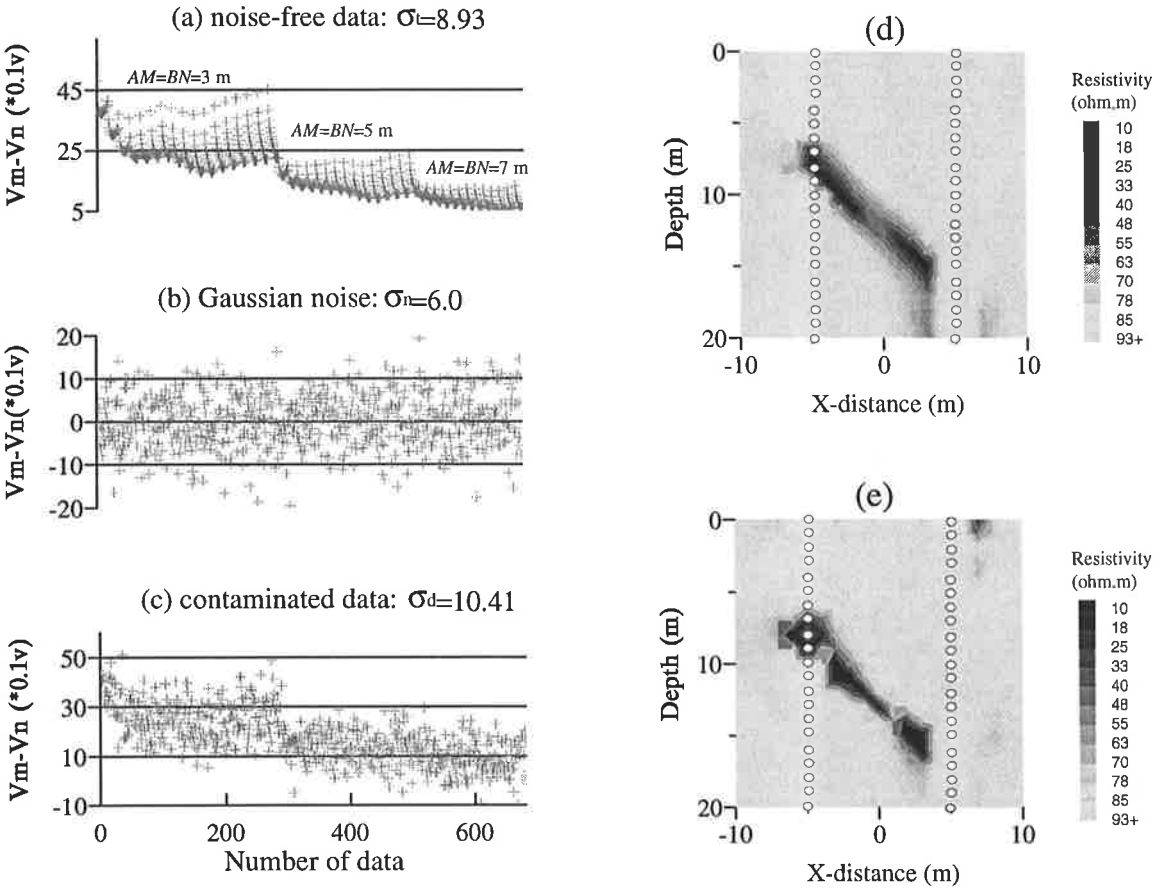

Fig.8-21 Synthetic data and imaging results obtained with crosshole bipole-bipole *AM-BN* configuration for Model-1. (a) noise-free data; (b) Gaussian noise; (c) contaminated data (=(a)+(b)); (d) inversion result with (a); (e) inversion result with (c). The standard covariances ($\sigma_t, \sigma_n, \sigma_d$) of the different data are given.

imaging results with those obtained earlier with other arrays, we find that they have fewer artefacts and minor distortion of the targets in the imaged results. These features are similar to the results using the pole-bipole *AM-N* (see Fig.8-15 and Fig.8-16) and bipole-pole *AM-B* configurations (see Fig.8-19 and Fig.8-20). The numerical imaging reflects that for crosshole resistivity imaging the *AM-BN* configuration is much better than the pole-pole *A-M* (see Fig.8-13 and Fig.8-14) and pole-bipole *A-MN* configurations (see Fig.8-17 and Fig.8-18).

From Fig.8-3, it is apparent that the bipole-bipole configurations *AM-BN* and *AM-NB* have not much difference in field geometry. By numerical tests of the two models, we found that the bipole-bipole *AM-NB* configuration (see Fig.8-3b) has very similar results to those shown in Fig.8-21 and Fig.8-22 which were obtained with the configuration

AM-BN. This implies that the two bipole-bipole configurations are not much different in crosshole resistivity imaging.

Another bipole-bipole configuration: *AB-MN* (see Fig.8-3c) has been examined because of the significant difference in data acquisition. As mentioned before, this configuration has a singularity problem in the computation of the apparent resistivity. So, we directly calculate the potential subtraction $V_M - V_N$ as the input data for the experiments. Fig.8-23 and Fig.8-24 give the synthetic data and the imaging results. From these figures, one can see that the synthetic data and imaging results are very similar to those obtained with the pole-bipole *A-MN* configuration (see Fig.8-17 and Fig.8-18). The potential difference $V_M - V_N$ for this configuration is generally much smaller than for the configuration *AM-BN*. The imaging results have many artefacts when the synthetic data are contaminated by Gaussian noise. So, this configuration has the same drawbacks as the pole-bipole *A-MN* configuration. These experiments reflect that the bipole-bipole

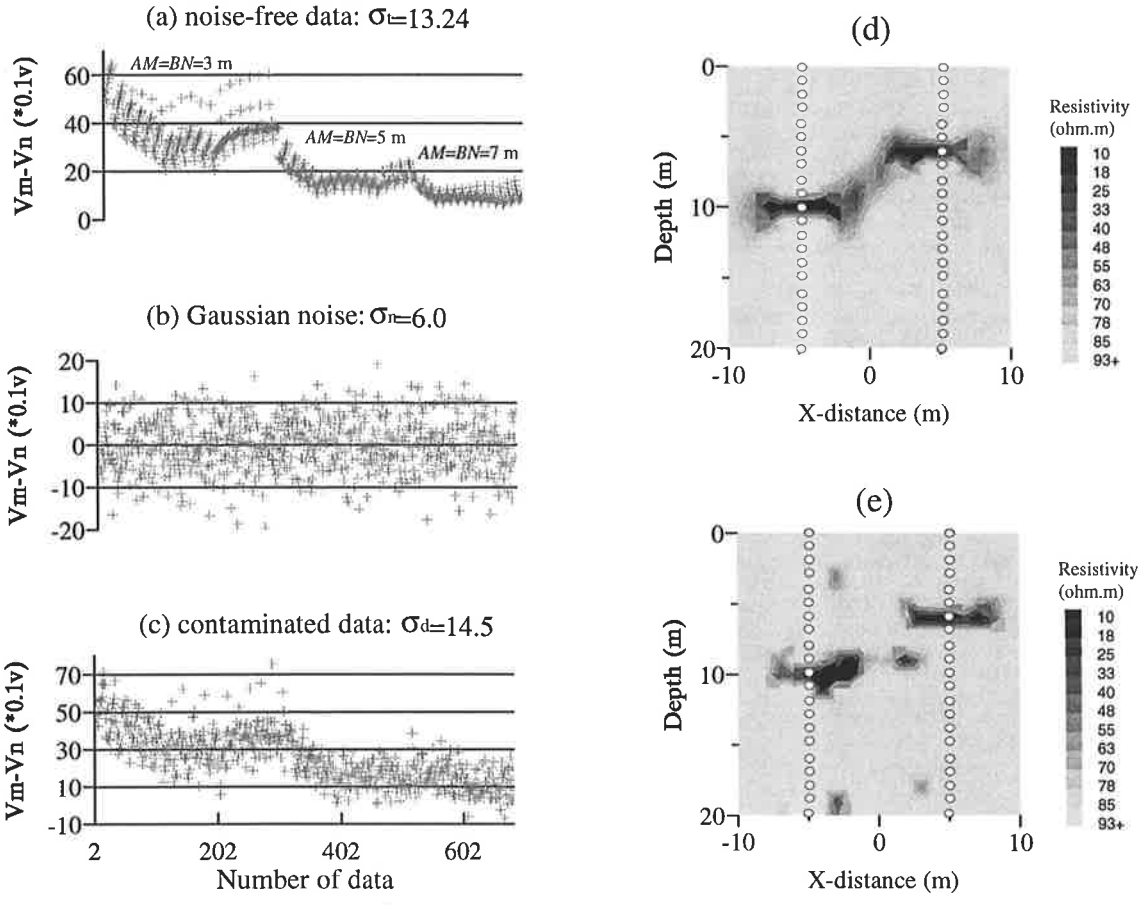

Fig.8-22 Synthetic data and imaging results obtained with crosshole bipole-bipole *AM-BN* configuration for Model-2. (a) noise-free data; (b) Gaussian noise; (c) noise-contaminated data (=(a)+(b)); (d) inversion result with (a); (e) inversion result with (c). The standard covariances ($\sigma_t, \sigma_n, \sigma_d$) of the different data are given.

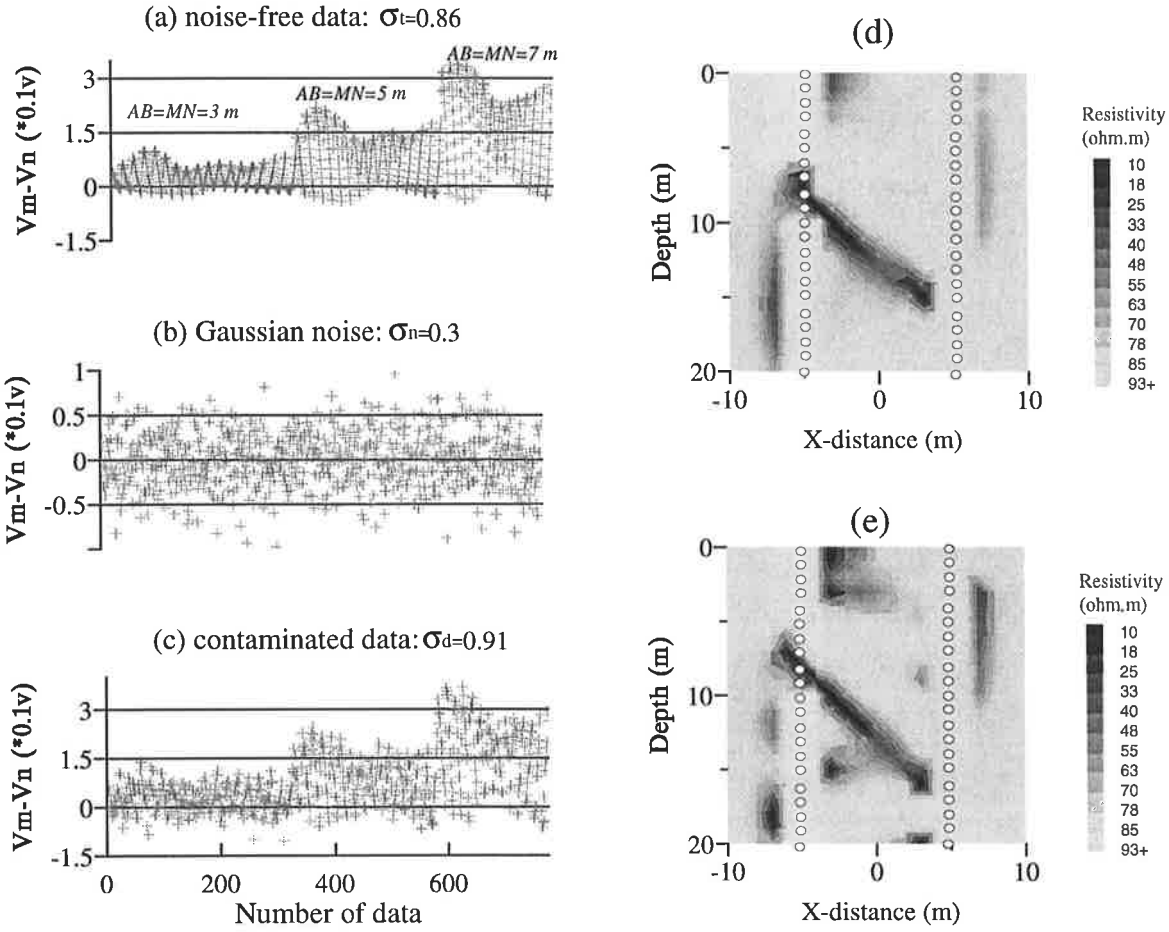

Fig.8-23 Synthetic data and imaging results obtained with crosshole bipole-bipole *AB-MN* configuration for Model-1. (a) noise-free data; (b) Gaussian noise; (c) noise-contaminated data (=(a)+(b)); (d) inversion result with (a); (e) inversion result with (c). The standard covariances ($\sigma_t, \sigma_n, \sigma_d$) of the different data are given.

AM-BN or *AM-NB* configurations may produce satisfactory images of the two models even when using the contaminated data and the imaging results are much better than that of the pole-pole *A-M* configuration.

In summary, *the quality variations of the images in the above numerical experiments can be attributed to the differences in the data, which have different sensitivity and anomaly effects for each configuration.* These imaging results show that *the images yielded by the pole-bipole AM-N, bipole-pole AM-B and bipole-bipole AM-BN data are much clearer and better resolved than the images obtained with the pole-pole A-M, pole-bipole A-MN (AB-M) and bipole-bipole AB-MN configurations.* Although the pole-pole imaging still can resolve the targets, there are more artefacts or distortions in the images than with the pole-bipole *AM-N*, bipole-pole *AM-B* and bipole-bipole *AM-BN*

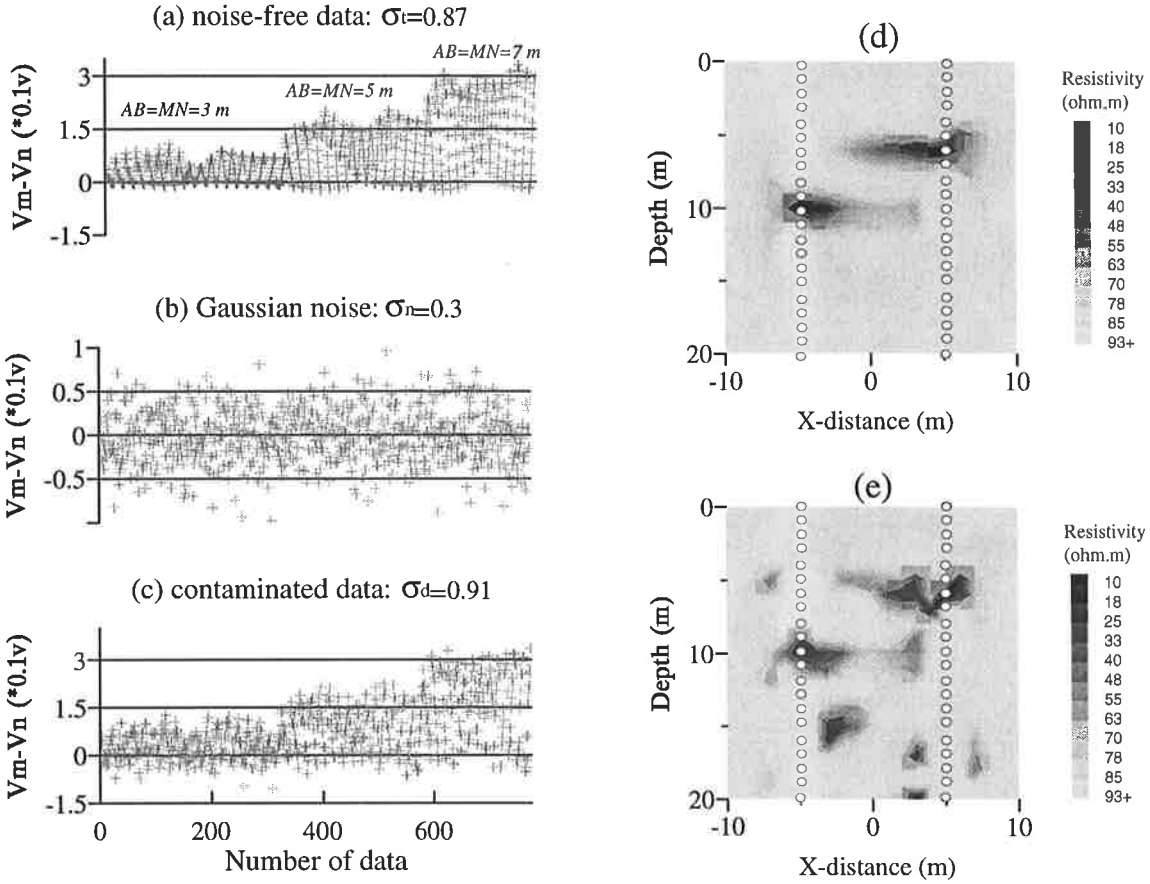

Fig.8-24 Synthetic data and imaging results of Model-2 with crosshole bipole-bipole *AB-MN* configuration. (a) noise-free data; (b) Gaussian noise; (c) contaminated data (=(a)+(b)); (d) inversion result with (a); (e) inversion result with (c). The standard covariances ($\sigma_t, \sigma_n, \sigma_d$) of the different data are given.

arrays. By conducting additional numerical experiments for imaging high contrast anomalies of these same two shaped models (the resistivities of the anomalies and the host medium are 10 Ωm and 1000 Ωm, respectively), we obtained similar results (Zhou and Greenhalgh, 1997). It seems that *these three- and four-electrode configurations are more sensitive to the targets between the two boreholes than is the pole-pole array*. This is consistent with the phenomenon mentioned in the previous section, that these data have better AE than the pole-pole data for square-shaped targets.

In addition, the synthetic data (simulation of crosshole measurement) show us that the pole-bipole *A-MN* , bipole-pole *AB-M* and bipole-bipole *AB-MN* configurations, besides having a singularity problem in computation of apparent resistivity, may produce small observed quantities (potential V_M or potential difference $V_M - V_N$) in practical application. The small voltages may easily be masked by the background noise. That is

why the imaging results for these configurations are not as good as ones from the pole-bipole *AM-N*, bipole-pole *AM-B* and bipole-bipole *AM-BN* configurations.

8.4 Numerical Experiments for Resistivity Profiling

From an inversion point of view, resistivity imaging with surface data (or resistivity profiling data) is similar to crosshole resistivity imaging except for the difference in data acquisition. So, our imaging algorithm can be directly applied to the inversion of surface resistivity profiling data.

As is well known, one of the common means of displaying/interpreting resistivity profiling data is through the ρ_a-pseudosection, which is a rough illustration of the resistivity variation in the subsurface. Automatic interpretation processes that can provide a more realistic resistivity image than the ρ_a-pseudosection have attracted much attention (Tripp et al., 1984; Smith and Vozoff, 1984; Shima, 1992; Li and Oldenburg, 1992; Dabas et al., 1994; Sasaki, 1994; Zhang et al, 1995; Loke and Barker, 1995, 1996). But most algorithms require an initial guess of the resistivity model. The guessed model must be close to the true model in order to achieve a successful inversion. But in most electrical applications, the interpreter has to face the situation that except for the ρ_a-pseudosection and the known surface geology there is no other information about the realistic resistivity distribution below the ground which can be used. An arbitrary guess or starting model having a uniform reference may lead to a false image of the subsurface because of the complexity of the real model and the multiple solutions to the inverse problem. Employing global optimisation algorithm, such as genetic or simulated annealing algorithms (Dittmer and Szymanski, 1995; Chunduru et al. 1995, 1996), costs huge computer resources for imaging (a large scale inversion).

Actually, no matter which electrode array is employed, the ρ_a-pseudosection more or less reflects the resistivity variations of the ground in both the horizontal and vertical directions, e.g. see Fig.3-10. In general, the shallow depth values in the ρ_a-pseudosection (obtained with smaller separations of the electrode arrays) are consistent with the real resistivity of the shallow parts of the subsurface and the deep values (obtained with larger separations of the electrode arrays) mainly reveal information on resistivity at

depth. However, the details are largely smoothed by including the shallow inhomogeneities. According to this property of the ρ_a-pseudosection, an initial model for inversion can be built around it. In the absence of other information, the comprehensive utilisation of the ρ_a-pseudosection is a natural and reasonable choice for a starting model in electrical resistivity inversion.

In this section, we apply the newly developed resistivity modeling and inversion algorithms to demonstrate electrical imaging with resistivity profiling data in which we employ the ρ_a-pseudosection, not only as the input data but also as the initial model. We then implement the inversion procedure subject to the near-surface constraints (which may be obtained from the ρ_a-pseudosection itself or the surface geology observations) to obtain the resistivity image of the subsurface. Three synthetic models: multiple resistive and conductive bodies (Fig.8-25a), a resistive basement step (Fig.8-26a) and a buried conductive target (Fig.8-27a)—computed for pole-pole and bipole-bipole arrays are used to examine the effectiveness of the method. The pole-pole profiling data are calculated with 21 electrodes (spacing 10 m) on the surface and sampling from 10 m to 200 m electrode separations. We have in total 420 data points available for inversion in each pole-pole array experiment. Meanwhile, the data in the depth range 0~60 m (of the ρ_a-pseudosection), to which are added some Gaussian noise, are used to plot the ρ_a-pseudosection and to form the initial model for inversion (see Fig.8-25b, Fig.8-26b and Fig.8-27b). Fig.8-25d, Fig.8-26d and Fig.8-27d give the imaging results from the pole-pole ρ_a-pseudosections. The bipole-bipole profiling data are calculated with 41 electrode positions (spacing 5 m) and 8 separations (n=8) ranging from a=10~45 m. In total, we have 196 data points for each model. In the same manner as above, the initial models for the three bipole-bipole imaging experiments were obtained from the ρ_a-pseudosections (see Fig.8-25c, Fig.8-26c and Fig.8-27c). Fig.8-25e, Fig.8-26e and Fig.8-27e give the imaging results (inversions) from the ρ_a-pseudosections. Examining the ρ_a-pseudosections in Fig.8-25, it is hard to recognize the existence of the three targets in the pole-pole or bipole-bipole ρ_a-pseudosections, but after inversion both imaging results for these two arrays disclose clear images of the three targets. Comparing the ρ_a-pseudosections with the imaging results in Fig.8-26 one can see that although the basement step is somewhat suggested in both ρ_a-pseudosections, the imaging results

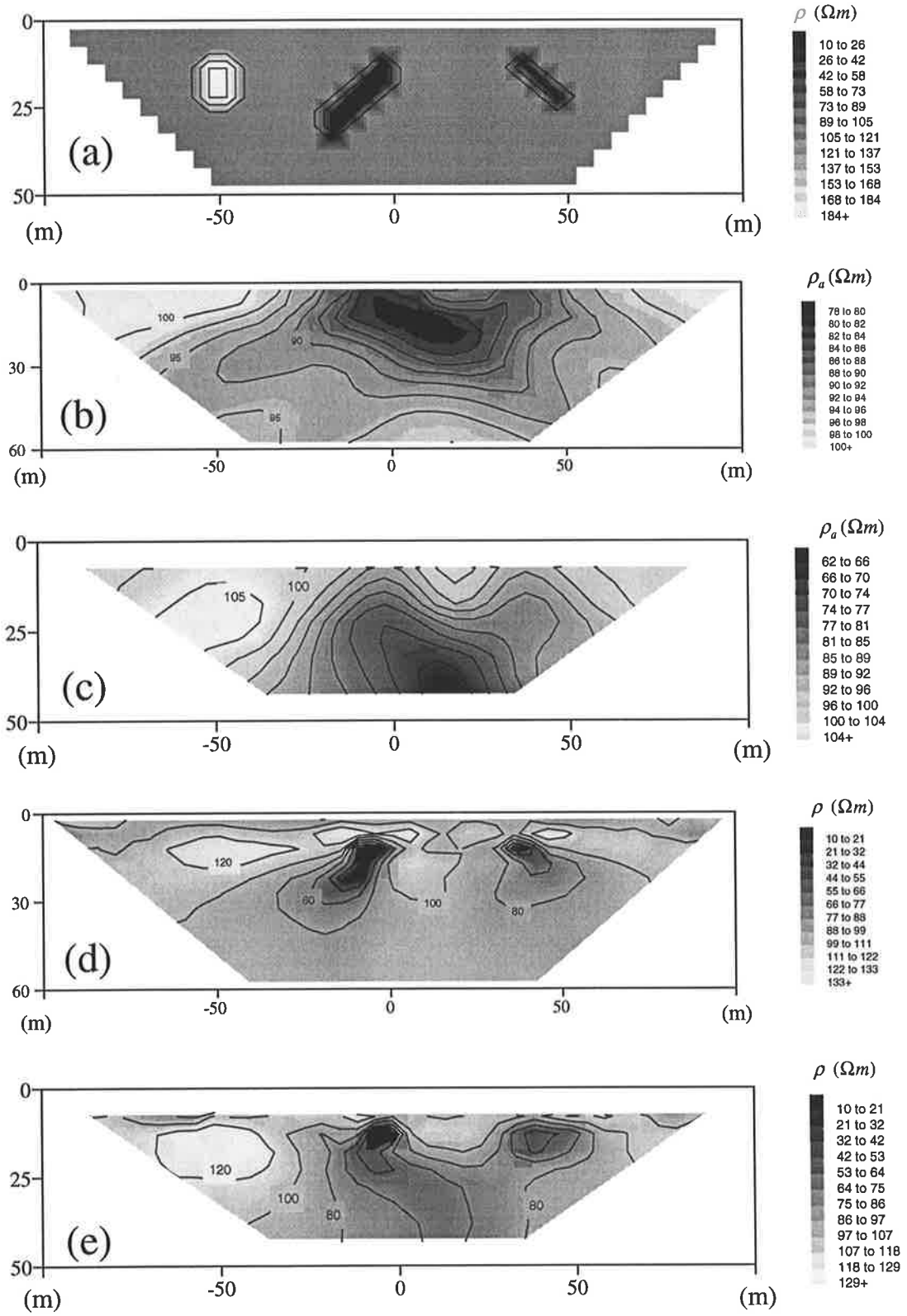

Fig.8-25 Imaging experiments for a multiple-target model with resistivity profiling data. (a) original model, (b) pole-pole ρ_a-pseudosection, (c) bipole-bipole ρ_a-pseudosection, (d) imaging result from (b), (e) imaging result from (c).

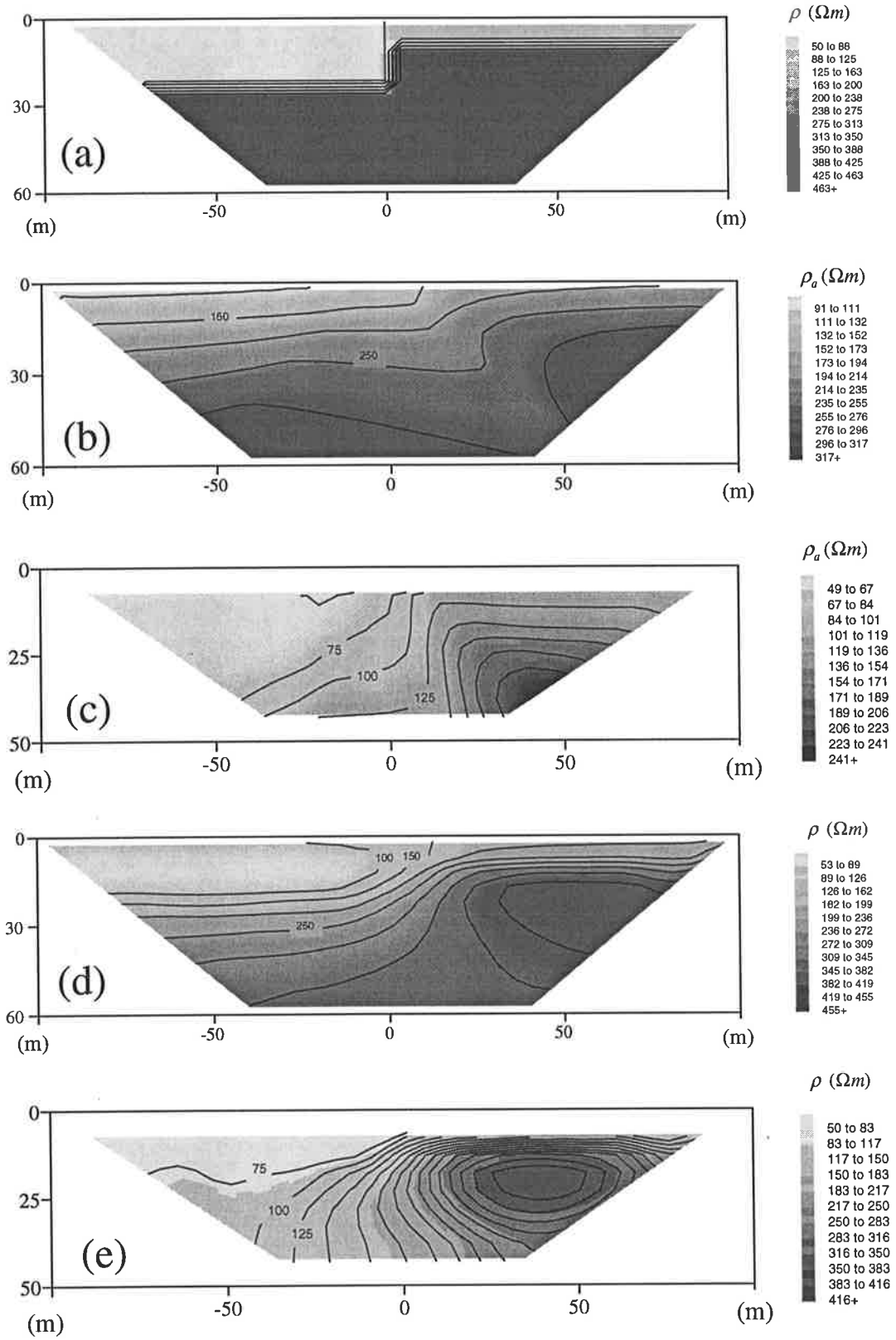

Fig.8-26 Imaging experiments for a resistive basement step model and resistivity profiling data. (a) original model, (b) pole-pole ρ_a-pseudosection, (c) bipole-bipole ρ_a-pseudosection, (d) imaging result from (b), (e) imaging result from (c).

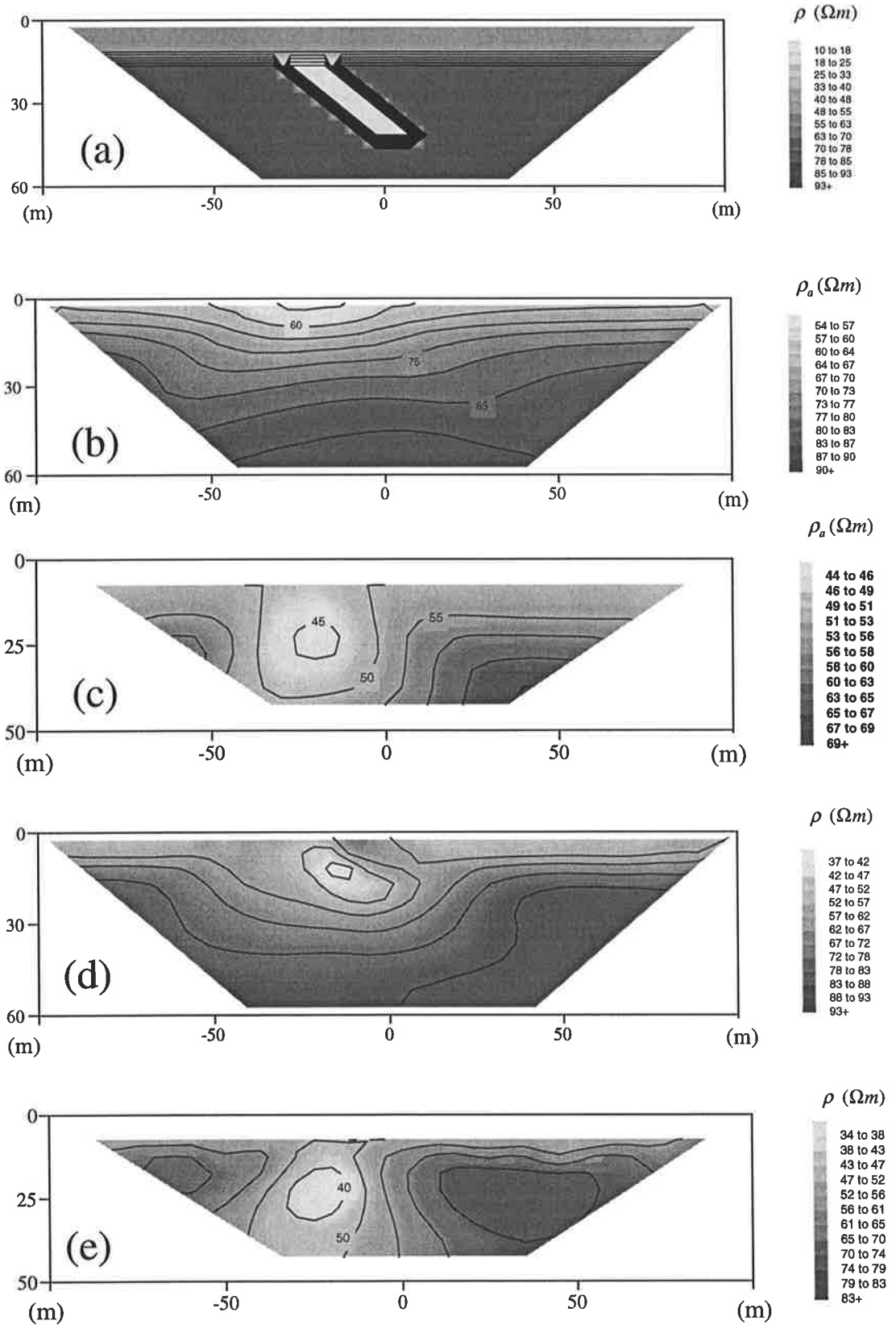

Fig.8-27 Imaging experiments for a buried conductive target with resistivity profiling data. (a) original model, (b) pole-pole ρ_a-pseudosection, (c) bipole-bipole ρ_a-pseudosection, (d) imaging result from (b), (d) imaging result from (c).

give a better match to the original model. In Fig.8-27, the buried conductive target is easily missed in the pole-pole ρ_a-pseudosection (see Fig.8-27b), but in the inversion result (Fig.8-27d) it is clearly imaged. Also, in this figure one can see that the bipole-bipole ρ_a-pseudosection gives a better illustration of the buried conductive target than the pole-pole ρ_a-pseudosection (Fig.8-27c), but the imaging result (Fig.8-27e) shows vast improvement in relation to the real model. In summary, these experiments show that the imaging procedure based on the ρ_a-pseudosection starting model may produce a much better image of the real resistivity distribution than the the ρ_a-pseudosection itself. In other words, the ρ_a-pseudosection can be used not only as the input data but also as the starting model to inversion so that even if no other data are available, a more satisfactory image of the subsurface is obtained. These experiments also demonstrate the difference in the ρ_a-pseudosections and the imaging effectiveness with pole-pole and bipole-bipole arrays. These two electrode arrays, as mentioned in Chapter 3, have different patterns of the ρ_a-pseudosection for the same model and it is shown again that the bipole-bipole ρ_a-pseudosection gives the features of the resistivity variation near-surface, while pole-pole ρ_a-pseudosection gives more information on the deeper structure. Both imaging results match the real model well. With the limited length of profile the imaging procedure using pole-pole data creates a better image than with bipole-bipole data.

8.5 Physical Model Imaging Experiments

A 3-D resistivity physical modeling system within the Geophysics Research Laboratory, Department of Geology and Geophysics, University of Adelaide was used to test our algorithm for crosshole resistivity imaging. Fig.8-28 is the sketch of the equipment used in the physical experiments. A SYSCAL-R2 digital resistivity instrument is

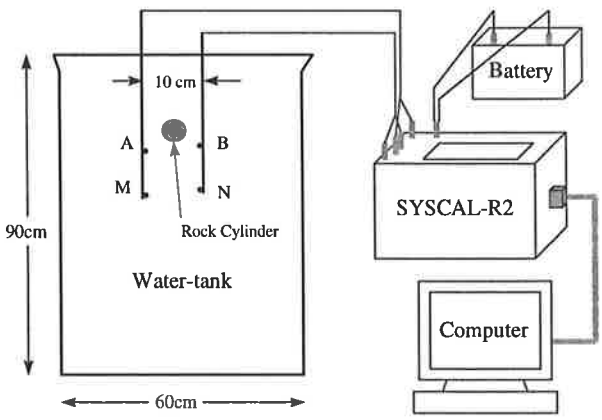

Fig.8-28 Physical modeling equipment used in the imaging experiments. *A* and *B* are current electrodes. *M* and *N* are potential electrodes.

interfaced to a PC and can store 390 set of measurements, each of which includes self-potential, current magnitude, voltage difference and information on the surveying configuration. Since the dimension of the water-tank (60×60×90cm) is not large enough for meaningful two- or three-electrode arrays (i.e. one or two electrodes at "infinity"), we only conducted experiments with the bipole-bipole *AM-BN* configuration.

The tank was filled with ordinary tap water and a resistive rock cylinder (diameter 5 cm) was suspended from string at a depth of 20 cm below the surface of water. The true resistivities of the tap water and the rock cylinder are unknown. The observed data were obtained at 1 cm spacing sampling with 5 cm separation of the electrodes *BN* (=*AM*) over the depth range 10cm 35 cm for each *AM* (see Fig.8-28). So in total there were 21×21=441 data points for imaging.

The first experiment was conducted without the rock cylinder, i.e. just water present in tank. Fig.8-29 gives the apparent resistivities, the imaging result and the inversion convergence curve. In theory, the apparent resistivities should be constant (real value of

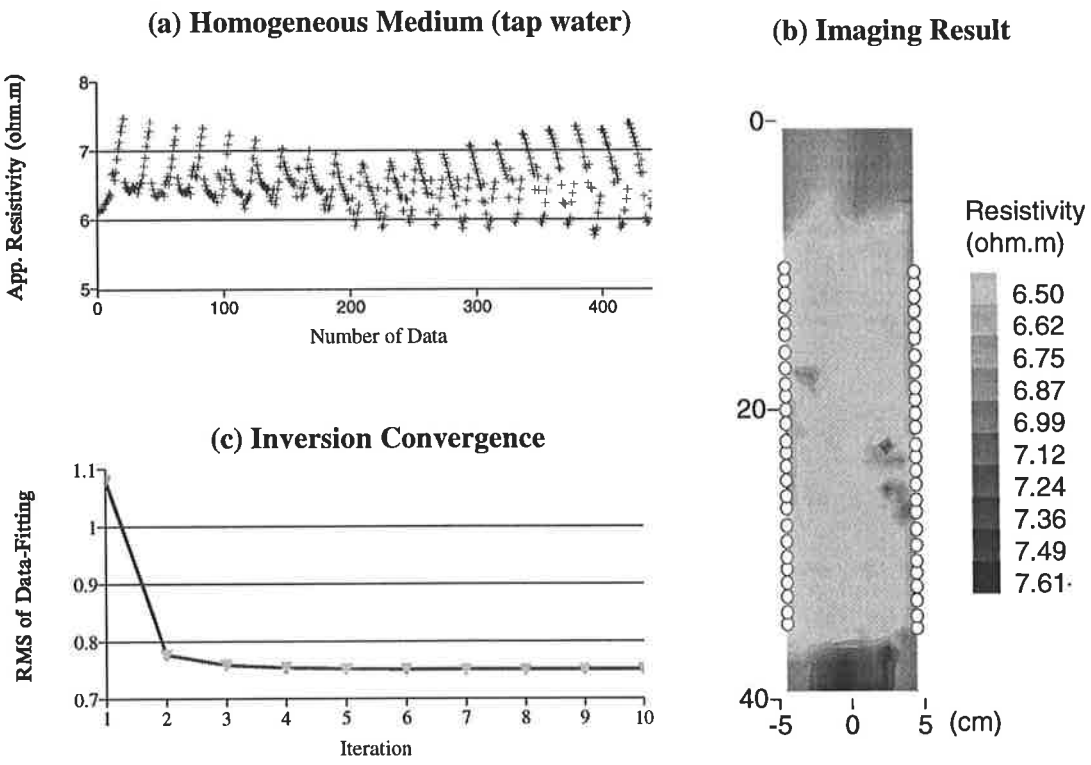

Fig.8-29 The physical modeling data and the imaging result with the crosshole bipole-bipole *AM-BN* configuration for pure tap water: (a) apparent resistivities, (b) imaging result and (c) inversion convergence curve.

the tap water) due to the homogeneous medium. But, the experimental data fluctuate in the range 570-750 Ωcm (see Fig.8-29a). This indicates that the data contain certain errors (e.g. random as well as systematic and location errors). However, we implemented the inversion using a constant 700 Ωcm starting model. The imaging result and the convergence curve (Fig.8-29b,c) show that the inversion procedure is successful, although a few artifacts appear in the final image due to the errors.

The second experiment was carried out by repeating the above procedure but with the rock cylinder in place within the tank. Fig.8-30 gives the results of the experiment, which shows that although the shape of the cylinder is distorted due to the limited illumination (coverage of the object was confined to the maximum angle range from -60° to +60°) and the location has been shifted up due to the electrode location errors (when the electrodes went deep inside the tank they were bent and crooked due to the position controller of the screw setting at the top of the tank), the imaging result gives a resolvable image of the resistive target. It shows that the bipole-bipole *AM-BN* configuration is indeed suitable for crosshole resistivity imaging.

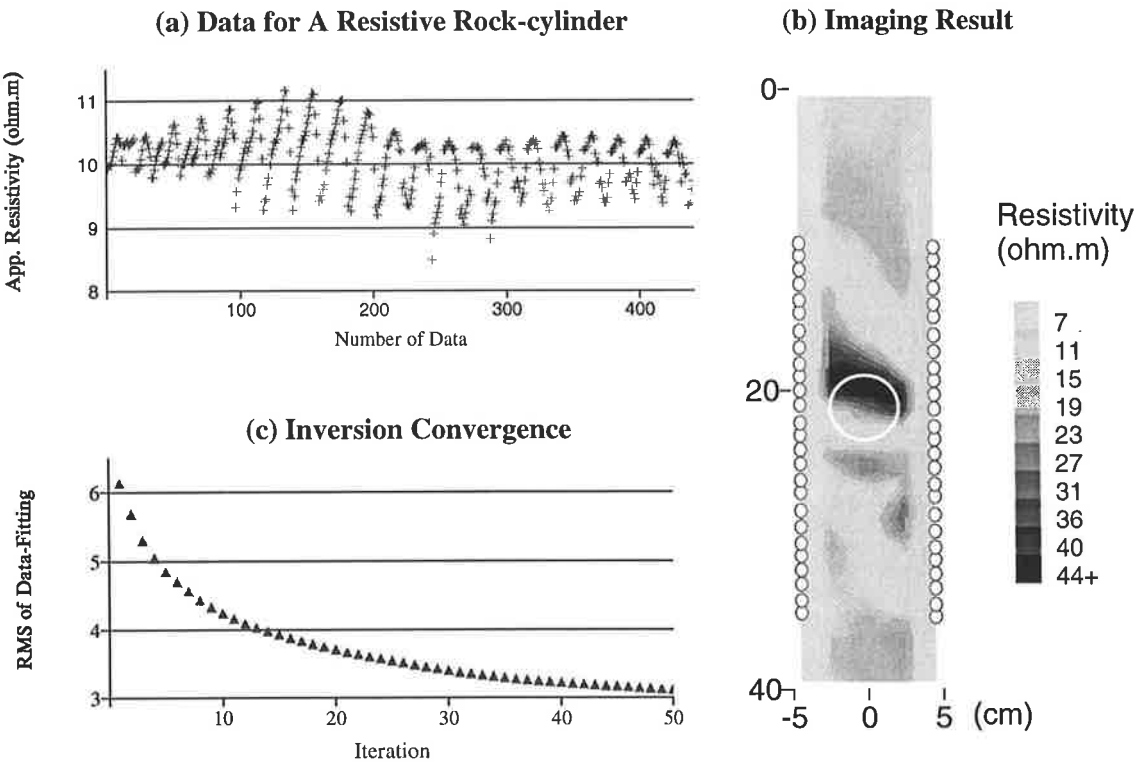

Fig.8-30 Physical modeling data and imaging result with the crosshole bipole-bipole *AM-BN* configuration for a resistive rock cylinder (shown by a white circle in (b)): (a) apparent resistivities, (b) imaging result and (c) inversion convergence curve.

Chapter 9
Numerical Simulations for Crosshole Acoustic Velocity Imaging

This chapter focuses on the question of full-waveform inversion and the use of crosshole full-waveform spectral data (Zhou and Greenhalgh, 1998c). It applies our new solution (the composite boundary-valued solution, Chapter 4) of the 2.5-D Helmholtz equation and the new computational algorithm for the Fréchet derivatives in the frequency-domain (Chapter 6). By performing numerical simulations, we examine the differences in effectiveness of each form of data (real, imaginary, amplitude, phase and Hartley spectra) and determine which is best for imaging the velocity distribution. In addition, we investigate an imaging scheme with an unknown source wavelet.

In the first section, we present a general form of solution for full-waveform inversion in the frequency-domain which incorporates the solution of the 2.5-D Helmholtz equation. The second section gives the formulation for the 2.5-D generalized diffraction tomography problem, which is considered as an approximate inversion of the 2.5-D Helmholtz equation with a spatially varying coefficient. Actually, this formulation is an extension of the 2-D case to the 2.5-D situation, from which one can see that 2.5-D generalized diffraction tomography is a specified form of full-waveform inversion. After that, we show the imaging effectiveness by means of numerical experiments with a known source-wavelet and different spectral data: real and imaginary components, amplitude and phase spectra, and the Hartley spectrum. Finally, a scheme for full-waveform inversion with an unknown source wavelet–inversion with normalized amplitude/Hartley spectral data, is investigated for crosshole acoustic velocity imaging.

9.1 Full-Waveform Inversion

Full-waveform inversion is generally used to image the Earth's subsurface with seismic waveform data, e.g to solve the Tikhonov regularization problem or Occam's inversion problem with seismic full-waveform time sequence or spectral data. The term 'full-

waveform' means that the waveform data include all the events lying in a specified time window $[t_1, t_2]$ or frequency window $[f_1, f_2]$ of a seismogram and the quantities of the waveform are calculated by solving a wave-equation rather than by a ray-tracing method. The full-waveform data may be a time sequence of seismograms in the time-domain or the spectral data in the frequency-domain, i.e. Fourier transform or Hartley transform of the seismograms. Tarantola (1984) and Sambridge et al. (1991) formulated full-waveform inversion in the time-domain. Mathematically, the equivalence of full-waveform inversion in the time-domain and in the frequency-domain has been proved by Bracewell's energy conservation with the l_2-norm criterion (Bracewell, 1978). The undesirable feature of full-waveform inversion in the time-domain is that the large number of pairs of source-geophones creates a formidable computational challenge for forward modeling. The main merit of full-waveform inversion in the frequency-domain is that it enables us to take the advantage of the spatial redundancy present in crosshole surveys and to form useful images of the interwell medium from single or multiple frequency components of the waveform spectral data (Pratt and Goulty, 1991; Woodward, 1992; Song and Williamson, 1995a, 1995b; Liao and McMechan, 1996). It is also shown by the above authors that the frequency-domain inversion is more efficient and flexible than that in the time domain.

Recalling the discussion in Chapter 6, full-waveform inversion in the frequency-domain may be described as the Tikhonov regularization solution or Occam's solution (see equation (6.4) and (6.6)) with some constrained condition:

$$\begin{cases} \min\{\left\|W_d[d_o - d(m)]\right\|^2 + \lambda\left\|W_m(m - m_0)\right\|^2\}, \\ m = Z_m(m), \end{cases} \tag{9.1}$$

or

$$\begin{cases} \min\{\left\|W_m(m - m_0)\right\|^2 + \lambda^{-1}(\left\|W_d[d_o - d(m)]\right\|^2 - \chi_d)\}, \\ m = Z_m(m), \end{cases} \tag{9.2}$$

where d_0 and $d(m)$ are the observed and computed frequency-domain full-waveform data. The models m and m_0 are the evaluated acoustic wavespeed distribution $c(r)$ and the average model $c_0(r)$. Z_m represents a constrained operator giving the range of the acceptable model m, e.g.

$$Z_m(m) = \begin{cases} a_i, & m_i \le a_i, \\ m_i, & a_i \le m_i, \\ b_i, & b_i \le m_i, \end{cases} \quad (i = 1,2,\ldots,N_m) \tag{9.3}$$

where $[a_i, b_i]$ is the range of the model parameter m_i. The constrained operator is easily combined with all iterative inversion algorithms discussed in Chapter 6 (see for example, Carrion, 1989; Zhou et al., 1992), which may be employed to approach the solutions of the above optimization problems.

In general, the spectral data of the waveform may be the Fourier transform (complex values) of the seismograms, which is represented by the real and imaginary components, or amplitude (magnitude response) and phase spectra. Alternatively, it may be the Hartley spectra (a real-valued transform, see Appendix A). In principle, all of the spectral forms may be used as the data either individually or in combination for the inversion.

In full-waveform inversion, one important step is to calculate the Fréchet and second derivatives of the data (see Chapter 6). Here, we neglect the second derivative in our inversion, because the values are much smaller than the Fréchet derivatives in the constant-density acoustic case (see Fig.7-10 and Fig.7-11). The Fréchet derivatives can be calculated in terms of the explicit expressions (7.54) or (7.56).

According to the definitions of these spectral data, we can directly write out the Fréchet derivatives for the real and imaginary components, and the Hartley spectra:

$$\text{Real component:} \quad \frac{\partial d_R(r_s,r_g)}{\partial c} = \mathrm{Re}\left[\frac{\partial \overline{P}(r_s,r_g)}{\partial c}\right], \tag{9.4}$$

$$\text{Imaginary component:} \quad \frac{\partial d_I(r_s,r_g)}{\partial c} = \mathrm{Im}\left[\frac{\partial \overline{P}(r_s,r_g)}{\partial c}\right], \tag{9.5}$$

$$\text{Hartley spectrum:} \quad \frac{\partial d_H(r_s,r_g)}{\partial c} = \mathrm{Re}\left[\frac{\partial \overline{P}(r_s,r_g)}{\partial c}\right] - \mathrm{Im}\left[\frac{\partial \overline{P}(r_s,r_g)}{\partial c}\right]. \tag{9.6}$$

where the subscripts R, I and H stand for the real, imaginary and Hartley spectral data, respectively, and $\overline{P}$ is the transformed pressure. For the amplitude and phase spectral data, using the following identity

$$\frac{\partial \ln \overline{\overline{P}}}{\partial c} = \frac{\partial}{\partial c}[\ln(\overline{A}e^{i\overline{\Psi}})] = \frac{\partial}{\partial c}[\ln \overline{A}] + i\frac{\partial \overline{\Psi}}{\partial c}, \tag{9.7}$$

we have $$\frac{\partial}{\partial c}(\ln \overline{A}) = \mathrm{Re}\{\frac{1}{\overline{\overline{P}}}\frac{\partial \overline{\overline{P}}}{\partial c}\}, \qquad \frac{\partial \overline{\Psi}}{\partial c} = \mathrm{Im}\{\frac{1}{\overline{\overline{P}}}\frac{\partial \overline{\overline{P}}}{\partial c}\}. \tag{9.8}$$

where $\overline{A}$ and $\overline{\Psi}$ represent the amplitude and phase spectra in the frequency-wavenumber domain. So, the Fréchet derivatives for the amplitude and phase spectra are obtained as:

$$\frac{\partial A}{\partial c} = F_c^{-1}[\frac{\partial \overline{A}}{\partial c}] = F_c^{-1}[\left|\overline{\overline{P}}\right| \mathrm{Re}(\frac{1}{\overline{\overline{P}}}\frac{\partial \overline{\overline{P}}}{\partial c})], \tag{9.9}$$

$$\frac{\partial \Psi}{\partial c} = F_c^{-1}[\frac{\partial \overline{\Psi}}{\partial c}] = F_c^{-1}[\mathrm{Im}(\frac{1}{\overline{\overline{P}}}\frac{\partial \overline{\overline{P}}}{\partial c})]. \tag{9.10}$$

Substituting equation (7.54) or (7.56) into these expressions (9.4)-(9.6) and (9.9)-(9.10), we obtain the derivatives with the constant-point or constant-block approximation so that one can individually implement the full-waveform inversion with these data. As the first step in the investigation, we plot the Fréchet derivatives for the spectral data to see what is the difference in the patterns of the derivatives, because the derivative may be viewed as a sensitivity function of the data or the wave-path in the frequency-domain (Woodward, 1992). The different patterns may reveal the spatial resolution of the data. Fig.9-1 and Fig.9-2 show the patterns of the Fréchet derivatives at two frequencies (100 Hz and 300 Hz) in a homogeneous model (c=3000 m/s) for the Hartley spectrum, amplitude and phase spectra (Fig.7-10 has shown the patterns for the real and imaginary components), respectively. From these figures, one can find that at the same frequency

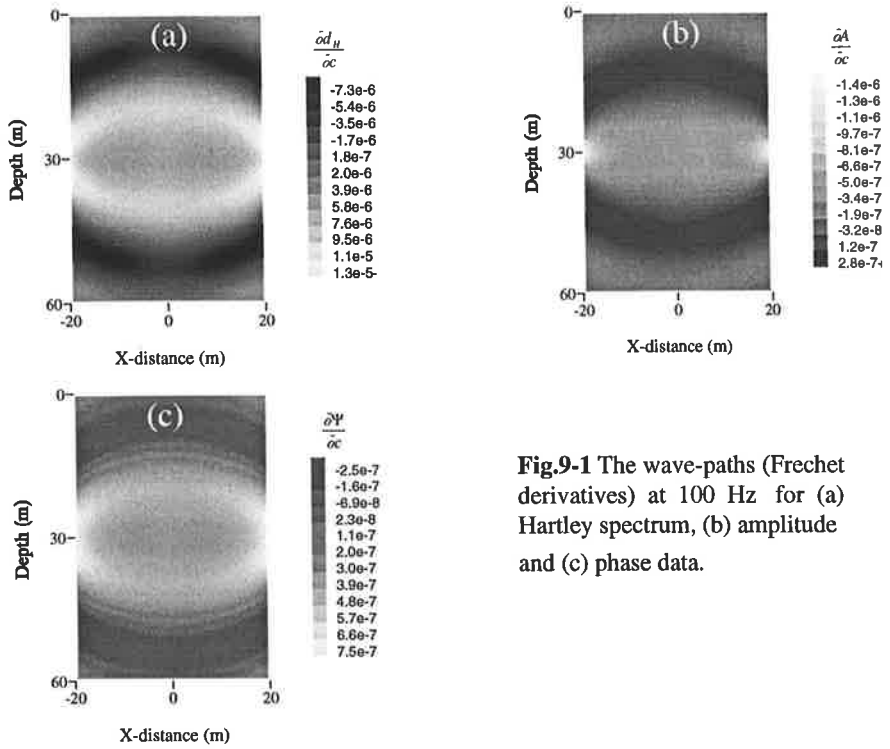

Fig.9-1 The wave-paths (Frechet derivatives) at 100 Hz for (a) Hartley spectrum, (b) amplitude and (c) phase data.

there is not much difference in the patterns of the Fréchet derivatives, except that the low-frequency patterns (100 Hz) have the tracks of a long wavelength wavefield and the high-frequency patterns (300 Hz) bring the impression of a short wavelength wavefield. This may cause varying effectiveness in spatial resolution when using the different frequency spectral data for crosshole acoustic velocity imaging.

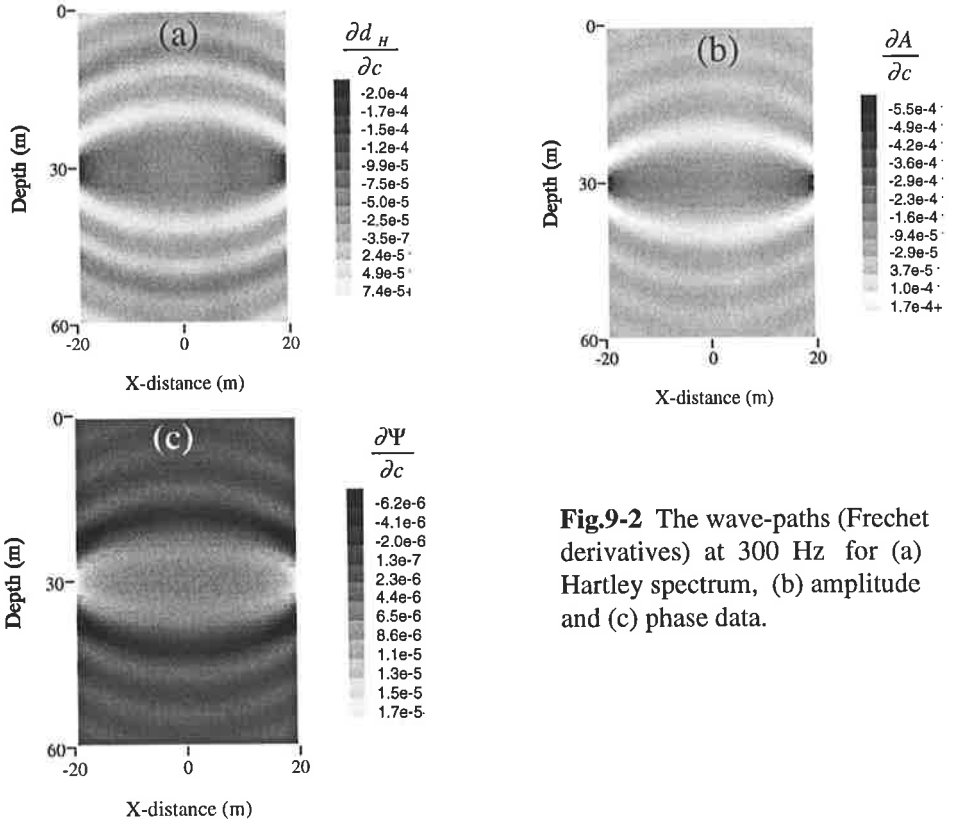

Fig.9-2 The wave-paths (Frechet derivatives) at 300 Hz for (a) Hartley spectrum, (b) amplitude and (c) phase data.

9.2 2.5-D Generalized Diffraction Tomography

Diffraction tomography is commonly considered as a solution for the inverse problem of the 2-D Helmholtz equation when the velocity contrast to the background medium is slight. According to the similarity of the 2-D and 2.5-D Helmholtz equations (see equations (2.1) and (2.24)), the 2-D formulation may be extended to the 2.5-D problem. Here, we follow Kaveh and Soumekh's (1981) 2-D formulation for the 2.5-D case so as to present both Born and Rytov approximations. Starting with the 2.5-D Helmholtz equation (2.24) and noting that the wavefield $\overline{\overline{P}}(r_s,r)$ is the form in the frequency-wavenumber domain, we present the scattered wavefield in the following form:

$$\overline{\overline{\Phi}}(r_s,r) = \overline{\overline{P}}_0(r_s,r)\overline{\overline{g}}(\alpha), \tag{9.11}$$

where $\overline{\overline{g}}(\alpha)$ represents a function of the parameter α, which is defined by

$$\alpha = \frac{\overline{\overline{P}}(r_s,r)}{\overline{\overline{P}}_0(r_s,r)}. \tag{9..12}$$

$\overline{\overline{P}}(r_s,r)$ and $\overline{\overline{P}}_0(r_s,r)$ are the wave responses to the actual medium $c(r)$ and the reference medium $c_0(r)$ in the frequency-wavenumber domain. Firstly, expanding the Laplacian operator for the scattered wavefield:

$$\nabla^2\overline{\overline{\Phi}} = \overline{\overline{g}}(\alpha)\nabla^2\overline{\overline{P}}_0 + \frac{d\overline{\overline{g}}}{d\alpha}[2\nabla\alpha\cdot\nabla\overline{\overline{P}}_0 + \overline{\overline{P}}_0\nabla^2\alpha] + (\nabla\alpha)^2\frac{d^2\overline{\overline{g}}}{d^2\alpha}\overline{\overline{P}}_0, \tag{9.13}$$

then using the following identity:

$$2\nabla\alpha\cdot\nabla\overline{\overline{P}}_0 + \overline{\overline{P}}_0\nabla^2\alpha = \nabla^2\overline{\overline{P}} - \alpha\nabla^2\overline{\overline{P}}_0, \tag{9.14}$$

and noting that both $\overline{\overline{P}}$ and $\overline{\overline{P}}_0$ satisfy equation (2.24), equation (9.13) can be rewritten as follows:

$$\nabla^2\overline{\overline{\Phi}} + (k_0^2 - k_y^2)\overline{\overline{\Phi}} = -S\overline{g}(\alpha) + \frac{d\overline{\overline{g}}}{d\alpha}[k_0^2O(r)\alpha\overline{\overline{P}}_0 + S(\alpha-1)] + (\nabla\alpha)^2\frac{d^2\overline{\overline{g}}}{d^2\alpha}\overline{\overline{P}}_0, \tag{9.15}$$

where $S = \frac{s(\omega)}{2}\delta(r-r_s)$ and $O(r) = 1 - c_0^2(r)/c^2(r)$. Applying the 2.5-D Green's function of the background medium to equation (9.15) and taking the integral over Ω, we have the explicit expression for the scattered wavefield:

$$\begin{aligned}\overline{\overline{\Phi}}(r_s,r_g) = -\int_{\Omega}[\alpha\frac{d\overline{\overline{g}}}{d\alpha}k_0^2O(r) + (\nabla\alpha)^2\frac{d^2\overline{\overline{g}}}{d^2\alpha}]\overline{\overline{P}}_0(r_s,r)\overline{\overline{G}}_0^{2.5D}(r_g,r)dr \\ + \frac{s(\omega)}{2}\overline{\overline{G}}_0^{2.5D}(r_g,r_s)[\overline{g}(\alpha) - \frac{d\overline{\overline{g}}}{d\alpha}(\alpha-1)]_{r=r_s}.\end{aligned} \tag{9.16}$$

Here we have used the symmetric property (or self-adjoint property) of the boundary operator B in equation (2.24).

Considering the Rytov approximation in which we define:

$$\overline{\overline{g}}(\alpha) = \ln(\alpha) = \ln(\frac{\overline{\overline{P}}}{\overline{\overline{P}}_0}), \tag{9.17}$$

it follows that $\overline{\overline{\Phi}} \approx \overline{\overline{P}}_0\ln(\frac{\overline{\overline{P}}}{\overline{\overline{P}}_0})$, $\alpha\frac{d\overline{\overline{g}}}{d\alpha} = 1$ and $\frac{d^2\overline{\overline{g}}}{d^2\alpha} = -\frac{1}{\alpha^2}$. Substituting these for equation (9.16) and assuming

$$\left|\frac{(\nabla\alpha)^2}{\alpha^2}\right| << 1, \tag{9.18}$$

equation (9.16) becomes:

$$\overline{\Phi}(r_s,r_g) = -k_0^2 s(\omega)\int_\Omega O(r)F_c^{-1}[\overline{\overline{G}}_0^{2.5D}(r_s,r)\overline{\overline{G}}_0^{2.5D}(r_g,r)]dr\,. \tag{9.19}$$

Here F_c^{-1} represents the inverse Fourier-cosine transform and we have used $\overline{\overline{P}}\,|_{r=r_s} = \overline{\overline{P}}_0\,|_{r=r_s}$ as $c(r_s) = c_0(r_s)$.

Considering now the Born approximation in which we defined:

$$\overline{\overline{g}}(\alpha) = \alpha - 1, \tag{9.20}$$

it follows that $\overline{\overline{\Phi}} \approx \overline{\overline{P}} - \overline{\overline{P}}_0$, $\frac{d\overline{\overline{g}}}{d\alpha} = 1$ and $\frac{d^2\overline{\overline{g}}}{d^2\alpha} = 0$. Equation (9.16) still reduces to equation (9.19) with the condition:

$$\left|k_0^2(\overline{\overline{P}} - \overline{\overline{P}}_0)O(r)\right| << 1. \tag{9.21}$$

So, equation (9.19) is the basic formula for 2.5-D generalized diffraction tomography, including both Born and Rytov approximations. It is very similar to the 2-D case (see equation 7, Wu and Toksöz, 1987). The difference only involves the inverse Fourier-cosine transform with respect to k_y in the 2.5-D case in that the Green's functions are obtained in the frequency-wavenumber domain instead of in the frequency-domain. Obviously, inequalities (9.18) and (9.21) are the available conditions for the Rytov and the Born approximations, both of which imply weak scattering ($|\overline{\overline{P}}(r_s,r) - \overline{\overline{P}}_0(r_s,r)|$ is small) or low velocity contrast ($O(r)$ is small). In order to image a complicated velocity variation with the condition, an inhomogeneous reference $c_0(r)$ may be chosen and the iterative formula can be employed:

$$\overline{\Phi}_l(r_s,r_g) = -s(\omega)\int_\Omega k_0^2 O_{l+1}(r)F_c^{-1}[\overline{\overline{G}}_l^{2.5D}(r_s,r)\overline{\overline{G}}_l^{2.5D}(r_g,r)]dr, \quad (l = 0,1,2,...); \tag{9.22}$$

where
$$\overline{\Phi}_l(r_s,r_g) = \begin{cases} \overline{P}_{ob}(r_s,r_g) - \overline{P}_l(r_s,r_g), & (Born) \\ \overline{P}_l(r_s,r_g)\ln[\overline{P}_{ob}(r_s,r_g)/\overline{P}_{l0}(r_s,r_g)], & (Rytov). \end{cases} \tag{9.23}$$

$$O_{l+1}(r) = 1 - \frac{c_l^2(r)}{c_{l+1}^2(r)}, \tag{9.24}$$

and $\overline{P}_{ob}(r_s,r_g)$ and $\overline{P}_l(r_s,r_g)$ are the observational spectrum and computational responses

to the current reference $c_l(r)$. Discretizing the integral range Ω into a number of small blocks $\Omega = \sum_e \Omega_e$ in equation (9.22) and representing $O_{l+1}(r)$ in the following form in the block Ω_e:

$$O_{l+1}(r) = \sum_k N_k^e(r) O_k^{(l+1)}, \tag{9.25}$$

where $N_k^e(r)$ and $O_k^{(l+1)}$ are the shape functions (or basic functions) and nodal values of $O_{l+1}(r)$ at the kth node, equation (9.22) becomes the linear equation system for all of the source-geophone pairs:

$$\tilde{d}_l = A_l \tilde{O}_{l+1}. \tag{9.26}$$

Here $\tilde{d}_l = \{\overline{\Phi}_1^{(l)}, \overline{\Phi}_2^{(l)}, ..., \overline{\Phi}_n^{(l)}\}$, $\tilde{O}_l = \{O_1^{(l+1)}, O_2^{(l+1)}, ..., O_m^{(l+1)}\}$ and $A_l = \left[A_{ij}^{(l)}\right]$ is the matrix calculated by

$$A_{ij}^{(l)} = -s(\omega) \sum_e \int_{\Omega_e} k_l^2 N_j^e(r) F_c^{-1} \{\overline{\overline{G}}_l^{2.5D}(r_{s_i}, r) \overline{\overline{G}}_l^{2.5D}(r_{g_i}, r)\} dr. \tag{9.27}$$

The inversion of the 2.5-D Helmholtz equation (2.25) reduces to solving the linear equation system (9.26), but the matrix $A_l = \left(A_{ij}^l\right)$ may be ill-posed due to noise-contamination and incomplete data $\tilde{d}_l$. So, a generalized inverse matrix A_l^{-g} of A_l must be sought (Menke, 1984). For example, we can seek the solution of the optimalization problem $\min\{\left\|W_d(\tilde{d}_l - A_l \tilde{Q}_{l+1})\right\|^2 + \lambda \left\|W_m \tilde{Q}_{l+1}\right\|^2\}$ for l=0,1,2...(Chapter 6). The solution may be represented as follows in terms of equation (6.14) or (6.22):

$$\tilde{O}_{l+1} = \tilde{O}_l + A_l^{-g}[W_m^{-1} A_l^T W_d (\tilde{d}_l - A_l \tilde{O}_l) - \lambda \tilde{O}_l], \quad (l = 0,1,2,...). \tag{9.28}$$

Here $A_l^{-g} = [W_m^{-1} A_l^T W_d A_l + \lambda I]^{-1}$ and we have taken the substitutions: $m_l = \tilde{O}_l$, $\partial d_i / \partial m_j^{(l)} = A_{ij}^{(l)}$ and $c_0(r)$ as the average model in equation (6.14) or (6.22) so that $m_0 = \tilde{O}_0 = [1 - c_0^2(r)/c_0^2(r)] = 0$. Once the reference $c_l(r)$ is given, the numerical methods described in Chapter 4 may be used to compute the Green's functions $\overline{\overline{G}}_l(r_{s_i}, r)$ and $\overline{\overline{G}}_l(r_{g_i}, r)$ in equation (9.27).

From the iterative formula (9.28), the matrix A_l given by equation (9.27) behaves as the Fréchet derivative $\partial \tilde{d}_l / \partial \tilde{O}$ or sensitivity matrix of the Born and Rytov data (see equation (9.23)). Reviewing equations (7.56) and (9.27), we see they are very similar.

The difference is only in the model parameter definitions (the former is $c(r)$ and the latter is $O(r)$) and model parametrizations. In fact, if the constant-block model parameterization is taken in equation (9.27):

$$N_k^e(r) = \delta(\Omega_e) = \begin{cases} 1, & r \in \Omega_e \\ 0, & others, \end{cases} \tag{9.29}$$

it becomes the same form as equation (7.56). This implies that the matrix A_l defined by equation (9.27) is the Fréchet derivative of the Born and Rytov data. On the other hand, the Born ($\tilde{d}_l = \overline{P}_{ob} - \overline{P}_l$) or Rytov data ($\tilde{d}_l = \overline{P}_l[\ln \overline{P}_{ob} - \ln \overline{P}_l]$) is actually a kind of measurement of the fit between the observed waveform $\overline{P}_{ob}$ and the computed waveform $\bar{P}_l$ in the frequency-domain, so 2.5-D generalized diffraction tomography is a specified form of full-waveform inversion in the frequency-domain.

9.3 Imaging with a Known Source Wavelet

It must be mentioned that in a practical application, full-waveform inversion or generalized diffraction tomography requires a known source spectrum $s(\omega)$ so as to compute the synthetic spectrum $\bar{P}$ (equation (2.31)) or $\overline{P}_l$ (equation (9.23)) and the Fréchet derivative (equation (7.54)) or the matrix A_{ij}^l (equation (9.27)). This prompts one to use some special technique to extract the source spectrum or perform extra field measurements to determine the source wavelet, e.g. Pratt and Worthington (1988) performed a scheme to extract the source wavlet; Ulrych et al. (1995) demonstrated a process of deconvolution. In this section, we assume the source wavelet is known and examine the imaging effectiveness of full-waveform inversion with different forms of the spectral data. In general, we assign a spike $\delta(t)$-source to the source wavelet ($s(\omega)$=1), because any other source wavelet may be expressed in terms of the $\delta(t)$-source.

To conduct numerical crosshole imaging experiments, three models (Fig.9-3) were used. Model-1 has three isolated diffraction points (c=3.5 km/s) in the host medium (c=3.0 km/s). This model is an impossible challenge for first-arrival transmission traveltime tomography, because the targets are very small in dimension. Model-2 and Model-3 involve a dipping low-velocity fracture and a faulted coal seam (c=2.5 km/s) embedded

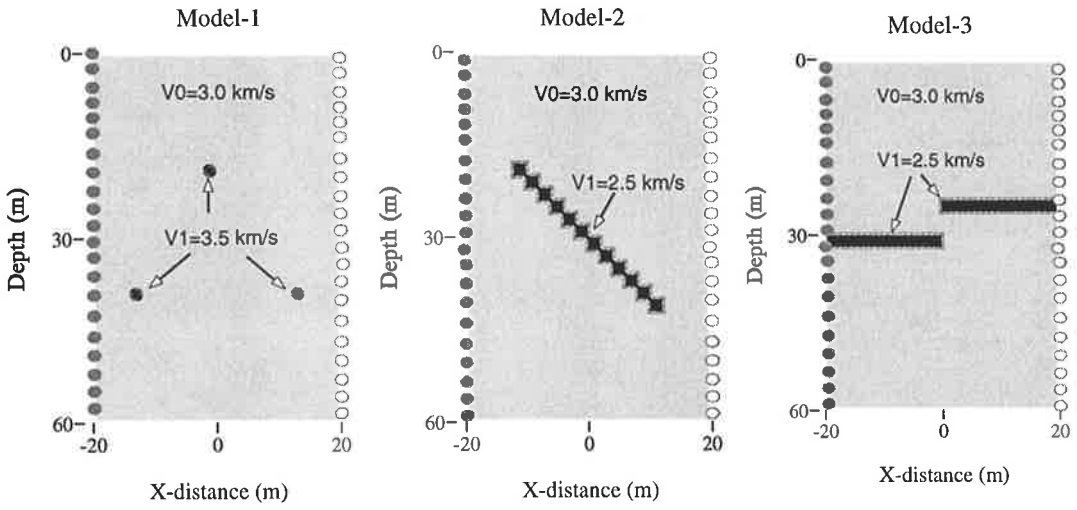

Fig.9-3 Three models for numerical simulation of 2.5-D crosshole acoustic velocity imaging. 21 sources and 21 receivers are distributed at an equal spacing along the left and right boreholes respectively.

in a high velocity host medium, respectively. We expect, by implementing full-waveform inversion with the three models, to indicate the imaging effectiveness of the different spectral data to various geological targets. In each model 21 sources and 21 receivers are distributed at an equal spacing along the left and right boreholes, respectively, as shown in Fig.9-3.

In the numerical simulations, we applied the algorithm of the composite-boundary solution in Chapter 4 to obtain the wavefield response d^i_{syn} (i=1,2,...,N) for the three models (the numerical imaging experiment with the damping method can be found in Zhou and Greenhalgh, 1998b), then added some Gaussian noise (white-noise) to form the observed data d^i_{ob} (i=1,2,...,N) for imaging. The noise-contaminated data ('observed data') were synthesized by the following formula:

$$d^i_{ob} = d^i_{syn} \cdot [1 + n\% \cdot GN(\sigma_N = 1, i \in N)] \quad (i=1,2,..,N), \tag{9.30}$$

where the integer n is used to control the noise level. $GN(\sigma_N = 1, i \in N)$ represents Gaussian noise whose standard deviation is unity. For Model-1, we used 5% (n=5) Gaussian noise and for Model-2 and Model-3 changed to 15% (n=15), considering the difference in the size of the targets. The observed data individually entail 21×21 monochromatic real, imaginary, amplitude, phase and Hartley spectral values at 300 Hz and 200 Hz. The use of the different frequency samples corresponds to illuminating the

media with incident waves of 15 m and 10 m wavelengths, respectively. For comparison, we used the same noise level, the same starting model (host medium) and the same inversion algorithm (Local-search quadratic approximation CGS, Chapter 6) for different spectral data.

(1) Using Real and Imaginary Components

The real and imaginary components are basic spectra of the Fourier transform. When inquiring into the effectiveness of crosshole acoustic velocity imaging, we individually implemented full-waveform inversion with the two components. Figures 9-4, 9-5 and 9-6 show the synthetic data and the imaging results obtained with the real components at 300 Hz. In the plots, the minimum and maximum of the data (noise-free data and Gaussian noise) used in the experiments are shown. Figures 9-7, 9-8 and 9-9 are the results obtained using the imaginary components at the same frequency. From these results, one can see that both forms of the spectral data yield very clear images with the noise-free data. In the noisy data cases, although some artifacts appear and the targets

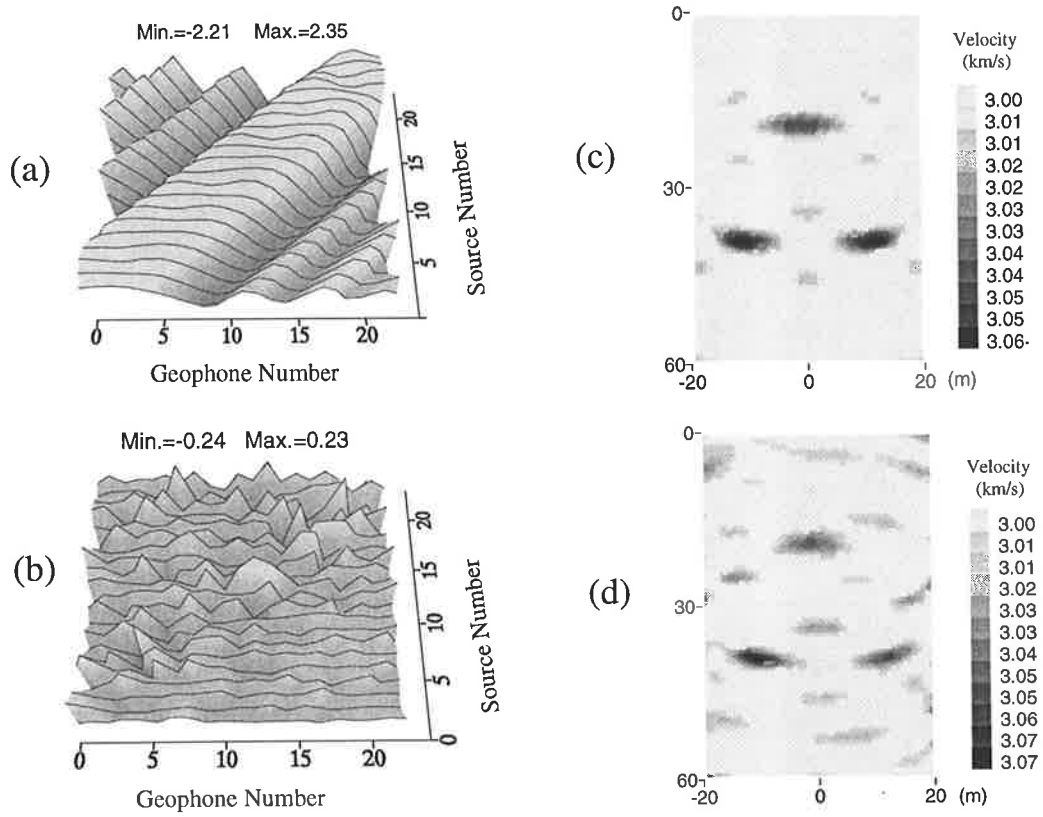

Fig.9-4 Synthetic data and imaging results obtained with the real components at 300 Hz for Model-1: (a) noise-free data, (b) 5% Gaussian noise, (c) imaging result with the noise-free data (a), and (d) imaging result with the noise-contaminated data (a)+(b).

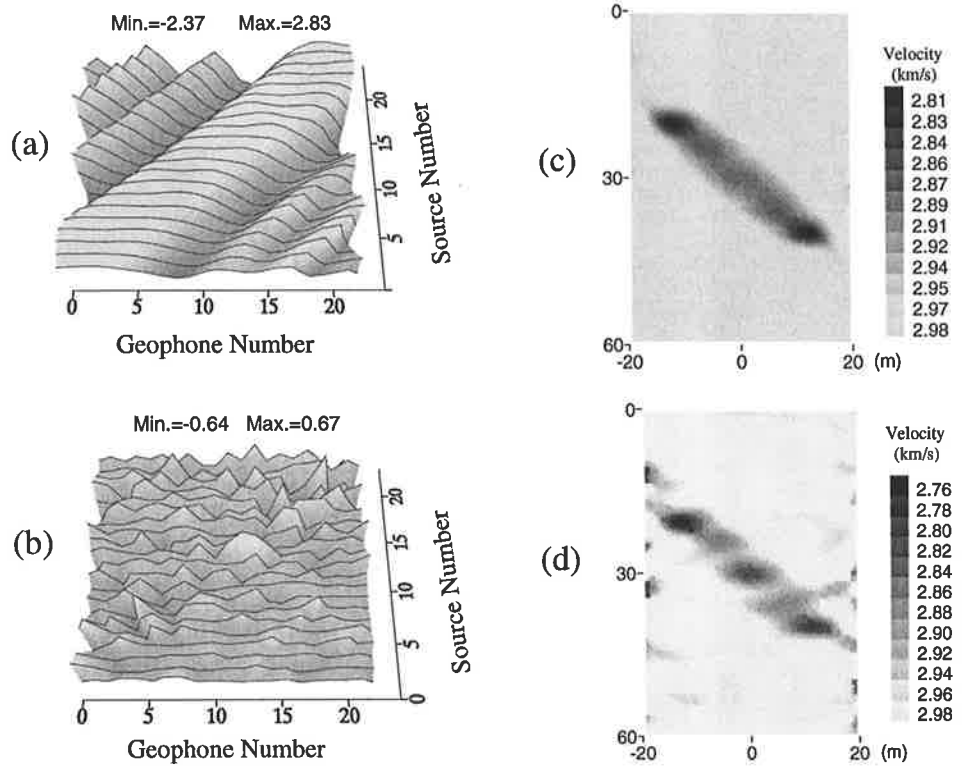

Fig.9-5 Synthetic data and imaging results obtained with the real components at 300 Hz for Model-2: (a) noise-free data, (b) 15% Gaussian noise, (c) imaging result with the noise-free data (a), and (d) imaging result with the noise-contaminated data (a)+(b).

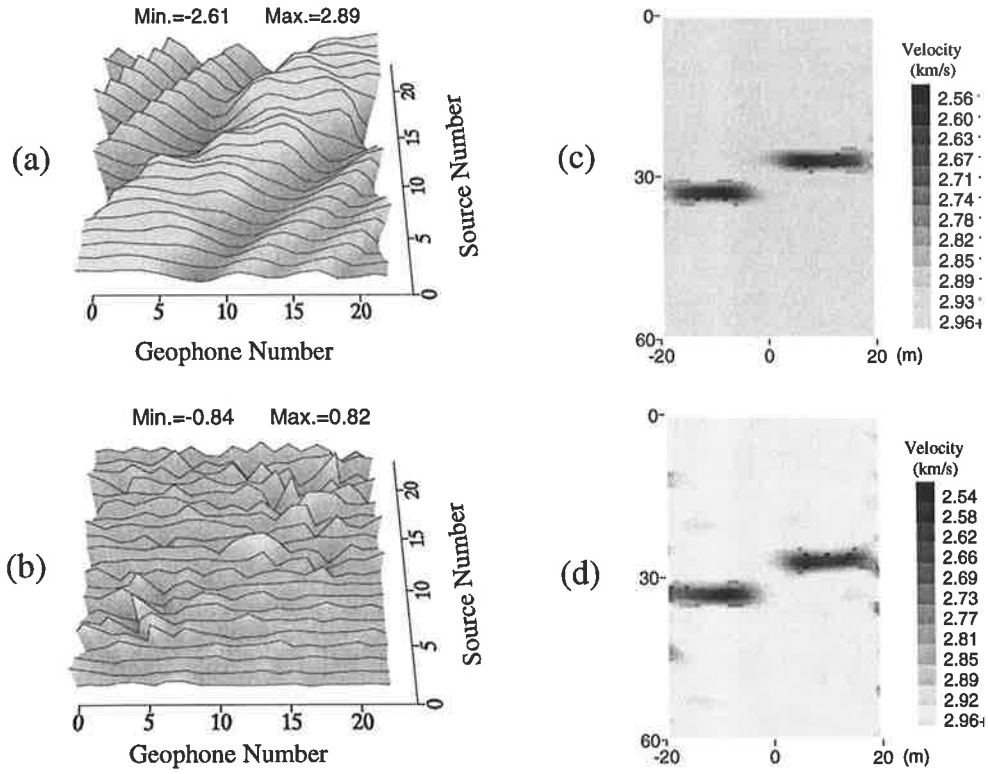

Fig.9-6 Synthetic data and imaging results obtained with the real components at 300 Hz for Model-3: (a) noise-free data, (b) 15% Gaussian noise, (c) imaging result with the noise-free data (a), and (d) imaging result with the noise-contaminated data (a)+(b).

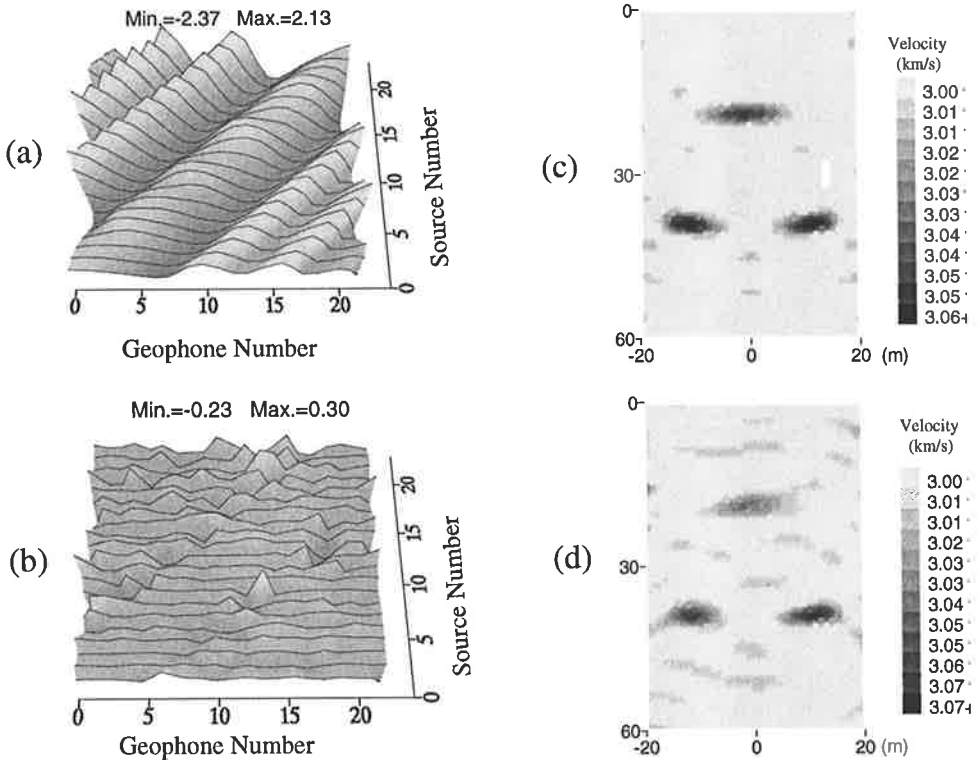

Fig.9-7 Synthetic data and imaging results obtained with the imaginary components at 300 Hz for Model-1: (a) noise-free data, (b) 5% Gaussian noise, (c) imaging result with the noise-free data (a), and (d) imaging result with the noise-contaminated data (a)+(b).

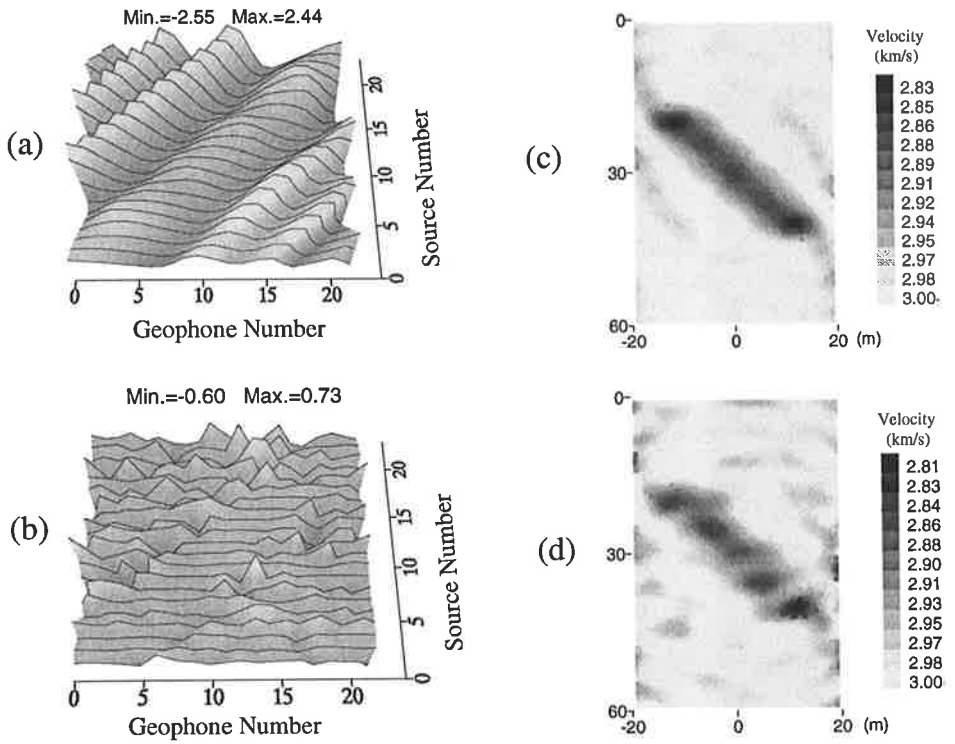

Fig.9-8 Synthetic data and imaging results obtained with the imaginary components at 300 Hz for Model-2: (a) noise-free data, (b) 15% Gaussian noise, (c) imaging result with the noise-free data (a), and (d) imaging result with the noise-contaminated data (a)+(b).

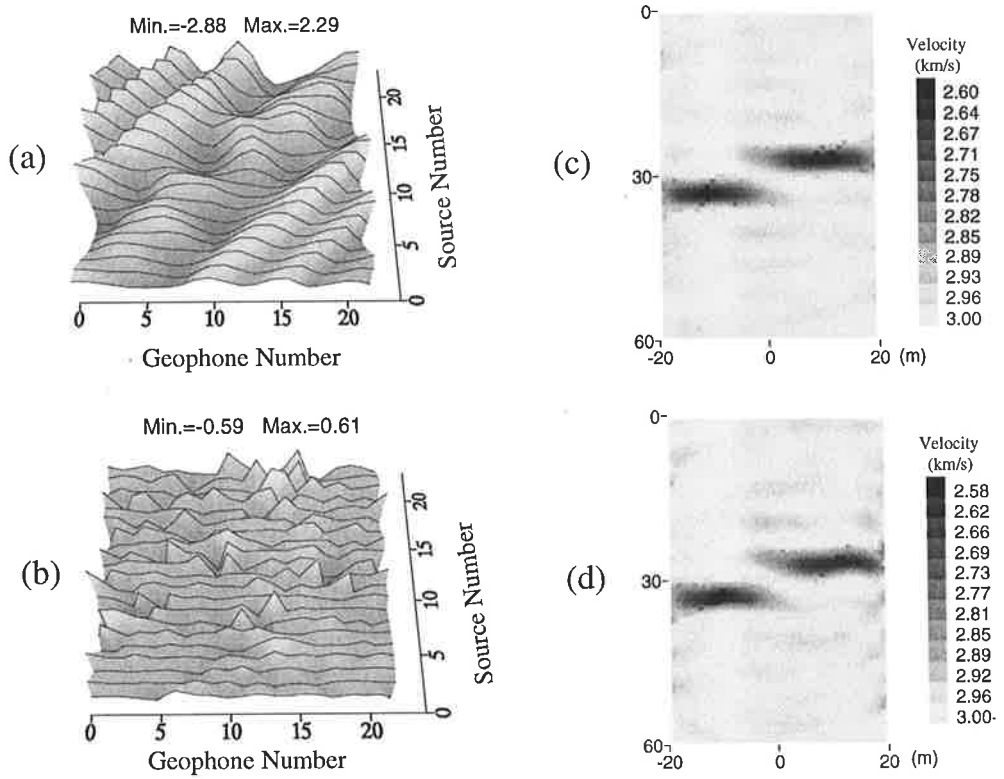

Fig.9-9 Synthetic data and imaging results obtained with the imaginary components at 300 Hz for Model-3: (a) noise-free data, (b) 15% Gaussian noise, (c) imaging result with the noise-free data (a), and (d) imaging result with the noise-contaminated data (a)+(b).

are somewhat distorted, the images of the anomalies are still clear and the imaginary spectral data produce almost the same quality images as the real component does for the three models. These experiments show that the real and imaginary components of the Fourier transform are useful for crosshole acoustic velocity imaging.

(2) Using Hartley-Spectral Data

The Hartley transform is a real-value transform and has some advantages in data processing, i.e. less memory requirement, a fast algorithm and no complex arithmetic. This transform may be applied to the conversion of a seismogram into the frequency-domain (Hartley spectrum). In application, the Hartley spectrum is easily obtained by performing the discrete Hartley transform or from the Fourier transformed spectrum in terms of the relationship between the two transforms (Appendix A). To investigate the effectiveness for crosshole acoustic velocity imaging, we repeated the above experiments but used the Hartley spectral data. Figures 9-10, 9-11 and 9-12 give the synthetic data and the imaging results at 300 Hz. Comparing these figures with the previous results, one can find that all the imaging results seem to be a little better than

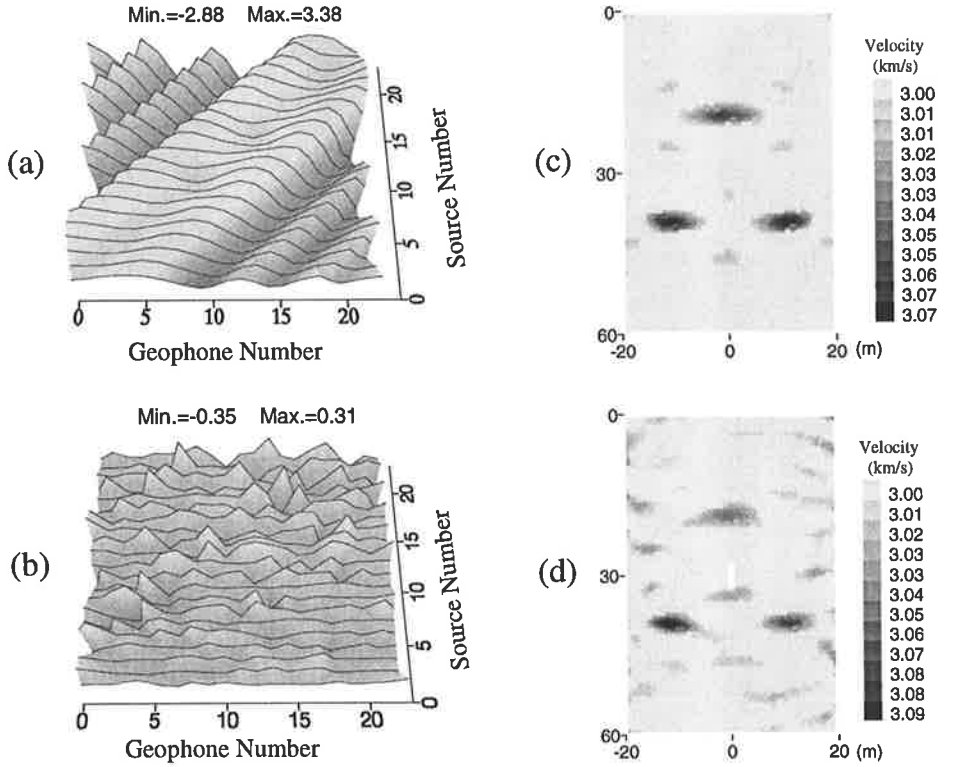

Fig.9-10 Synthetic data and imaging results obtained with the Hartley spectra at 300 Hz for Model-1: (a) noise-free data, (b) 5% Gaussian noise, (c) imaging result with the noise-free data (a), (d) imaging result with the noise-contaminated data (a)+(b).

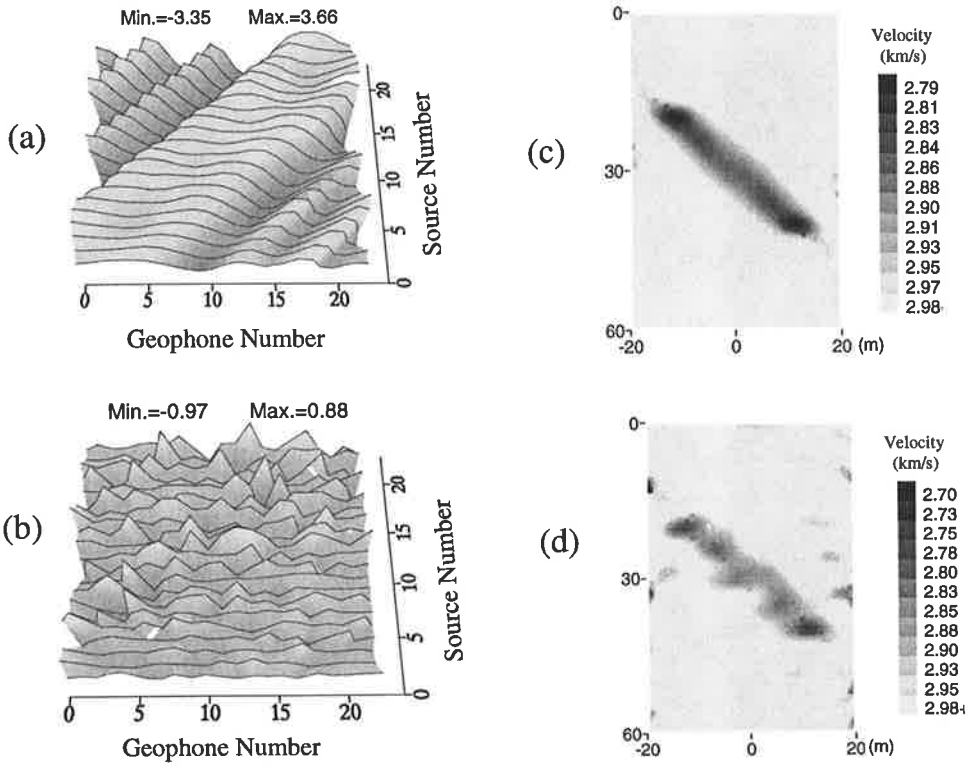

Fig.9-11 Synthetic data and imaging results obtained with the Hartley spectra at 300 Hz for Model-2: (a) noise-free data, (b) 15% Gaussian noise, (c) imaging result with the noise-free data (a), (d) imaging result with the noise-contaminated data (a)+(b).

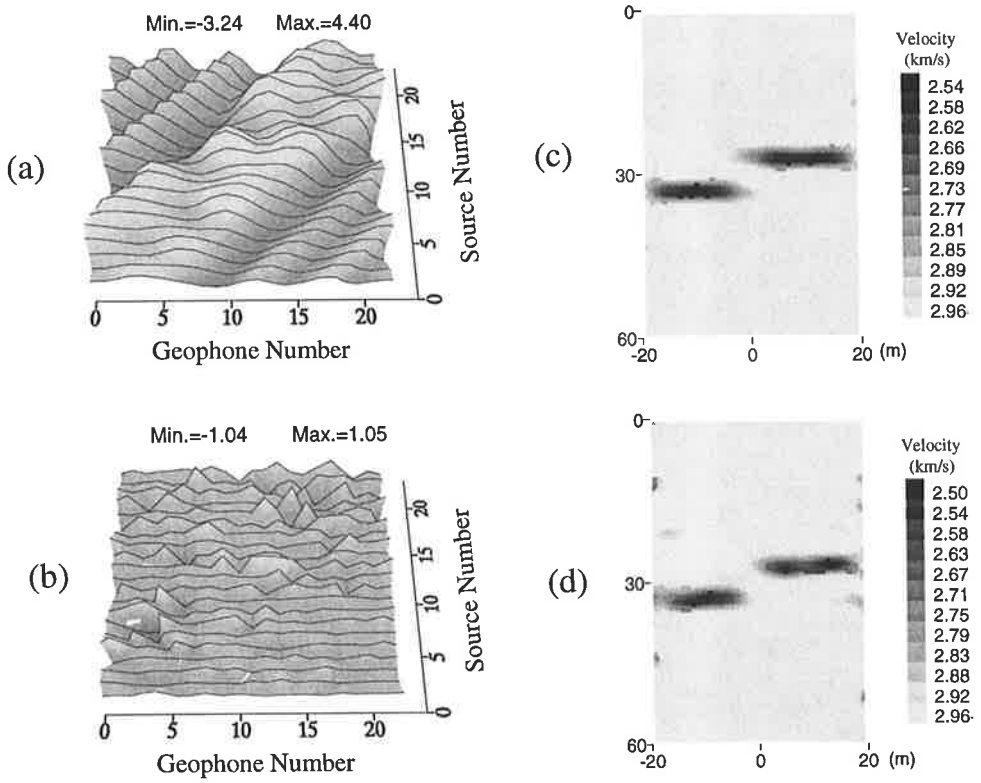

Fig.9-12 Synthetic data and imaging results obtained with the Hartley spectra at 300 Hz for Model-3: (a) noise-free data, (b) 15% Gaussian noise, (c) imaging result with the noise-free data (a), (d) imaging result with the noise-contaminated data (a)+(b).

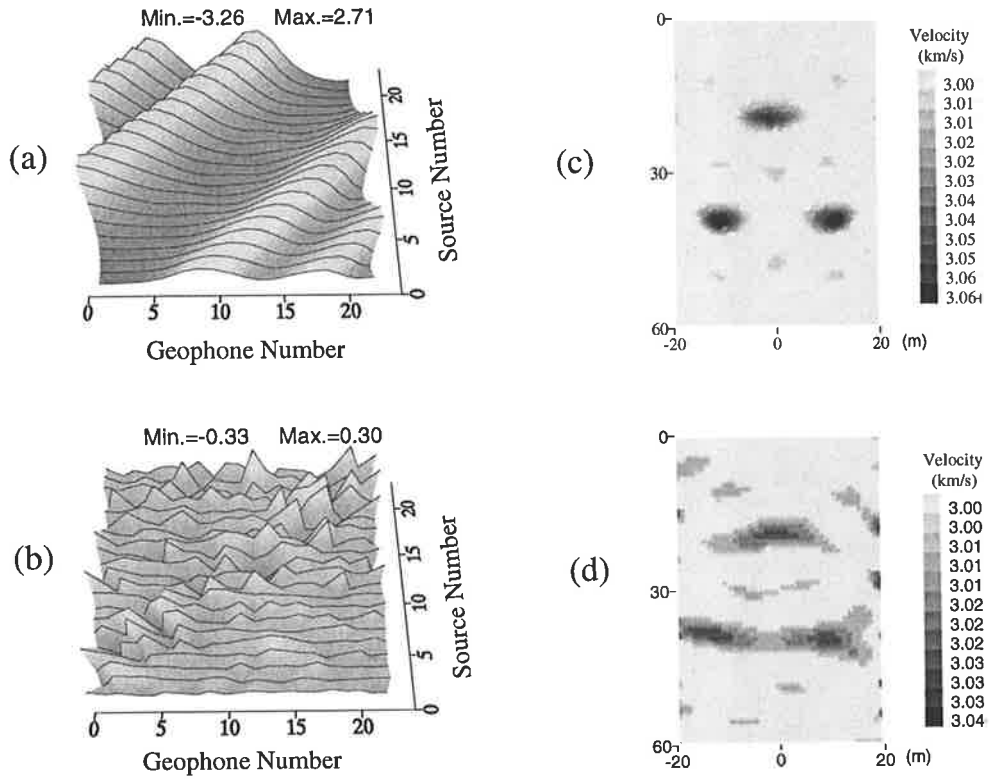

Fig.9-13 Synthetic data and imaging results obtained with the Hartley spectra at 200 Hz for Model-1: (a) noise-free data, (b) 5% Gaussian noise, (c) imaging result with the noise-free data (a), (d) imaging result with the noise-contaminated data (a)+(b).

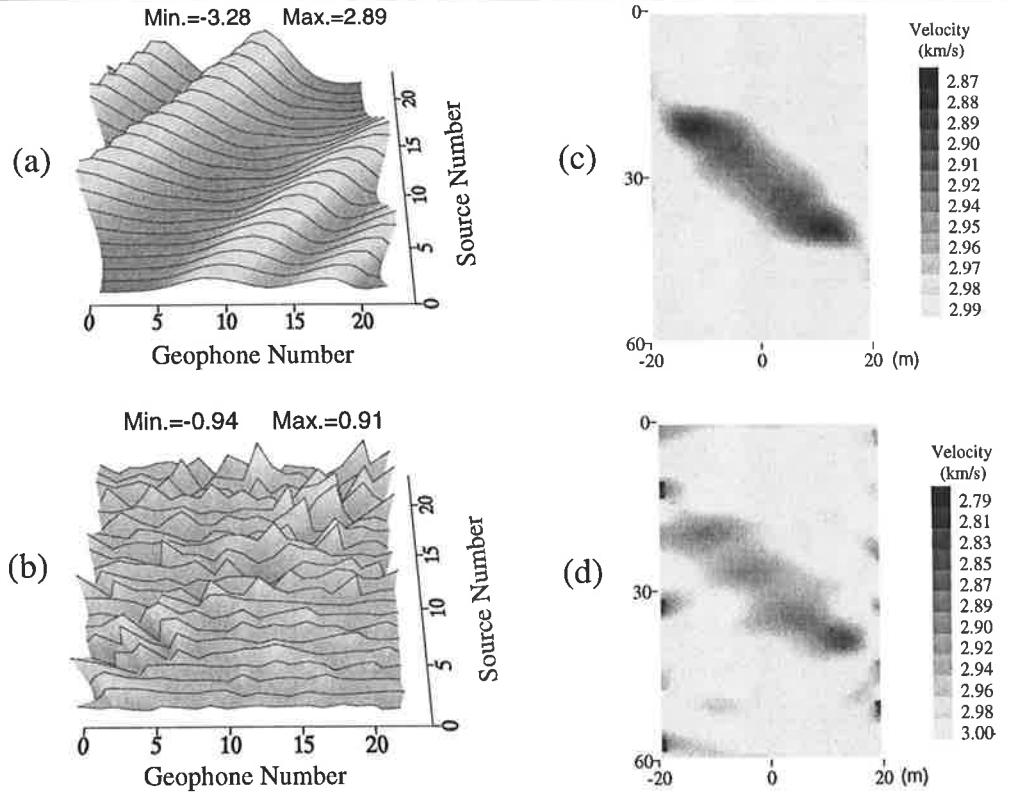

Fig.9-14 Synthetic data and imaging results obtained with the Hartley spectra at 200 Hz for Model-2: (a) noise-free data, (b) 15% Gaussian noise, (c) imaging result with the noise-free data (a), (d) imaging result with the noise-contaminated data (a)+(b).

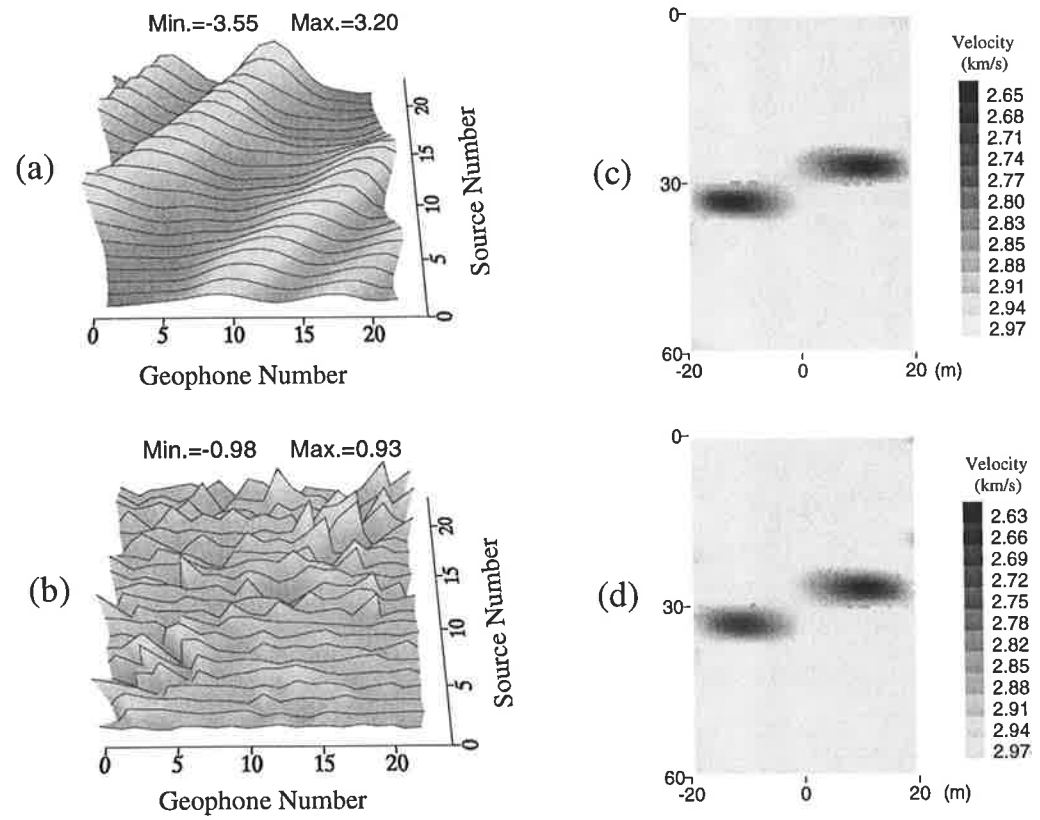

Fig.9-15 Synthetic data and imaging results obtained with the Hartley spectra at 200 Hz for Model-3: (a) noise-free data, (b) 15% Gaussian noise, (c) imaging result with the noise-free data (a), (d) imaging result with the noise-contaminated data (a)+(b).

the ones obtained with the real and imaginary components. All the images of the anomalies are very clear, even when using the 15% noise-contaminated data. It follows that the Hartley spectral data may be employed in the full-waveform inversion. So, considering the merits of the Hartley transform, we prefer the Hartley spectral data to the individual real and imaginary components for velocity imaging. The Hartley data is a real spectrum and contains all information on the wavespeed variation in media. It is equivalent to doing a combined real and imaginary component inversion. However, using the individual component is somewhat incomplete for full-waveform inversion due to the complex spectrum which contains the medium information. Furthermore, we repeat the experiments with the 200 Hz Hartley spectral data. Figures 9-13, 9-14 and 9-15 give the results, which show that the 200 Hz Hartley spectral data still yield clear images for all of the anomalies except small change of the spatial resolution–the size of the anomaly in the images becomes a little larger than the true targets. The difference in the spatial resolution is related to the longer wavelength of the impressed wavefield.

(3) Using Amplitude and Phase Spectra

The amplitude and phase spectra are alternative forms of the Fourier transform in the frequency-domain. They are calculated with the definitions:

$$A(\omega) = \sqrt{[\mathrm{Re}(\overline{P})]^2 + [\mathrm{Im}(\overline{P})]^2}\,, \tag{9.30}$$

$$\Psi(\omega) = arctg[\frac{\mathrm{Im}(\overline{P})}{\mathrm{Re}(\overline{P})}] + 2\pi l\,, \quad (\forall l, integer). \tag{9.31}$$

By numerical tests, we found that the inversion using the logarithmic amplitude (d_A=log(A)) gives better images than directly using the definition (9.30), and the Fréchet derivative for d_A can be simplified by the following form:

$$\frac{\partial d_A}{\partial c} = \frac{\partial}{\partial c}[\log(A)] = \frac{1}{A} F_c^{-1}[\Big|\overline{\overline{P}}\Big| \mathrm{Re}(\frac{1}{\overline{\overline{P}}} \frac{\partial \overline{\overline{P}}}{\partial c})] \approx F_c^{-1}[\mathrm{Re}(\frac{1}{\overline{\overline{P}}} \frac{\partial \overline{\overline{P}}}{\partial c})]. \tag{9.32}$$

Figures 9-16, 9-17 and 9-18 show the synthetic data and imaging results obtained with the logarithmic amplitudes at 300 Hz. From these figures, one can see that all the anomalies (targets) in the three models are successfully imaged by full-waveform inversion, but it is apparent that even using the noise-free data the imaging results exhibit more artifacts (see Figures 9-16c and 9-17c) and inferior spatial resolution (see Fig.9-17) than the previous results. The imaging procedures were repeated with the 200 Hz data. Figures 9-19, 9-20 and 9-21 give the results, which show that the noise-free

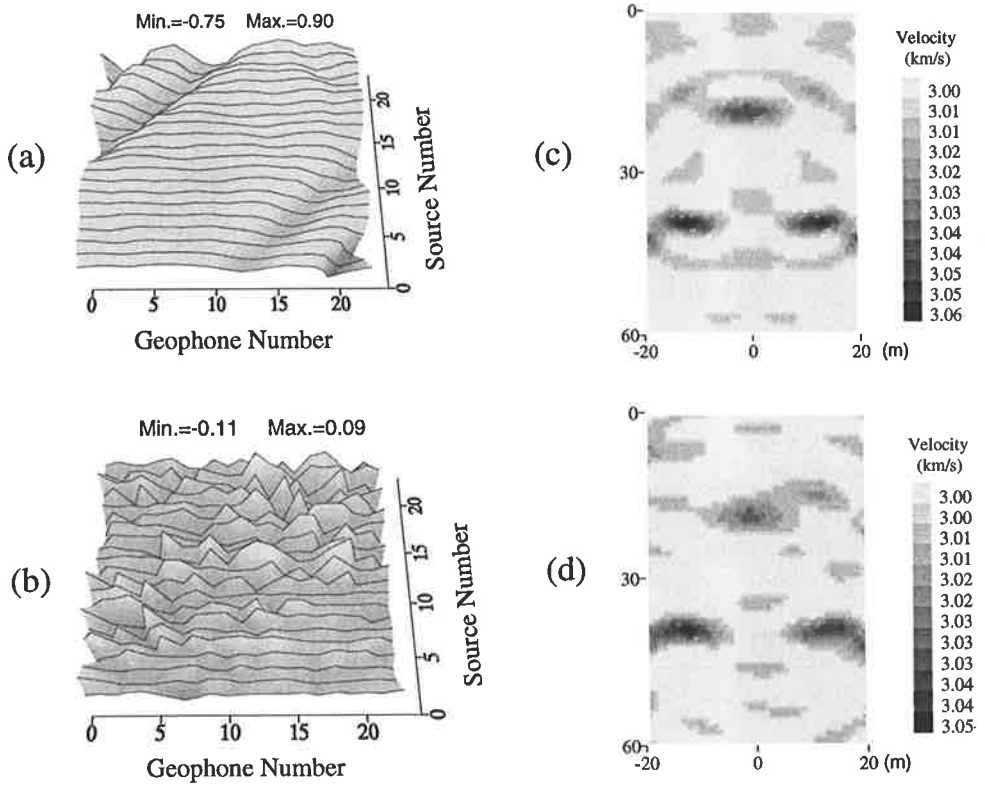

Fig.9-16 Synthetic data and imaging results obtained with the logarithmic amplitude at 300 Hz for Model-1: (a) noise-free data, (b) 5% Gaussian noise, (c) imaging result with the noise-free data (a), and (d) imaging result with the noise-contaminated data (a)+(b).

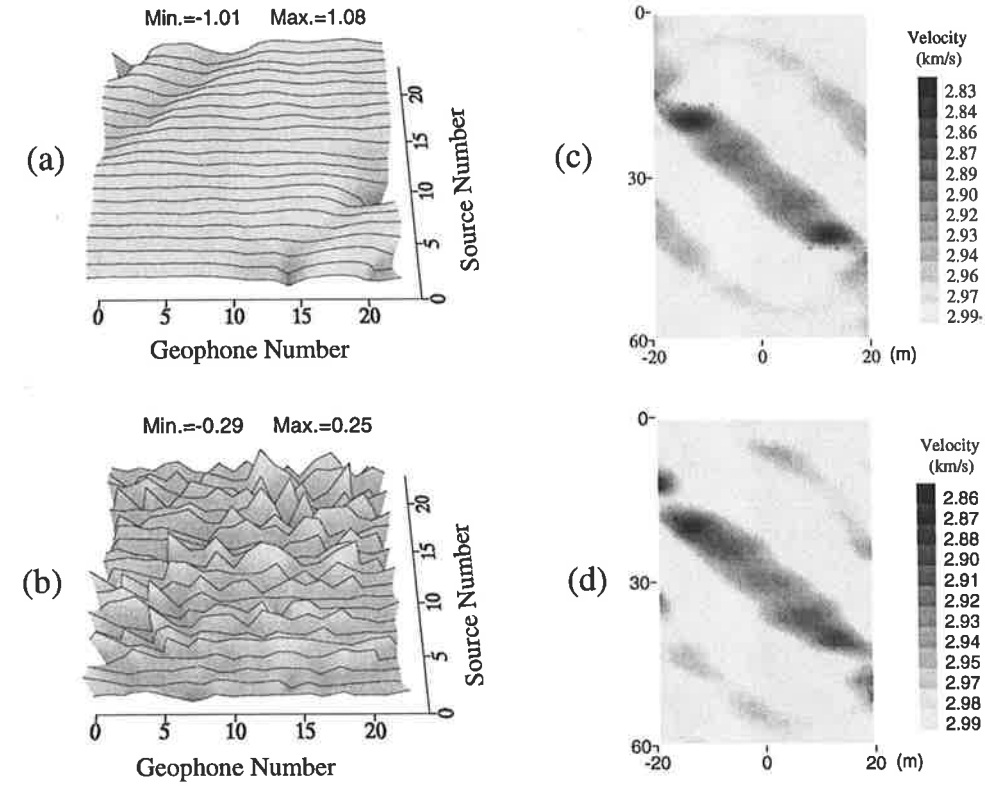

Fig.9-17 Synthetic data and imaging results obtained with the logarithmic amplitude at 300 Hz for Model-2: (a) noise-free data, (b) 15% Gaussian noise, (c) imaging result with the noise-free data (a), (d) imaging result with the noise-contaminated data (a)+(b).

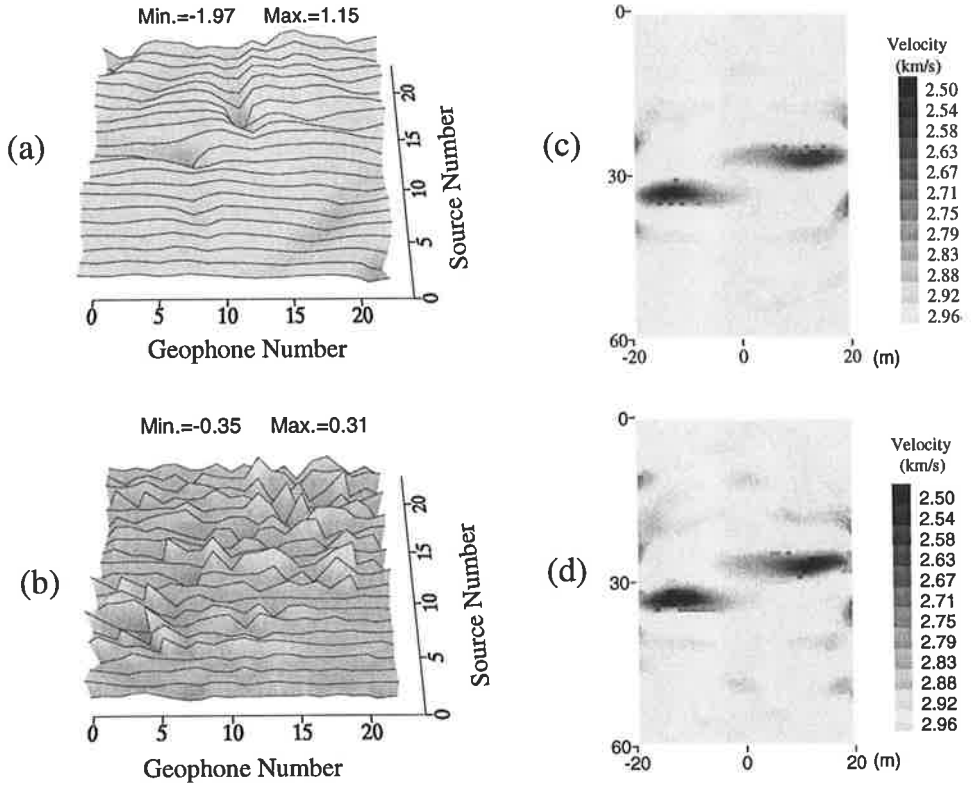

Fig.9-18 Synthetic data and imaging results obtained with the logarithmic amplitude at 300 Hz for Model-3: (a) noise-free data, (b) 15% Gaussian noise, (c) imaging result with the noise-free data (a), and (d) imaging result with the noise-contaminated data (a)+(b).

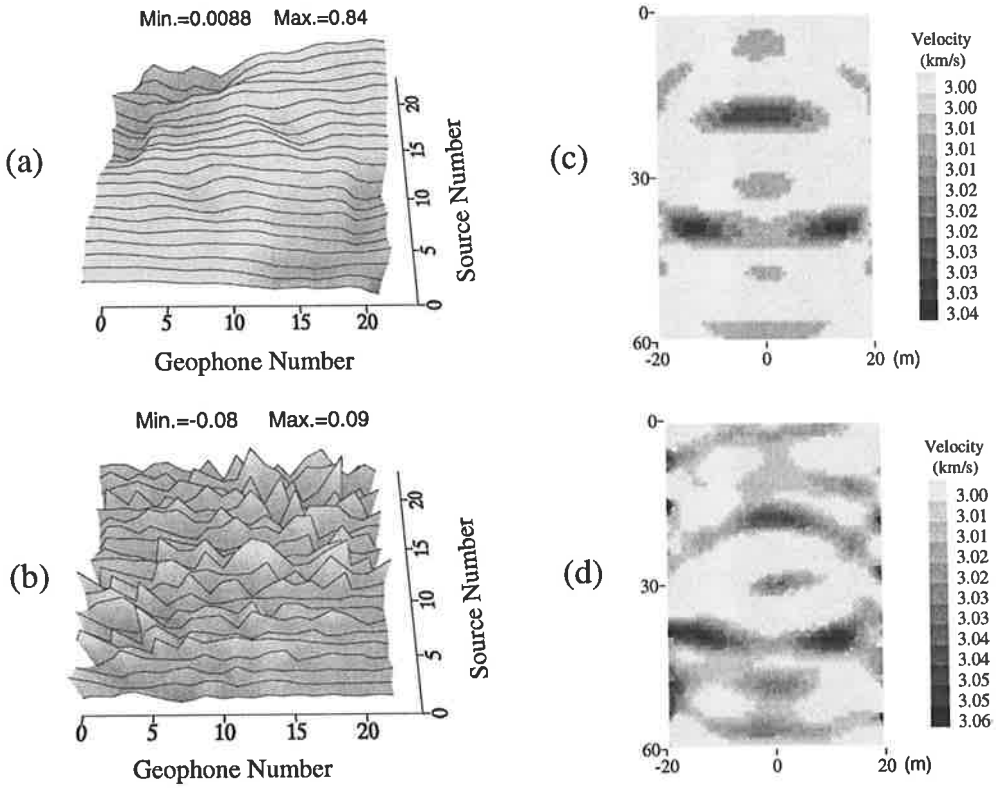

Fig.9-19 Synthetic data and imaging results obtained with the logarithmic amplitude at 200 Hz for Model-1: (a) noise-free data, (b) 5% Gaussian noise, (c) imaging result with the noise-free data (a), and (d) imaging result with the noise-contaminated data (a)+(b).

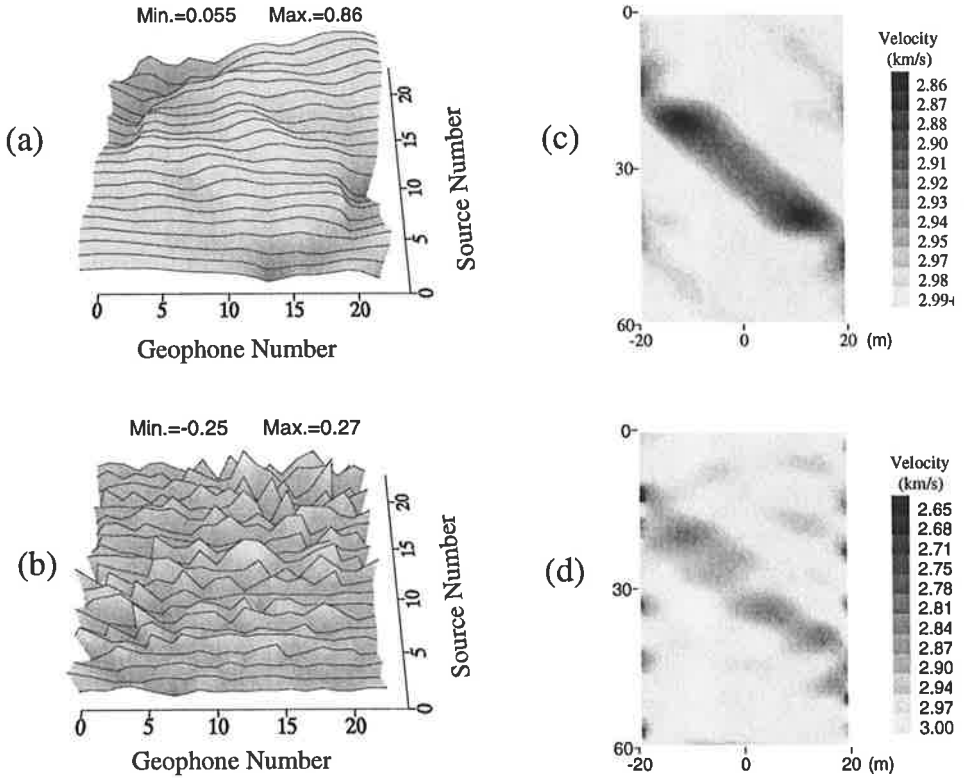

Fig.9-20 Synthetic data and imaging results obtained with the logarithmic amplitude at 200 Hz for Model-2: (a) noise-free data, (b) 15% Gaussian noise, (c) imaging result with the noise-free data (a), (d) imaging result with the noise-contaminated data (a)+(b).

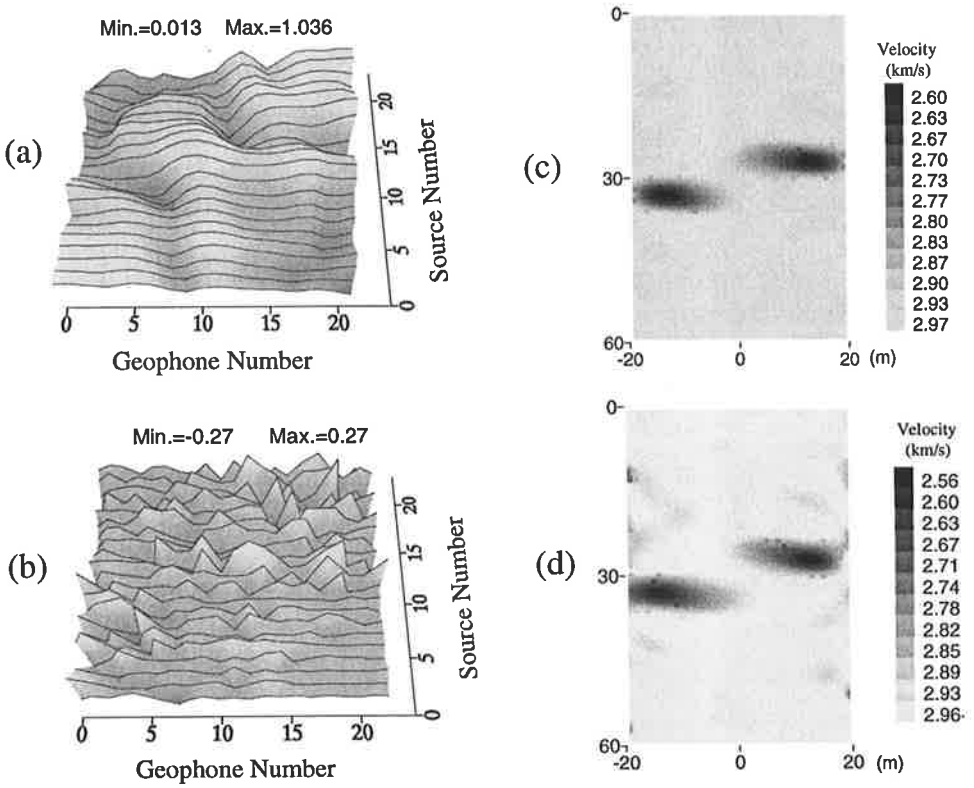

Fig.9-21 Synthetic data and imaging results obtained with the logarithmic amplitude at 200 Hz for Model-3: (a) noise-free data, (b) 15% Gaussian noise, (c) imaging result with the noise-free data (a), (d) imaging result with the noise-contaminated data (a)+(b).

data yield satisfactory images of the targets, but the noise-contaminated data give somewhat distorted images for Model-1 and Model-2 (see Fig.9-19d and Fig.9-20). However, these experiments show that the logarithmic amplitude spectra are available for velocity imaging with full-waveform inversion, but they yield more artifacts and inferior spatial resolution in the imaging results than other spectral forms.

Considering the usage of the phase data for crosshole velocity imaging, Schuster (1991) proposed a wave-equation phase inversion in the frequency-domain, in which he used the first-arrival traveltime solution of the eikonal equation to approach specified phases on the seismograms (Schuster and Quintus-Bosz, 1993). Actually, the method is similar to ray tomography and did not use the full-waveform phase data. As is well known, when dealing with the phase data, one has to recover the true unwrapped phase values, because of the multiple values of the phase spectra defined by equation (9.31) at each frequency point. There are several algorithms to obtain the unwrapped phase values, e.g. Tribolet (1977) proposed an adaptive numerical integration scheme that combines the information contained in both the phase derivative and the principal value; Poggiagliolmi et al. (1982) suggested a simple way that uses both the principal value and the phase increment. All those algorithms at least require the neighbouring values of the principal phase at each frequency. This means that if performing an iterative procedure of the full-waveform inversion with the unwrapped phase, one has to compute the entire seismogram sequence or the neighbouring values for each principal phase to determine the unwrapped phase in every iteration. This significantly increases the computations with 2.5-D modeling and defeats the benefits of inversion in the frequency-domain.

Our intention is to test the imaging with the principal values of the phase data ($l=0$ in equation (9.31)), because we found not much of a difference in the patterns of the Fréchet derivatives (wave-paths) between the phase data and other forms (see Fig.9-1 and Fig.9-2). Unfortunately, all imaging experiments with the phase data were unsuccessful. The results are not reasonable images of the anomalies for the three models. These failures prompt us to investigate the cause. One way is to examine the shape of the data misfit function for all the principal phase data. So, we computed the profile of the data misfit function in the neighbourhood of the real solution by fixing the velocity of the host rock (c=3.0 km/s) and changing the target velocity. The results for

the three models give the rough shape of the misfit function for the monochromatic principal phase data; the others are much smoother. For example, Fig.9-22 shows the normalised curves of the profile for Model-1 from which one can see that the curve of the phase data appears as several steps and is not as smooth as the others. Actually, according to the definition of the principal phase ($l=0$ in equation (9.31)), the rough shape may be due to the sensitivity to a small value of the real component of the spectrum in the denominator. This implies a difficulty of seeking a global minimum in the inversion if using the monochromatic principal phase data. The experiments simply show the ineffectiveness of pure monochromatic principal phase data for imaging even simple models.

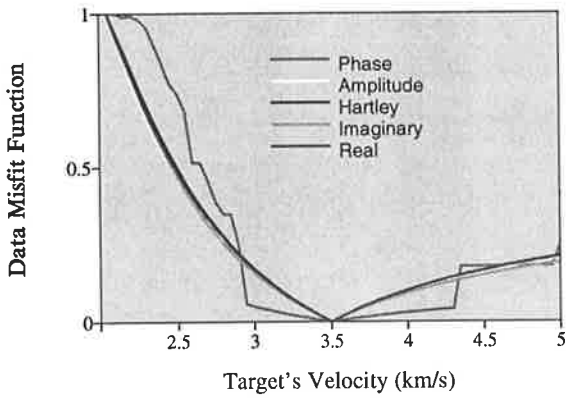

Fig.9-22 Normalized curves of the spectral data misfit function in the neighbourhood of the true solution in the case of Model-1.

In summary, the experiments for Model-1 show that even if the dimension of the target is much smaller (2m) than the wavelength (15m at 200 Hz), the real, imaginary, Hartley and amplitude spectral data can yield very clear images of the point targets. However, the imaged velocity value (about c=3.07 km/s) of the target is different from that of the original model value (c=3.5). The deviation may relate to the small size of the target and the limited illumination coverage. The experiments for Model-2 and Model-3 show that *the real, imaginary and Hartley spectral data yield good quality images for the dipping fracture and horizontal faulted seam; the images obtained from the amplitude spectra exhibits inferior spatial resolution and more artifacts than the others. The principal value of the phase spectrum cannot be used for full-waveform inversion due to the rough shape of the data misfit function. To use the unwrapped phase data requires a great deal of additional computations to obtain the information on neighbouring variations of the phase, which defeats the benefits of the inversion in the frequency-domain. The preferable form of the spectral data seems to be the Hartley spectra, because it not only has pronounced advantages in data processing but also yields clear images.*

9.4 Imaging with an Unknown Source Wavelet

As mentioned before, to carry out generalized diffraction tomography or full-waveform inversion, the source wavelet spectrum $s(\omega)$ must be known. But, nowadays the determination of the source wavelet from the seismograms is still a popular research topic in geophysics. Alternatively, it is more practical to develop an inversion scheme involving an unknown source wavelet. A few researchers have made efforts in this regard. For example, Dobroka et al. (1992) proposed a double-trace scheme in seismic ray tomography in which the source time is no longer required for velocity imaging. Recently, Frazer et al. (1997) and Frazer and Sun (1998) demonstrated an inversion of sonic waveforms with unknown source and receiver functions. They showed the method for estimation of a few model-parameters. Here, we investigate a new simple scheme that implements full-waveform inversion with normalized spectral data for crosshole velocity imaging. The aim of this study is to explore what kinds of normalised data are available for full-waveform inversion when the source wavelet is unknown. The forthcoming section describes the normalizing procedure for the amplitude and Hartley spectral data from which one can see that the source wavelet is removed in this kind of data. In the following section, numerical experiments for the three models studied before are used to show the effectiveness of crosshole velocity imaging.

(1) Normalized Spectral Data

As is well known, the wavefield $\overline{P}(\omega,r_s,r_g)$ can be expressed by the multiplication of a source wavelet $S(\omega)$ with the Green's function $\overline{G}(\omega,r_s,r_g)$ in the frequency-domain, ie

$$\overline{P}(\omega,r_s,r_g) = S(\omega)\overline{G}(\omega,r_s,r_g)\,. \tag{9.33}$$

If we have N_s traces of a common-shot gather, then the normalized spectral data may be obtained in the following manner: (1) taking the average spectrum as a reference, that is

$$\overline{P}_a(\omega,r_s) = \frac{1}{N_s}\sum_j^{N_s}\overline{P}(\omega,r_s,r_{g_j}) = \frac{S(\omega)}{N_s}\sum_j^{N_s}\overline{G}(\omega,r_s,r_{g_j}); \tag{9.34}$$

(2) calculating the normalized spectral data in terms of the following definition:

$$d_i = \frac{\overline{P}(\omega,r_s,r_{g_i})}{\overline{P}_a(\omega,r_s)} = \frac{\overline{G}(\omega,r_s,r_{g_i})}{\frac{1}{N_s}\sum_j^{N_s}\overline{G}(\omega,r_s,r_{g_j})}. \tag{9.35}$$

from which one can see that *the normalized spectral data contain only the Green's functions. It means that this kind of data is independent of the source wavelet.* If such data are available for full-waveform inversion, the source wavelet is no longer required. This formula encourages us to investigate the effectiveness of crosshole velocity imaging with this kind of spectral data.

The Fréchet derivative for the normalized data can be calculated from equation (9.35):

$$\frac{\partial d_i}{\partial c} = \frac{1}{\overline{G}_a(\omega, r_s)}\left[\frac{\partial \overline{G}(\omega, r_s, r_{g_i})}{\partial c} - \frac{d_i}{N_s}\sum_j^{N_s}\frac{\partial \overline{G}(\omega, r_s, r_{g_j})}{\partial c}\right], \tag{9.36}$$

where $\overline{G}_a(\omega, r_s) = \sum_j^{N_s} \overline{G}(\omega, r_s, r_{g_j}) / N_s$. Apparently, the derivative also has no relation to the source wavelet $S(\omega)$. So, these synthetic quantities (d_i and $\frac{\partial d_i}{\partial c}$) for full-waveform inversion can be obtained from the Green's functions.

A form of the normalized spectral data is the amplitude spectrum, because it has a similar expression to equation (9.33) in the 2.5-D case (see equation (2.31)):

$$A(\omega, r_s, r_{g_i}) = \frac{1}{2} A_s(\omega) A_G(\omega, r_s, r_{g_i}), \tag{9.37}$$

where $A(\omega, r_s, r_{g_i})$, $A_s(\omega)$ and $A_G(\omega, r_s, r_{g_i})$ represent the amplitude spectra of the wavefield, source wavelet and Green's function, respectively. So, the normalized amplitude spectral data can be calculated according to the definition (9.35):

$$d_i^A = \frac{A(\omega, r_s, r_{g_i})}{A_a(\omega, r_s)} = \frac{A_G(\omega, r_s, r_{g_i})}{A_a^G(\omega, r_s)}, \tag{9.38}$$

where $A_a(\omega, r_s)$ and $A_a^G(\omega, r_s)$ stand for the average spectra of the wavefield and the Green's functions respectively. The average amplitude $A_a(\omega, r_s)$ can be obtained in either the time-domain or the frequency-domain in terms of equation (9.34).

Substituting for equations (9.38) and (9.9), the derivative (9.36) becomes

$$\begin{aligned}\frac{\partial d_i^A}{\partial c} = \frac{1}{A_a^G(\omega, r_s)}\{&F_c^{-1}[\left|\overline{\overline{G}}_i^{2.5D}\right| \mathrm{Re}(\frac{1}{\overline{\overline{G}}_i^{2.5D}}\frac{\partial \overline{\overline{G}}_i^{2.5D}}{\partial c})] - \\ &\frac{d_i^A}{N_s}\sum_j^{N_s} F_c^{-1}[\left|\overline{\overline{G}}_j^{2.5D}\right| \mathrm{Re}(\frac{1}{\overline{\overline{G}}_j^{2.5D}}\frac{\partial \overline{\overline{G}}_j^{2.5D}}{\partial c})]\}.\end{aligned} \tag{9.39}$$

Another form of the normalized spectral data may be the Hartley spectrum, because when applying the Hartley transform to the 3-D constant-density acoustic wave equation (2.18) with respect to time, one can obtain the Hartley-spectral form of the 2.5-D Helmholtz equation. It is found that this form is the same as that obtained using the Fourier transform due to the same property of the two transforms for the second derivative with respect time (see Appendix A). If the natural boundary condition (it vanishes at an infinite boundary) is considered for both cases, the appearances of the two defined problems are completely the same. This means that we have the following relation for the wavefield in the Hartley spectral form:

$$\overline{P}_H(\omega, r_s, r_{g_i}) = \frac{1}{2} S_H(\omega) \overline{G}_H(\omega, r_s, r_{g_i}), \tag{9.40}$$

where $\overline{P}_H(\omega, r_s, r_{g_i})$, $S_H(\omega)$ and $\overline{G}_H(\omega, r_s, r_{g_i})$ represent the Hartley transform of a seismogram, source wavelet and Green's function. All of them become real-valued quantities due to the Hartley transform being real-valued. So, the normalized Hartley spectral data and the derivative can be calculated by the following formulas:

$$d_i^H = \frac{\overline{P}_H(\omega, r_s, r_{g_i})}{\overline{P}_a^H(\omega, r_s)} = \frac{\overline{G}_H(\omega, r_s, r_{g_i})}{\overline{G}_a^H(\omega, r_s)}, \tag{9.41}$$

$$\frac{\partial d_i^H}{\partial c} = \frac{1}{\overline{G}_a^H(\omega, r_s)} \left[\frac{\partial \overline{G}_H(\omega, r_s, r_{g_i})}{\partial c} - \frac{d_i^H}{N_s} \sum_j^{N_s} \frac{\partial \overline{G}_H(\omega, r_s, r_{g_j})}{\partial c} \right], \tag{9.42}$$

where $\overline{P}_a^H(\omega, r_s)$ and $\overline{G}_a^H(\omega, r_s)$ are the average Hartley spectra of the wavefield and the Green's function.

The Fréchet derivative may be used to delineate the wave-path in the frequency-domain (Woodward, 1992), so we calculated the derivatives for the normalized amplitude and Hartley spectral data to show the pattern of the wave-paths. Fig.9-23 gives the results for two receivers of a common-shot gather ($N_s = 21$) for the two normalized spectral data. From this figure, one can find that the patterns of the normalized amplitude and normalized Hartley spectrum differ widely from the normal one (comparing Fig.9-23 with Fig.9-2). This shows that the significant values radiate from the source and do not converge on any receiver, and all the source-receiver pairs in the common-shot gather have the same patterns except for the absolute values. This feature shows that no matter

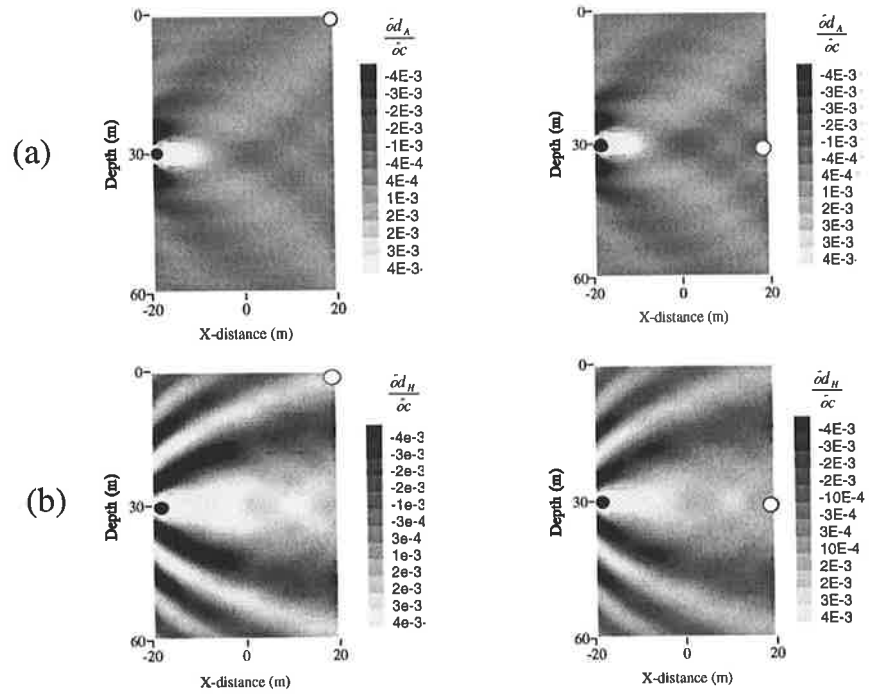

Fig.9-23 The Fréchet derivatives (wave-paths) of the normalised spectral data in a homogeneous medium (f=300 Hz, c=3000 m/s): (a) Amplitude spectrum; (b) Hartley spectrum. The black and white circles stand for the source and receiver, respectively.

where the receiver is, the normalized spectral data have the same sensitive area from the source.

(2) Numerical Imaging Experiments

To test the utility of the normalized amplitude and Hartley spectral data for crosshole seismic imaging, the same three models depicted in Fig.9-3 were used again. The 'observed data' are simulated by combining the theoretic response to the models with certain levels of Gaussian noise, i.e. the normalized amplitude spectral data were obtained in the following manner: adding n% Gaussian noise to the theoretical values of the amplitude spectra (equation 9.30), then normalizing the contaminated data in terms of equation (9.38). We assigned the complex value $s(\omega)\big|_{f=300Hz} = (1000,800)$ to the source wavelet (supposed it is unknown, see equation (9.37)) for the 'observed amplitude' spectra and $s(\omega)\big|_{f=300Hz} = (10,10)$ for the inversion. In the normalized Hartley spectral data experiments, the 'unknown' source wavelet was given a real value $s_H(\omega) = 1000$ (see equation (9.40)) and we used $s_H(\omega) = 10$ in the imaging.

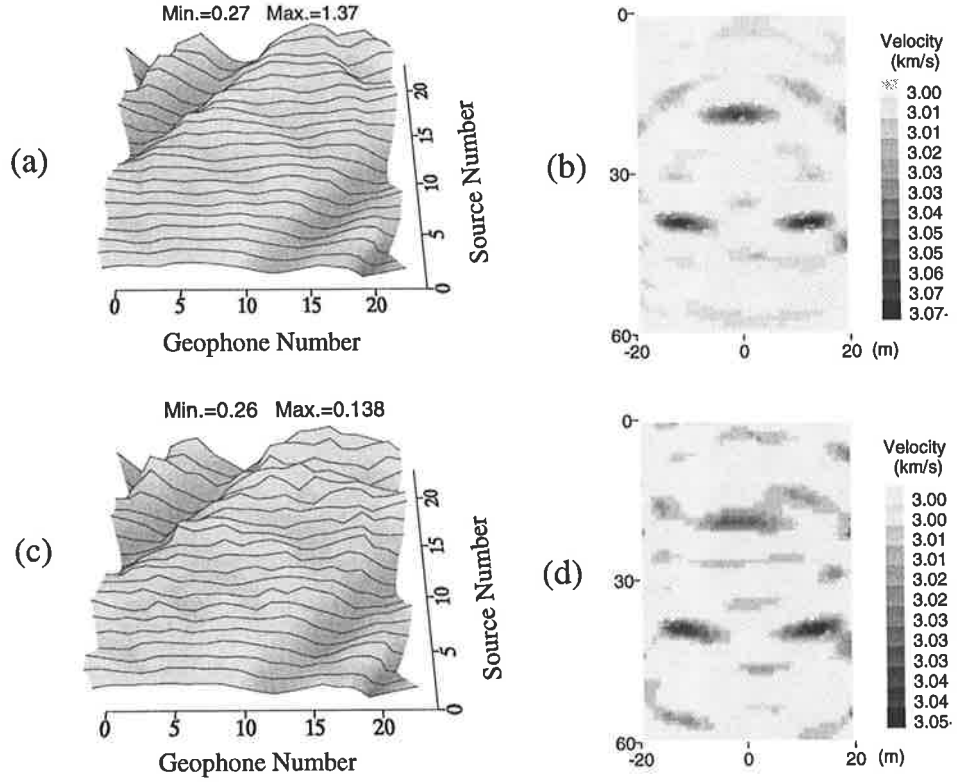

Fig.9-24 The synthetic normalized amplitude data at 300 Hz and imaging results for Model-1: (a) noise-free data; (b) imaging result obtained from (a); (c) data contaminated by 15% Gaussian noise; (d) imaging result obtained from (c).

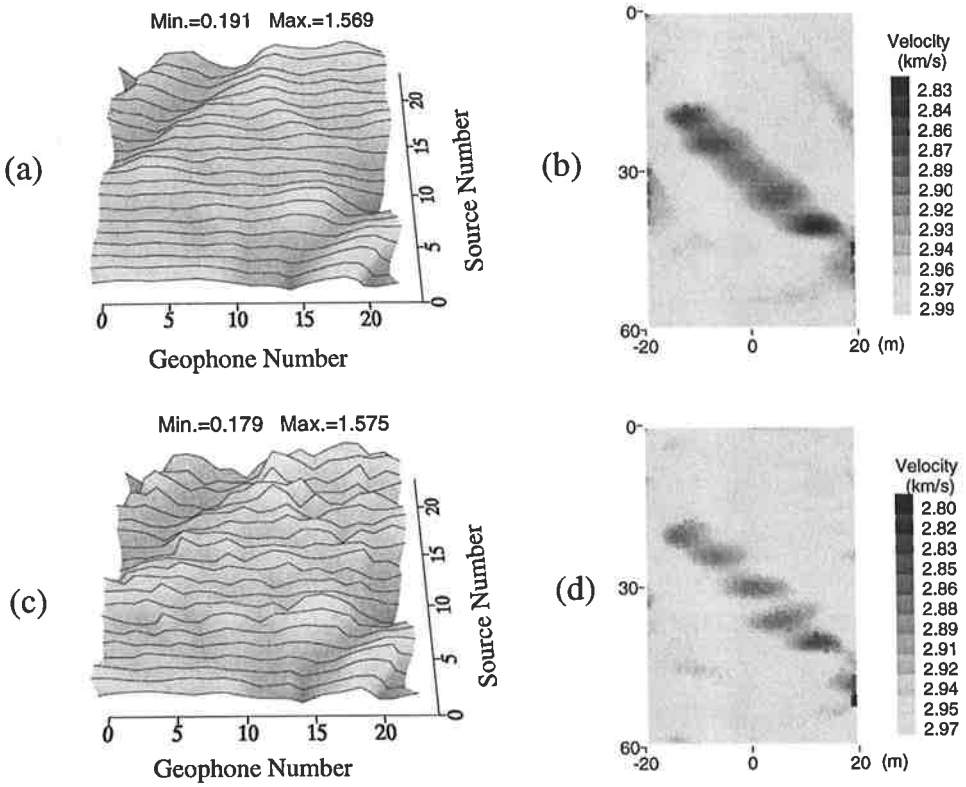

Fig.9-25 The synthetic normalized amplitude data at 300 Hz and imaging results for Model-2: (a) noise-free data; (b) imaging result obtained from (a); (c) data contaminated by 15% Gaussian noise; (d) imaging result obtained from (c).

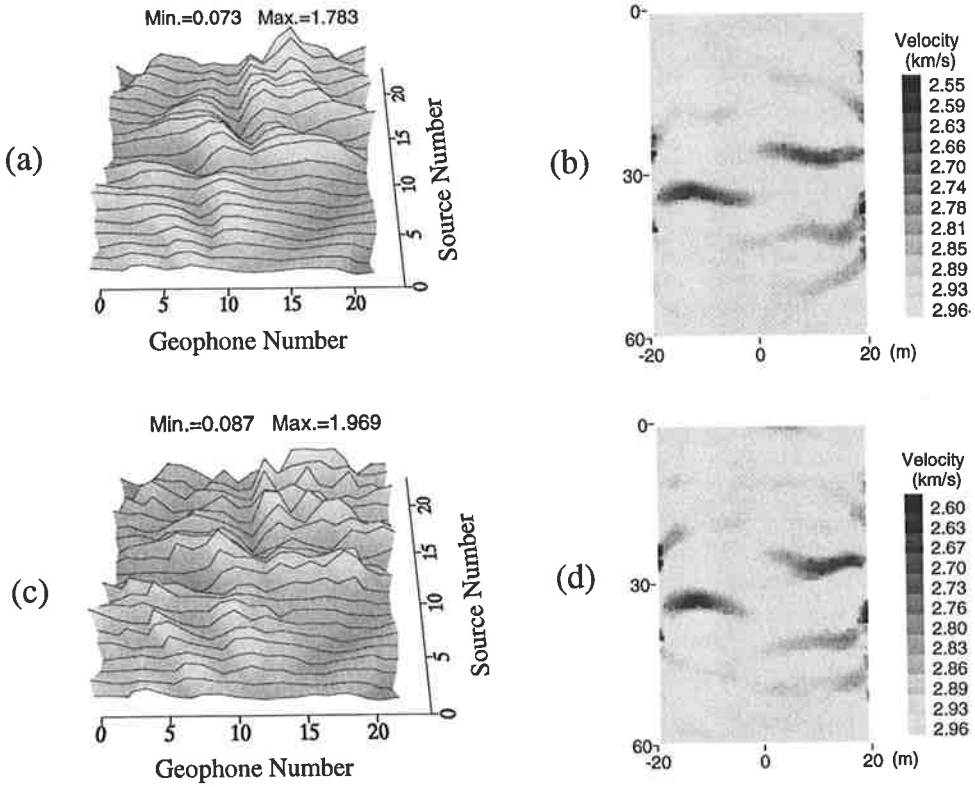

Fig.9-26 The synthetic normalized amplitude data at 300 Hz and imaging results for Model-3: (a) noise-free data; (b) imaging result obtained from (a); (c) data contaminated by 15% Gaussian noise; (d) imaging result obtained from (c).

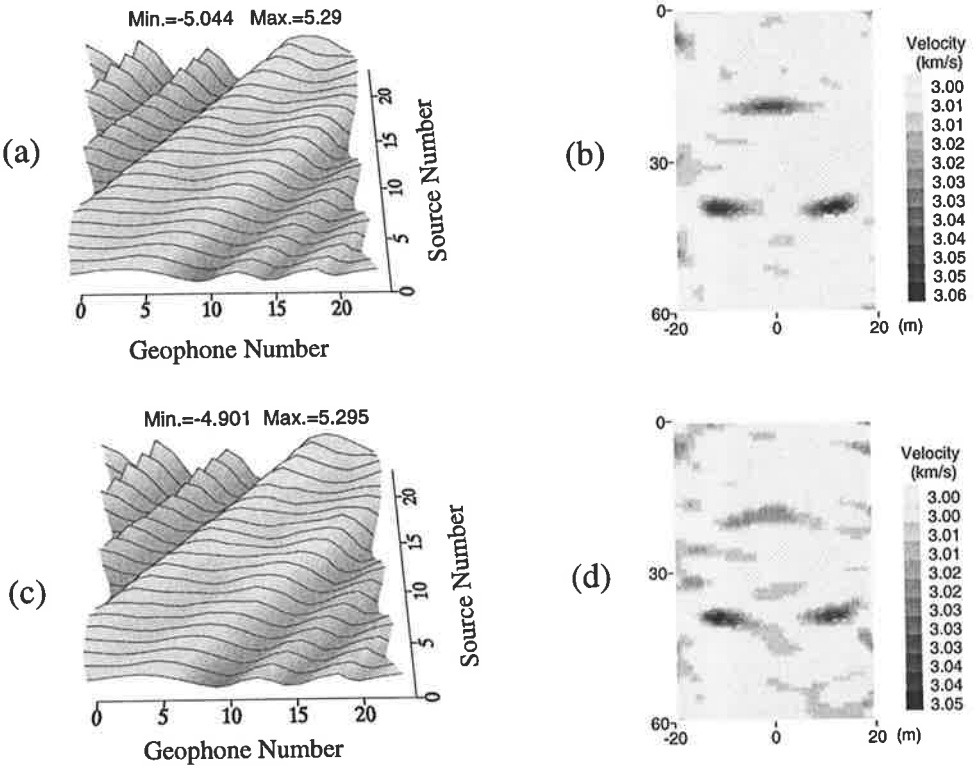

Fig.9-27 The synthetic normalized Hartley spectral data at 300 Hz and imaging results for Model-1: (a) noise-free data; (b) imaging result obtained from (a); (c) data contaminated by 5% Gaussian noise; (d) imaging result obtained from (c).

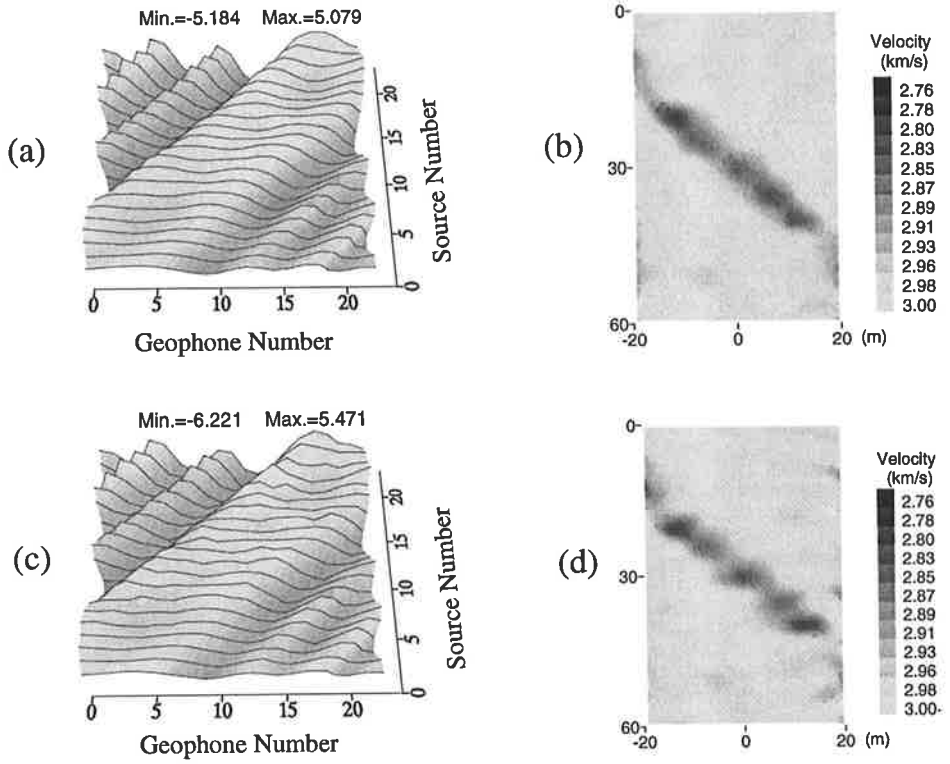

Fig.9-28 The synthetic normalized Hartley spectral data at 300 Hz and imaging results for Model-2: (a) noise-free data; (b) imaging result obtained from (a); (c) data contaminated by 15% Gaussian noise; (d) imaging result obtained from (c).

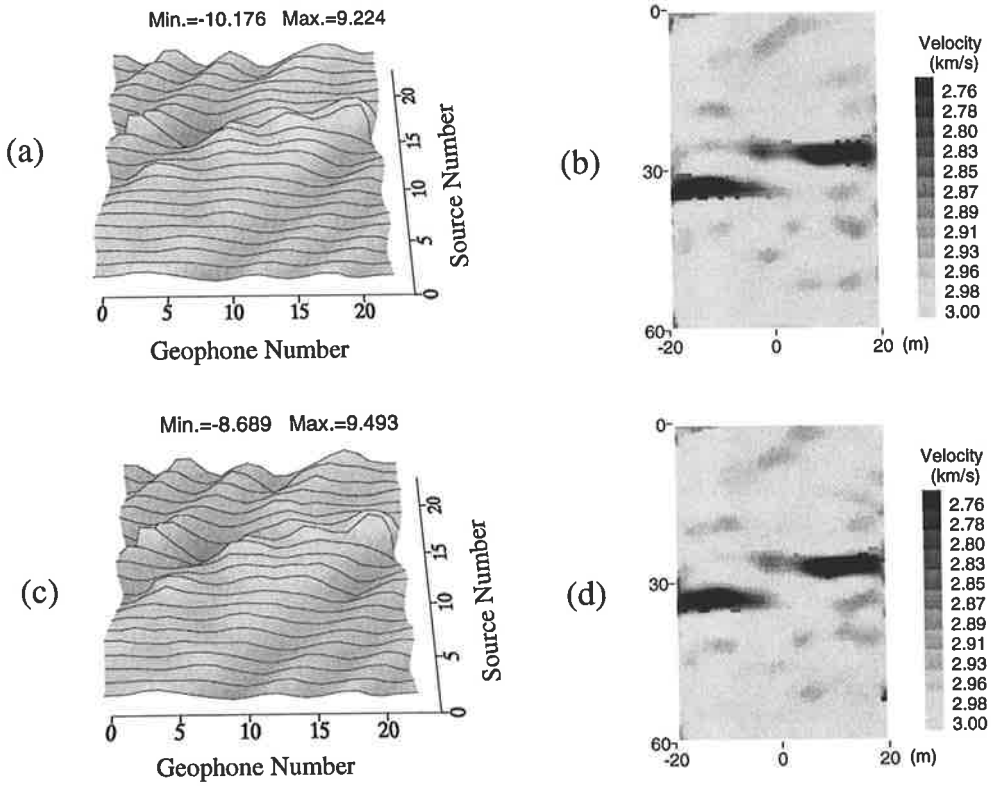

Fig.9-29 The synthetic normalized Hartley spectral data at 300 Hz and imaging results for Model-3: (a) noise-free data; (b) imaging result obtained from (a); (c) data contaminated by 15% Gaussian noise; (d) imaging result obtained from (c).

Figures 9-24, 9-25 and 9-26 show the synthetic data and the imaging results obtained with the normalized amplitude spectra. Comparing these figures with Fig.9-16, Fig.9-17 and Fig.9-18, one can find that the normalized amplitude data retain the same shaped curves as the non-normalized data (see (a) in these figures) and for all three models they yield very similar results to the previous ones obtained from the logarithmic amplitude data (see (b) and (d) in these figures). Obviously, although some artifacts appear in the imaging results, all the targets (anomalies) are reasonably well imaged even with the noise-contaminated normalized data, and for Model-1 and Model-2 the normalized amplitude data yield fewer artefacts than the logarithmic amplitude spectra (see Fig.9-16, Fig.9-17 and Fig.9-24, Fig.9-15). From these experiments it follows that *the normalized amplitude spectral data are suitable for crosshole seismic imaging when the source wavelet is unknown.*

Figures 9-27, 9-28 and 9-29 show the synthetic normalized Hartley spectral data and the imaging results. Comparing these figures with the previous results obtained from the Hartley spectral data (Figures 9-10, 9-11 and 9-12), one can see that the normalized Hartley spectral data also have the same shaped curves as the original Hartley spectral data except for the large difference in the absolute values, but the imaging results obtained from the normalized data are not as good as in the case of a known source wavelet. Figures 9-27b, 9-28b and 9-29b show that even when using the noise-free normalized data the imaging results have some artifacts, which do not appear in the results from the non-normalized Hartley spectra (see Figures 9-10b, 9-11b and 9-12b). It seems that the normalization procedure for the Hartley spectral data may introduce some imaging distortions. The cause of the difference in the images may be due to the quite different wave-paths in the frequency-domain (see Figures 9-2a and 9-23b). Fortunately, the experiments with the noise-contaminated data show that the imaging results have some additional distortions relative to the noise-free data, but all the anomalies between the boreholes can be recognized from the imaging results (see Figures 9-27d, 9-28d and 9-29d). So, these experiments demonstrate that *the normalized Hartley spectra may be another available form of full-waveform spectral data for crosshole seismic imaging with an unknown source wavelet.*

Chapter 10
Conclusions and Future Research

This dissertation has been concerned with acoustic and electric modeling and inversion. Specific new algorithms have been developed and tested on synthetic data. The thesis contains original work in a number of areas, as summarised below.

10.1 Forward Modeling

- I have shown that crosshole resistivity imaging (or tomography) and seismic acoustic velocity imaging (generalized diffraction tomography and waveform inversion with the acoustic approximation) may reduce to the modeling and inversion of a 2.5-D Helmholtz equation in which the 2.5-D Green's function of the equation is the basic computational quantity. The finite element method can be applied to obtain the numerical solutions of the 2.5-D Green's function.

- I have presented a flexible and efficient finite element method (FEM) scheme for 2.5-D resisvitity modeling, which is used to calculate the 2.5-D Green's function for arbitrary media so that it is available for two-, three- and four-electrode arrays with any survey configuration (surface and crosshole measurements). Also, it can be directly used as the basic tool to calculate the Fréchet and second derivatives for inversion. The numerical tests show that the accuracy of the method mainly depends on the choices of the wavenumber range and the number of samples. In general, the accuracy is improved by increasing the k_y-samples in the chosen range, but the improvement is gradual and does not increase monotonically with increasing k_y-samples. An appropriate range for the k_y sampling may be evaluated by detecting the significant values of the transformed potential for a homogeneous half-space with the practical surveying configurations. The modeling examples show the method is applicable to resistivity profiling, mineral exploration and hydrological engineering.

- The composite boundary-valued solution with the FEM is an efficient and effective algorithm to compute the 3-D wavefield or Green's function for arbitrary 2-D

acoustic media. The algorithm can be used to calculate the response of a specified source for wave modeling and the Fréchet derivatives for waveform inversion in the frequency- and time-domain. The numerical modeling experiments have shown that (a) the composite boundary condition, which consists of a general form of 2.5-D absorbing boundary condition for the wave propagating field and a mixed boundary condition for the evanescent field, is available for arbitrary media and suitable for the FEM; (b) the k_y-domain solution of an arbitrary medium involves the wavefield of the medium particle vibration and the no-vibration evanescent field, which depends on whether the wavenumber k_y is under or over the critical value of the medium; (c) for each frequency the maximum k_y value can be rationally determined in terms of the critical value of the medium around a source; it should be just larger than the critical value so as to avoid the omission of the wave energy and to save computer resources; (d) the accuracy of the frequency-domain solution is relatively insensitive to the number of k_y samples in the homogeneous case, but not necessarily improved by increasing the k_y samples in the inhomogeneous case due to the complicated wavefield. A reasonable sampling (not many samples) in the k_y-domain can save much computer time and yet retains adequate precision in the computations.

- The damping method, incorporated with the FEM in the wavenumber-frequency domain, is a simple and easy-to-build scheme to compute the 3-D wavefield or 2.5-D Green's function for arbitrary acoustic media. The main advantages of the method are the avoidance of absorbing boundary conditions and the neglect of the singularity problem in the wavenumber when the composite boundary solution is sought with the FEM in the wavenumber-frequency domain. The numerical tests have shown that the choice of time-damper with the method is important to the solution. An under-estimated or over-estimated value will disturb the solution in the central area of the region. Generally, the time-damper is a function of the frequency, wavenumber and the width of the absorbing zone (or mesh size). Although there is no general way to choose the time-damper in the wavenumber-frequency domain, it can be determined in terms of the modeling or inversion situation, e.g. the frequency range, wavenumber extent and mesh size. The smaller the range of frequency and wavenumber and the bigger the mesh size, the easier it is to determine a correct time-

damper. Our experiments illustrate that a linear damper with frequency- and wavenumber-dependent coefficients can be chosen and a reasonable number of k_y-components can produce a satisfactory solution in both the frequency- and time-domain for arbitrary media. The numerical solutions can be used to calculate the Fréchet derivative for seismic full-waveform inversion. An undesirable feature of the method is the requirement of a large FEM mesh. So, it consumes much more computer time than the composite boundary-valued solution.

- A FEM scheme is formulated for 2.5-D elastic wave modeling, which shows that the two forms of the non-reflection boundary conditions, a viscous boundary condition of the stress form and an absorbing boundary condition of the gradient form, may be used for the modeling in the frequency-domain.

10.2 Imaging Algorithms

- I obtained the general forms of the Fréchet and second derivatives for 2-D and 3-D resistivity inversion with different electrode arrays. Also, we presented the expressions of the Fréchet and second derivatives for the 2.5-D acoustic wavefield problem. All the derivatives are expressed by the 2.5-D Green's functions associated with the source, receiver and model-parameter locations. These formulas allow us to employ some optimization algorithms involving both derivatives in geophysical inversion. The computation of the derivatives is a two-step procedure: (a) using the FEM to obtain the 2.5-D Green's functions; (b) calculating the derivatives with the Green's functions in terms of the explicit expressions. The first step is the same as the normal modeling of the 2.5-D Helmholtz equation and it just involves carrying out more backsubstitutions in solving the FEM linear equation system for the derivatives; it does not cost much computer time. But for computing the second derivatives a large memory is required to store all the Green's functions. For the second step, two model parameterizations–constant-point and constant-block approximations–may be used. The former is a faster scheme to form the Jacobian matrix for a large-scale inversion; the latter has the advantage of reducing the number of inverse parameters by choosing an appropriate number of the constant blocks in the model parameterization.

The numerical results of the Fréchet derivative in DC resistivity imaging show that they have different patterns with the various crosshole measurement configurations of the four kinds of electrode arrays. There is a major weighting of the model parameters just around the electrodes, but the second derivatives of all the configurations have the similar feature and are quite different from the Fréchet derivatives in the dominant weighting. For the acoustic problem, the numerical result of the second derivative of a uniform medium shows that the most of the values are much smaller than the Fréchet derivative in view of the absolute quantities, so the second derivative has much less weighting effect than the Fréchet derivative if involved in an inversion.

The computation of the second derivative needs much more memory (in the first step) and computer time (for the second step) than the computation of the Fréchet derivative. With the development of computer technology, it is worth incorporating the effect of the second derivative in non-linear geophysical inversions.

- From the practical implementation viewpoint, the iterative inversion algorithms, based on the local-search optimisation for the Tikhonov regularization solution, the smoothest model solution and the subspace solution, have the following inter-relations: (a) the general iterative solution, iteratively linearized solution and Levenberg-Marquardt solution are three equivalent solutions for the Tikhonov regularization solution, all of which are a specified form of the steepest descent method; (b) the smoothest model solution is a subset of the Tikhonov regularization solutions and a practical scheme for the smoothest model solution consist of the algorithm for the Tikhonov regularization solution incorporating the data-fitting tolerance; (c) the subspace solution can be obtained from both the Tikhonov regularization solutions and the smoothest model solutions with the model-parameter transform so long as the chosen basis vectors span the whole model space, which are reasonable for inversion. So, the generalised iterative algorithms for the three kinds of the solutions are obtained based on the local-search quadratic approximation of the conjugate gradient method, which is a pure form of the Newton method.

10.3 Numerical Imaging Results

- For crosshole resistivity imaging, the synthetic imaging experiments demonstrate that, besides the pole-pole array, some specific three- and four-electrode configurations,

such as *AM-N*, *AM-B* and *AM-BN*, can be employed; these configurations, compared with the pole-pole survey, have quite different sensitivity patterns in the detection area and different anomaly effects due to the target between the boreholes. The sensitivity and the anomaly effect of these arrays can be adjusted by choosing the separation of the electrodes of the array and conducting scanning observations. The data from these configurations are better suited than the pole-pole array for crosshole resistivity imaging. These kinds of measurement configurations yield greater flexibility for crosshole resistivity imaging.

The crosshole pole-bipole *A-MN* , bipole-pole *AB-M* and bipole-bipole *AB-MN* configurations have a singularity problem in computing apparent resistivity. For practical applications, it will lead to small readings of the potential or potential difference which can easily be obscured by noise. The synthetic study shows that the effectiveness of resistivity imaging with these configurations are not as good as with the others.

- 2.5-D numerical simulations demonstrate the effectiveness of 2.5-D acoustic velocity imaging with full-waveform inversion using monochromatic real, imaginary, Hartley and amplitude spectral data. These experiments show that all these kinds of data can be used to image inhomogenities between two boreholes. The real and imaginary components produce nearly the same quality images of the anomalies. The amplitude spectra yield resolvable images of the targets, but with more artifacts than the others. Hartley spectral data seems to give the best images of all the forms, because it is a real spectrum and includes all the information on variation of acoustic velocity in a medium, unlike the individual forms of the Fourier spectrum share the information. So, the preferable form of the spectral data for seismic velocity imaging may be the Hartley spectrum due to the merits of the transform and their behaviours in the numerical imaging experiments. The monochromatic principal phase data are unsuitable for full-waveform inversion, because of the rough shape of the data misfit function, which leads to getting stuck in local minima during the attempted global optimisation. The rough shape may relate to small values of the real components, which causes a loss of precision. Using unwrapped phase data for full-waveform inversion significantly increases the computations of 2.5-D acoustic wave modeling due to the requirement of knowing neighbouring values of the principal phase for the

phase unwrapping procedure. It defeats the benefits of implementation of the inversion in the frequency-domain.

- The numerical simulations have shown that although the normalised amplitude/ Hartley spectral data do not yield as good as the images in the known wavelet cases, they reconstruct a reasonable images of the targets between boreholes when a source wavelet is unknown. This imaging scheme is very useful for practical applications, because it not necessary to evaluate the source wavelet from the seismograms, or in performing extra field work to obtain the source spectrum.

10.4 Future Research

All the conclusions for crosshole resistivity and acoustic velocity imaging have been drawn from the synthetic simulations and a few physical model experiments, but they are basic and important aspects to explore the imaging techniques and make them applicable. The results in the thesis will guide us and direct future work, which should involve the following aspects:

- More experiments using physical modeling data or real data to further investigate the effectiveness of resistivity imaging with the specified three- and four-electrode arrays.
- Field experiments for crosshole acoustic velocity imaging using the Hartley spectral data and the normalized amplitude/Hartley spectral data.
- Finite element modeling for 2.5-D elastic waves, especially for computation of 2.5-D Green's function tensor for arbitrary medium, which leads to the analysis of source dynamics and the use of 3-component seismograms.
- The effect of the second derivatives in a non-linear inversion for crosshole resistivity and acoustic velocity imaging.

As a new 3-D physical modeling system is built, and as suitable field sites for geophysical exploration become available to other researchers at Adelaide University, it should be possible to apply, refine and extend some of the novel modeling and imaging/inversion procedures developed in this study.

Appendix A

The Hartley Transform

The Hartley transform is briefly described here. Details on the formulation and the discrete algorithm can be found in Bracewell's book (1986). In the following text, the subscripts H and F are used to stand for Hartley and Fourier transforms, respectively. The Hartley transform is defined by a pair of real integrals:

$$\begin{aligned} f_H(\omega) &= \frac{1}{\sqrt{2\pi}} \int_{-\infty}^{\infty} f(t) cas(\omega t) dt, \\ f(t) &= \frac{1}{\sqrt{2\pi}} \int_{-\infty}^{\infty} f_H(\omega) cas(\omega t) d\omega, \end{aligned} \tag{A-1}$$

where $cas(\omega t) = \cos(\omega t) + \sin(\omega t)$. From the definition, it is found that the forward and inverse Hartley transform have the same form and both are real quantities. The relationship between the Hartley and Fourier transforms are easily shown

$$f_H(\omega) = \mathrm{Re}[f_F(\omega)] - \mathrm{Im}[f_F(\omega)], \tag{A-2}$$

$$f_F(\omega) = \{\frac{f_H(\omega) + f_H(-\omega)}{2}\} - i\{\frac{f_H(\omega) - f_H(-\omega)}{2}\}. \tag{A-3}$$

So, one can use these relations to convert between the transforms. Another characteristic of the Hartley transform is preservation of most properties of the Fourier transform. The followings are useful properties:

(a) linear relation

$$a_1 f_1(t) + a_2 f_2(t) \xleftrightarrow{H} a_1 f_{H1}(\omega) + a_2 f_{H2}(\omega), \tag{A-4}$$

(b) Scaling property

$$f(at) \xleftrightarrow{H} \frac{1}{a} f_H(\omega / a), \tag{A-5}$$

(c) derivative property

$$\begin{aligned} \partial_t f(t) &\xleftrightarrow{H} -\omega f_H(-\omega), \\ \partial_{tt} f(t) &\xleftrightarrow{H} -\omega^2 f_H(\omega), \end{aligned} \tag{A-6}$$

Corresponding to a pair of integrals (A-1), if the length of a sequence is $N = 2^M$, the discrete Hartley transform is expressed by

$$f_H(k) = \frac{1}{N}\sum_{n=0}^{N-1} f(n)cas(\frac{2\pi}{N}kn), \qquad 0 \le k \le N-1. \tag{A-7}$$

Separating the sequence $f(n)$ $(n=0,1,2,...N-1)$ into two sub-sequences: $f(2r)$ and $f(2r+1), 0 \le r \le N/2-1$, equation (A-7) can be rewritten as

$$f_H(k) = G(k) + \cos(\frac{2\pi}{N}k)H(k) + \sin(\frac{2\pi}{N}k)H(\frac{N}{2}-k), \tag{A-8}$$

where

$$\begin{aligned} G(k) &= N^{-1}\sum_{r=0}^{N/2-1} f(2r)cas(\frac{2\pi}{N/2}rk), \\ H(k) &= N^{-1}\sum_{r=0}^{N/2-1} f(2r+1)cas(\frac{2\pi}{N/2}rk). \end{aligned} \tag{A-9}$$

For simplicity, letting $c(k) = \cos(2\pi k / N)$ and $s(k) = \sin(2\pi k / N)$, a fast algorithm for the discrete Hartley transform can be formed form equation (A-8) and (A-9). In fact, taking k=0 and k=N/4 into equation (A-8), four identities are obtained:

$$\begin{aligned} f_H(0) &= G(0) + H(0), \\ f_H(\frac{N}{2}) &= G(0) - H(0), \\ f_H(\frac{N}{4}) &= G(\frac{N}{4}) + H(\frac{N}{4}), \\ f_H(\frac{3N}{4}) &= G(\frac{N}{4}) - H(\frac{N}{4}). \end{aligned} \tag{A-10}$$

Meanwhile, another four expressions can be written out

$$\begin{aligned} f_H(k) &= G(k) + [c(k)H(k) + s(k)H(\frac{N}{2}-k)], \\ f_H(\frac{N}{2}+k) &= G(k) - [c(k)H(k) + s(k)H(\frac{N}{2}-k)], \\ f_H(\frac{N}{2}-k) &= G(\frac{N}{2}-k) + [s(k)H(k) - c(k)H(\frac{N}{2}-k)], \\ f_H(N-k) &= G(\frac{N}{2}-k) - [s(k)H(k) - c(k)H(\frac{N}{2}-k)]. \end{aligned} \qquad N \ge 8, \quad 0 < k < \frac{N}{4} \tag{A-11}$$

Equations (A-10) and (A-11) are elementary formulae for radix-2 decimation fast Hartley transforms. From the above formulation, the Hartley formulation of a real

integral transform makes it possible to dispense with the need for complex representation. What distinguishes the Hartley Transform plane, apart from the fact that the transform value assigned to each point is real, is the absence of redundancy. It deals only with real numbers, which are the only kind of data we have in the world of experiment, and proceeds straight to the answers we need, which are also usually expressed in real terms, without the need to move into the complex domain. It has been shown that there are two major advantages for application to geophysical problems (Saatcilar et al., 1990):(1) all geophysical quantities become real and (2) the discrete Hartley transform is two times faster than the Fourier transform.

Appendix B

Computation of The Boundary Integral

Taking a rectangular boundary (see Fig.4-1), the boundary integral in equation (4.28) can be expressed by

$$\begin{aligned} -\int_{\partial} N_i \frac{\partial \overline{\overline{G}}^{2.5D}}{\partial n} d\Gamma &= -\{\int_{\Gamma_1} + \int_{\Gamma_2} + \int_{\Gamma_3} + \int_{\Gamma_4}\} N_i \frac{\partial \overline{\overline{G}}^{2.5D}}{\partial n} d\Gamma, \\ &= \{\int_{\Gamma_1} - \int_{\Gamma_2}\} N_i \frac{\partial \overline{\overline{G}}^{2.5D}}{\partial z} dx + \{\int_{\Gamma_3} - \int_{\Gamma_4}\} N_i \frac{\partial \overline{\overline{G}}^{2.5D}}{\partial x} dz. \end{aligned} \tag{B-1}$$

Substituting equation (4.27) into equation (B-1), the boundary integral can be classified into the following two types:

$$\begin{aligned} &\int_{\Gamma_{1,2}} N_i [\nu \overline{\overline{G}}^{2.5D} + \beta \frac{\partial^2 \overline{\overline{G}}^{2.5D}}{\partial^2 x}] dx, \\ &\int_{\Gamma_{3,4}} N_i [\nu \overline{\overline{G}}^{2.5D} + \beta \frac{\partial^2 \overline{\overline{G}}^{2.5D}}{\partial^2 z}] dz, \end{aligned} \tag{B-2}$$

where the imaginary i is omitted as a common factor and $\Gamma_{1,2} = \Gamma_1, \Gamma_2$ and $\Gamma_{3,4} = \Gamma_3, \Gamma_4$, respectively. Note that the second term in equation (B-2) can be reduced to the integral involving only the first derivatives by partial integration, e.g. for the first integral in equation (B-2) we have

$$\begin{aligned} \int_{\Gamma_{1,2}} \beta N_i \frac{\partial^2 \overline{\overline{G}}^{2.5D}}{\partial^2 x} dx &= \int_{\Gamma_{1,2}} \frac{\partial}{\partial x} [\beta N_i \frac{\partial \overline{\overline{G}}^{2.5D}}{\partial x}] dx - \int_{\Gamma_{1,2}} \frac{\partial}{\partial x} (\beta N_i) \frac{\partial \overline{\overline{G}}^{2.5D}}{\partial x} dx, \\ &= \beta N_i \frac{\partial \overline{\overline{G}}^{2.5D}}{\partial x}\Big|_{x_0}^{x_n} - \int_{\Gamma_{1,2}} \frac{\partial}{\partial x} (\beta N_i) \frac{\partial \overline{\overline{G}}^{2.5D}}{\partial x} dx, \end{aligned} \tag{B-3}$$

where x_0 and x_n are the x-coordinates of the two end-points of $\Gamma_{1,2}$. If supposing the derivative $\left|\frac{\partial \overline{\overline{G}}^{2.5D}}{\partial x}\right|$ goes to zero at the two end-points (also $\left|\frac{\partial \overline{\overline{G}}^{2.5D}}{\partial z}\right|$ for the second integral in equation (B-2), this assumption is reasonable when the four corner points are

far away from a source), the first term of the R.H.S of equation (B-3) vanishes. So, equation (B-2) becomes

$$\int_{\Gamma_{1,2}} [\nu N_i \overline{\overline{G}}^{2.5D} - \frac{\partial}{\partial x}(\beta N_i)\frac{\partial \overline{\overline{G}}^{2.5D}}{\partial x}]dx,$$
$$\int_{\Gamma_{3,4}} [\nu N_i \overline{\overline{G}}^{2.5D} - \frac{\partial}{\partial z}(\beta N_i)\frac{\partial \overline{\overline{G}}^{2.5D}}{\partial z}]dz. \qquad \text{(B-4)}$$

Let us calculate the first integral. The second integral can be treated in the same manner as the first. Dividing the boundary $\Gamma_{1,2}$ into the finite segments $\Gamma_{1,2} = \sum_{e=1}^{N_e} \Gamma_e$ so that the whole boundary integral becomes the summation of the segment integrals, and approximating the Green's function with the combination of the shape functions in the rectangular element one side of which coincides with the segment:

$$\overline{\overline{G}}^{2.5D} = \sum_p N_p(x,z)\overline{\overline{G}}_p^e, \qquad (p = i,j,k,l), \qquad \text{(B-5)}$$

where $\overline{\overline{G}}_p^e$ is a nodal value of the Green's function (unknown) and $p = i,j,k,l$ are the four order-number of the nodes in the rectangular element, the first integral can be rewritten as follows:

$$\int_{\Gamma_{1,2}} [..]dx = \sum_{e=1}^{N_e}\sum_p \{\int_{\Gamma_e} [\nu^{(e)} N_i N_p - \beta^{(e)}\frac{\partial N_i}{\partial x}\frac{\partial N_p}{\partial x}]dx\}\overline{\overline{G}}_p^e = \sum_{e=1}^{N_e} B^e \tilde{G}^e, \qquad \text{(B-6)}$$

where $\nu^{(e)}$ and $\beta^{(e)}$ are the element values of ν and β. The boundary element matrix B^e and the vector $\tilde{G}^e$ are expressed by $B^e = \left(B^e_{pq}\right)_{4\times4}$ and $\tilde{G}^e = \{\overline{\overline{G}}_p^e\}$ $(p,q = i,j,k,l)$ respectively. From equation (B-6), the element of B^e is

$$B^e_{pq} = \int_{\Gamma_e} [\nu^{(e)} N_p N_q - \beta^{(e)}\frac{\partial N_p}{\partial x}\frac{\partial N_q}{\partial x}]dx, \quad \Gamma_e \in \Gamma_{1,2}. \qquad \text{(B-7)}$$

In similar fashion, we have the following expression for the second integral in equation (B-4):

$$B_{pq}^{e} = \int_{\Gamma_e} [\nu^{(e)} N_p N_q - \beta^{(e)} \frac{\partial N_p}{\partial z} \frac{\partial N_q}{\partial z}] dz, \quad \Gamma_e \in \Gamma_{3,4}. \tag{B-8}$$

Once the shape functions N_p ($p = i, j, k, l$) are chosen, B_{pq}^{e} can be calculated with an analytic method. Equations (B-7) and (B-8) show that the boundary element matrix B^e is symmetric. This means that the boundary operator B in equation (4.27) has a symmetric property with the boundary integral in the FEM, that is

$$\int_{\partial\Omega} vBud\Gamma = \int_{\partial\Omega} uBvd\Gamma, \tag{B-9}$$

for any v and u, which are approximated by the combination of the shape functions (B-5) and satisfy the acoustic wave equation (called Galerkin's solutions).

Appendix C

Semi-Analytic Acoustic Solution for Two Semi-Infinite Media in Contact

The analytic solution for the two semi-infinite constant-density acoustic media in contact can be written in integral form (Ewing et al., 1957, p97-105):

$$\overline{P_1} = \int_0^\infty \frac{\upsilon_1 \cosh(\upsilon_1 \xi_1) + \upsilon_2 \sinh(\upsilon_1 \xi_1)}{\upsilon_1(\upsilon_1 + \upsilon_2)} \exp(-\upsilon_1 \xi_2) J_0(kr) k dk,$$
$$(z < h, \xi_1 = z, \xi_2 = h; \quad z > h, \xi_1 = h, \xi_2 = z), \tag{C-1}$$
$$\overline{P_2} = \int_0^\infty \frac{\exp(\upsilon_2 z - \upsilon_1 h)}{(\upsilon_1 + \upsilon_2)} J_0(kr) k dk, \quad z < 0,$$

where $J_0(x)$ is a zero-order Bessel Function, $\overline{P_1}$ and $\overline{P_2}$ are the Fourier spectra of the pressure in the two media, and the parameters: υ_1 and υ_2 that may be a real or pure imaginary values are defined by

$$\upsilon_{1,2} = \begin{cases} \upsilon_{1,2} = \sqrt{k^2 - k_{c_{1,2}}^2}, & k_{c_{1,2}}^2 < k; \\ i\upsilon_{1,2} = i\sqrt{k_{c_{1,2}}^2 - k^2}, & k_{c_{1,2}}^2 > k; \end{cases} \qquad k_{c_{1,2}} = \omega / c_{1,2}. \tag{C-2}$$

Here ω is angular frequency; c_1 and c_2 are the wavespeeds of the two media. Other parameters in equation (C-1) are defined in Fig.4-13.

Obviously, there is no singularity in the integrands of equation (C-1). Using the Fourier-cosine transform identity (Bateman, 1954),

$$\int_0^\infty J_0(k\sqrt{x^2 + y^2}) \cos(k_y y) dy = \begin{cases} \dfrac{\cos(x\sqrt{k^2 - k_y^2})}{\sqrt{k^2 - k_y^2}}, & k_y < k; \\ 0, & k_y > k; \end{cases} \tag{C-3}$$

the wavenumber-domain solution of equation (C-1) can be obtained as:

$$\overline{\overline{P}}_1 = \int_{k_y}^{\infty} \frac{\upsilon_1 \cosh(\upsilon_1 \xi_1) + \upsilon_2 \sinh(\upsilon_1 \xi_1)}{\upsilon_1(\upsilon_1 + \upsilon_2)} \exp(-\upsilon_1 \xi_2) \frac{\cos(x\sqrt{k^2 - k_y^2})}{\sqrt{k^2 - k_y^2}} k dk,$$

$$(z < h, \xi_1 = z, \xi_2 = h; \quad z > h, \xi_1 = h, \xi_2 = z), \tag{C-4}$$

$$\overline{\overline{P}}_2 = \int_{k_y}^{\infty} \frac{\exp(\upsilon_2 z - \upsilon_1 h)}{(\upsilon_1 + \upsilon_2)} \frac{\cos(x\sqrt{k^2 - k_y^2})}{\sqrt{k^2 - k_y^2}} k dk, \qquad z < 0,$$

where $\overline{\overline{P}}_1$ and $\overline{\overline{P}}_2$ represent the double Fourier transform of the acoustic pressure field with respect to time and the y-coordinate respectively. So both of them are complex functions. For simplification, we prefer to obtain the Hartley spectra of the pressure with respect to time rather than the Fourier transformed pressure, because the Hartley spectrum is a real function instead of complex function (Appendix A). As an example, supposing $c_1 > c_2$, then for a given frequency ω, we have $k_{c_1} < k_{c_2}$. For this model, there are three cases to consider for a wavenumber k_y: (1) $k_y \le k_{c_1} < k_{c_2}$; (2) $k_{c_1} \le k_y \le k_{c_2}$; (3) $k_{c_1} < k_{c_2} \le k_y$. Obviously, in case (3), υ_1 and υ_2 are real values (see equation C-2) and the integrands in equation (C-4) are real functions so that their Hartley spectra are the same as their Fourier spectra. We can calculate the integrals with the numerical method for case (3). For case (1) or (2), first substituting equation (C-2) for (C-4) and using the relation between the Hartley and Fourier transforms to obtain the Hartley spectra for $\overline{\overline{P}}_1$ and $\overline{\overline{P}}_2$, then rewriting the integrals over the range (k_y, ∞) as a few segments integrals, we get

case (1):
$$\begin{cases} \overline{\overline{P}}_1^{(H)} = \int_{k_y}^{\infty} F_1^{(H)} dk = \int_{k_y}^{k_{c1}} F_{11}^{(H)} dk + \int_{k_{c1}}^{k_{c2}} F_{12}^{(H)} dk + \int_{k_{c2}}^{\infty} F_{13}^{(H)} dk, \\ \overline{\overline{P}}_2^{(H)} = \int_{k_y}^{\infty} F_2^{(H)} dk = \int_{k_y}^{k_{c1}} F_{21}^{(H)} dk + \int_{k_{c1}}^{k_{c2}} F_{22}^{(H)} dk + \int_{k_{c2}}^{\infty} F_{23}^{(H)} dk, \end{cases} \tag{C-5}$$

case (2):
$$\begin{cases} \overline{\overline{P}}_1^{(H)} = \int_{k_y}^{\infty} F_1^{(H)} dk = \int_{k_y}^{k_{c2}} F_{12}^{(H)} dk + \int_{k_{c2}}^{\infty} F_{13}^{(H)} dk, \\ \overline{\overline{P}}_2^{(H)} = \int_{k_y}^{\infty} F_2^{(H)} dk = \int_{k_y}^{k_{c2}} F_{22}^{(H)} dk + \int_{k_{c2}}^{\infty} F_{23}^{(H)} dk, \end{cases} \tag{C-6}$$

where the superscript H denotes the Hartley transform with respect to time; $F_1^{(H)}$ and $F_2^{(H)}$ are the Hartley spectra of the integrands of equation (C-4); the other integrands in equation (C-5) and (C-6) can be obtained as follows:

$$F_{11}^{(H)} = \frac{\{\upsilon_2 \sin(\upsilon_1\xi_1)[\cos(\upsilon_1\xi_2)+\sin(\upsilon_1\xi_2)] - \upsilon_1 \sin(\upsilon_1\xi_1)[\sin(\upsilon_1\xi_2)-\cos(\upsilon_1\xi_2)]\}}{\upsilon_1(\upsilon_1+\upsilon_2)\sqrt{k^2-k_y^2}\{k\cos(x\sqrt{k^2-k_y^2})\}^{-1}}, \quad \text{(C-7)}$$

$$F_{12}^{(H)} = \frac{\exp(-\upsilon_1\xi_2)\{\upsilon_1^2\cosh(\upsilon_1\xi_1)+\upsilon_2^2\sinh(\upsilon_1\xi_1)-\upsilon_1\upsilon_2[\sinh(\upsilon_1\xi_1)-\cosh(\upsilon_1\xi_1)]\}}{\upsilon_1(\upsilon_1^2+\upsilon_2^2)\sqrt{k^2-k_y^2}\{k\cos(x\sqrt{k^2-k_y^2})\}^{-1}}, \quad \text{(C-8)}$$

$$F_{13}^{(H)} = \frac{\exp(-\upsilon_1\xi_2)[\upsilon_1\cosh(\upsilon_1\xi_1)+\upsilon_2\sinh(\upsilon_1\xi_1)]}{\upsilon_1(\upsilon_1+\upsilon_2)\sqrt{k^2-k_y^2}\{k\cos(x\sqrt{k^2-k_y^2})\}^{-1}}, \quad \text{(C-9)}$$

$$(z<h,\quad \xi_1=z,\xi_2=h;\quad z>h,\quad \xi_1=h,\xi_2=z),$$

$$F_{21}^{(H)} = \frac{[\sin(\upsilon_2 z-\upsilon_1 h)+\cos(\upsilon_2 z-\upsilon_1 h)]}{(\upsilon_1+\upsilon_2)\sqrt{k^2-k_y^2}\{k\cos(x\sqrt{k^2-k_y^2})\}^{-1}}, \quad \text{(C-10)}$$

$$F_{22}^{(H)} = \frac{\exp(-\upsilon_1 h)[\upsilon_1(\cos\upsilon_2 z-\sin\upsilon_2 z)+\upsilon_2(\sin\upsilon_2 z+\cos\upsilon_2 z)]}{(\upsilon_1^2+\upsilon_2^2)\sqrt{k^2-k_y^2}\{k\cos(x\sqrt{k^2-k_y^2})\}^{-1}}, \quad \text{(C-11)}$$

$$F_{23}^{(H)} = \frac{\exp(\upsilon_2 z-\upsilon_1 h)k\cos(x\sqrt{k^2-k_y^2})}{(\upsilon_1+\upsilon_2)\sqrt{k^2-k_y^2}}. \quad \text{(C-12)}$$

It is found that the integrands $F_{13}^{(H)}$ and $F_{23}^{(H)}$ decrease exponentially with k and the others have no singularity except for $k = k_y$, at which we used the approximation

$$\int_{k_y}^{\varepsilon} f(k)dk \approx f(k_y)\cdot\varepsilon. \quad \text{(C-13)}$$

So, all the other integrals in equation (C-5) and (C-6) can be calculated by a numerical algorithm. We call this result a semi-analytic solution in the wavenumber-domain, because the result is computed using a numerical integral algorithm based on the analytic solution. It should be mentioned that following the computational scheme the semi-analytic solution in the wavenumber-domain for $c_1 < c_2$ can be also calculated.

Appendix D

A Constant-Block Approximation in The Computation of The Fréchet and Second Derivatives for Resistivity Imaging

For calculating the integrals of equations (7.30) and (7.31), we take Ω_e and $\Omega_{e'}$ as two rectangles (see Fig.D-1) in which the Green's functions are approximated by the combination of the four linear shape functions $N_i(r)$ (i=1,2,3,4) as:

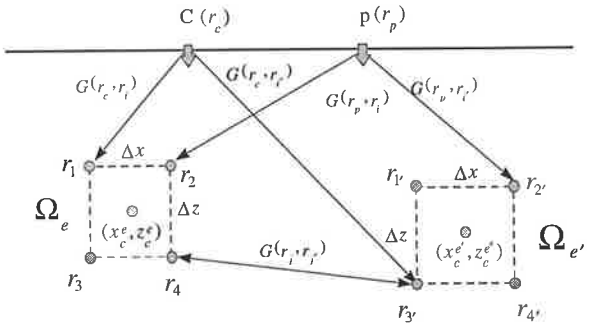

Fig.D-1 Sketch of the geometry for computing the Fréchet and second derivatives with the constant-block approximation for resistivity imaging.

$$\overline{\overline{G}}^{2.5D}(r_c,r) = \sum_{i-1}^{4} N_i(r)\overline{\overline{G}}^{2.5D}(r_c,r_i), \qquad r \in \Omega_e, \Omega_{e'};$$

$$\overline{\overline{G}}^{2.5D}(r_p,r) = \sum_{j=1}^{4} N_j(r)\overline{\overline{G}}^{2.5D}(r_p,r_j), \qquad r \in \Omega_e, \Omega_{e'}; \tag{D-1}$$

$$\overline{\overline{G}}^{2.5D}(r,r') = \sum_{j,j'=1}^{4} N_j(r)N_{j'}(r')\overline{\overline{G}}^{2.5D}(r_j,r_{j'}), \quad r \in \Omega_e, r' \in \Omega_{e'}.$$

where

$$N_i(r) = \frac{1}{4}[1+\xi(x)\xi(x_i)][1+\eta(z)\eta(z_i)], \tag{D-2}$$

and $$\xi(x) = \frac{2}{\Delta x}(x - x_c^e), \quad \eta(z) = \frac{2}{\Delta z}(z - z_c^e). \tag{D-3}$$

The geometry of the variables in equations (D-1)-(D-3) is shown in Fig.D-1. Substituting equation (D-1) for equations (7.30) and (7.31), the Fréchet and the second derivatives finally have the following forms:

$$\frac{\partial U}{\partial \sigma_e} = -\frac{I}{2} F_c^{-1}\{\sum_{i,j=1}^{4} \overline{\overline{G}}^{2.5D}(r_c, r_i)[M_{ij}^{(1)} + k_y^2 M_{ij}^{(2)}]\overline{\overline{G}}^{2.5D}(r_p, r_j)\}, \tag{D-4}$$

$$\begin{aligned}\frac{\partial^2 U}{\partial \sigma_e \partial \sigma_{e'}} = \frac{I}{4} F_c^{-1}\{ &\sum_{i,j,i',j'=1}^{4} [\overline{\overline{G}}^{2.5D}(r_c, r_{i'})\overline{\overline{G}}^{2.5D}(r_p, r_i) + \\ &\overline{\overline{G}}^{2.5D}(r_c, r_i)\overline{\overline{G}}^{2.5D}(r_p, r_{i'})]\overline{\overline{G}}^{2.5D}(r_j, r_{j'}) M_{iji'j'}\},\end{aligned} \tag{D-5}$$

where the matrices are

$$M_{ij}^{(1)} = \frac{\xi(x_i)\xi(x_j)}{4}[1.+\frac{\eta(z_i)\eta(z_j)}{3}](\frac{\Delta z}{\Delta x}) + \frac{\eta(z_i)\eta(z_j)}{4}[1.+\frac{\xi(x_i)\xi(x_j)}{3}](\frac{\Delta x}{\Delta z}), \tag{D-6}$$

$$M_{ij}^{(2)} = \frac{1}{4}[1+\frac{\xi(x_i)\xi(x_j)}{3}][1+\frac{\eta(z_i)\eta(z_j)}{3}], \tag{D-7}$$

$$M_{iji'j'} = M_{ij}^{(1)} M_{i'j'}^{(1)} + k_y^2 (M_{ij}^{(1)} M_{i'j'}^{(2)} + M_{i'j'}^{(1)} M_{ij}^{(2)}) + k_y^4 M_{ij}^{(2)} M_{i'j'}^{(2)}. \tag{D-8}$$

Equations (D-4) and (D-5) can be generalized to the apparent resistivity for any electrode array (see equations (3.49) and (3.50)) , and become

$$\frac{\partial \rho_a}{\partial \sigma_e} = -\frac{K}{2} F_c^{-1}\{\sum_{i,j=1}^{4} \delta\overline{\overline{G}}_{AB}(r_i)[M_{ij}^{(1)} + k_y^2 M_{ij}^{(2)}]\delta\overline{\overline{G}}_{MN}(r_j)\}, \tag{D-9}$$

$$\begin{aligned}\frac{\partial^2 U}{\partial \sigma_e \partial \sigma_{e'}} = \frac{K}{4} F_c^{-1}\{ &\sum_{i,j,i',j'=1}^{4} [\delta\overline{\overline{G}}_{AB}(r_{i'})\delta\overline{\overline{G}}_{MN}(r_i) + \\ &\delta\overline{\overline{G}}_{AB}(r_i)\delta\overline{\overline{G}}_{MN}(r_{i'})]\overline{\overline{G}}^{2.5D}(r_j, r_{j'}) M_{iji'j'}\}.\end{aligned} \tag{D-10}$$

Equations (D-9) and (D-10) show that once all the Green's functions are obtained, these formulas can be employed to calculate the Fréchet and second derivatives.

Bibliography

Aki, K., and Richards, P.G., 1980, *Quantitative seismology, theory and methods*, W.H. Freeman and Co.

Bateman, H., 1954, *Tables of integral transforms*, McGraw-Hill book Company.

Bayliss, A., Gunzburger, M., and Turkel, E., 1982, Boundary conditions for the numerical solution of elliptic equations in exterior regions, *SIAM J. Appl. Math.*, **42**, 430-451.

Bleistein, N., Jack, K., and Hagin, F.G., 1987, Two-and one-half dimensional Born inversion with an arbitrary reference, *Geophysics*, **52**, 26-36.

Boerner, E., and Holladay, J. S., 1990, Approximate Fréchet derivative in inductive electromagnetic soundings, *Geophysics* **55**, 1589-1595.

Bracewell, R., 1978, *The Fourier transform*, Oxford University press.

Bracewell, R., 1986, *The Hartley transform*, Oxford University press.

Broyden, C. G., 1965, A class of methods for solving nonlinear simultaneous equations, *Mathematics of Computation*, **19**, 577-593.

Cao, S., and Greenhalgh, S. A., 1997, 2.5D acoustic wave modeling in the wavenumber-frequency domain, *Exploration Geophysics*, **28**, 11-15.

Cao, S., and Greenhalgh, S, 1998, Attenuating boundary conditions for numerical modeling of wave propagation, *Geophysics*, **63**, 231-243.

Carrion, P. M., 1989, Generalized non-linear elastic inversion with constraints in model and data spaces, *Geophysical Journal*, **96**, 151-162.

Chunduru, R., Sen, M. K., Stoffa, P. L., and Nagendra, R., 1995, Non-linear inversion of resistivity profiling data for some regular geometrical bodies, *Geophysical Prospecting,* **43**, 979-1003.

Chunduru, R., Sen, M. K., and Stoffa, P. L, 1996, 2-D resistivity inversion using spline parameterization and simulated annealing, *Geophysics,* **61,** 151-161.

Clayton, R.L., and Engquist, B., 1977, Absorbing boundary conditions for acoustic and elastic wave equations, *Bull. Seism. Soc. Am.*, **67**, 1529-1540.

Coggon, J. H., 1971, Electromagnetic and electrical modeling by the finite element method, *Geophysics*, **36**, 132-155.

Constable, S. C., Parker, R. L., and Constable, C. G., 1978, Occam's inversion: A practical algorithm for generating smooth models from electromagnetic sounding data, *Geophysics*, **52**, 289-300.

Dabas, M., Tabbagh, A., and Tabbagh, J., 1994, 3-D inversion subsurface electrial surveying—I . Theory, *Geophys. J. Int.*, **119**, 975-990.

Daniels, J. J., 1977, Three-dimensional resistivity and induced-polarisation modeling using buried electrodes, *Geophysics*, **42**, 1006-1019.

Daniels, J. J., and Dyck, A., 1984, Borehole resistivity and electromagnetic methods applied to mineral exploration, *IEEE, Trans.* **GE-22**, 80-87.

Daily, W., and Owen, E., 1991, Cross-borehole resistivity tomography, *Geophysics*, **56**,1228-1235.

Das, U. C., and Parnasis, D. S., 1987, Resistivity and induced polarization responses of arbitrarily shaped 3-D bodies in a two-layered earth, *Geophysical Prospecting,* **35**, 98-109.

Deregowski, S. M., and Brown, S. M., 1983, A theory of acoustic diffractions applied to 2-D models, *Geophysical Prospecting,* **31**, 293-333.

Devaney, A. J., 1984, Geophysical diffraction tomography, *Trans. IEEE*, **GE-22**, 3-13.

Dey, A., and Morrison, H. F., 1979a, Resistivity modeling for arbitrarily shaped two-dimensional structure, *Geophysical Prospecting,* **27**, 106-136.

Dey, A., and Morrison, H. F., 1979b, Resistivity modeling for arbitrarily shaped three-dimensional structure, *Geophysics,* **44**, 753-780.

Dickens, T. A., 1994, Diffraction tomography for crosswell imaging of nearly layered media, *Geophysics,* **59**, 694-706.

Dieter, K., Paterson, N. R., and Grant, F. S., 1969, IP and resistivity type curves for three-dimensional bodies, *Geophysics*, **34**, 615-632.

Dittmer, J. K., and Szymenski, J. E., 1995, The stochastic inversion of magnetics and resistivity data using the simulated annealing algorithm, *Geophysical Prospecting*, **43**, 397-416.

Dobroka, 1992, Tomographic inversion of normalized data: Double-trace tomography algorithm, *Geophysical Prospecting*, **40**, 1-14.

Ellis, R. G., and Oldenburg, D. W., 1994a, Applied geophysical inversion, *Geophys. J. Int.,* **116,** 5-11.

Ellis, R. G., and Oldenburg, D. W., 1994b, The pole-pole 3-D-resistivity inverse problem: a conjugate-gradient approach, *Geophys. J. Int.*, **119**, 187-194.

Ewing, W. M., Jardetzky, W. S., and Press, F., 1957, *Elastic waves in layered media,* McGraw-Hill Book Company, Inc.

Flett, T. M., 1980, *Differential analysis*, Cambridge University Press, Cambridge.

Frazer, L. N., Xinhua Sun and Wilkens, R. H., 1997, Inversion of sonic waveform with unknown source and receiver functions: *Geophys. J. Int.* **129**, 579-586.

Frazer, L. N., and Xin-hua Sun, 1998, New objective function for waveform inversion: *Geophysics,* **63**, 213-222.

Furumura, T., and Takenaka, H., 1996, A 2.5-D modeling of elastic waves using the pseudospectral method, *Geophys. J. Int.*, **124**, 820-832.

Fox, R. C., Hohmann, G. W., Killpack, T. J., and Rijo, L., 1980, Topographic effects in resistivity and induced-polarization surveys, *Geophysics*, **45**, 75-93.

Gan, H., Levin, P. L., and Ludwig, R., 1993, Finite element formulation of acoustic scattering phenomena with absorbing boundary conditions in the frequency domain, *J. Acoust. Soc. Am.*, **94**,1651-1661.

Gan, H, Ludwig, R., and Levin, P. L., 1994, Non-linear diffraction inverse scattering for multiple scatterers in inhomogeneous acoustic background media, *J. Acoust. Soc. Am.,* **97**, 764-776.

Gelius, L. J., 1995a, Generalized acoustic diffraction tomography, *Geophysical Prospecting*, **43**, 3-29.

Gelius, L. J., 1995b, A sample of controlled experiments in diffraction tomography, *Geophysical Prospecting*, **43**, 31-50.

Gelius, L. J., 1995c, Limited-view diffraction tomography in a nonuniform background, G*eophysics*, **60**, 580-588.

Griffel, D. H., 1981, *Applied functional analysis*, Ellis Horwood Limited.

Higdon, R.L., 1991, Absorbing boundary conditions for elastic waves, *Geophysics*, **56**, 231-241.

Holcombe, H. T., and Jiracek, G. R., 1984, Three-dimesional terrain corrections in resistivity surveys, *Geophysics*, **49**, 439-452.

Huebnent, K. H., 1975, *the finite element method for engineers*, John Wiley Lsons.

Hughes, T. J. R., 1987, *The finite element method,* Prentice-Hall Inc.

James, B. A., 1985, Efficient microcomputer-based finite difference resistivity modeling via Polozhii decomposition, *Geophysics*, **50**, 443-465.

Kaveh, M., Soumekh, M., and Muller, R. K., 1981, A comparison of Born and Rytov approximations in acoustic tomography, in Powers, S. P. Ed., *Acoustical Imaging*, **11**, 325-335.

Kennett, B. L. N., and Williamson, P. R., 1988, Subspace methods for large-scale non-linear inversion, *Mathematical Geophysics, a survey of recent developments in seismology and geodynamics*, pp. 139-154, eds Vlaar, N. J., Nolet, G., Wortel, M. J. R. and Cloetingh, S. A. L., D. Reidel, Dordrecht.

Kirsch, A., 1996, *An introduction to the mathematical theory of inverse problems*, Springer-Verlag.

LaBrecque, D., Miletto, M., Daily, W., Ramirez, A., and Owen, E., 1996, The effects of " Occam" inversion of resistivity tomography data, *Geophysics*, **61**, 538-548.

Lee, T., 1975, An integral equation and its solution for some two and three-dimensional problems in resistivity and induced polarization, *Geophys. J.*, **42**, 81-95.

Li, Y. G., and Oldenburg, D. W., 1992, Approximate inverse mapping in DC resistivity problems, *Geophys. J. Int.*, **109**, 343-362.

Liao, Q., and McMechan, G. A., 1996, Multifrequency viscoacoustic modeling and inversion, *Geophysics*, **61**, 1371-1378.

Liner, C. L., 1991, Theory of a 2.5-D acoustic wave equation for constant density media, *Geophysics*, **56**, 2114-2117.

Lines, L. R., and Treitel, S., 1984, Tutorial: A review of least-squares inversion and its application to geophysical problems, *Geophysical Prospecting,* **32**, 159-186.

Loke, M. H., and Barker R. D., 1995, Least-squares deconvolution of apparent resistivity pseudosections, *Geophysics*, **60**, 1682-1690.

Loke, M. H., and Barker R. D., 1996, Rapid least-squares inversion of apparent resistivity pseudosections by a quasi-Newton method, *Geophysical Prospecting*, **44**, 131-152.

Lowry, T., Allen, M. B., and Shive, P. N., 1989, Singularity removal: A refinement of resistivity modeling techniques, *Geophysics*, **54**, 766-774.

Luco, J. E., Wong, H. L., and De Barros, F. C. P., 1990. Three-dimensional response of a cylindrical canyon in a layered half-space, *Earthq. Eng. Struct. Dyn.*, **19**, 799-817.

Luenberger, D. G., 1984, *Linear and nonlinear programming*, Addison-Wesley Publishing Company.

Lysmer, J., M. ASCE and Roger, K. A. M. ASCE, 1970, Finite dynamic model for infinite media, *J. Engin. Mech. Am. So. Civil Engin.*, **95**, 859-877.

Marfurt, K. J., 1984, Accuracy of finite difference and finite element modeling of scalar and elastic wave equations, *Geophysics*, **49**, 533-549.

McGillivray, P. R., and Oldenbury, D.W., 1990, Method for calculating Fréchet derivatives for the non-linear inverse problem: a comparative study, *Geophysical Prospecting*, **38**, 499-524.

Menke, W., 1984, *Geophysical data analysis: discrete inverse theory*, Academic Press, Inc., New York.

Mikhlin, 1964. *Variational methods in mathematical physics*, Macmillan Co.

Militer, H., Rosler, R., and Losch, W., 1979, Theoretical and experimental investigations for cavity research with geoelectrical resistivity methods, *Geophysical Prospecting,* **27**, 640-652.

Mines and Energy Resources, South Australia, 1997, Aquifer storage and recovery: direction for water resource management, Information Sheet.

Minoux, M., 1986, *Mathematical programming theory and algorithms*, John Wiley and Sons.

Mora, P., 1989, Inversion=migration+tomography, *Geophysics*, **54**, 1575-1586.

Mufti, I. R., 1976, Finite difference resistivity modeling for arbitrary shaped two-dimensional structures, *Geophysics*, **41**, 62-78.

Mundry, E., 1984, Geoelectical model caculations for two-dimentional resistivity distributions, *Geophysical Prospecting*, **32**, 124-131.

Okabe, M., 1981, Boundary element method for the arbitrary inhomogeneity problem in electrical prospecting, *Geophysical Prospecting*, **29**, 39-59.

Okamoto, T., 1994, Teleseismic synthetics obtained from 3-D calculations in 2-D media, *Geophys J. Int.*, **118**, 613-622.

Oldenburg, D. W., McGillicray, P. R., and Ellis, R. G., 1993, Generalised subspace methods for large-scale inverse problems, *Geophys. J. int.*, **114**, 12-20.

Oldenburg, D. W., and Yaoguo Li, 1994, Inversion of induced polarization data, *Geophysics*, **59**, 1327-1341.

Owen, E.,1983, Detection and mapping of tunnels and caves, *Development in geophysical exploration method-5*, Applied science publishers.

Pai, D. M., 1989, Diffraction tomography in Layered background, *39th Ann. Intern. Mtg., SEG, Expanded Abstracts*, 915-917.

Pai, D. M., 1990, Crosshole seismic using vertical eigenstates, *Geophysics*, **55**, 815-820.

Pao, C. V., 1992, *Nonlinear parabolic and elliptic equations*, Plenum Press.

Park, S. K., and Van, G. P., 1991, Inversion of pole-pole data for 3-D resistivity structure beneath arrays of electrodes, *Geophysics*, **56**, 951-960.

Parker, R., 1994, *Geophysical inverse theory*, Princeton University Press, princeton, New Jersey.

Pedersen, H. A., Sánchez-Sesma, F. J., and Campillo, M., 1994. Three-dimensional scattering by two-dimensional topographies, *Bull. Seism. Soc. Am.*, **84**, 1169-1183.

Pedersen, H. A., Maupin, V., and Campillo, M., 1996. Wave diffraction in multilayered media with the indirect boundary element method: application to 3-D diffraction of long-period surface waves by 2-D lithospheric structures, *Geophys. J. Int.*, **125**, 545-558.

Pelton, W. H., Rijo, L., and Swift, JR. C. M., 1978, Inversion of two-dimensional resistivity and induced-polarization data, *Geophysics*, **43**, 788-803.

Poggiagliolmi, E., Berkhout, A. J. And Boone, M. M., 1982, Phase unwrapping, possibilities and limitations, *Geophys. Prosp.*, **30**, 281-291.

Pratt, R. G., and Goulty, N.R., 1991, Combining wave-equation imaging with traveltime tomography to form high-resolution images from crosshole data, *Geophysics*, **56**, 208-224.

Pratt, R. G., and Worthington, M. H., 1988, The application of diffraction tomography to crosshole seismic data, *Geophysics,* **53**, 1284-1294.

Pratt, R. G., and Worthington, M. H., 1990, Acoustic wave equation inverse theory applied to multi-source cross-hole tomography, Part I acoustic wave-equation method, *Geophysical Prospecting*, **38**, 287-310.

Press, W.H., Tenkolsky, S.A., Vetterling, W.T., and Flannery, B.P., 1986, *Numerical recipes in Fortran, the art of scientific computation*, Cambridge University Press.

Pridmore, D., Hohmann, G. W., Ward, S. H., and Sill, W. R., 1981, An investigation of finite element modeling for electrical and electromagnetic modeling data in three dimensions, *Geophysics*, **46**, 1009-1024.

Queralt, J. P., and Marcuello, A., 1991, 2-D resistivity modeling: An approach to arrays parallel to the strike direction, *Geophysics*, **56**, 941-950.

Ramahi, O. M., Khebir, A., and Mittra, R, 1991, Numerical derived absorbing boundary condition for the solution of open region scattering problems, *IEEE, Trans. Antennas and Propagation*, **39**, 350-353.

Randall, C. J., 1991, Multipole acoustic waveforms in nonsymmetric boreholes and formations, *J. Acoustic. Soc. Am.*, **90**, 1620-1631.

Reiter, D. T., and Rodi, W., 1996, Nonlinear waveform tomography applied to crosshole seismic data, *Geophysics*, **61**, 902-913.

Reynolds, A. C., 1978. boundary conditions for the numerical solution of wave propagation problems, *Geophysics*, **43**, 1099-1110.

Saatcilar, R., Ergintav, S., and Canitez, N., 1990, The use of the Hartley transform in geophysical applications, *Geophysics*, **55**, 1488-1495.

Sambridge, M.S., Tarantola, A., and Kennett, B.L.N., 1991, An alternative strategy for non-linear inversion of seismic waveforms, *Geophysical Prospecting*, **39**, 723-736.

Sasaki, Y., 1994, 3-D resistivity inversion using the finite element method, *Geophysics*, **59**, 1839-1848.

Scales, J. A., and Smith, M. L., 1994, *Introductory Geophysical inverse theory*, Samizdat Press Golden. White River Junction.

Schuster, G. T., 1991, Wave-equation phase inversion in the frequency-domain, *61st Annual International Meeting, SEG, Expanded Abstract*, 909-912

Schuster, G. T., and Quintus-Bosz, A., 1993, Wavepath eikonal traveltime inversion: Theory, *Geophysics*, **58**, 1314-1323.

Sengbush, R. L., 1983, *Seismic exploration methods*, International Human Res. Dev. Corp.

Serón, F. J., Badal, J., and Sabadell, F. J., 1996, A numerical laboratory for simulation and visualzation of seismic wavefields, *Geophysical Prospecting*, **44**, 603-642.

Shima, H., 1992, 2-D and 3-D resistivity imaging reconstruction using crosshole data, *Geophysics*, **55**, 682-694.

Skilling, J., and Bryan, R. K., 1984, Maximum entropy image reconstruction, general algorithm, *Mon. Not. R. ast. Soc.*, **211**, 111-124.

Smith, N. C., and Vozoff, K., 1984, Two-dimensional DC resistivity inversion for dipole-dipole data, *IEEE Trans. Geoscience Rem. Sens.*, **GE-22**, 21-28.

Snyder, D. D., 1976, A method for modeling the resistivity and IP response of two-dimensional bodies, *Geophysics*, **41**, 997-1015.

Sochacki, J. R., Kubicheck R., George J., Fletcher W. R., and Smitheson S., 1987, Absorbing boundary conditions and surface wave, *Geophysics*, **52**, 60-71.

Song, Z. M., and Williamson, P. R., 1995a, Frequency-domain acoustic wave modeling and inversion of crosshole data: Part 1-2.5D modeling, *Geophysics*, **60**, 784-795.

Song, Z. M., and Williamson, P. R., 1995b, Frequency-domain acoustic wave modeling and inversion of crosshole data: Part 2-inversion, *Geophysics*, **60**, 786-808.

Spitzer, K., 1995, A 3-D finite-difference algorithm for DC resistivity modeling using conjugate gradient methods, *Geophys. J. Int.*, **123**, 903-914.

Stoffa and Sen, 1991, Nonlinear multiparameter optimization using a genetic algorithm, *Geophysics*, **56**, 1794-1810.

Takenaka, H., Kennett, B.L.N., and Fujiwara, H., 1996, effect of 2-D topography on the 3-D seismic wavefield using a 2.5-D discrete wavenumber-boundary integral equation method, *Geophys. J. Int.*, **124**, 741-755.

Takenaka, H., and Kennett, B.L.N., 1996a, 2.5-D time-domain elastodynamic equation for plane-wave incidence, *Geophys. J. Int.*, **125**, F5-F9.

Takenaka, H., and Kennett, B.L.N., 1996b, A 2.5-D time-domain elastodynamic equation for a general anisotopic medium, *Geophys. J. Int.*, **127**, F1-F4.

Tarantola, A., and Vallette, B., 1982, Generalized non-linear inverse problem solved using the least-squares criterion, *Rev. Geophys. Space Phys*, **20**, 219-232.

Tarantola, A, 1984, Inversion of seismic reflection data in the acoustic approximation, *Geophysics*, **49**, 1259-1266.

Tarantola, A., 1987, *Inverse problem theory, methods for data fitting and model parameter estimation*, Elsevier.

Tikhonov, A. N., and Arsenin, V. Y., 1977, *Solution of ill-posed problems*, Winston and Sons.

Tribolet, J. M., 1977, A new phase unwrapping algorithm, *IEEE Trans. Acoust. Signal Processing,* **25**, 170-178.

Tripp, A. C., Hohmann, G. W., and Swift, Jr., C. M., 1984, Two-dimensional resistivity inversion, *Geophysics*, **49**, 1708-1717.

Tura, M. A. C, Johnson, L.R., Majer, E. L., and Peterson, J. E., 1992, Application of diffraction tomography to fracture detection, *Geophysics*, **57**, 245-257.

Ulrych, T. J., Velis, D. R., and Sacchi, M. D., 1995, Wavelet estimation revisited, *The Leading Edge*, **14**, 1139-1143.

Van, G. P., and Park, S. K. and Hamilton, P., 1991, Monitoring leaks from storage ponds using resistivity methods, *Geophysics*, **56**, 1267-1270.

Williamson, P. R., 1991., A guide to the limits of resoulution imposed by scattering in ray tomography, *Geophysics*, **56**, 202-207.

Williamson P. R., and Pratt, R. G., 1995, A critical review of the acoustic wave modeling procedure in 2.5 dimensions, *Geophysics*, **60**, 591-595.

Woodward, M. J., 1992, Wave-equation tomography, *Geophysics*, **57**, 15-26.

Wu Ru-shan and Toksöz, M., N., 1987, Diffraction tomography and multisource holography applied to seismic imaging, *Geophysics*, **52**, 11-25.

Xu B., and Noel M., 1993, On the completeness of data sets with multi-electrode systems for electical resistivity survey, *Geophysical Prospecting*, **41**, 791-801.

Xu, S. Z., Gao, Z. C., and Zhao, S. K., 1988, An integral formulation for three-dimensional terrain modeling for resistivity surveys, *Geophysics*, **53**, 546-552.

Zhang, J. Mackie, R., and Madden, T., 1995, 3-D resistivity forward modeling and inversion using conjugate gradients, *Geophysics*, **60**, 1313-1325.

Zhao, S., and Yedlin, M., 1996, Some refinements on the finite-difference method for 3-D dc resistivity modeling, *Geophysics*, **61**, 1301-1307.

Zhou, B., Greenhalgh, S., and Sinadinovski, C., 1992, Iterative algorithm for the damped minimum norm, least squares and constrained problem in seismic tomography, *Exploration Geophysics*, **23**, 497-505.

Zhou, B., and Greenhalgh, S., 1995, A fast approach to Fréchet derivative computation for resistivity imaging with different electrode arrays, *Geotomography* Vol.III *Fracture imaging,* Society of Exploration Geophysicists of Japan, 252-264.

Zhou, B., and Greenhalgh, S.A., 1997, A Synthetic study on crosshole resistivity imaging with different electrode arrays, *Exploration Geophysics*, **28**, 1-5.

Zhou, B., and Greenhalgh, S.A., 1998a, Composite boundary-valued solution of 2.5-D Green's function for arbitrary acoustic media, *Geophysics*, **63**, 1813-1823.

Zhou, B., and Greenhalgh, S.A., 1998b, A damping method for 2.5-D Green's function for arbitrary acoustic media, *Geophys. J. Int.*, **133**, 111-120.

Zhou, B., and Greenhalgh, S.A., 1998c, Crosshole acoustic velocity imaging with full-waveform spectral data: 2.5-D numerical simulations, *Exploration Geophysics*, **29**, 680-684.

Zhou, B., and Greenhalgh, S.A., 1998d, Explicit expressions and numerical calculations for the Fréchet and second derivatives in 2.5-D Helmholtz equation inversion: Geophysical Prospecting, in press.

Zhou, X. X., and Zhong B. S., 1984, *Numerical Modeling techniques for electrical prospecting,* Sichuan Science and Technology Press.

Zienkiewicz, 1971, *The finite element method in engineering science*, McGraw-Hill Book Company, Inc.